In vivo Molecular Targeted Imaging of Cancer

by

Quan Zhou

A dissertation submitted in partial fulfillment
of the requirements for the degree of
Doctor of Philosophy
(Biomedical Engineering)
in The University of Michigan
2017

Doctoral Committee:
Professor Thomas D. Wang, Chair
Professor Cheri Deng
Professor J. Brian Fowlkes
Professor Alnawaz Rehemtulla

© 2017

Quan Zhou

zhouquan@umich.edu

ORCID iD: 0000-0002-9351-5614

DEDICATION

To

My Parents

The true heroes of my life

ACKNOWLEDGMENTS

Last but not least, it is my father's tough love and my mother's unconditional love that brought me where I am. They gave me the gift of life and the freedom to pursue my dreams. Their passionate dedication to science and education is the source of inspiration all my life.

TABLE OF CONTENTS

LIST OF TABLES

LIST OF FIGURES

LIST OF VIDEOS

LIST OF ABBREVIATIONS

AFP	**alphafetoprotein**
ANSI	**American National Standards Institute**
AUC	**area under the curve**
BBB	**blood-brain barrier**
CD24	**cluster of differentiation 24**
CT	**computed tomography**
DLS	**dynamic light scattering**
EGFR	**epidermal growth factor receptor**
EMA	**European Union agency**
EPR	**enhanced permeability and retention**
FDA	**Food and Drug Administration**
GNS	**gold nanoshell**
GPC3	**glypican-3**
HAADF	**high angle annular dark field**
HBV	**hepatitis B virus**
HCC	**hepatocellular carcinoma**
HCV	**hepatitis C virus**
H&E	**hematoxylin and eosin**
HPLC	**high performance liquid chromatography**
ICG	**indocyanine green**
ICP-OES	**inductively coupled plasma - optical emission spectroscopy**
ID	**injection dose**
IF	**immunofluorescence**
IHC	**immunohistochemistry**
ISI	**Institute for Scientific Information**
LA	**lipoic acid**

LR	**liver resection**
MIP	**maximum intensity projection**
MPS	**mononuclear phagocyte system**
MRI	**magnetic resonance imaging**
MRS	**magnetic resonance spectroscopy**
NHS	**N-hydroxysuccinimide**
NIR	**near-infrared**
NP	**nanoparticle**
PA	**photoacoustic**
PAI	**photoacoustic imaging**
PBS	**phosphate-buffered saline**
PDX	**patient derived xenograft**
PEG	**polyethylene glycol**
PET	**positron emission tomography**
PTT	**photothermal therapy**
RES	**reticuloendothelial system**
ROC	**receiver operating characteristic**
ROI	**region of interest**
RT	**room temperature**
siRNA	**short interfering ribonucleic acid**
SPR	**surface plasmon resonance**
STEM	**scanning transmission electron microscopy**
T/B	**target-to-background**
TBS	**tris-buffered saline**
TEM	**transmission electron microscopy**
US	**ultrasound**

ABSTRACT

Hepatocellular carcinoma (HCC) presents a global healthcare problem. It is the second most lethal cancer worldwide, causing ~745,000 deaths annually. HCC accounts for 70% to 90% of primary liver cancer cases with rising incidence in developed countries. Newly diagnosed cases in the U.S. are expected to increase by 10% in three years. Symptoms of HCC typically do not appear until advanced stage, leaving surgical resection the primary therapy. However, HCC patients suffer from dire prognosis of less than 5% five-year survival rate and >50% incidence of tumor recurrence, due to poor contrast of HCC against surrounding liver tissue limiting resection accuracy. Using a molecular imaging system that targets differentially expressed tumor specific surface biomarkers may help detect HCC neoplasm missed by surgeons and preserve viable liver tissue to reduce recurrence and improve patient recovery. This dissertation presents the HCC targeting and imaging methods developed to specifically identify HCC neoplasm with high contrast, fast kinetics and deep penetration.

Two cancer cell surface biomarkers, epidermal growth factor receptor (EGFR) and glypican-3 (GPC3), are important in the development of HCC. To create a molecular imaging strategy for HCC detection, short peptide sequences specifically binding to these biomarkers have been selected and validated. They demonstrated high target affinities (k_d < 75 nM) and fast cellular binding kinetics (<10 min). After conjugating with near-infrared organic dye, these molecular targeting probes were able to home to the HCC tumor xenograft *in vivo* after intravenous administration. *Ex vivo* and *in vivo* optical imaging was conducted with fluorescent laparoscopy,

whole body fluorescent imaging, and hand held dual-axis confocal microscopy. *In vivo* cell surface binding of peptide probe to HCC xenograft in mice was observed at subcellular resolution in both horizontal (1000×1000 μm^2) and vertical (1000×430 μm^2) planes. Tumor margins were automatically detected with computerized segmentation algorithm. High target-to-background ratios (2.99 and 6.2 respectively) were achieved at tumor sites after 6 and 2 hours respectively, and targeting probes were cleared from the animal system within 24 hours. In addition, targeted *in vivo* photoacoustic tomography (PAT) imaging visualized probe penetration inside the tumor 1.8 cm beneath intact skin.

Plasmonic nanoparticles absorb light more efficiently than organic dyes. By coating GPC3 targeting peptide onto gold nanoshell (GNS) surface, *in vivo* photoacoustic imaging contrast was improved from 2.25 to 4.45 and imaging depth reached 2.1 cm. Peak probe uptake *in vivo* occurred at 2 hours and clearance took place within 12 hours, which are desirable pharmacokinetics for clinical settings of intraoperative imaging guidance. Specific binding, biodistribution and toxicity were investigated in cultured cells, *ex vivo* tissues (human and mouse) as well as in mouse models. The GPC3 targeting probe was able to distinguish HCC from non-HCC human patient biopsies (n=41) at 93% sensitivity and 88% specificity, with area under the receiver operator characteristic curve (AUC) value reaching 0.98. These studies showed that affinity peptide based molecular imaging is an enabling technology which will allow clinicians to perform functional imaging during surgery to identify resection margin with high contrast, sensitivity and speed.

Chapter 1   Introduction

1.1   Hepatocellular carcinoma

Cancer, and in particular, hepatocellular carcinoma (HCC), presents a global healthcare problem. It is found in countries all over the world especially in the Asia-Pacific region [1]. Worldwide, HCC is the second most lethal cancer, causing ~745,000 deaths annually [2], Figure 1.1. HCC has a high incidence rate of 31.4/100K in population [3]. HCC accounts for 70% to 90% of primary liver cancer cases [4]. Although it was historically more prevalent in developing countries, such as China and India [1], we are now seeing a rising incidence in developed countries as well [5]. In the United States, age-adjusted incidence rates of liver cancer more than tripled between 1975-2013 [6]. The number of newly diagnosed cases is expected to increase by 10% in three years [7]. With less than 5% 5-yr survival rate, HCC patients suffer from dismal outcome of the disease [8].
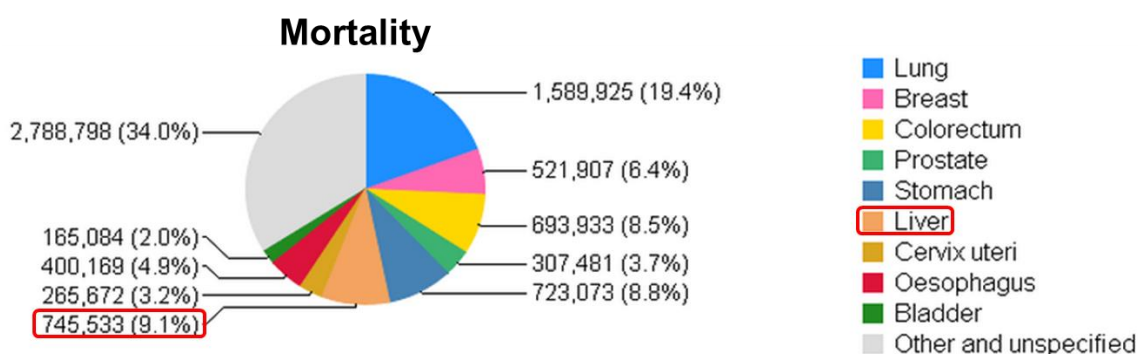
Figure 1.1 Global cancer mortality distribution. Liver cancer is the second most lethal cancer worldwide, following lung cancer, and accounted for more than seven million deaths in 2012. Adapted from GLOBOCAN 2012: Estimated Cancer Incidence, Mortality and Prevalence Worldwide in 2012, by J. Ferlay, I. Soerjomataram, et al., Retrieved from http://globocan.iarc.fr/Pages/fact_sheets_population.aspx.

1.2 Challenges and motivation

HCC patients suffer from dire prognosis. Symptoms of HCC typically do not appear until the cancer is advanced [7]. Only 10% to 20% of HCC tumors are diagnosed early enough for effective treatment [9-11]. Only 10% of patients receive liver transplants due to donor shortage [12]. Ablation is another option, usually in combination with other treatment methods [13]. Surgical resection remains the primary therapy [14, 15]. Liver resection (LR), also known as partial hepatectomy, is a potentially curative surgical treatment option for patients with HCC [16]. The goal of LR is to remove the HCC with an adequate margin, while preserving as much functional liver parenchyma with minimal blood loss and no complications [17]. Unfortunately, the incidence of tumor recurrence is >50% [18].
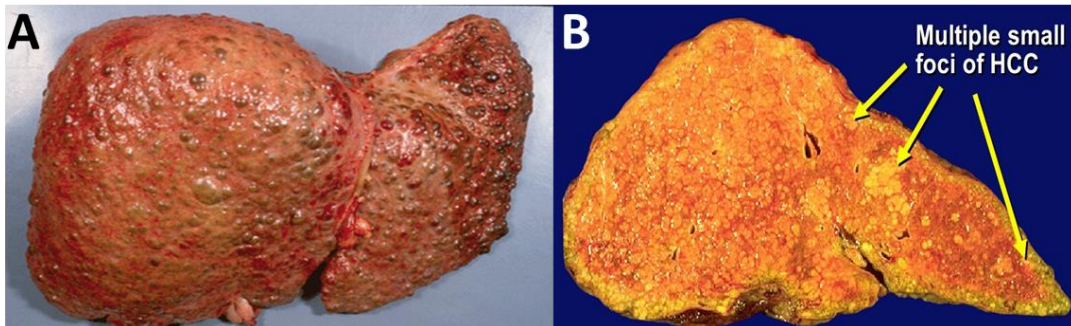
Figure 1.2 More than 80% HCC result from HBV related cirrhosis (A) a cirrhotic liver. Adapted from What is a liver transplant, 2015, retrieved from https://www.ucl.ac.uk/immunity-transplantation/diseases-and-treatments/transplantation/liver (B) multiple HCC foci in the background of cirrhotic liver. Adapted from Hepatocellular Carcinoma, by T. Hargrave. 2009, retrieved from http://slideplayer.com/slide/7043320.

The high recurrence rate is largely due to limited resection accuracy because the surgeons often cannot discern the exact sites of lesion from the background [19]. Patients with cirrhosis are at increased risk for developing HCC [20-22], and represent an important surveillance population [23-25]. Since more than 80% HCC cases result from HBV related cirrhosis, Figure 1.2(A), it is typical to resect HCC lesion in a background of cirrhotic liver [26]. HCC can have multiple small foci and difficult to be distinguished from the surrounding normal liver [27], Figure 1.2(B).

The lack of clear tumor margin forces the surgeon to remove more tissue than necessary and miss satellite locations [28]. A lack of effective and accurate surgical removal leads to poor prognosis resulting from either inadequate liver function or recurrence [29]. Therefore, intrasurgical detection with high contrast imaging of tumor biomarkers on transformed cells is critical for improving the survival of patients.

1.3 Molecular targets in cancer

Differentially expressed and tumor specific molecular targets on cancer cells can be visualized in pre-cancerous lesions well before gross architectural changes of cancer become apparent [30], and may be useful for early detection [31]. Recently, targeted imaging with peptides has been demonstrated as a diagnostic and visualization tool in both preclinical and clinical studies to guide surgical margins and enhance therapy in various cancers [32-36].

Biomarkers expressed on the plasma membrane are accessible to binding and imaging by molecular probes upon systemic delivery through blood and thus adopted as targets for the imaging strategy [37-39]. There are intracellular targets and genetic mutations [40-43], or proteins expressed on the cell surface, such as epidermal growth factor receptor (EGFR) [44-46], Epcam [47], c-MET [48, 49] and cluster of differentiation 24 (CD24), Figure 1.3. Among them, cell surface targets, EGFR and GPC3, have been examined in this thesis as molecular targets for HCC. Both are known to play important roles in cell proliferation, survival and migration of solid tumors including HCC [50-54].
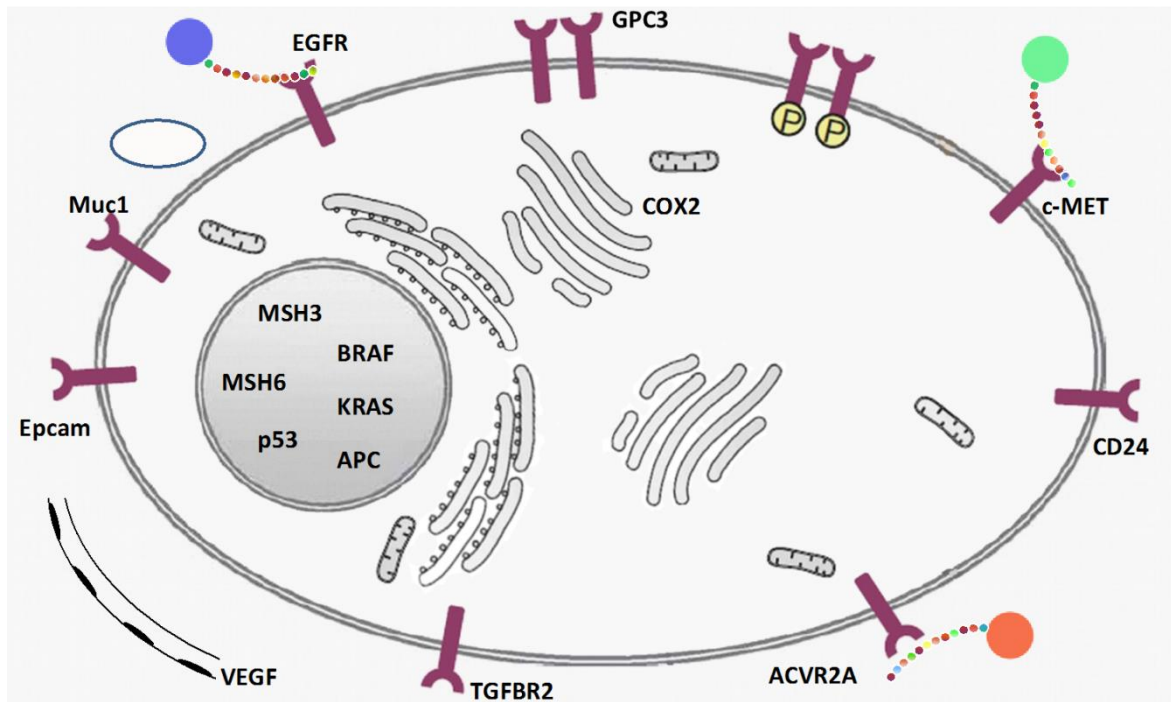
Figure 1.3 Molecular Targets in Cancer. Cancer cell can present a series of surface biomarkers as molecular targets. They are accessible for binding and imaging by molecular imaging probes.

EGFR was targeted first. The first sequencing of the primary liver cancer genome revealed a total of 11,731 somatic mutations [55]. Following studies showed that the CTNNB1, TP53, and EGFR genes were frequently mutated in liver cancer [56-59]. There is already a known peptide targeting it developed for colon cancer [60] and it is known to be exuberantly expressed on the membrane of HCC cells [61, 62]. Imaging HCC with EGFR-targeting peptide will provide proof of concept evidence for whether the molecular imaging strategy works in liver cancer.

A second biomarker, Glypican 3, was identified and targeted as well, because biomarkers on cancer cells can be heterogeneous [62-64]. Thus, it is important to multiplex different markers in order to capture a large percentage of patients [64, 65]. Glypican-3 (GPC3) is a heparan sulfate proteoglycan that is not found in normal adult liver, but is anchored to the cell surface of neoplastic hepatocytes and thus is accessible for imaging [66, 67]. It regulates the signaling

4

activity of several growth factors including Wnts [68, 69]. GPC3 promotes HCC growth by stimulating Wnt signaling, and has expression levels that reflect tumor stage [16].

1.4 Peptides as molecular probes

A variety of molecular probe platforms are available for imaging [70-72]. For instance, photoacoustic imaging has used molecular probes for targeted detection [73]. A protease sensitive oligomer labeled with Atto-740 was used to detect furin-like activity [74]. However, DMSO was needed to improve solubility, and the oligomers were found to aggregate and form nanostructures that trapped the reporter molecule inside the cells. For another instance, antibodies labeled with gold nanoparticles have been used to image molecular targets, such as Her-2, EGFR, CXCR4 and LYVE-1 [75-79]. Antibodies are high in molecular weight (thus bigger in size), and have long circulatory half-lives [80]. They also have limited ability to extravasate from the vasculature, penetrate into tumor, and clear from interstitial space [80, 81]. All of these properties increase imaging background. Antibodies are also prone to immunogenicity that limits repetitive use [82]. In contrast, RGD peptides have been used to target integrins in tumor-associated blood vessels that arise from angiogenesis and metastasis that occur at a late stage of tumor development [83-86]. Compared to antibodies, peptides are small in size and molecular weight. Thus, they can extravasate deep into tumor tissue and be cleared from the system with fast acting kinetics [87-89]. What takes days for antibody only requires hours for peptides [90, 91].
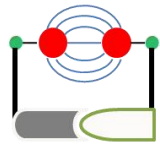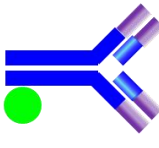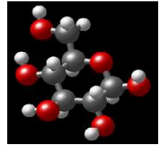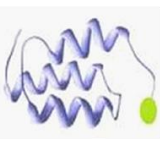
	Activatable	Antibody	Aptamer	Small molecule	Lectin	Peptide
Molecular Probe						
Strengths	amplification ↑T/B ratio targets	↑ specificity ↑ diversity ↑ affinity known targets	↑ specificity ↑ diversity ↑ affinity known targets	intracellular targets ↑T/B ratio	↑ specificity ↓ toxicity ↓ cost	↑ penetration ↑ kinetics ↑ clearance ↓ toxicity
Weaknesses	↓ specificity ↓ kinetics ? toxicity	↓ kinetics ↑ cost ↑ toxicity ↑ immunogenicity	↓ kinetics ↑ cost ? toxicity ↑ immunogenicity	↓ kinetics ↑ cost ↑ toxicity	↓ diversity ↓ affinity ↓ contrast	↓affinity ?immunogenicity

Table 1.1 Molecular probe platforms. A variety of molecular probe platforms (activatable, antibody, aptamer, small molecule, lectin and peptide) are available for imaging. They each have different strengths and weaknesses in term of affinity, specificity, kinetics, target-to-background (T/B) ratio, cost and immunogenicity. Affinity peptide possesses combination of features that are desirable for the clinically relevant molecular imaging strategy for HCC detection.

Table 1.1 highlights the major strengths and weaknesses of molecular probe platforms. Peptides have small size and low molecular weight that result in ideal pharmacokinetic properties for deep tissue imaging [91, 92]. Compared with bulky monoclonal antibodies, peptides provide an attractive alternative for visualizing tissue targets that would otherwise be difficult to penetrate or access [93]. Peptides have high diversity [94, 95], and can achieve high specificity with binding affinities on the nanomolar scale [60, 89, 96, 97]. This probe platform has flexibility to be labeled with a broad range of fluorophores [60, 89], and is inexpensive to produce in large quantities [98, 99]. It is also less immunogenic [100, 101] despite of having lower affinity than antibodies [102]. Thus labeled peptides were used in the following studies.

Peptides can also be used for image-guided surgery. This approach has been demonstrated using nonspecific dyes, such as indocyanine green (ICG) [103-105]. By targeting overexpression of biomolecules that are specific for HCC, better signal and lower background can be obtained [106, 107]. Improved visualization of tumor during resection may achieve a better balance between complete tumor resection and maintenance of liver function. The remaining volume of "normal"

liver parenchyma needed to optimize post-operative function can then be maximized [108, 109]. While molecular specificity may also be achieved in theory with frozen sections, at least 30-60 minutes are required for tissue processing while patients wait under general anesthesia [110]. Real time imaging can also be performed intra-operatively with ultrasound [111], but molecular specificity is difficult to achieve using this method.

1.5   Optical imaging as cancer diagnostic method

Optical imaging combined with molecular targeting is what this study is proposing as imaging method for HCC diagnosis. The existing diagnostic methods for HCC include ultrasound, CT, MRI and PET/CT scans [107, 112, 113], Table 1.2. These non-optical imaging modalities have limited ability to visualize multiple targets concurrently in real time [113]. On the other hand, the limitations of optical imaging are lack of penetration depth and use of exogenous contrast agents such as fluorescent dyes [114-116]. Combined with molecular targeting, optical imaging techniques can provide the speed and resolution needed to observe cellular and molecular events in real time [117-119].
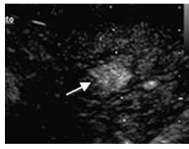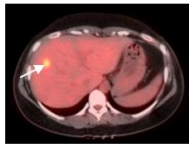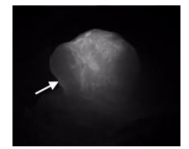
Modality	Ultrasound	CT scan	MRI	PET/CT	Optical imaging
Focal lesions					
Strengths	↑availability ↓cost validated	↑sensitivity ↓exam time ↑resolution	↑sensitivity label free ↑resolution	functional extrahepatic ↑contrast	targeted real time ↑contrast ↑resolution
Weaknesses	↓contrast structural speckle	↓ contrast structural radiation	structural ↑ cost ↓ throughput	↓ resolution ↑ cost ↓ throughput	↓ depth exogenous

Table 1.2 Methods for imaging HCC. Ultrasound is readily available and low in cost, but also has low contrast and resolution. CT and MRI are sensitive and high in resolution, but they only provide structural information, with the exception of metabolism

information on potential tumors from magnetic resonance spectroscopy (MRS) [120, 121]. PET/CT can offer functional information to identify extra hepatic metastasis, but can be costly and slow. Combined with molecular targeting, optical imaging techniques can provide the speed and resolution needed to observe cellular and molecular events in real time.

The NIR window is ideally suited for deep tissue *in vivo* imaging. The near-infrared (NIR) window defines the range of wavelengths from 650 to 950 nm [122], where light has its maximum depth of penetration in tissue, Figure 1.4. Minimal light absorption by hemoglobin (<650 nm) and water (>950 nm) makes probes absorbing within NIR range particularly useful [123]. By tuning the optical absorption of exogenous contrast agents to fall in the "tissue optical window" where tissue components have minimal absorption, it is possible to increase the imaging depth and contrast [124].
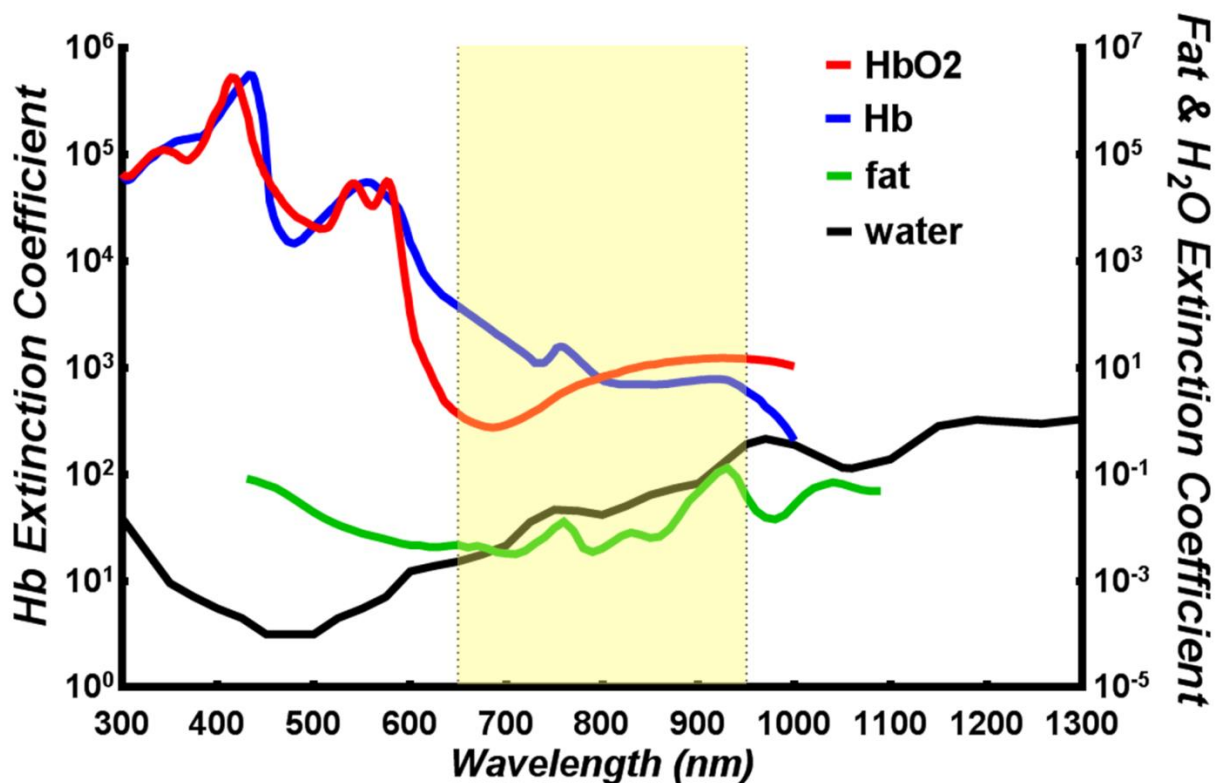
Figure 1.4 Light extinction property of Hb and water. The near-infrared (NIR) window defines the range of wavelengths from 650 to 950 nm where light has its maximum depth of penetration in tissue. At lower wavelength, hemoglobin (both oxygenated and deoxygenated) has higher light extinction and at higher wavelength, fat and water in tissue has increased light extinction. These endogenous agents can interfere with the *in vivo* imaging contrast and depth.

With molecular targeting and NIR fluorophore labeling we can improve the contrast and imaging depth specifically at tumor site. Antibodies, affibodies, and peptides are being developed for use as molecular probes to improve detection specificity with molecular imaging [125-129]. These targeting moieties can be labeled with bright fluorescent dyes to achieve high contrast and produce near-infrared (NIR) emission for deep tissue imaging [128, 130]. However, clinical usefulness of some probes has been limited by slow binding onset, long circulation times, and increased background [87, 131]. In contrast, peptides are well-suited for clinical use because of rapid binding kinetics, deep tissue penetration, lack of toxicity, and affordable cost [132]. Compared with conventional clinical imaging methods, optical imaging of NIR dye labeled peptide probes may improve cancer detection in the clinic.

For deep tissue imaging, probes absorbing in the NIR spectral range are desirable [133]. Two NIR contrast agents were attached to targeting probes in this study. One was a NIR fluorescent dye, Cy5.5, with peak absorption wavelength at $\lambda_{ex} = 677$ nm [134]. This organic dye label had the versatility to be imaged in various fluorescence imaging modalities necessary for *ex vivo* and *in vivo* validation of probe binding, as well as in photoacoustic tomography imaging to acquire depth information [60, 89, 135]. In order to push the contrast of deep tissue imaging further, a more optimal photoacoustic contrast agent was employed, namely gold nanoshell with peak light extinction wavelength at $\lambda_{ex} = 770$ nm [136, 137].

1.6   Summary

Hepatocellular carcinoma poses a significant medical challenge to global healthcare with limited treatment options. Surgical resection is currently the primary potential curative measure for HCC patients, but proved ineffective due to difficulty associated with low contrast of tumor margin against cirrhotic background during surgery. Therefore, high contrast imaging method that

specifically identifies the HCC lesion is critical for patient survival. And molecular targeted imaging of HCC with affinity peptide probe operating in the near-infrared spectral range was proposed to address the current challenge. Two surface biomarkers on HCC cells, namely EGFR and GPC3, were chosen as molecular targets for affinity peptides with deep tissue infiltration and fast kinetics. Combined with optical imaging technology, high contrast images in real time can be obtained beneath the surface of tissue to provide functional information in detection of cancer cells at improved accuracy.

Chapter 2   *In vivo* imaging of EGFR overexpression in cancer

In this chapter, EGFR targeting peptide previously used to collect fluorescence images endoscopically from mouse colonic adenomas with topical administration was labeled with NIR dye Cy5.5 and validated in both colorectal dysplasia and HCC cell lines. The use of *in vivo* optical and photoacoustic imaging to visualize HCC xenograft tumors in living mice with a peptide specific for EGFR was demonstrate. Peptide probe delivery inside tumor was also investigated. This body of work presented here has been published in peer-reviewed literature as contribution to the field: [138] for Section 2.2.1, [139] for Section 2.3 and [135] for Section 2.4.

2.1   Peptide targeting EGFR overexpression

2.1.1   EGFR as HCC target

Epidermal growth factor receptor (EGFR) overexpression is important for HCC progression [62]. The EGFR pathway plays an essential role in cell proliferation, survival and migration [50-54]. EGFR is overexpressed in various cancers including lung [140], breast [141], and esophagus [142], pancreas [143], head and neck [144], and was found to promotes solid tumor growth [145]. Its altered activity has been implicated in the development and growth of many tumors including HCC [146-148]. In previous studies, EGFR has been found to be overexpressed in 40-70% of HCC [44, 149-153], most likely contributing to aggressive growth characteristics [154, 155], metastasis formation, and resistance to therapy [152, 156-158].

EGFR has been an attractive target for biologics (e.g. peptide and affibody [127]) or antibodies in applications such as tumor-targeted imaging and therapy [159-161]. EGFR has served as

cancer biomarker and imaging target in previous studies to provide molecular information at tumor site after being labeled with different contrast agents including organic dyes [162-164] and metallic nanoparticles [77, 79, 165]. The EGFR inhibitor Gefitinib has been found to significantly reduce the incidence of HCC in an animal model [150]. Existing evidence led us to believe EGFR targeted imaging may improve detection specificity for HCC.

2.1.2   EGFR targeting peptide

An ideal platform for cell surface biomarker targeting with clinical translation potential should be target specific, fast binding and affordable [166]. A number of targeting platforms have being developed for use in precision medicine [167]. They include antibodies [168, 169], antibody fragments [170] aptamers [171], small molecules [172], vitamins [173] and lectins [174]. These agents were used to provide a biological basis for disease detection, establish patient prognosis, guide therapy, and monitor treatment response. Antibodies, such as those against EGFR and VEGF, have high specificity and affinity, and have been most commonly used in the clinic [175-177]. These moieties are large in size, high in molecular weight, and have long plasma half-lives[178]. High concentrations are needed for therapeutic effect [179, 180], resulting in increased costs. The long circulatory time and high cost of antibodies as targeting moiety in imaging could potentially inhibit acceptance for clinical translation as a diagnostic tool. This motivates our present study to explore feasibility for use of a cost-efficient and fast acting EGFR targeting peptide.

Here, we aim to demonstrate the use of a peptide specific for EGFR to target HCC tumors in a pre-clinical xenograft model. In contrast to antibody, peptides have small size and low molecular weight that result in ideal pharmacokinetic properties for deep tissue imaging. Peptides clear rapidly from non-target tissues, resulting in reduced background [135, 181]. Peptides can be

structurally altered to improve stability against proteolytic degradation, increase circulatory half-life, and enhance capillary permeability [182]. All of these attributes promote deep penetration into tissue and more effective targeting [183]. Previously, a peptide specific for domain 2 (extracellular) of EGFR has been developed [60]. This peptide was used previously to collect fluorescence images endoscopically from mouse colonic adenomas with topical administration. We now show that specific binding to EGFR can also occur with systemic administration in liver cancer mouse model.

2.1.3 Synthesis of EGFR peptide

Previously identified EGFR targeting peptide sequence, QRHKPRE (hereafter QRH*), was synthesized using standard Fmoc-mediated solid-phase synthesis [184]. We extended the monomeric linear peptide with a linker sequence GGGSK (same as the sequence on its 7-mer phages display library [185, 186]) to prevent interference of the dye in peptide binding, arriving at molecular weight of 1336.48 g/mol. Near-infrared dye Cy5.5 labeled EGFR targeting peptide probe, QRH*-Cy5.5, was synthesized by coupling QRH*-GGGSK peptide with water soluble sulfo-Cy5.5-N-hydroxysuccinimide ester (Lumiprobe LLC) respectively overnight with N,N-diisopropylethylamine, followed by HPLC purification. Cy5.5 has a delocalized positive charge in its chromophore and possesses high quantum yield (0.22 at 678 nm), good chemical stability, easy conjugation, and high sensitivity (mole extinction coefficient ~250,000 mol/cm) [187, 188]. The excitation/emission wavelength is 674/692 nm for Cy5.5, where hemoglobin and water have their lowest absorption coefficients [189].

Cy5.5-labeled peptides using standard Fmoc-mediated solid-phase synthesis was described below. We used Fmoc and Boc protected L-amino acids, and synthesis was assembled on rink amide MBHA resin. The peptide was synthesized on a PS3 automatic synthesizer (Protein

Technologies Inc). The C-terminal lysine was incorporated as Fmoc-Lys (ivDde)-OH, and the N-terminal amino acid was incorporated with Boc protection to avoid unwanted Fmoc removal during deprotection of the ivDde moiety prior to fluorophore labeling. Upon complete assembly of the peptide, the resin was transferred to a reaction vessel for manual labeling with the dye. The ivDde side chain protecting group was removed with 5% hydrazine in DMF (3x10 min) with continuous shaking at room temperature (RT). The resin was washed with dimethylformamide (DMF) and dichloromethane (DCM) 3X each for 1 min. The protected resin-bound peptide was incubated overnight with Cy5.5-NHS ester (Lumiprobe LLC) with DIEA, and the completion of the reaction was monitored by a qualitative Ninhydrin test. Upon completion of labeling, the peptide was cleaved from the resin using TFA: TIS: H_2O (95:2.5:2.5 v/v/v; Sigma-Aldrich) for 4 hours with shaking in the dark at RT. After separation of the peptide from the resin, the filtrate was evaporated with N_2 gas followed by precipitation with chilled diethyl ether and stored overnight at -20°C. The precipitate was centrifuged at 3000 rpm for 5 min and washed with diethyl ether 3X and centrifuged in between each washing step. The crude peptides were dissolved in 1:1 Acetonitrile/H_2O (v/v) and purified by prep-HPLC with a C18 column (Waters Inc) using a water (0.1% TFA)-acetonitrile (0.1% TFA) gradient. The final purity of the peptides was confirmed by analytical C18-column. Further characterization was performed with either ESI (Waters Inc) or Q-TOF (Agilent Technologies) mass spectrometry. The scrambled (control) peptide PEH*-Cy5.5 was synthesized, labeled, and purified in the same manner, hereafter PEH*-Cy5.5. After lyophilization, the peptides were stored at -80ºC and dissolved in water at a concentration of 300 µM. Molecular graphics and analyses of the peptides were performed with the UCSF Chimera package (v. 1.10.2, University of California, San Francisco).
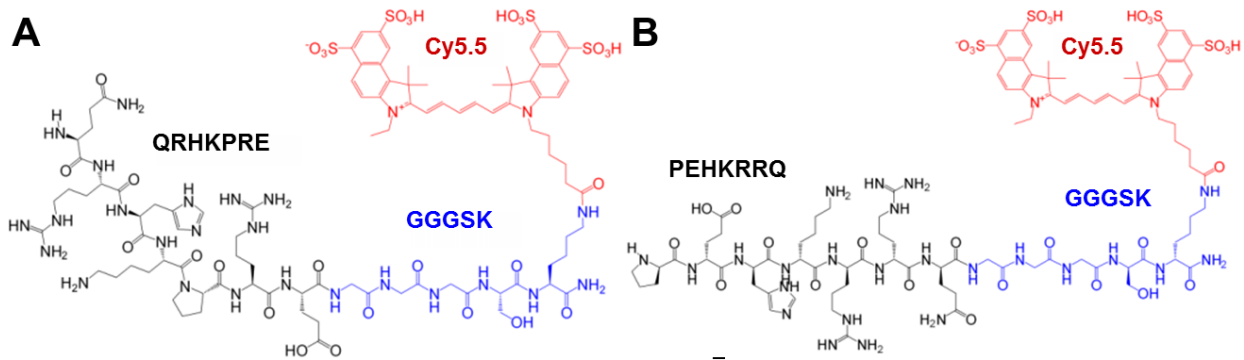
Figure 2.1 NIR dye labeled EGFR targeting peptides. (A) Chemical structure of QRHKPRE peptide (black) with GGGSK linker (blue) and Cy5.5 fluorophore (red), hereafter QRH*-Cy5.5. (B) Scrambled control peptide PEHKRRQ, hereafter PEH*-Cy5.5.

As illustrated in the structural schematics, EGFR targeting 7-mer peptide, QRHKPRE (black), was labeled on the C-terminus with Cy5.5 (red) via a GGGSK linker (blue), Figure 2.1(A). A scrambled control peptide, PEHKPRE, was also synthesized by scrambling the targeting peptide sequence without changing the amino acid make up, Figure 2.1(B).

2.1.4   EGFR targeting probe characterization

After scrambling the targeting peptide, the 3D structure as well as chemical environment changed significantly, Figure 2.2 (A-B), which explains the difference in their target binding abilities. The arrows mark the positions of labeled dye, Cy5.5, while the arrow heads indicate the starting amino acids in the peptide sequences. This is a computationally modeled structure rather than an actual determined structure. Ultimately, X-ray crystallography would determine the most accurate structures of purified and crystalized peptides. But such endeavor is beyond the scope of this thesis.
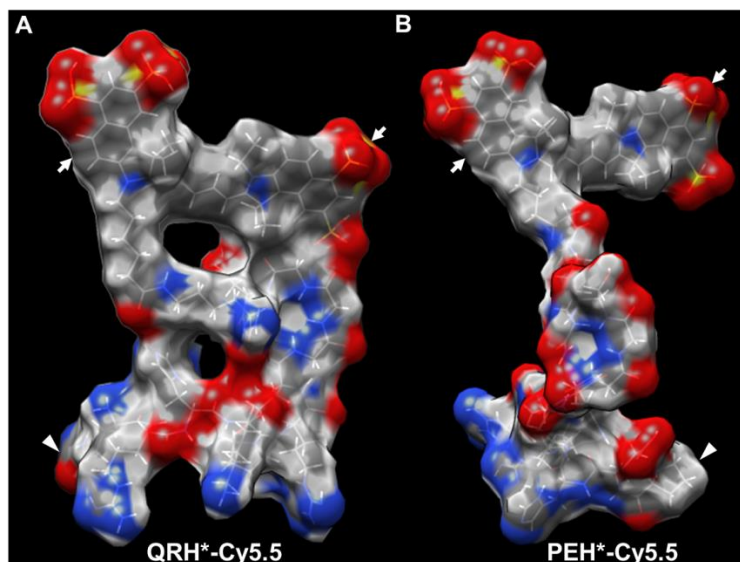
Figure 2.2 3D space filling structure of EGFR targeting probe and corresponding scrambled control probe. Structural differences were observed between (A) targeting and (B) scrambled control peptides. Cy5.5 dye was labeled on C-terminal of each 7-mer peptide and the sulfonated benzo-fused indolenine rings are marked with arrows. The N-terminals of peptides where the 7-mer sequences begin are denoted with arrow heads. Both the overall shapes and local chemical environments are different in the two probes. Color code: grey-C; white-H; red-O; blue-N; yellow-S.

Using a structural model, a binding energy of E_t = -554.81 kcal/mol was found for docking to crystal structure of human EGFR complex extracellular domains (Protein Data Bank index: 1IVO) [60]. By comparison, we found E_t = -535.37 kcal/mol for the scrambled (control) peptide, PEH*-Cy5.5. In the model, QRH*-Cy5.5 binds to amino acids 230–310 of EGFR (extracellular domain 2), Figure 2.3(A). The absorption spectra of QRH*-Cy5.5 and PEH*-Cy5.5 at 100 µM concentration in water shows a peak at λ_{abs}=677 nm, Figure 2.3(B). The fluorescence spectra of QRH*-Cy5.5 and PEH*-Cy5.5 at 100 µM concentration in water shows a peak at λ_{em}=708 nm when excited by λ_{em}=671 nm laser, Figure 2.3(C).

16
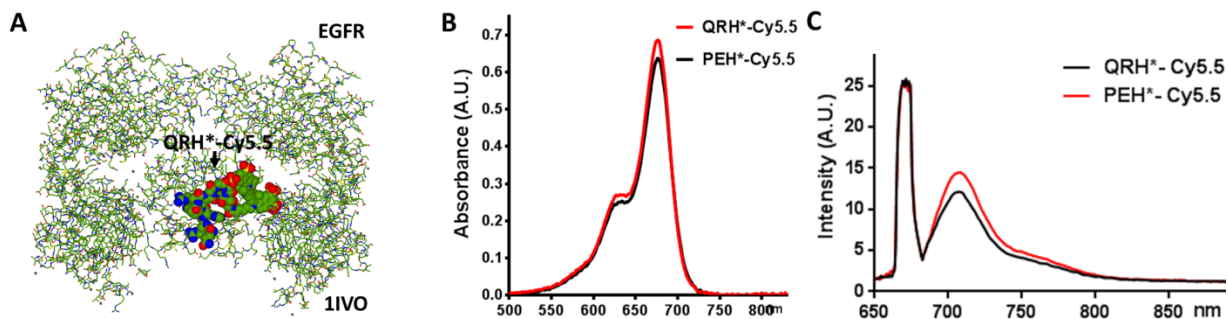
Figure 2.3 Modeling of EGFR peptide binding and spectral analysis (A) QRH*-Cy5.5 was found on the structural model (1IVO) to bind EGFR extracellular domain 2. (B) Absorbance spectra of Cy5.5-labeled peptides shows peak at $\lambda ex = 677$ nm. (C) Maximum fluorescence emission peak occurred at λ_{em}=708 nm when excited by λ_{em}=671 nm laser.
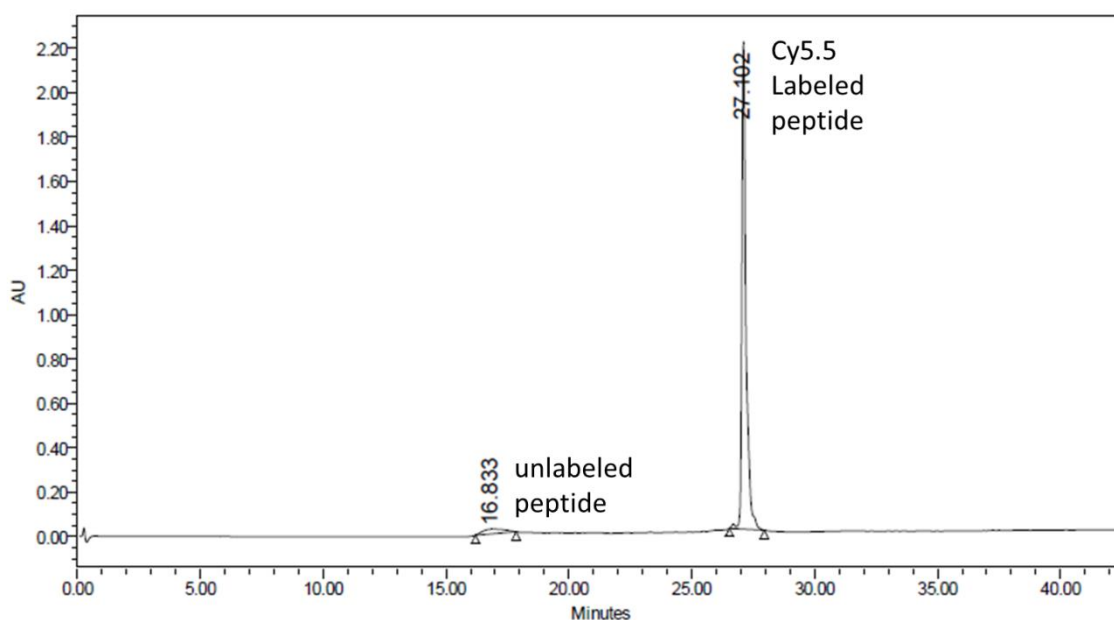
	RT (min)	Peak Type	Area (µV*sec)	% Area	Height (µV)	% Height	Integration Type	Peak Codes	Points Across Peak
1	16.833	Unknown	1262070	4.66	20661	0.93	bb	I08	99
2	27.102	Unknown	25795299	95.34	2198424	99.07	bb		85

Figure 2.4 Purification of EGFR peptide in HPLC. Cy5.5 labeled QRH* peptide is eluded at 27min on HPLC while the unlabeled peptide is eluded at 17min. The purity of dye labeled peptide reached 95.34% as quantified by the area under the peaks.

Cy5.5-labeled peptides were purified to >95% on HPLC, Figure 2.4, detected at 214 nm which is absorbed by peptide bonds. This result was confirmed on mass spectrometry. We found a molecular weight of 2232.88 g/mol, which agrees with the expected value, Figure 2.5(A-B).
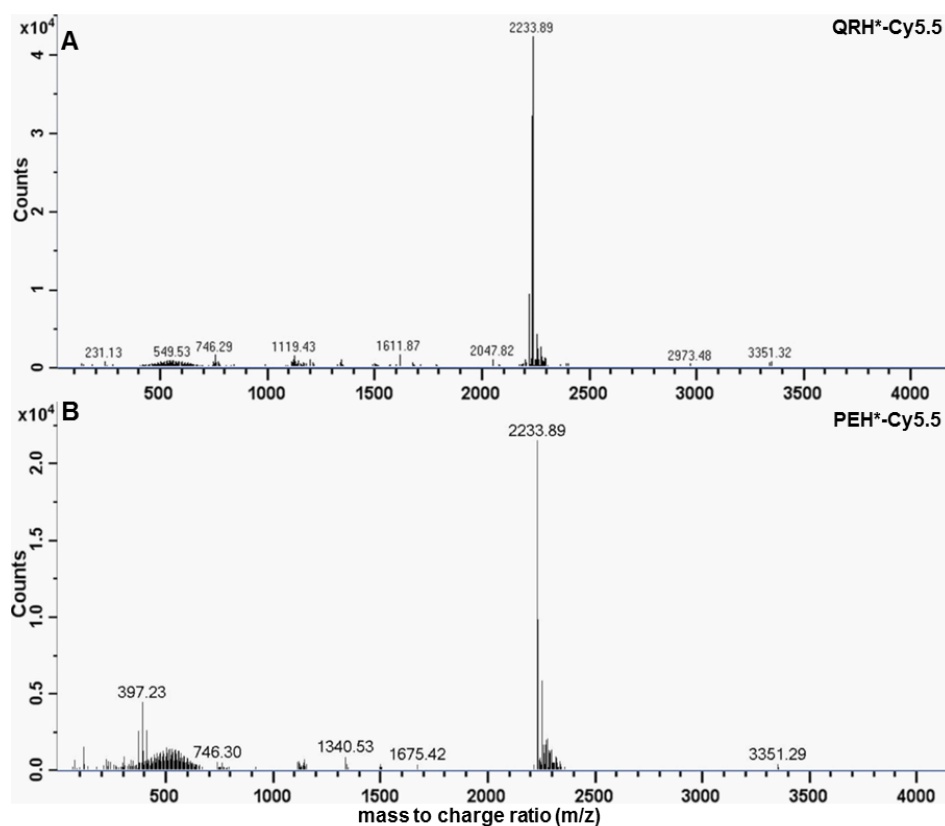
Figure 2.5 Mass spectroscopy of Cy5.5 labeled EGFR peptide. Experimental mass-to-charge (m/z) ratios for (A) QRH*-Cy5.5 and (B) PEH*-Cy5.5 were found to be 2233.89 (with one C-13), and agreed with the expected values.

2.2 Validation of EGFR targeting peptide

Unlike in the previous study where the targetability of NIR dye labeled EGFR targeting peptide QRH* was validated in colon cancer [60], the Cy5.5 label on QRH* in this study was customized and modified with four sulfo-groups to improve its solubility. Therefore, it is critical to revalidate its targetability in colon cancer after labeling with the more soluble version of Cy5.5 before moving on to its validation and imaging applications in HCC.

2.2.1 Validation in colonic dysplasia

We used the same colorectal cancer mouse model for EGFR peptide validation as previously described [5]. Transgenic *CPC;Apc* mouse spontaneously developed pre-malignant (dysplasia) lesions in the distal colon where they are accessible by the front-view endomicroscope [190].

These mice are genetically engineered to sporadically delete the APC gene, which is mutated in >80 of human colorectal carcinomas [6]. The results presented here were published in peer-reviewed journal article [138].

2.2.1.1 *In vivo* wide field fluorescent colonoscopy

Wide field fluorescent colonoscopy helped confirm the peak fluorescence intensity time point after EGFR targeting probe injection. Subsequently experiment mice were sacrificed and subject to *ex vivo* binding validations with other imaging methods. During imaging, 12-week-old *CPC;Apc* mice were anesthetized with 2% isoflurane (Fluriso; MWI Veterinary Supply Co.). We first used a wide-field small animal endoscope (27030BA, Karl Storz Veterinary Endoscopy) with white light illumination to examine the colon for presence of grossly visible adenomas, Figure 2.6(A). We waited 90 min after intraperitoneal injection of 300μM of QRH*-Cy5.5 solution in a volume of 600 μL to allow the peptide to bind to its target. Increased fluorescence signal in colon polyp was observed, Figure 2.6(B) in endoscopic image. Reflectance image had even intensity at polyp and surrounding normal tissue,

Figure 2.6(C), indicating the increased fluorescence signal observed at colon polyp was not due to its vicinity to the laser source at the center. No auto-fluorescence was detected in mouse colon prior to peptide injection.
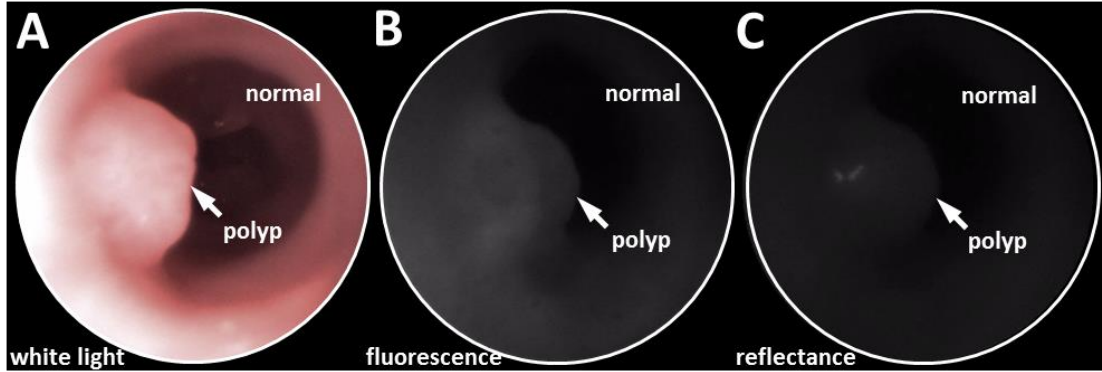
Figure 2.6 *In vivo* small animal endoscopy of colonic adenoma in mouse. (A) White light image of CPC;Apc mouse colon collected *in vivo* with wide-field endoscope shows location of spontaneous adenoma (arrow). (B) Maximum uptake of the NIR-labeled EGFR peptide QRH*-Cy5.5 is seen from the adenoma ~90 minutes after systemic administration. (C) Reflectance image at the same field of view.

2.2.1.2 Macroscopic fluorescent imaging

After completion of *In vivo* wide field fluorescent colonoscopy imaging, the animals were euthanized, and the colon was excised, flushed with PBS, and divided longitudinally for macroscopic imaging (IVIS 200, Caliper Life Sciences), to validate specific uptake of QRH*-Cy5.5 by adenomas. NIR fluorescence images were collected using a Cy5.5 filter with $\lambda_{ex} = 675$ nm excitation and 720 nm emission with 0.05 sec exposure. A ruler was placed next to the specimen to determine the distance from the anus for registration with the endoscopy and histology images.

Representative NIR fluorescence image showed increased fluorescence intensity from adenomas (lower dotted rectangle) compared with adjacent normal colonic mucosa (upper dotted rectangle), Figure 2.7(A). Fluorescence intensities were measured from rectangular regions of interest (ROI) around the dysplasia and a rectangle of equal area over adjacent normal (Living Image 4.0 software PerkinElmer). The intensity was defined by the sum of the radiance from each pixel inside the ROI/number of pixels (photons/s/cm^2/sr). The target-to-background ratio for each adenoma was calculated by dividing average radiance in ROI of dysplasia with that of normal

20

colon. We measured a T/B ratio of 3.47±1.87 from n = 6 mice. The co-registered white light image confirms the locations of adenomas, Figure 2.7(B).
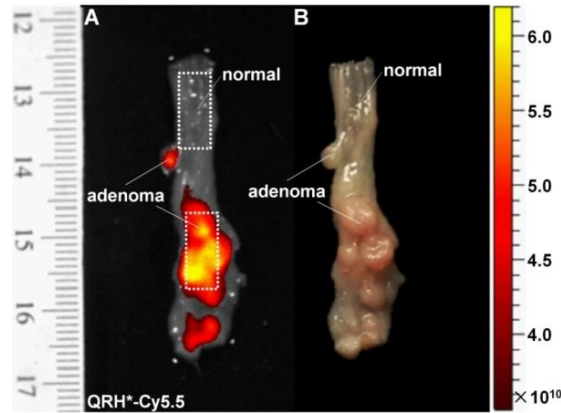
Figure 2.7 Macroscopic fluorescent imaging of peptide binding to colonic adenoma. (A) Representative NIR fluorescence image collected *ex vivo* showed selective uptake of QRH*-Cy5.5 in adenomas compared with adjacent normal colonic mucosa. Intensities were measured from the ROIs defined by the dotted rectangles. We calculated a mean T/B ratio of 3.47±1.87 from the group of n = 6 mice. (B) Co-registered white light image of exposed mucosal surface confirms locations of adenomas.

2.2.1.3 Microscopic immunofluorescent staining

Resected adenomas and normal colonic mucosa from n = 6 mice were cut in 5 μm thick sections, and mounted onto glass slides (Superfrost Plus, Fischer Scientific). The tissues were deparaffinized, and antigen retrieval was performed using standard methods. Briefly, the sections were incubated in xylene for 3 min three times, washed with 100% ethanol for 2 min two times, and washed with 95% ethanol for 2 min two times. Rehydration was performed by washing the sections twice in dH$_2$O for 5 min. Antigen unmasking was performed by heating the slides in 10mM sodium citrate buffer with 0.05% Tween at pH 6.0, and then maintaining at a sub-boiling temperature for 15 min. The slides were cooled for 30 min. The sections were washed three times in dH$_2$O for 3 min, Blocking was performed with DAKO protein blocking agent (X0909, DAKO) for 1 hour at RT, followed by rinsing with PBS. The sections were then incubated with 1:1000 dilution of primary monoclonal mouse anti-EGFR antibody (Thermo Scientific, #MS-396, clone 199.12, IgG2a isotype) overnight at 4 °C. Afterwards, the sections were washed 3X with

PBS, and further incubated with 1:500 dilution of AF488-labeled secondary goat anti-mouse IgG antibody (Life Technologies, #A-11029) for 1 hour at RT, washed 3X, and then mounted on glass slides with ProLong Gold reagent containing DAPI (Invitrogen)) using #1 cover glass (1.5 μm thickness). Confocal fluorescence images were collected with AF488 and DAPI filters using a confocal microscope (Leica TCS SP5 Microsystems). The mean fluorescence intensities from 3 boxes with dimensions of 30×30 μm^2 located completely within the surface epithelium of each specimen were measured. Regions that showed saturated intensities were avoided.

In parallel, we validated specific binding of the EGFR peptide to pre-cancerous crypts with immunofluorescence. Fresh whole mount tissues from sacrifice mice at 90 min post i.p. injection of EGFR targeting probe was imaged with confocal microscope (Leica SP5 Upright, Germany) with Cy5.5 and DAPI filters. The colon was then fixed in 10% buffered formalin and paraffin embedded for routine histology (H&E). Sections were cut in the plane parallel to the mucosal surface. A low magnification view shows specific staining of the EGFR peptide to dysplastic crypts, Figure 2.8(A) and Video 2.1. On the magnified view of dashed red box in Figure 2.8(A), increased intensity (arrow) is seen at the cell surface of dysplastic colonocytes, Figure 2.8(B). A similar result is found for AF488-labeled anti-EGFR antibody to an adjacent section, Figure 2.8(C). We observed greatly reduced staining of both the EGFR peptide and antibody to sections of normal colon, Figure 2.8(D-F). Representative histology (H&E) is shown for dysplasia and normal, Figure 2.8(G-H). The mean fluorescence intensities from 3 boxes with dimensions of 30×30 μm^2 located completely within the surface epithelium of each specimen were measured. Regions that showed saturated intensities were avoided. We found significantly greater mean fluorescence intensities for dysplasia compared with that of normal in n = 6 mice, Figure 2.8(I).
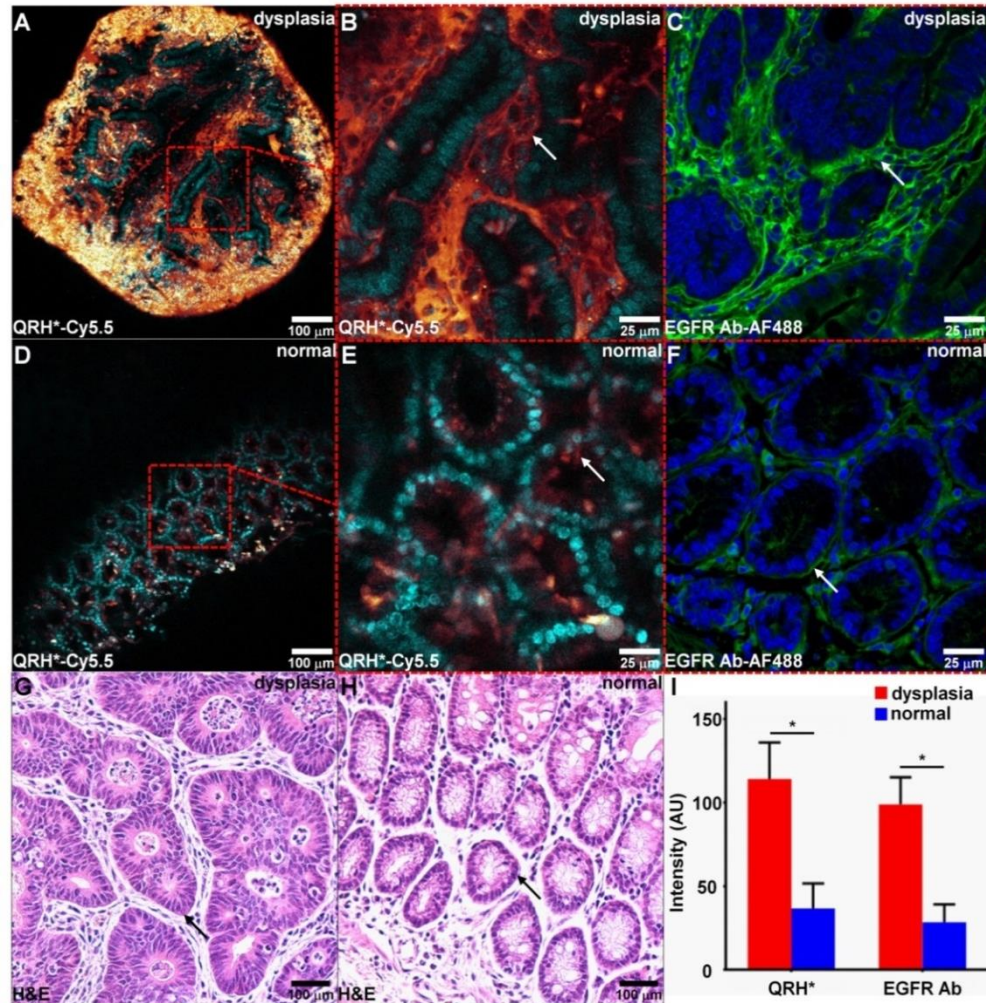
Figure 2.8 Immunofluorescence staining of EGFR targeting peptide to mouse colonic adenoma. (A) Strong fluorescence intensity is seen from staining of the EGFR peptide QRH*-Cy5.5 to dysplasia. Magnified view of dashed red box in (A) show specific binding of (B) the peptide (arrow) and (C) known AF488-labeled anti-EGFR antibody (arrow) to the surface of dysplastic colonocytes. (D) Minimal uptake of QRH*-Cy5.5 is seen in normal colonic mucosa. Magnified views of dashed red box in (D) show faint binding of (E) the peptide (arrow) and (F) AF488-labeled anti-EGFR antibody (arrow) to surface of normal colonocytes. Representative histology (H&E) of (G) dysplasia and (H) normal colonic mucosa. (I) Confocal microscopy images from n = 6 mice showed a mean±SD fluorescence intensity for dysplasia that was significantly greater than that for normal with QRH*-Cy5.5, 114.3±21.8 versus 36.8±14.9, *P = 3.0×10^{-5}, and AF488 anti-EGFR antibody, 99.1±16.1 versus 28.4±10.7, *P = 3.5×10^{-4}, respectively, by paired two-way t-test.
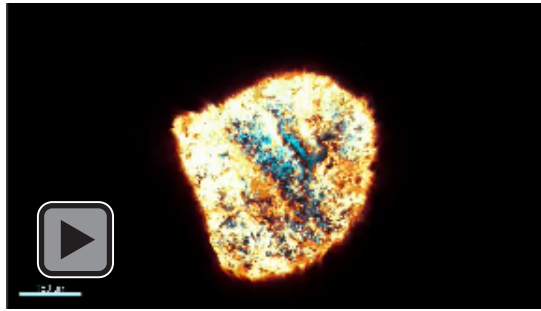
Video 2.1 Peptide (red) binding to whole mount mouse colon polyp 2D flythrough

2.2.1.4 Microscopic immunohistochemical staining

We then performed immunohistochemistry on sections of mouse colon with EGFR antibody. Formalin-fixed sections of human HCC and normal liver were deparaffinized, and antigen retrieval was performed using standard methods. Briefly, the sections were incubated in xylene for 3 min 3X, washed with 100% ethanol for 2 min 2X, and washed with 95% ethanol for 2 min 2X. Rehydration was performed by washing 2X in dH_2O for 5 min. Antigen unmasking was performed by heating the slides in 10 mM sodium citrate buffer with 0.05% Tween at pH 6.0, and then maintaining at a sub-boiling temperature for 15 min. The slides were cooled for 30 min. The sections were washed 3X in dH_2O for 3 min, and then incubated in 3% H_2O_2 in H_2O for 10 min. The sections were washed 3X in dH_2O for 2 min and in PBST for 5 min. We used 1:500 dilution of polyclonal goat anti-rabbit antibody (GαR; Cell Signaling Technology, #2232). Blocking was performed with DAKO protein blocking agent (X0909, DAKO) for 45 min at RT. The sections were incubated overnight at 4ºC and then washed in PBS for 5 min 3X. A 1:200 dilution of secondary antibody (goat anti-rabbit IgG) was added to each section and incubated for 30 min at RT. The secondary antibody solution was removed by washing 3X with PBS for 5 min. Pre-mixed Elite Vectastain ABC reagent (Vector Labs) was added to each section and incubated for 30 min at RT. The sections were washed 3X in PBST for 5 min, and developed with DAB substrate. The reaction was monitored for 3 min, and then quenched by immersing the slides in dH_2O. Hematoxylin was added as a counterstain for ~20 sec, and the sections were dehydrated in

increasing concentrations of ethyl alcohol (70%, 80%, 95% 2X, 100% 2X). Coverslips were attached using permount mounting medium (Fisher, #SP15-100) in xylene. Much higher expression in dysplasia, Figure 2.9(A) than normal colon tissue of the mouse was observed on immunohistochemistry, Figure 2.9(B).
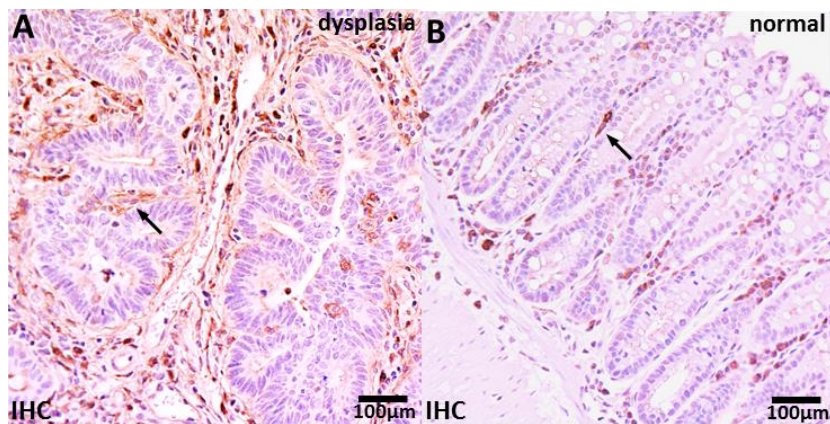
Figure 2.9 IHC of EGFR expression in colon dysplasia. Representative immunohistochemistry images of (A) dysplasia and (B) normal colonic mucosa.

2.2.2 Validation in HCC

As Section 2.2.1 demonstrated, EGFR peptide probe with highly soluble Cy5.5 label, QRH*-Cy5.5, proved to bind specifically to EGFR overexpression in colorectal dysplasia. This prompted us to examine its performance in a different cancer, HCC. Some quick and simple experiments to see if QRH*-Cy5.5 probe actually binds to EGFR on surface of human HCC cell lines were first conducted *in vitro* before *in vivo* delivery and imaging in HCC mouse model was undertaken.

2.2.2.1 EGFR expression in HCC cell lines

Rather than mouse tissue, three human HCC cell lines with high, low and negative EGFR expression levels were used to validate specific peptide probe binding to EGFR. Human HCC cells, SK-Hep1, Hep3B and HepG2, were purchased from the ATCC (Manassas, VA) and

cultured in Eagle's Minimum Essential Medium (EMEM). All cells were cultured at 37ºC in 5%

CO_2, and supplemented with 10% fetal bovine serum (FBS) and 1% penicillin/streptomycin.

Western blot was performed using a 1:1000 dilution of primary polyclonal rabbit anti-EGFR

antibody (#2232S, Cell Signaling Technology) per manufacturer instructions. Loading was

controlled with a 1:500 dilution of monoclonal mouse anti-β-tubulin (#32-2600, Invitrogen).

Western blot of cells was shown in Figure 2.10. The differential EGFR expression levels in these

three HCC cell lines served as the testing field for the specificity of EGFR binding by peptide

probe. Binding intensity in each cell line was expected to correlate with EGFR abundance and

was measured through the fluorescence signal on immunofluorescent imaging.
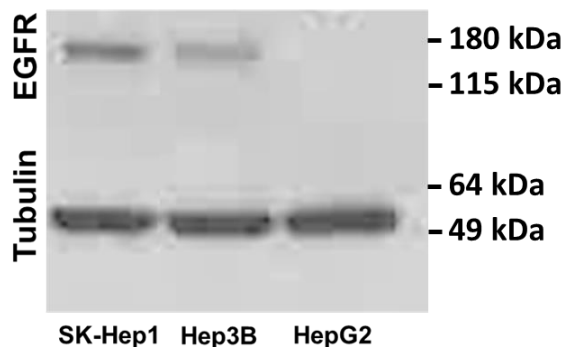
Figure 2.10 Western blot shows EGFR expression levels for HCC cells. EGFR has a molecular weight of 170 kDa and is overexpressed in SK-Hep1 cells, moderately expressed in Hep3B cells and didn't express in HepG2 cells. Loading control was performed with tubulin (molecular weight = 50 kDa).

2.2.2.2 *In vitro* immunofluorescent imaging

~10^3 cells (SK-Hep1 Hep3B and HepG2) were grown on coverslips to ~80% confluence, washed

with PBS and incubated with 5 μM of QRH*-Cy5.5 and PEH*-Cy5.5 for 10 min at RT

respectively. The cells were then washed 3X in PBS, fixed with ice cold 4% paraformaldehyde

(PFA) for 10 min, washed 1X with PBS, and then mounted on glass slides with ProLong Gold

reagent containing DAPI (Invitrogen). Confocal fluorescence images were collected with Cy5.5,

and DAPI filters. Confocal microscopy (Leica Inverted SP5X) was performed using a 63X oil-

immersion objective. Fluorescence intensities from 5 cells in 2 independent images were quantified using custom Matlab (Mathworks) software. For antibody staining, the cells were pre-fixed with cold methanol for 10 min at -20ºC and blocked with 2% BSA for 30 min at RT. Cells were incubated with 1:1000 dilution of anti-EGFR antibody overnight at 4ºC. The cells were washed 3X with PBS and processed for secondary staining. Goat-anti rabbit Alexa-Fluor 488 (AF488) was added to the cells and incubated for 1 hour at RT. Cells were further washed 3X with PBS and mounted onto glass cover slips.
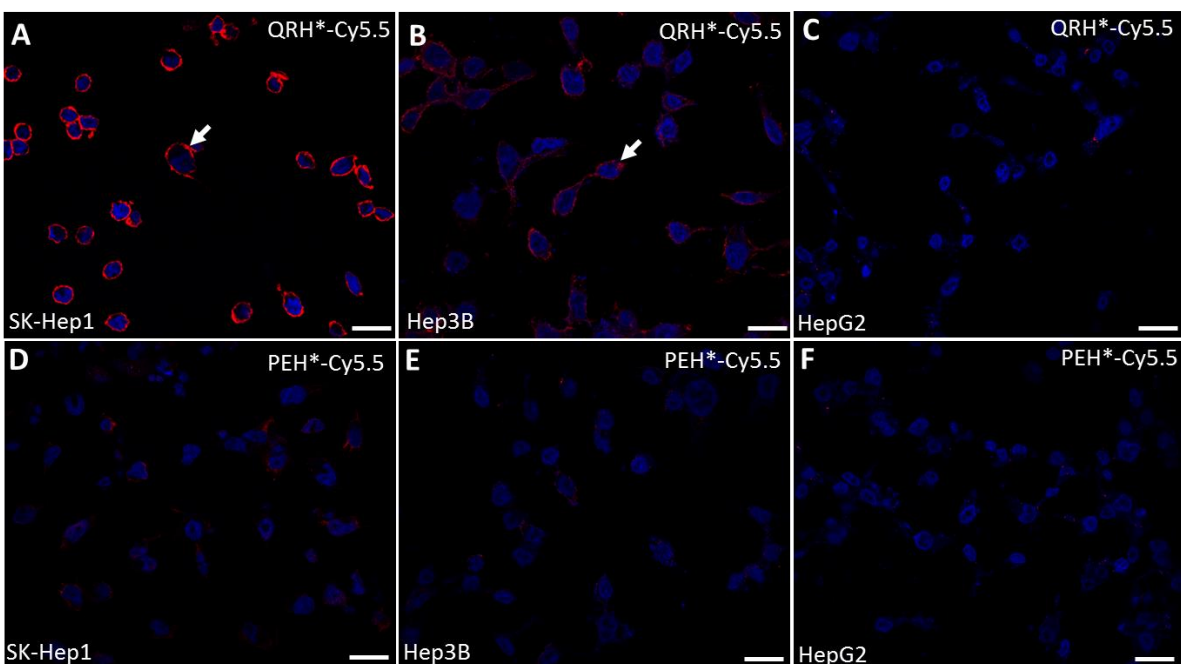
Figure 2.11 Immunofluorescent staining of EGFR peptide on HCC cell lines. On confocal microscopy, we observed fluorescence at the surface (arrow) of (A) SK-Hep1, (B) Hep3B, and (C) HepG2 cells that have different levels of EGFR expression after incubation with QRH*-Cy5.5. D-F) Minimal signal is observed with PEH*-Cy5.5 for all cells.

On confocal microscopy, we assessed binding of QRH*-Cy5.5 and PEH*- Cy5.5 to human HCC cells SK-Hep1, Hep3B, and HepG2 cells that expressed different levels of EGFR, respectively. For QRH*-Cy5.5, we observed different strengths of binding to the cells, Figure 2.11(A–C). High resolution confocal imaging allowed for clear visualization a thin ring of staining from cell surface binding (arrows). Minimal binding was observed for PEH*-Cy5.5 (control) to all cells,

Figure 2.11(D–F). Additional validation with siEGFR knockdown experiment was performed previously on EGFR overexpressing cell line, HT29, with both peptide and EGFR antibody [60].

We measured significantly greater fluorescence intensity from QRH*-Cy5.5 compared to PEH*-Cy5.5 for SK-Hep1 and Hep3B cells but not for HepG2, Figure 2.12. Quantified measurements showed that QRH*-Cy5.5 has significantly greater intensities than PEH*-Cy5.5 on binding to SK-Hep1 and Hep3B cells (5.72 and 6.57 fold-change, $P=1.63\times10^{-5}$ and 1.05×10^{-5}, respectively). A non-significant difference was found for HepG2 cells (1.02 fold-change, $P=0.91$). Differences between QRH*-Cy5.5 and PEH*-Cy5.5 for SK-Hep1 and Hep3B were significantly greater than that for HepG2 (5.63 and 6.46 fold-change, $P=1.25\times10^{-4}$ and 8.12×10^{-5}, respectively). We fitted two-way ANOVA models with terms for 3 cell lines, 2 peptides, and their interactions to log-transformed data. Measurements are an average of 5 randomly chosen cells on 2 slides for each condition.
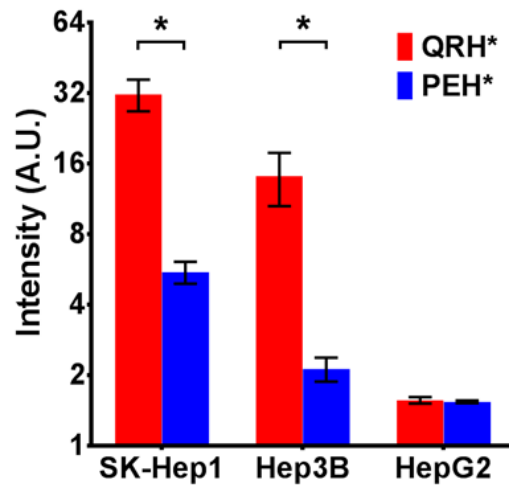
Figure 2.12 Quantification of peptide staining on HCC cell lines. Quantified measurements showed that QRH*-Cy5.5 has significantly greater intensities than PEH*-Cy5.5 on binding to SK-Hep1 and Hep3B cells (5.72 and 6.57 fold-change, $P=1.63\times10^{-5}$ and 1.05×10^{-5}, respectively). A non-significant difference was found for HepG2 cells (1.02 fold-change, $P=0.91$). Differences between QRH*-Cy5.5 and PEH*-Cy5.5 for SK-Hep1 and Hep3B were significantly greater than that for HepG2 (5.63 and 6.46 fold-change, $P=1.25\times10^{-4}$ and 8.12×10^{-5}, respectively).

2.3 *In vivo* optical imaging of EGFR in HCC

The *ex vivo* and *in vitro* validations in Section 2.2 of QRH*-Cy5.5 probe binding to EGFR in both colorectal dysplasia tissue and HCC cell lines respectively have provided valuable evidence of QRH*-Cy5.5 probe's ability to detect cell surface EGFR overexpression in multiple cancer types. Rather than being applied directly onto tumor cells as in the *in vitro* experiment before, animal tumor model challenges the delivery of peptide to tumor site after injecting it into the blood stream of the mouse. Therefore, the probe's performance in *in vivo* imaging of HCC mouse model would inform the potential of clinical translation value of the probe in HCC patients. The results presented here were published in peer-reviewed journal article [139].

2.3.1 Customized laparoscopic fluorescence imaging system

To investigate the feasibility of using peptide probe for intraoperative surgical guidance, a standard laparoscope used during hepatobiliary surgery on human patients was customized to detect fluorescent signal. NIR laser was delivered through the light guide, while both reflectance and fluorescence signals from the tumor were collected to detect the location of tumor during surgery.
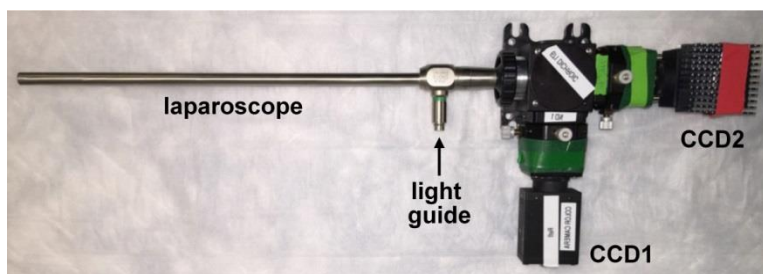
Figure 2.13 NIR fluorescence laparoscope. An imaging module that contains the optics, filters, and cameras was attached to the the proximal end of a standard laparoscope used for surgical resection of HCC. Fluorescence excitation at λ_{ex} = 671 nm was delivered through a fiber optic light guide attached on the side.

We used a standard surgical laparoscope (#49003 AA, HOPKINS® II Straight Forward Telescope 0°, Karl Storz) that is commonly used by surgeons to perform radical resection of

HCC. The laparoscope was ~10 mm in diameter and had a 31 cm length rigid sheath to collect reflectance and fluorescence concurrently. On the proximal end, we attached either a color camera to collect conventional white light images or an imaging module to collect co-registered reflectance and fluorescence images, Figure 2.13. Reflectance was used to help identify the location of the tumor when the color camera is not attached. Excitation at λ_{ex} = 660 nm was delivered into the fiber optic light guide. The imaging module contained the optics, filters, and cameras. This instrument was handled easily by a hepatobiliary surgeon (Dr. Zhao Li) who is experienced with laparoscopic procedures.
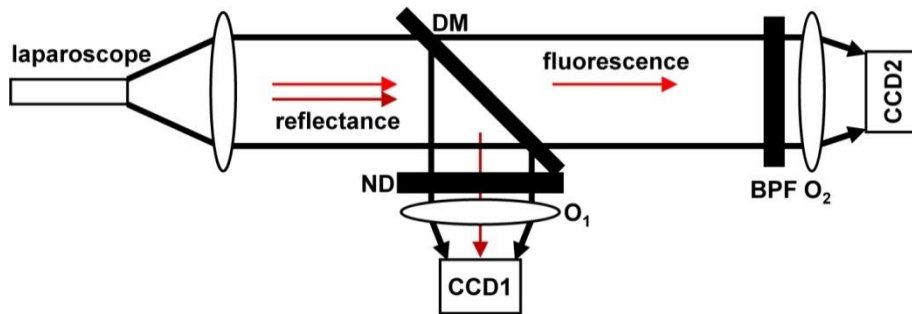
Figure 2.14 Customized laparoscope system schematic. Light exiting laparoscope is split by dichroic filter (DF). Reflectance at λ_{ex} = 660 nm is attenuated by neutral density filter (ND) and focused by objective (O1) onto CCD1. NIR fluorescence is bandpass filtered (BPF) at center wavelength λ = 716 nm over a 40 nm band and is focused by objective (O2) onto CCD2.

The above schematic explains the optical design of light collection in reflectance and fluorescence arms, Figure 2.14. A solid state diode laser (660-S, Toptica Photonics) delivered excitation at λ_{ex} = 660 nm into the fiber optic light guide of the laparoscope. Reflectance light entering the laparoscope was reflected by a dichroic mirror DM (FF685-Di02-25x36, Semrock) through a neutral density filter ND (Thorlabs, #ND10B), and was focused by an achromatic doublet O_1 (49-766, Edmund Optics) onto a color CCD camera CCD1 (#GX-FW-28S5C-C, Point Grey Research).

30

On the other optical arm, fluorescent light entering the laparoscope passed through a bandpass filter BPF (67-039, Edmund Optics) with 40 nm bandwidth centered at 716 nm, optical density OD ≥ 6.0, and 93% transmission efficiency and was focused by an achromatic doublet O_2 (49-766, Edmund Optics) onto a monochromic CCD camera CCD2 (Point Grey Research, #GX-FW-28S5M-C). Both cameras weighed 86 grams, and collected images with a maximum of 2.8 megapixels, 1932×1452 resolution, and 26 frames per second. The imaging module weighed 977 grams (2.15 lbs), and did not interfere with handling of the laparoscope during the imaging procedure.

2.3.2   Mouse model of HCC overexpressing EGFR

In order to simulate the EGFR overexpressing HCC tumor and test the delivery of QRH*-Cy5.5 probe to tumor site in a surgical resection setting, a mouse xenograft model with implanted human HCC cell line overexpressing EGFR (confirmed by Western Blot, Figure 2.10), SK-Hep1, was adopted. SK-Hep1 cells were diluted in growth factor reduced (GFR) Matrigel Matrix (Corning), and subcutaneously injected into one flank of female (to avoid male dominance within a cage) nude athymic mice (nu/nu, Jackson Laboratory) at 4 to 6 weeks of age with weight between 20 to 25 grams. $\sim 5 \times 10^6$ cells were implanted per mouse. Anesthesia was induced and maintained via a nose cone with inhaled isoflurane mixed with oxygen at a concentration of 2 to 4% at a flow rate of ~ 0.5 L/min for all *in vivo* animal experiments. Tumor growth and volumes were monitored weekly with both ultrasound (US) and magnetic resonant imaging (MRI) for 12 weeks (experiment end point) post implantation as described below.

2D ultrasound (US) images were collected from each xenograft tumor using a portable ultrasound scanner (SonixTablet, Ultrasonix, Analogic Corp) designed for small animal imaging. During image acquisition, the mice were placed on a heated stage. Anesthesia was induced and

maintained with 2% isofluorane (Fluriso; MWI Veterinary Supply Co.). Warm (37°C) ultrasound gel (Aquasonic 100, Parker Laboratories) was applied to the tumors. The ultrasound transducer (40 MHz) was used in B-mode, and translated along the length and width of the tumor. 3 images were taken in each direction to calculate tumor volume. Each image had a 12×12 mm^2 field of view with an in-plane pixel resolution of 50×50 µm^2 [191].

Volumes of tumors were estimated as ellipsoid using $\pi abc/6$, where a, b, and c are dimensions measured from the US images [192]. a is defined by the largest dimension in the sagittal plane, while b is the value perpendicular to a. c is the parameter orthogonal to both a and b in the transverse plane. Each measurement was performed 3 times [193]. SK-Hep1 cells were inoculated subcutaneously in n = 8 nude mice at 4 to 6 weeks of age.

Tumor size was confirmed with MRI images collected with a 7T horizontal bore small animal MRI system (SGRAD 205/120/HD/S, Agilent Technologies) using a volume-based transmit/receive quadrature radio frequency coil with an inner diameter of 3.5 cm. The animals were given an intra-peritoneal (i.p.) injection of macrocyclic gadolinium chelate (Gadoteridol, ProHance) at a dose of 2.5 mmol Gd/kg body weight. Body temperature was maintained at 37°C by blowing hot air into the magnet through a feedback control system. ~12 to 15 min after injection of gadolinium, transverse T1-weighted sections were acquired with a scout sequence in 3 orthogonal axes to identify tumor location. A 256×128 matrix was obtained in 5 min by conventional spin-echo multi-slice pulse sequence using repetition time (TR) = 8.5 ms, echo time (TE) = 2.6 ms, average = 2, in-plane field of view (FOV) = 35×35 mm^2, 25-mm slab thickness of 1 mm thick interleaved slices with no gap in between. Tumor volume was assessed with the freehand region of interest (ROI) function of NIH Image J software. Areas were measured on each MRI slice (1 mm thickness) and added together to reconstruct the 3D tumor volume.

Representative images of subcutaneous HCC tumor (arrow) at 6 weeks post-inoculation are shown with ultrasound (US), Figure 2.15(A), and MRI (T1 weighted contrast-enhanced), Figure 2.15(B). A peak tumor volume (±SD) of 761±160 and 936±148 mm^3 was found on US and MRI, respectively, Figure 2.16(A). A correlation of r = 0.98 was found between tumor size on US and MRI, Figure 2.16(B). Log-log plot was suggested by biostatistician to reduce overlap and better visualize data points smaller in value given the large range in volumes. The transformation did not contribute to the goodness of fit (for comparison, r = 0.995 by linear regression without log transformation).
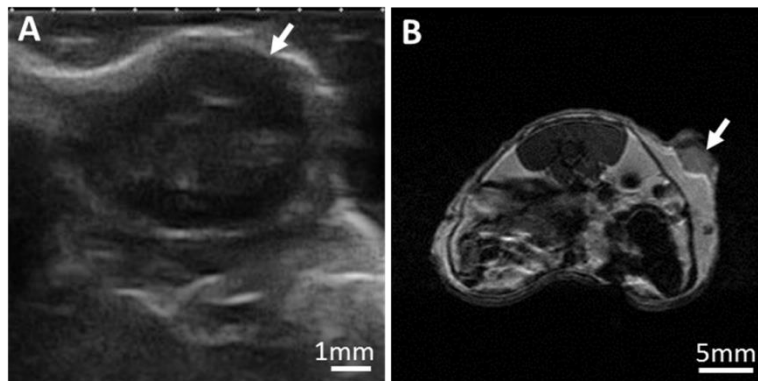
Figure 2.15 Mouse xenograft monitoring with ultrasound and MR imaging. Representative images of subcutaneous HCC tumor (arrow) at 6 weeks post-inoculation are shown with (A) ultrasound (US) and (B) MRI (T1 weighted contrast-enhanced).

Since small HCC lesions are easily missed during surgery, it is desirable to have smaller tumor size in order to test the sensitivity of peptide probe to detect tumor. Therefore, imaging was performed at 6 weeks post implantation before exponential growth would take place.
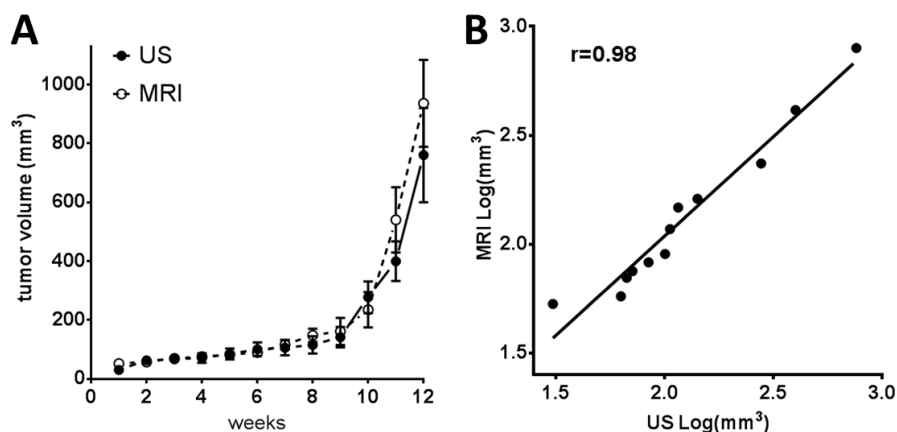
Figure 2.16 Tumor growth curve and correlation of two imaging methods. (A) Mean (±SD) dimensions for n=8 tumors from US and MRI images from post inoculation weeks 1-12 are shown. (B) Positive correlation of r=0.98 was found for tumor size measured with US and MRI.

2.3.3 Pharmacokinetics of EGFR peptide in HCC

The peak and clearance time points following systemic delivery of peptide probe are important metrics for its clinical application during guided surgery. These pharmacokinetics parameters were assessed with a time course imaging study in HCC xenograft bearing mice. The mice were first anesthetized via a nose cone with inhaled isoflurane mixed with oxygen at a concentration of 2 to 4% and flow rate of ~0.5 L/min. The peptides were injected via tail vein at a concentration of 150 mM (i.e. 2.7mg/kg) in a volume of 200 μL ~6 weeks after inoculation when the tumors reached ~1-2 cm in size. Imaging was performed first using a standard color camera (S3 3-chip camera head, Storz) with white light illumination, Figure 2.17(A, H). Then, the laser was directed into the light guide of the laparoscope, and the imaging module was attached to collect reflectance/fluorescence concurrently. Fluorescence images from the HCC xenograft tumors in intact mice were collected over time (0-24 hrs). Representative fluorescence images were shown in Figure 2.17(B-G). The same experiment was repeated with scrambled control peptide over the same period of time on different group of mice, Figure 2.17(I-N). Images were

34

collected at 5 frames/sec with a laser power of 1.2 mW. Mice were fed alfalfa-free diet (TD.97184, Harlan Teklad, WI) to prevent auto fluorescence from chlorophyll in food.
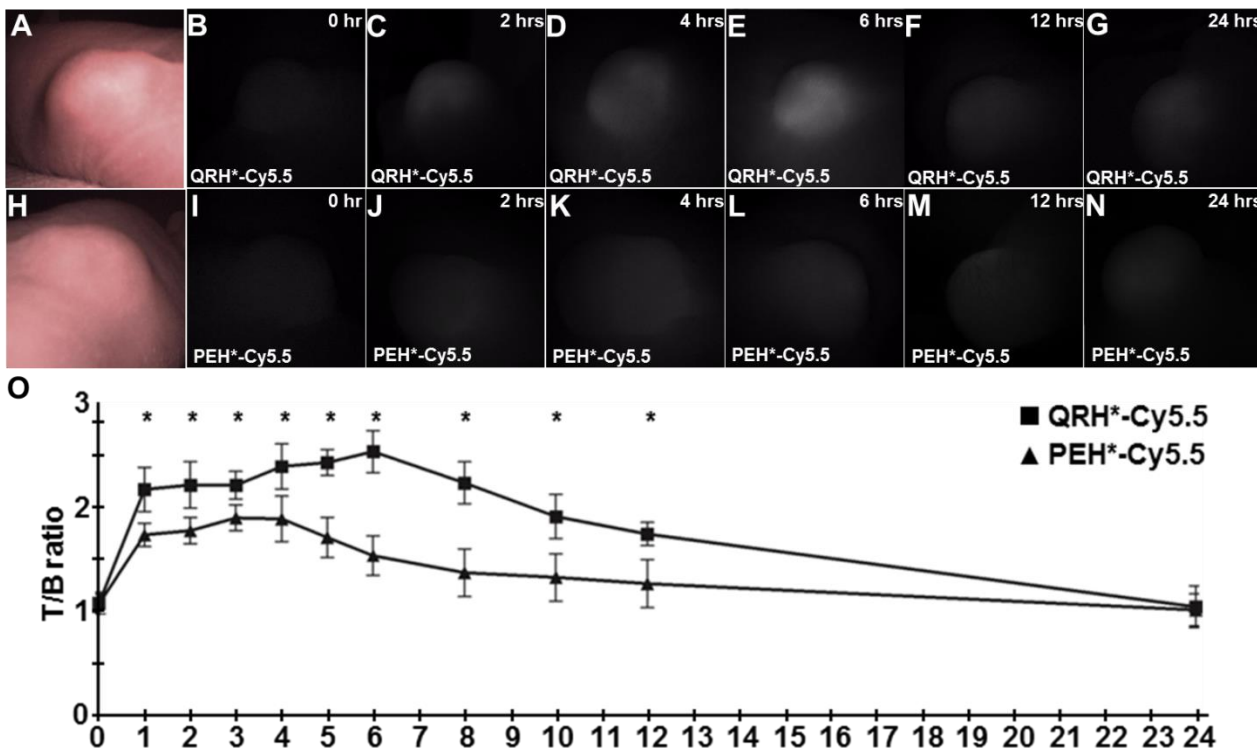
Figure 2.17 Pharmacokinetics of EGFR peptide in HCC xenograft. (A, H) White light images of HCC subcutaneous xenograft tumors in live mice. (B-G) Representative fluorescence images from the HCC xenograft tumors in intact mice were collected over time (0-24 hrs) to evaluate the pharmacokinetics for tumor uptake of QRH*-Cy5.5 peptide. (I-N) Representative fluorescence images for scrambled control peptide PEH*-Cy5.5. (O)T/B was measured from HCC xenograft tumors (n = 13 tumors , n = 5 mice) over time following injection of either QRH*-Cy5.5 or PEH*-Cy5.5. For QRH*-Cy5.5, the TBR achieved a maximum value of 2.53 ± 0.20 at 6 hours. For PEH*-Cy5.5, the T/B was significantly less at each time point, *P < 0. 01 by unpaired t-test.

Fluorescence intensities from n = 13 HCC xenograft tumors (from n = 5 mice) for both QRH*-Cy5.5 and PEH*-Cy5.5 were quantified to evaluate the time course for maximum uptake and clearance, Figure 2.17(O). After the peptide injection, the target-to-background ratio was measured every hour until the maximum value was observed. For QRH*-Cy5.5, the T/B exceeded 2.0 after the first hour, and reached a peak value of 2.53 ± 0.20 at 6 hours. After ~24 hours, the peptide appeared to clear from the circulation, and the T/B ratio dropped back to ~1.

The T/B ratio for PEH*-Cy5.5 was significantly less than that for QRH*-Cy5.5 at each time point.

2.3.4 *In vivo* laparoscopic images of HCC xenograft

To assess the feasibility of image guided resection with peptide probe, the xenograft tumors were exposed to examine the tumor margins at the peak uptake time 6 hours post probe injection. 6 hours after injection of QRH*-Cy5.5, a wide excision was performed in the skin overlying the xenograft tumors for direct laparoscopic visualization. Representative white light (Video 2.2, reflectance (Video 2.3), and fluorescence (Video 2.4) videos are shown, along with representative images collected with QRH*-Cy5.5, Figure 2.18(A-C), and PEH*-Cy5.5, Figure 2.18(D-F). For QRH*-Cy5.5, we observed strong fluorescence signal from the HCC xenograft tumors with high contrast and clear tumor margins. For PEH*-Cy5.5, we found only minimal fluorescence intensity. We measured the T/B ratio from HCC xenograft tumors (n = 13 tumors from n = 5 mice), and found a significantly greater contrast for QRH*-Cy5.5 than for PEH*-Cy5.5 of 2.99 ± 0.22 versus 1.81 ± 0.16, $P<0.0001$ by unpaired t-test, Figure 2.18(G). Despite of our effort to implant HepG2 xenografts to serve as negative control and benchmark the EPR effect, it was not achievable for this cell line is non-tumorigenic [194].
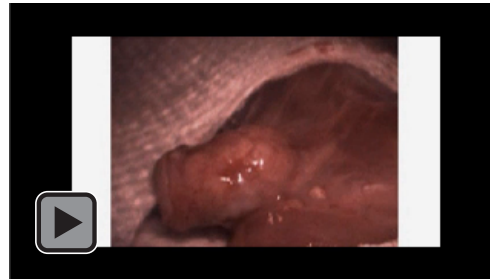
Video 2.2 Laparoscopic white light HCC image

Video 2.3 Laparoscopic reflectance HCC image
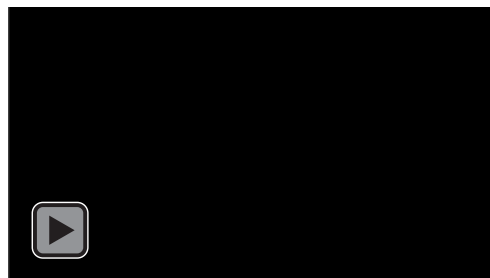
Video 2.4 Laparoscopic fluorescence HCC image
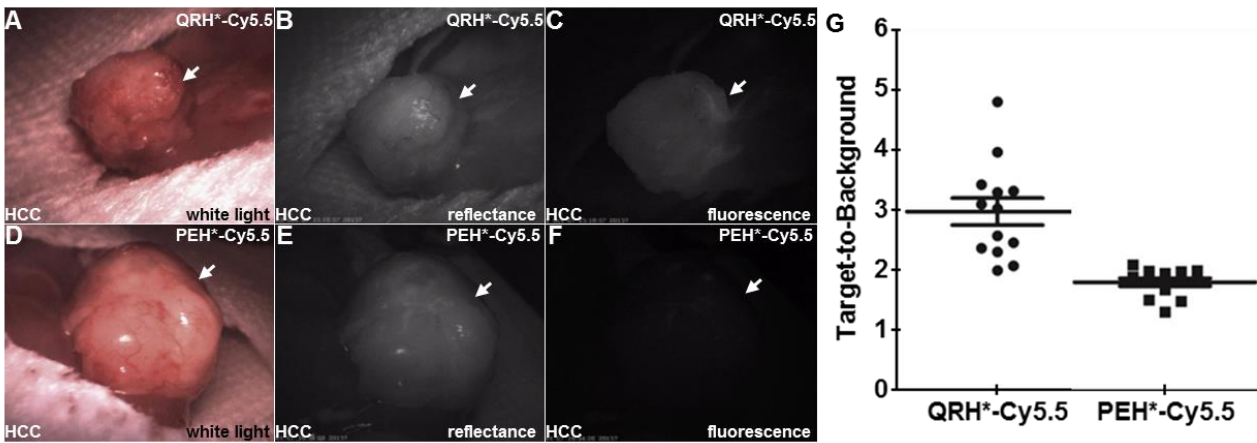
Figure 2.18 *In vivo* laparoscopic images of HCC xenograft. (A) White light, (B) reflectance, and (C) fluorescence images collected with EGFR peptide QRH*-Cy5.5. (D) White light, (E) reflectance, and (F) fluorescence images collected with scrambled (control) peptide PEH*-Cy5.5. (G) A significantly greater target-to-background ratio from HCC xenograft tumors for QRH*-Cy5.5 (n = 13 tumors from n = 5 xenograft mice) than for PEH*-Cy5.5 (n = 13 tumors from n = 5 xenograft mice) of 2.99 ± 0.22 versus 1.81 ± 0.16 from the *in vivo* images, P < 0.0001 by unpaired t-test.

2.3.5   Automatic ROI recognition

37

Fluorescence, reflectance, and white light images were collected with the NIR laparoscope after intravenous injection of the EGFR peptide. A heat map of fluorescent signal was used to automatically identify regions of interest (ROIs) with an edge-detecting segmentation algorithm. This takes the guesswork out of the equation for surgeons and adds confidence to the clinical application of the peptide probe.

Fluorescence and reflectance images, Figure 2.19(A-B), were collected with the NIR laparoscope 6 hours after intravenous injection of the EGFR-targeting peptide, QRH*-Cy5.5, in SK-Hep1 xenograft bearing mice. The same set of images were collected with scrambled peptide PEH*-Cy5.5 in different group of tumor bearing mice, Figure 2.19(E-F), but no tumors were detected. White light images were collected for mice injected with targeting peptide QRH*-Cy5.5, Figure 2.19(I), and scrambled peptide PEH*-Cy5.5, Figure 2.19(J).

Fluorescence images of mouse HCC xenograft taken at 6 hrs post peptide injection were registered with corresponding reflectance images taken simultaneously. The fluorescence intensity of each pixel in the image was divided by intensity of corresponding pixel in the reflectance image in order to account for the difference in distance between each pixel and the laser source. A heat map image was generated from the resulting ratios at each pixel. Image segmentation was performed automatically by custom Matlab (Mathworks) software program using Ostu's Method [62]. Target-to-background ratio of each processed image was calculated by dividing the average intensity of pixels inside the segmented tumor and that of those within 30 pixels outside of segmentation outline.
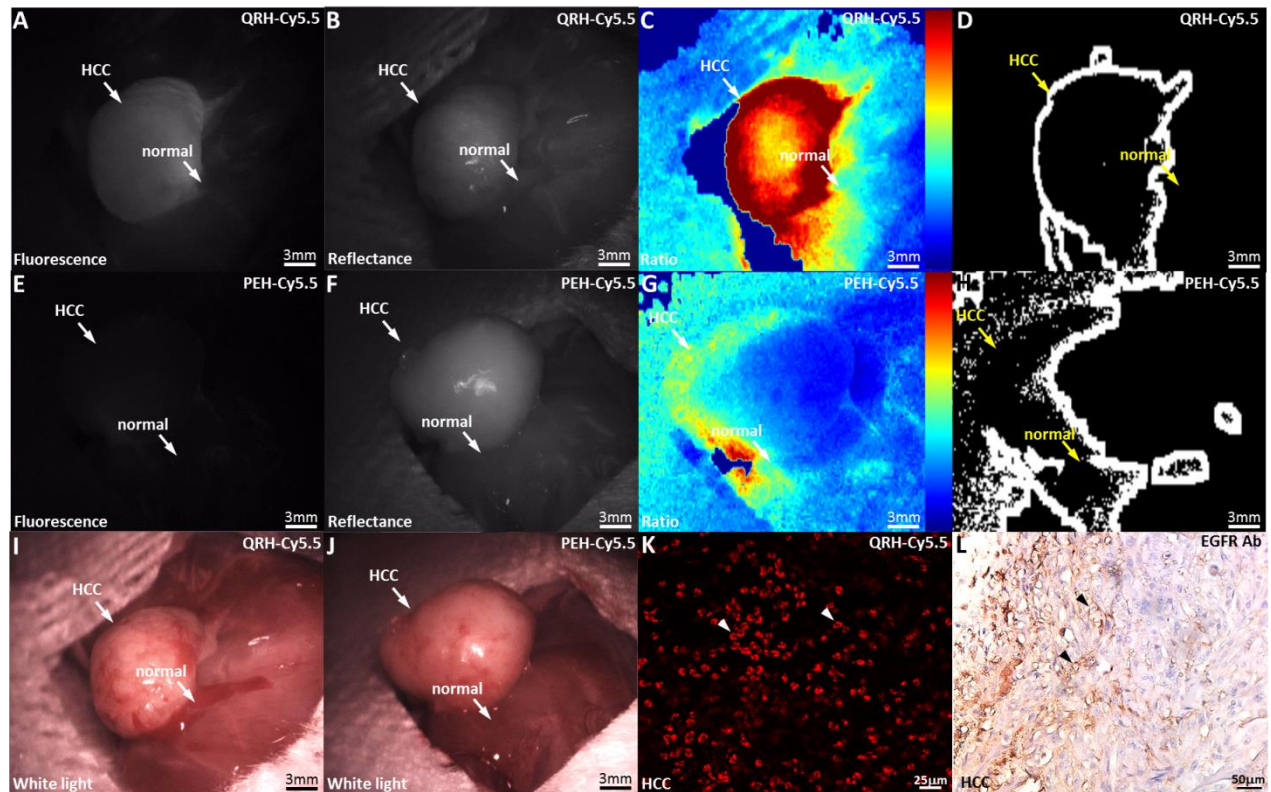
Figure 2.19 Automatic ROI recognition. (A) Fluorescence and (B) reflectance images of exposed xenograft tumor in live mice were collected with the NIR laparoscope 6 hours after intravenous injection of QRH *-Cy5.5. (C) Heat map corrects for imaging distance by taking the ratio between co-registered fluorescence and reflectance images. (D) Region of interest was segmented by imaging processing algorithm using ratio image. (I) Representative white light images of mouse injected with QRH*-Cy5.5 and (J) PEH*-Cy5.5. (K) Immunofluorescence image of fresh resected HCC tumor xenograft in whole mount 6 hours after QRH*-Cy5.5 injection showed surface staining (arrowheads) of peptide probe on individual HCC cells of the tumor. (L) Immunohistochemical image of EGFR antibody staining (arrowheads) on fresh resected HCC tumor xenograft. (E-H) The same set of images were collected with scrambled peptide PEH*-Cy5.5 in a different tumor.

Heat map digital image that rectifies imaging distance was generated by taking the ratio between corresponding fluorescence and reflectance images pixel by pixel, Figure 2.19(C). Region of interest (ROI) was segmented by automatic imaging processing from ratio image following Otsu's method, Figure 2.19(D). The same set of images were analyzed for scrambled peptide PEH*-Cy5.5 in a different group of tumor bearing mice, Figure 2.19(G-H).

Hoechst 33342 (H1399, Life Technologies) at a dose of 10 mg/kg diluted in 200 μL of PBS was delivered intravenously via a tail vein injection to stain the cell nuclei 30 minutes before sacrificing the mouse. Xenograft tumors were resected and confocal fluorescence images were

collected with Cy5.5 and DAPI filters 50μm beneath the surface using a confocal microscope (Leica SP5X Upright 2-Photon Confocal Microscope). Immunofluorescence image of fresh resected HCC tumor xenograft in whole mount 6 hours after QRH*-Cy5.5 injection showed intense cell surface staining (arrowheads) of peptide on human HCC cells under confocal microscopy to confirm the specific cell binding, Figure 2.19(K). Immunohistochemical image of EGFR antibody staining (arrowheads) on fresh resected HCC tumor xenograft, Figure 2.19 (L), confirmed EGFR expression in tumor as would have been done in a clinical setting.

To quantify the accuracy of the computerized ROI algorithm, an independent observer was asked to view white light images of tumor and mark the positions of the center of tumors without any prior information on the purpose of the experiment or exposure to the computerized ROI graphs. Afterwards, the human-identified tumor centers were overlaid on the computerized ROI. If the human-identified tumor center fell inside the computer generated ROI, then it was considered a successful identification. All 13 tumors from 5 mice injected with QRH*-Cy5.5 peptide were identified with computerized ROI while the PEH-Cy5.5 injected tumors had centers positioned outside of the ROIs.

2.3.6   Post imaging validation of EGFR expression *ex vivo*

In addition to fluorescent *in vivo* imaging at the surface of xenograft tumor, harvested tumor post laparoscopic imaging was sectioned and microscopically imaged to confirm the delivery of peptide probe to the interior of tumor by i.v. injection. After *in vivo* imaging was completed, mice were euthanized, and their tumors were excised and sectioned for examination with confocal fluorescence microscopy. We observed intense staining of QRH*-Cy5.5 to surface (arrow) of SK-Hep1 human HCC cells but not for PEH*-Cy5.5 injected mouse tumors, Figure 2.20(A-B).
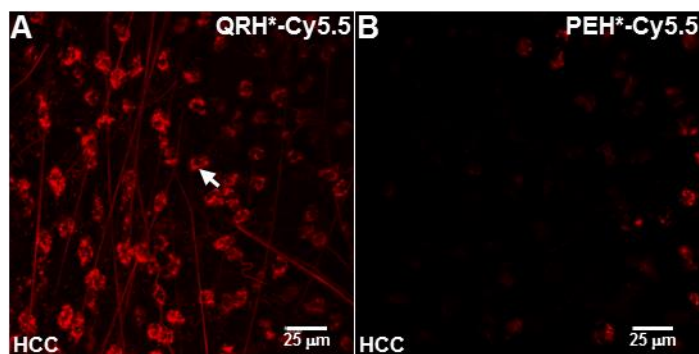
Figure 2.20 Peptide binding to EGFR. Peptide binding results were validated on confocal fluorescence microscopy of tumor sections for (A) QRH*-Cy5.5 and (B) PEH*-Cy5.5 after imaging was completed and the mice were euthanized. Note intense staining of QRH*-Cy5.5 to surface (arrow) of SK-Hep1 human HCC cells.

2.4   *In vivo* photoacoustic imaging of EGFR in HCC

One of the limits of fluorescence imaging, discussed in Section 1.5, is lack of penetration depth due to light scattering. With photoacoustic imaging, high contrast *in vivo* imaging beneath the tumor surface could be acquired to confirm the penetration of peptide probe inside the tumor with systemic delivery. The results presented here were published in peer-reviewed journal article [135].

2.4.1   Photoacoustic as imaging modality

Photoacoustic imaging is a non-invasive imaging modality which allows structural, functional and molecular imaging. Despite the fact that the PA effect was discovered by the legendary scientist Alexander G. Bell in the 1880s when experimenting with long-distance sound transmission [195], its application to biomedicine and microscopy was not achieved until a century later, in the 1980s [196, 197], after reliable and intense optical sources were developed. It has been intensively studied ever since [198]. In the past 20 years, photoacoustic imaging has become an emerging imaging modality that provides greater depth than optical methods and better resolution than ultrasound. Previous studies has reported the ability of hybrid plasmonic contrast agent gold nanotube (GNT) to achieve picomolar sensitivity compared to nanomolar

41

levels for conventional agents [199]. Moreover, indocyanine green (ICG) labeled with single walled carbon nanotubes (SWNT-ICG) can improve photoacoustic contrast by ~300-fold [84].

Compared to imaging methods for HCC diagnosis in the clinic, photoacoustic imaging has the merits of high resolution, fast turnover and low risk. The photoacoustic images in the current study were collected with a spatial resolution of 280 μm in all dimensions. By comparison, ultrasound at the same central frequency of 5 MHz without 3D data acquisition and image reconstruction can achieve 470 μm axial and ~1-5 mm lateral resolution [200]. Nuclear imaging methods (PET and SPECT) have spatial resolution in the ~1 to 2 mm range [73, 201]. Our *in vivo* images required a short image acquisition and reconstruction time (~2 min) than MRI or CT. With faster lasers and more efficient algorithms even real time image-guided surgery with a photoacoustic endoscope can be possible. This technique does not involve non-ionizing radiation, and can be more cost-effective and easier to use than MRI, PET, and SPECT.

2.4.2 Working principle

The method relies on the photoacoustic effect which describes conversion between light and acoustic waves due to absorption of electromagnetic waves and localized thermal excitation [202]. The principle of photoacoustic imaging is illustrated in Figure 2.21: short pulses of electromagnetic radiation, mostly short laser pulses, are used to illuminate a sample. The local absorption of the light is followed by rapid heating, which subsequently leads to thermal expansion. Finally, broadband acoustic waves are generated. By recording the outgoing ultrasonic waves with adequate ultrasonic transducers outside of the sample, the initial absorbed energy distribution can be recovered. Thus, photoacoustic imaging is a hybrid technique making use of optical absorption and ultrasonic wave propagation [203]. Thereby the advantages of both

techniques are combined: the high contrast of optical imaging and the high resolution of ultrasonic imaging.
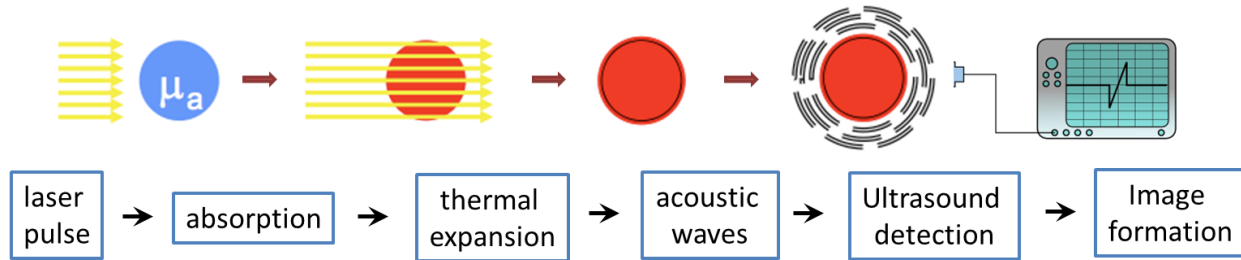
Figure 2.21 Working principle of photoacoustic imaging. Tissue is irradiated with a short laser pulse. Optical energy is absorbed by tisssue and converted into thermal energy. Optical absorption of short pulse of light leads to rapid thermal expansion of tissue and generation of acoustic (pressure) transients. The acoustic signal, recorded using ultrasound transducer, is usded to form an image.

In this study, a major implementation of photoacoustic imaging principle called photoacoustic tomography (PAT) was employed. In PAT a semitransparent sample is illuminated by an expanded laser beam rather than a focused laser in PAM, thus illuminating the whole sample volume. The spatial varying local absorption leads to generation of ultrasonic waves which are recorded by an ultrasonic transducer. By moving the transducer around the sample, or by using an array of transducers, a dataset of pressure curves is acquired. By using adequate reconstruction algorithms the absorption of light within the sample (= image information) can be reconstructed. The resolution of PAT is determined by the duration of the excitation laser pulse and the bandwidth of the transducers, and is typically below 100μm.

PAT has the unique capability of scaling its spatial resolution and imaging depth across both optical and ultrasonic dimensions [204]. In the optically diffusive region, the spatial resolution is acoustically defined. While a higher central frequency transducer provides a higher spatial resolution, the frequency-dependent acoustic attenuation (~1 dB/MHz/cm in muscle) limits the imaging depth. Low frequency (< 10 MHz) transducers are commonly used in PACT systems to provide an imaging depth greater than 1 cm. Above 10 cm, the imaging depth is also limited by

light attenuation, which is a combined effect of optical absorption and scattering. With recent advances in optical wave-front engineering [205, 206], we expect the attenuation through optical scattering to be minimized, and PAT to eventually image tens of centimeters deep in tissue. By ultrasound measurement, a normal human liver is less than 16 cm in the midclavicular line [207]. All *in vivo* photoacoustic imaging in this study involved mouse subcutaneous HCC xenograft tumor. All tumors were imaged before the dimension reached 1cm. Thus low frequency (5 MHz) transducers were used to achieve ~1cm imaging depth. This imaging depth is sufficient for subcutaneous xenografts and potentially for orthotopic xenograft in mouse liver (<3cm in length and <1cm in thickness [208]). The most likely application in the clinic for PAT is intraoperative image guided surgery where the resection edge will be imaged for confirmation of negative margin. For that purpose, 1cm imaging depth would be sufficient.

2.4.3 Near-infrared labeled photoacoustic imaging probe

Compared to ultrasound, Photoacoustic (PA) imaging offers higher resolution, contrast and capability for targeted detection [209]. Previous photoacoustic imaging studies have used endogenous contrast from hemoglobin and melanin [210], and others have relied on the enhanced permeability and retention (EPR) effect [211, 212]. The EPR effect can be variable and produce false positives in highly vascular tissues [213] for nano-sized or smaller delivery agents [214]. These strategies are based on non-specific detection mechanisms. The use of a targeting moiety can improve tumor homing, increase signal, and improve contrast by tuning absorption to specific wavelengths [73].

NIR dye labeled EGFR targeting peptide probe was used in the *in vivo* photoacoustic imaging study. Nanoparticles have 3-10 times higher extinction coefficient than organic dyes [215], and can absorb more energy from light per mass density. However, nanoparticles have not received

FDA approval for clinical imaging [216]. On the other hand, organic dyes have a benign toxicity profile [217] and pharmacokinetic characteristics are compatible with clinical translation. While prolonged circulation time of conventional nanoprobes may enhance targeted drug delivery [218, 219], peptides may offer advantages for improved deep tumor penetration and accumulation with reduced biodistribution to non-target tissues [220, 221]. Nonetheless, metallic nanoparticle as optimized *in vivo* photoacoustic imaging contrast agent will be covered in Chapter 4, to push the envelope of clinical imaging for future applications.

2.4.4 Photoacoustic imaging system

We used a photoacoustic tomography system (Nexus128, Endra Inc.) that provided laser excitation at 7 ns pulses, 20 Hz repetition rate, 25 mJ/pulse, and wavelength range 680−950 nm. Ultrasound was collected by 128 unfocused 3 mm diameter transducers with 5 MHz center frequency arranged in a helical pattern in a hemispherical bowl filled with water, Figure 2.22 (A). A transparent imaging tray located above the transducers was used to contain anesthetized animals. The console also included data acquisition/reconstruction software, servo motors to rotate the bowl, and a temperature monitor. We optimized the imaging protocol to collect 120 views with 10 pulses/view, covering an imaging volume of $25 \times 25 \times 25$ mm^3 with a voxel size of 280 μm^3. Each dataset required ~2 min for acquisition and reconstruction. The animals were administered QRH*-Cy5.5 at 300 μM in 250 μL (75 nmol), and placed inside the tray with the subcutaneous tumor positioned inside a water-filled dimple to couple the ultrasound signal, Figure 2.22(B).
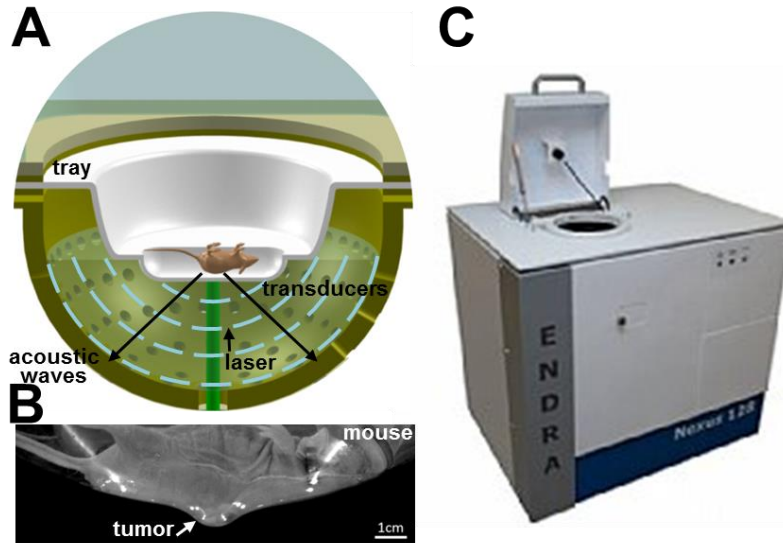
Figure 2.22 System schematic of photoacoustic imaging instrument (A) Laser pulses at l = 680 nm (green) are absorbed by the tumor to produce acoustic waves that are detected by 128 ultrasound transducers arranged in a helical pattern. Water between the imaging tray and transducer array provides acoustic coupling. (B) Photograph of live animal under anesthesia with tumor positioned inside a dimple in the center of the tray. C) The entire system is integrated and packaged inside a portable cart, reproduced with permission from http://www.endrainc.com.

The entire imaging system was integrated and packaged inside a portable cart, Figure 2.22(C). The laser output 7ns 25mJ pulses at 20Hz in the tunable range of 680-950nm. The ultrasound transducers had 5MHz central frequency and 3mm in diameter. The acquisition operated at 40MHz without multiplexing. This system can acquire image volumes of 25mm in each dimension with a spatial resolution of 280um.

2.4.5 *In vivo* photoacoustic imaging of HCC

At 6 weeks post inoculation, representative photoacoustic images collected with λ_{ex} = 680 nm at 0, 1, 3, 6, 12, and 24 hours after injection of 300 μM in 250 μL of QRH*-Cy5.5 i.v. were shown as maximum intensity projection (MIP) images at a mean (±SD) depth of 8.1±1.3 mm with range 0 to 1.8 cm below the skin surface. At this time, the tumors had reached a mean (±SD) size of 100±23 mm^3 by US. For anatomic context, the field of view in photoacoustic imaging is 2.5×2.5cm^2 centered at the dimple (dashed circle) of imaging tray where the xenograft tumor (arrow) is placed, Figure 2.23(V). The tumors showed increased signal in a heterogeneous

pattern with visible blood vessels, Figure 2.23(A-F). Just after injection, there was minimal signal at the tumor. After 1 hr, tumor site as well as surrounding tissue lit up. After 3hrs, signal from surrounding normal area was cleared leaving contrast coming from the tumor alone. A 3D volume rendered image of the tumor at 3 hours post injection was shown (Video 2.5), Figure 2.23(T). We can see the blood vessels feeding the tumor from behind. After that the peptide will be cleared from the system by 24 hrs post injection. Preliminary study (data not shown) confirmed wash out of either QRH-Cy5.5 or PEH-Cy5.5 from the animals' system occurred by 24 hrs post injection and no difference in signal intensity or pattern were associated to injection order.

Imaging was repeated with PEH*-Cy5.5 and Cy5.5 alone (dye without peptide) 48 hours later in the same animals after the targeting peptide had cleared, Figure 2.23(G-L). We saw more signals inside the blood vessels rather than in the tumor. For additional control, images from HCC with free Cy5.5 alone, Figure 2.23(M-R), and the signal represented the enhanced permeability and retention effect at the tumor. Minimal signal was observed in the normal tissue after targeting peptide injection, Figure 2.23(S).

The 3D image was reconstructed after completion of imaging using data acquired from all 128 transducers at each view with a back-projection algorithm [199]. This algorithm corrected for pulse to pulse variations in laser intensity and small changes in temperature that affected the velocity of acoustic waves in water. The reconstructed raw data was analyzed using Osirix 6.5.2 software (Pixmeo) to generate a maximum intensity projection (MIP) image, which was converted to a color map using Matlab (R2013a, ver 8.1, Mathworks) software. 3D visualization of the reconstructed photoacoustic signals was performed using Amira software (ver 5.4.3, FEI Corporation), including volume rendering technique (VRT) with specular shading and physics

color map. The alpha value was set at 0.7 in order to reveal blood vessel structures underneath the tissue surface.

The photoacoustic intensity from the tumor (target) was measured using a circular ROI with diameter determined from US (illustrated in Figure 2.23 (U) where the longer axis of the eclipse on ultrasound imaging was used as the diameter of circular ROI in photoacoustic imaging), and an adjacent annulus with area equal to that of the target ROI was used to measure background, indicated by white circles in Figure 2.23(C & I).
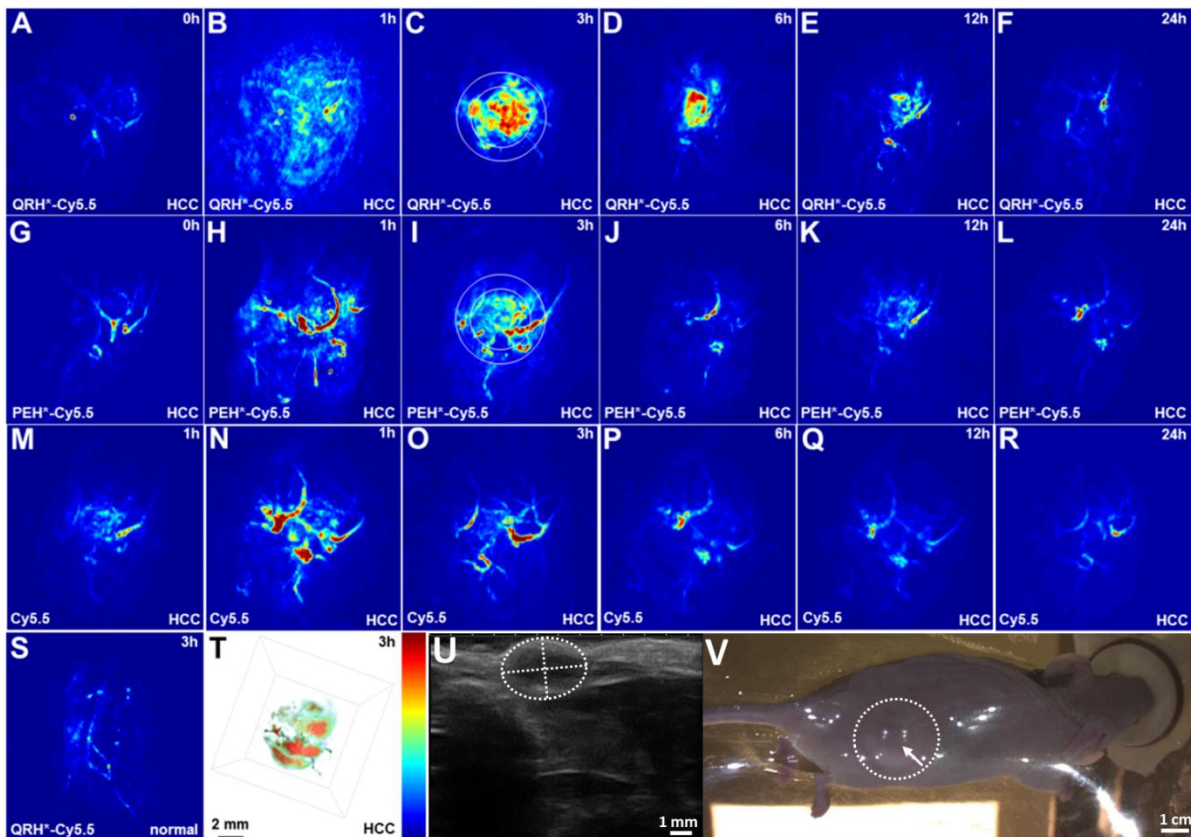
Figure 2.23 Time course of PAI in HCC. Representative MIP images at depth of 1.8 cm were collected at 0, 1, 3, 6, 12 and 24 hours after injection with (A-F) QRH*-Cy5.5 and G-L) PEH*-Cy5.5 are shown. In panel (C), inner circle represents regions of interest (ROI) used to measure signal from tumor, and adjacent annulus with equal area was used to measure background. (M-R) Images of tumor with injection of Cy5.5 alone (no peptide) at 0 to 24 hours post injection. (S) Image of normal area at 3 hours after QRH-Cy5.5 injection. (T) 3D reconstruction of tumor images. (U) Ultrasound image of subcutaneous tumor with dashed oval marking the tumor ROI. The longer axis of the oval was used as the circular ROI diameter in photoacoustic image

quantification. (V) Photograph of xenograft bearing mouse inside photoacoustic imaging tray with marked field (dashed circle) of view and tumor position (arrow) assisted with anatomic context.
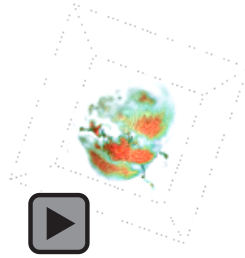
Video 2.5 3D PAI of QRH*-Cy5.5 on HCC
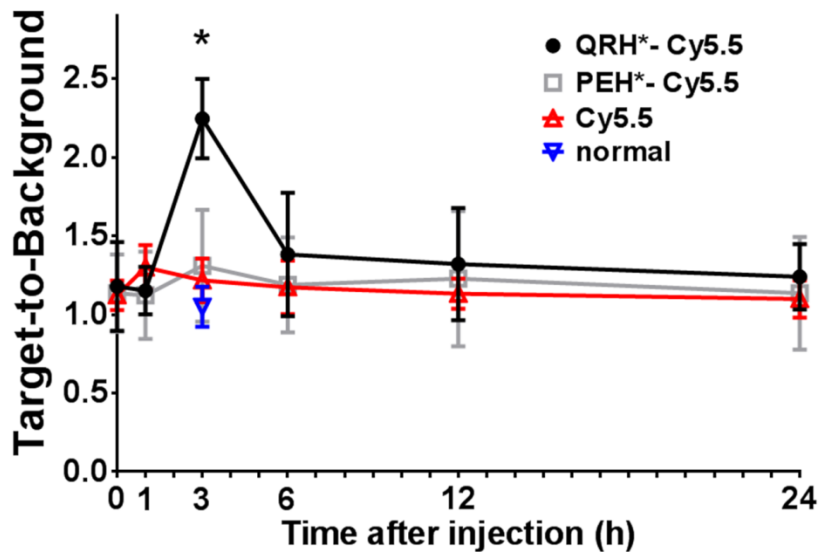
Figure 2.24 Quantification of time course photoacoutic imaging. Images collected over time showed peak tumor QRH*-Cy5.5 uptake at 3 hours after i.v. injection. T/B ratio of 2.25±0.25 was significantly greater than 1.31±0.36 for PEH*-Cy5.5, P = 1.2×10^{-3} by paired t-test. Injection of Cy5.5 dye alone produced peak T/B ratio, 1.30±0.14, at 1 hour post injection at tumor site. T/B ratio of 1.22±0.14 at tumor site and 1.05±0.13 at adjacent normal tissue were observed at 3 hours respectively. Wash out of probe was observed within 24 hours.

HCC tumors showed a higher T/B ratio for the EGFR peptide compared with that of the control peptide at each time point up to 24 hours. Tumor uptake of QRH*-Cy5.5 increased steadily after injection to a peak value at 3 hours, Figure 2.24. This peak time differed from the previous *in vivo* laparoscopic imaging and was due to the difference in sensitivity by different imaging instruments and different injection doses. The 3-hr peak time is clinically relevant as it would allow surgeons to inject the peptide probe at the beginning of surgery and check tumor margin

49

for fluorescent signal by peak time before finishing the surgery. It would eliminate the need to perform biopsy and histology staining which can take days before getting results. In the case where positive margins were found, the patient has to schedule and undergo a second surgery. The more than 2-fold increase in target-to-background ratio ensures that the tumor can be distinguished from surrounding normal tissue. The T/B ratio then decreased over time to near baseline by 24 hours. This time frame is significantly faster than most antibodies, which can take hours to home to the tumor and even longer to clear [222, 223]. Meanwhile, non-tumor exhibited minimal uptake. The HCC image with Cy5.5 alone (no peptide) showed a small effect of tumor permeability and retention [213, 224]. Injection of Cy5.5 dye alone produced peak T/B ratio, 1.30±0.14, at 1 hour post injection at tumor site.
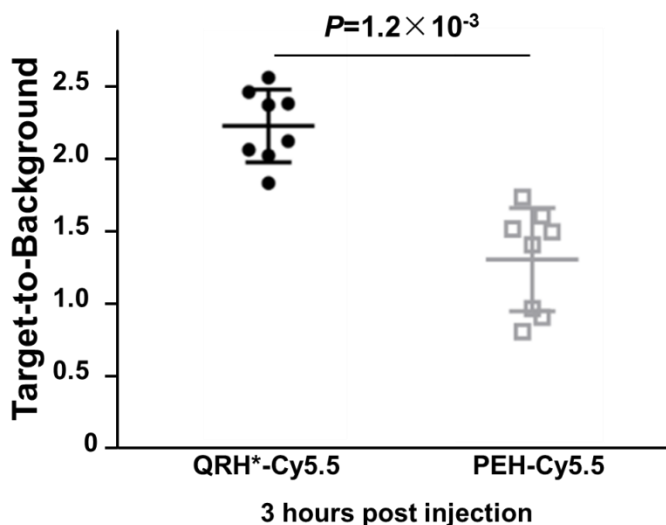
Figure 2.25 Quantification of target-to-background ratio at 3 hrs post injection. Individual data points for T/B ratios at 3 hours are shown

We measured a T/B ratio of 1.22±0.14 at the tumor site and 1.05±0.13 from adjacent normal tissue at 3 hours respectively. Peak T/B ratios for the EGFR and control peptides at 3 hours were plotted, Figure 2.25. Each individual mice are color coded to track the change in T/B ratio over six different time points (0h, 1h, 3h, 6h, 12h, 24h) post injection, Figure 2.26.
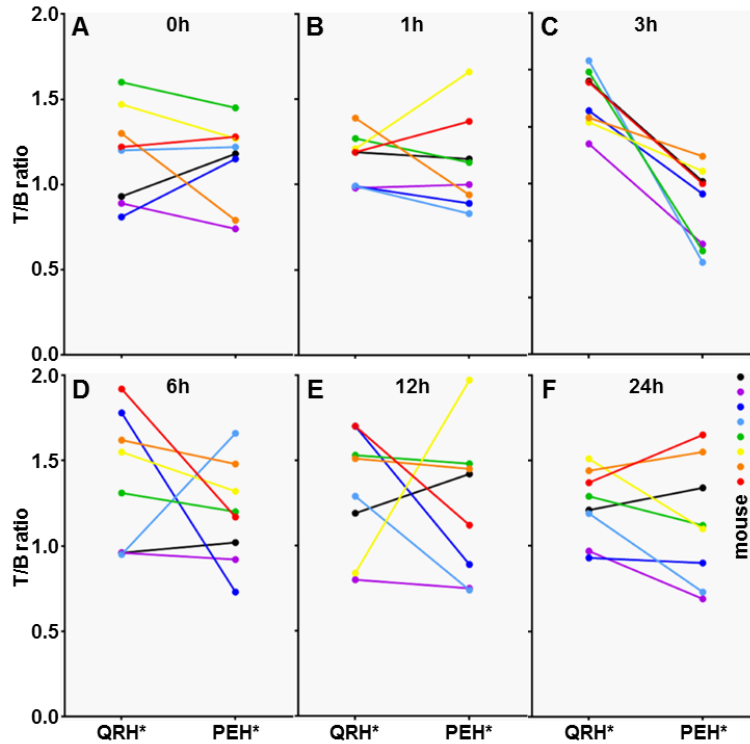
Figure 2.26 Target-to-background ratio of each individual mouse over time course. Each experiment mouse was color coded to track the change in T/B ratio over six different time points (0h, 1h, 3h, 6h, 12h, 24h) post injection.

The typical shape of tumor xenografts in this study was oblate ellipsoid with almost equal dimensions parallel to skin surface but much shorter in depth beneath the skin (i.e. $b < a \approx c$). Thus approximation of tumor area with circular ROI was adopted in PA signal intensity measurement for 2D MIP images. Two independent individuals each took three attempts to select ROI on ultrasound images and the average was taken to determine the diameter of circular ROI on photoacoustic images being quantified. Since ROIs on PA images were drawn at the center of field of view, its accuracy is dependent on whether the tumor was actually placed at the center of the dimple. Movement of the mice due to breathing could displace the tumor from the center by a couple millimeters. But this did not seem to affect background intensity value or the T/B ratio in any substantial way. In addition, 3D volumetric quantification of PA images could potentially give a more accurate intensity measurement if an algorithm capable of defining

51

arbitrary oblate ellipsoid as ROI and taking into account the illumination attenuation along tissue depth were available.

2.4.6 *Ex vivo* validation of EGFR expression

After *in vivo* PAI, *ex vivo* validation of EGFR binding by targeting peptide were performed on resected xenografts and the results were consistent with the *in vivo* findings. Resected tumor and normal liver (n = 24 mice) were formalin-fixed, paraffin embedded and cut in 10 μm thick sections. Deparaffinization, rehydration and antigen unmasking was performed, as described previously. Blocking was performed with DAKO protein blocking agent (X0909, DAKO) for 1 hour at RT. Sections were then incubated with 5 μM QRH*-Cy5.5 in 2% BSA for 10 min at RT. The sections were washed 3 times with PBS and mounted with Prolong Gold reagent containing DAPI (Invitrogen). Confocal microscopy was performed using λ_{ex} = 670 and 405 nm for Cy5.5 and DAPI, respectively, at 63X magnification. Fluorescence intensities were measured from 3 randomly positioned boxes with dimensions of $20{\times}20$ μm^2. Regions that showed intensity saturation were avoided.
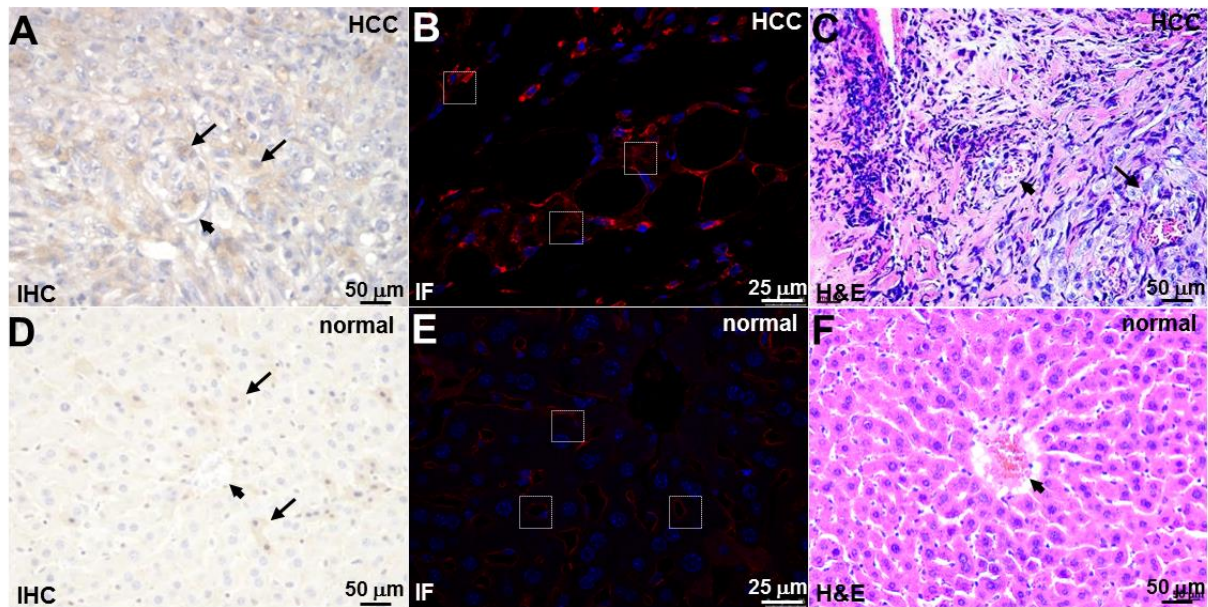
Figure 2.27 Immunostaining of HCC xenograft and normal liver with EGFR peptide. (A) Immunohistochemistry (IHC) with anti-EGFR antibody shows increased reactivity to HCC. A nest of tumor cells with large irregular round nuclei (arrows) and infiltrating blood vessels lined with flattened endothelial cells (arrowhead) can be seen. (B) Immunofluorescence (IF) with QRH*-Cy5.5 shows binding to surface of HCC cells. Fluorescence intensities were measured from sets of 3 (dashed white) boxes with dimensions of 20×20 μm2. (C) Corresponding histology (H&E) of tumor. (D) IHC of normal mouse hepatocytes show few lightly stained cells (arrows) surrounding the central vein (arrowhead). (E) IF of normal mouse liver shows minimal signal. (F) Histology of normal mouse liver shows lobule with central vein (arrowhead) surrounded by radially aligned plates of hepatocytes.

On immunohistochemistry (IHC), we observed strong staining of EGFR in HCC tumors, Figure 2.27(A). On immunofluorescence (IF), strong signal from QRH*-Cy5.5 is seen on the surface of tumor cells, Figure 2.27(B). In normal mouse liver, a few lightly stained hepatocytes (arrow) can be seen surrounding the central vein (arrowhead) with IHC, Figure 2.27(D). Minimal signal from QRH*-Cy5.5 was seen in normal liver with IF, Figure 2.27(E). Corresponding histology (H&E) of tumor and normal is shown, Figure 2.27(C, F).
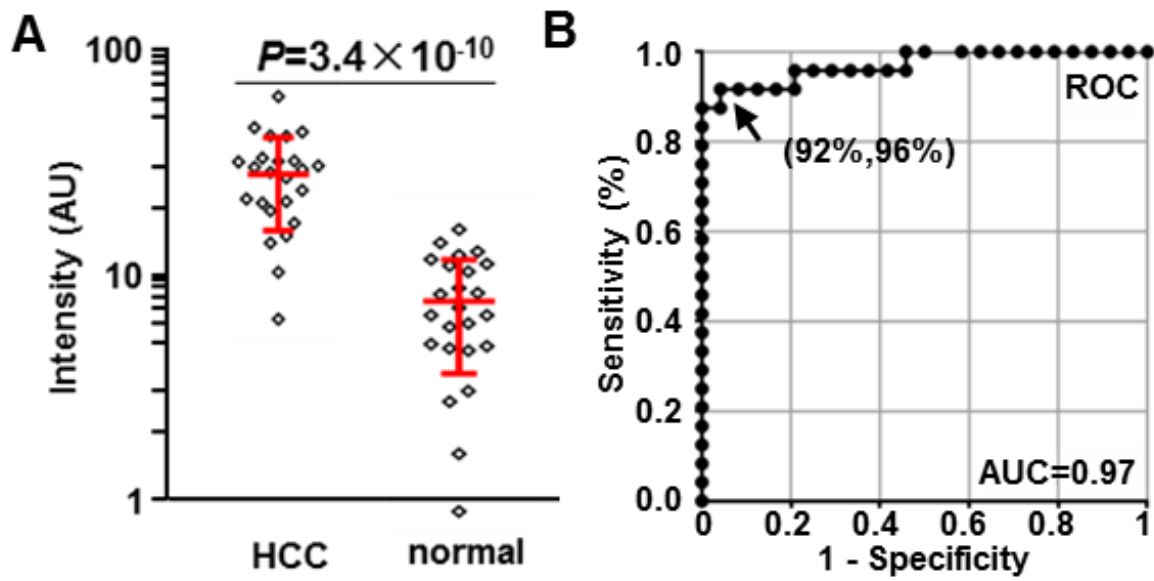
Figure 2.28 Quantification of immunostaining in HCC xenograft with EGFR peptide. (A) Mean (±SD) fluorescence intensities for HCC (n=24 tumors) are significantly higher than that for normal liver (n =24), 27.8±11.5 versus 7.37±3.80 by 3.77-fold, $P=3.4\times10^{-10}$ by paired t-test. (B) ROC curve shows 92% sensitivity and 96% specificity with area under curve (AUC) of 0.97 for distinguishing HCC from normal liver using QRH*-Cy5.5.

We found the mean fluorescence intensity from HCC to be significantly greater ($P=3.4\times10^{-10}$) than that of normal by 3.8-fold, Figure 2.28(A). The corresponding receiver operating characteristic (ROC) curve shows 92% sensitivity and 96% specificity for distinguishing HCC from normal liver with an area under the curve (AUC) = 0.97, Figure 2.28(B), indicating the probe would be an excellent diagnostic tool. Scattered dot plot was adopted to show the individual data points without overlapping.

2.5 Discussions

In this study, we used a version of Cy5.5 that has four additional hydrophilic –SO_3H groups, Figure 2.1(A), to improve water solubility [135]. With the previous fluorophore, probe concentration of 100 μM was used, which was adequate for topical administration to detect pre-malignant disease in mouse colon [60]. In this study, we achieved a ~3-fold greater concentration, and used systemic (intravenous injection through tail vein) administration to deliver the peptide

to a solid tumor. The improved probe solubility by sulfo-group modification on Cy5.5 dye label allowed for a smaller injection volume to deliver the desired dose. Because the peak absorption of Cy5.5 occurs below 700 nm, the imaging depth can be further improved with organic dyes, such as ICG and Licor IRDye800 [86, 225], that absorb at longer wavelengths and avoids hemoglobin absorbance and minimizes tissue scattering.

We used human SK-Hep1 cells that overexpress EGFR to introduce HCC xenograft tumors. This technique may produce higher levels of EGFR expression and less heterogeneity than that found in sporadic human HCC [226]. In the future, we will use patient derived xenograft (PDX) models that include stroma and better reflect clinically relevant EGFR expression levels [227] and tumor microenvironment [228]. PDX models can also be effective for evaluating new drugs [229-231]. Both subcutaneous [228, 232, 233] and orthotopic [234] PDX models of HCC have been developed by other groups. Also, detection of multiple targets simultaneously may be needed to address the genetic diversity of HCC [235-237]. Our imaging system can use a broad range of wavelengths (680-950 nm). This spectrum covers the absorption peaks of many NIR dyes (Cy5.5, ICG, IRDye800) and nanoparticles (Au, SWNT and Co [75, 238, 239]). A panel of peptides labeled in spectrally distinct regions may be needed to achieve high detection sensitivity in the clinic. Adapting functionalized nanoparticles for excitation at different wavelengths would allow for multiplexed imaging to be performed [240].

2.6   Summary

EGFR targeting peptide previously used to collect fluorescence images endoscopically from mouse colonic adenomas with topical administration was labeled with NIR dye Cy5.5 and validated in both colorectal dysplasia and HCC cell lines. The use of *in vivo* optical and photoacoustic imaging to visualize HCC xenograft tumors in living mice with a peptide specific

for EGFR was demonstrate. It was shown that specific binding to EGFR can also occur with systemic administration and tumor margins were clearly visible with on fluorescent laparoscope. Photoacoustic imaging at a depth down to 1.8 cm with low background confirmed peptide probe delivery deep inside tumor. We found peak uptake at 3 hours post injection and clearance by ~24 hours. This time frame is significantly faster than most antibodies and applicable in clinical settings.

Chapter 3   Selection and validation of GPC3 targeting peptide for HCC

3.1   GPC3 specific peptide as HCC targeting strategy

In order to tackle the challenge of tumor heterogeneity, a second biomarker was investigated for *in vivo* HCC imaging with the potential for multiplexed detection. Since we are concerned about heterogeneity of human HCC patients, it makes sense to look for the best potential HCC biomarker from gene expression profiles of HCC patient specimens.

3.1.1   Identification of GPC3 as HCC target

We analyzed gene expression profiles of HBV-related HCC specimens from the GSE14520 and GSE44074 datasets [241-243]. GSE14520 provided the most comprehensive data. A total of n = 213 pairs of HBV-related HCC and non-tumor specimens were analyzed using 22,268 probe-sets on an Affymetrix HT_U133A platform. We refined the data based on the following criteria: P-value $<1\times10^{-40}$, average fold-change >2, and location on plasma membrane.

Gene	GSE14520		GSE44074	
	p-value (paired T-test)	FC (tumor vs non-tumor)	p-value (2-sample t-test)	FC (tumor vs non-tumor)
CCT3	6.9E-85	3.0	8.4E-08	1.8
CAP2	1.2E-82	6.0	8.1E-02	1.2
ACLY	1.0E-80	3.1	3.5E-09	1.6
PRC1	4.7E-80	5.5	#N/A	#N/A
GPC3	1.1E-70	29.3	3.5E-15	4.4
IRAK1	1.8E-68	2.5	3.4E-02	1.3
ENAH	7.2E-68	3.9	#N/A	#N/A
HSPB1	2.3E-67	2.9	1.5E-02	1.4
HSP90AB1	6.2E-63	2.3	#N/A	#N/A
ROBO1	4.8E-62	6.8	2.7E-05	1.3
ITGA6	3.0E-61	2.8	4.9E-02	1.3

Table 3.1 potential HCC targets. Glypican-3 (GPC3) is high, significant and specific expression in HCC extracellular membrane. Gene expression of GPC3 is elevated in HCC compared with non-tumor. A) Gene expression profiles from datasets GSE14520 We used paired T-tests on log-transformed data, and obtained 1397 probe sets with P-value $<1\times10^{-40}$, of which 111 had GO terms indicating they appeared in plasma membrane, and were increased in tumors. Of these, GPC3 (red box) gave P-value = 1.1×10^{-70} (5th best), and average fold-change of 29.261 (highest in tumors). We then analyzed log-transformed data for 8516 transcripts from dotted arrays measured in GEO series GSE44074, consisting of 34 HCC samples and 71 normal liver samples. A two-sample T-test gave 549 genes with P < 0.001, of which 49 were increased in tumors and on plasma membrane. Of these GPC3 gave both the largest fold-change and smallest p-value (4.5 fold increase, P = 3.5×10^{-15}).

We then analyzed log-transformed data for 8516 transcripts from dotted arrays measured in GEO series GSE44074, consisting of 34 HCC samples and 71 normal liver samples. A two-sample T-test gave 549 genes with P < 0.001, of which 49 were expressed on plasma membrane (thus accessible for imaging) and were found to increase in tumors compared to normal. Of these, glypican-3 (GPC3) gave both the largest fold-change and smallest p-value (4.5 fold increase, P = 3.5×10^{-15}). A panel of promising cell surface targets, including CAP2, GPC3, and ROBO1, were overexpressed in HCC that can be developed for imaging, Table 3.1. GPC3 showed the largest fold-change of 29.26 between tumor and non-tumor with lowest P-value.

Differences are reflected by the distribution of gene expression levels of individual tumors, Figure 3.1(A). Significant difference in GPC3 gene expression between HCC and non-tumor

specimens from n = 213 specimen pairs was found, P-value <0.001 by paired t-test, from GSE14520. Expression levels of normal and HCC liver samples were plotted with P-value <0.001 by 2-sample t-test, from GSE44074. The ROC curve for this data shows 87% sensitivity and 90% specificity with an area-under-the curve (AUC) of 0.92, Figure 3.1(B). These results show that GPC3 is a promising biomarker for HCC. GPC3 is high, significant and specific expression in HCC extracellular membrane. Gene expression of GPC3 is elevated in HCC compared with non-tumor.
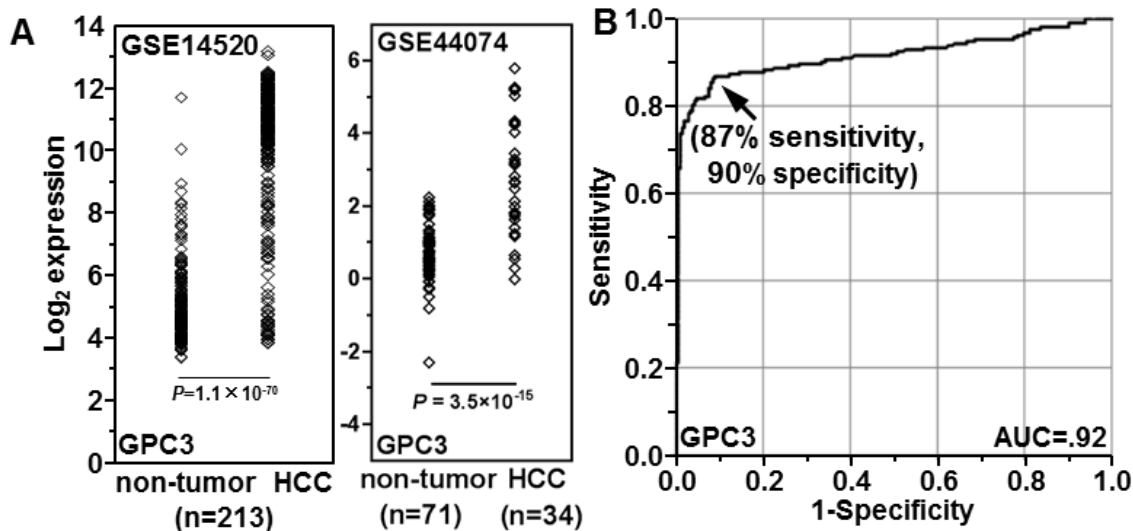
Figure 3.1 GPC3 overexpression in HCC. (A) Significant difference in GPC3 gene expression between HCC and non-tumor specimens from n = 213 specimen pairs was found, P-value <0.001 by paired t-test, from GSE14520. Expression levels of normal and HCC liver samples were plotted with P-value <0.001 by 2-sample t-test, from GSE44074. (B) ROC curve for GSE14520 shows area under the curve (AUC) of 0.92 with 87% sensitivity and 90% specificity.

3.1.2 Significance of GPC3 as HCC target

Previous studies have established GPC3 as a promising HCC-specific target [244-246]. Glypicans (GPCs) are a family of heparin sulfate proteoglycans that anchor on the cell membrane with a glycosylphosphatidylinositol (GPI) linkage [247], Figure 3.2. This family consists of six members (GPC1-GPC6) in mammals. GPC3, a 70kDa protein, is composed of a core protein and two heparin sulfate chains [248]. GPC3 has been found to be significantly more

sensitive and specific for HCC than alphafetoprotein (AFP), a serum biomarker widely used in HCC surveillance [249, 250]. A significant increase in serum AFP level is detected in a considerable number of patients with chronic liver disease [251, 252] including 15%–58% of patients with chronic hepatitis and 11%–47% with cirrhosis [250]. On the other hand, GPC3 is a promising HCC-specific target on the cell surface [9, 21, 22, 253], whose expression is absent in normal adult tissues, but is significantly over-expressed in up to 80% of human HCC's [9, 22, 254]. A number of immunochemistry studies have found its expression is significantly elevated in HCC, but rarely detected in benign liver lesions cirrhosis, low-grade, and high-grade dysplasia [254-259]. Given the high expression in HCC, the usefulness of GPC3 as a target for both antibody and cell based immunotherapies have been explored [253, 260, 261].
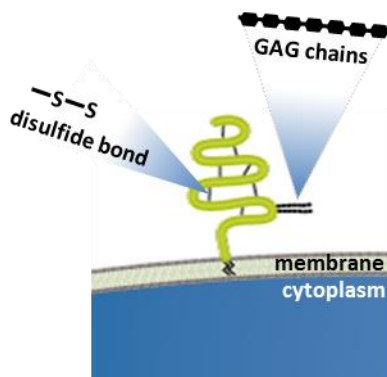
Figure 3.2 Structure of Glypican 3 on cell surface. Glypican 3 is anchored to the cell surface via a GPI linkage, has a conserved pattern of 14 cysteine residues, which contribute to intramolecular disulfide linkages, and displays GAG attachment sites predominantly near the membrane. Figure is adapted from Glypicans in Cancer (https://www.rndsystems.com/resources/artices/glypicansin-cancer).

GPC3 participates in a variety of pathways related to HCC, such as Wnt [262, 263], Yap, BMP-7 and FGF [264]. Through interactions with these signaling pathways, GPC3 can regulate HCC development, metastasis, and angiogenesis [247, 258, 265-267]. For example, overexpressed GPC3 is capable of binging Wnt [268] and facilitating Wnt/Frizzled interactions, which are believed to be vital in the progression of many cancers, including HCC [9, 265, 267]. Its expression profiling is an independent prognostic indicator in patients with HCC and is

correlated with the clinical malignant behavior of HCC [20, 269, 270]. Furthermore, it has been

shown that mutations in GPC3 or knockdown of its function can inhibit HCC growth, reinforcing

the important roles of GPC3 in HCC development [266, 271, 272].

An ideal marker should be able to differentiate malignant from normal and benign lesions with

high sensitivity and specificity, and should be a marker in the early transition phase from

premalignancy to malignancy [273-275]. HCC can develop from a variety of risk factors,

including cirrhosis, HBV and HCV [276-278]. Many studies have shown that GPC3 is highly

and specifically expressed in 70–100% cases of HCC, and could be used as a maker to

differentiate HCC from benign liver tissues [279-282]. The sensitivity and specificity of a

positive GPC3-staining for the diagnosis of HCC in small focal lesions was 77% and 96%,

respectively, in resected cases, and 83% and 100%, respectively, for needle biopsies [283]. A

diversity of targeting strategies, including antibody[284], antibody fragment [285], chimeric

antigen receptor expressing T cells [286], have been explored for imaging and therapy of GPC3

overexpressing HCC. The above evidence has led us to believe GPC3 has great potential as

biomarker for HCC imaging.

3.1.3 GPC3 targeting peptide selection

GPC3 antibodies have been extensively incorporated in targeted probes for HCC imaging as they

demonstrated superior targetability and specificity, with the limitation of long incubation time

and high cost [287, 288]. ^{89}Zr-labeled anti-glypican-3 monoclonal antibody was able to delineate

HCC patient derived orthotopic xenografts in PET, with tumor/liver ratios of 2.31-4.21 after 169

hrs post injection [284]. In other studies, tumor to liver ratio reached nearly 32.5 on day 7 post-

injection of ^{89}Zr-αGPC3 in orthotopic HCC xenografts [289]. Fragmented antibody can reduce

the incubation time as well as blood half-life while retaining specificity of antibody. In the same

study, fragment of aGPC3 IgG1 was conjugated to ^{89}Zr and visualized tumor on PET 4 hour after administration at contrast ratio of 23.3 [285].

By comparison, small molecules such as peptide have the advantage of fast tumor uptake and clearance from the system as described in detail in Section 1.4. Thus, we selected a peptide sequence specific for GPC3 by biopanning phage display library against GPC3 core protein below.

3.1.3.1 Phage display

We adopted phage display [290] as our peptide selection strategy, Figure 3.3. Purified human GPC3 core protein (62 kDa, Sino Biological Inc.) expressed in human cells was immobilized to select peptide candidates that bind specifically to GPC3 protein. A library of M13 bacteriophages with $>10^9$ unique sequences was incubated with the GPC3 recombinant protein to identify high affinity binding interactions. After the washing step, unbound phages are removed and bound phages are eluded and isolated for identification. Amplification of purified phage clones generates enough phages for molecular characterization and application.
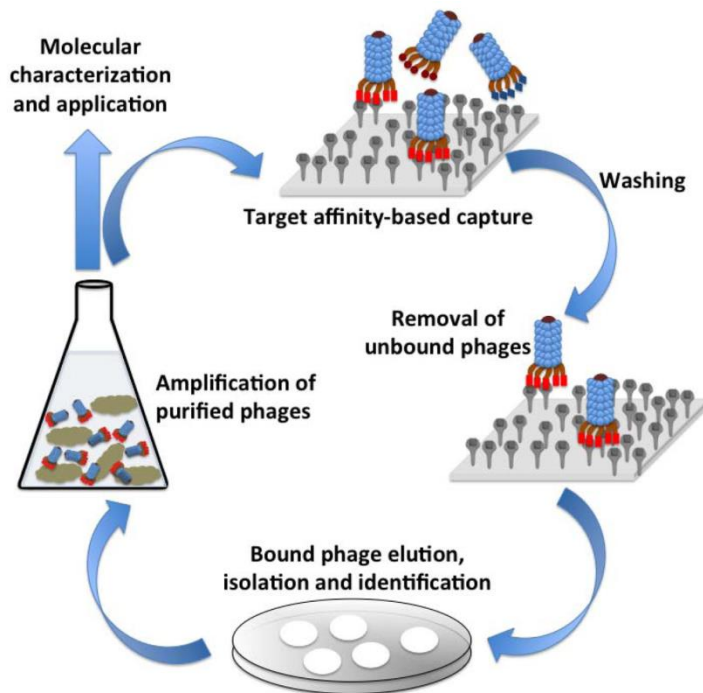
Figure 3.3 Peptide selection strategy: phage display. A schematic of affinity-based selection procedure adapted in phage display technology. The phage libraries can be screened against an immobilized target of interest, the unbound phages are washed away and the tightly bound phages are eluted, propagated and are used as probes against that target. Various events are illustrated in the phage affinity-based selection for probe development against a target. Figure was adapted from reference [291].

3.1.3.2 Library selection

A linear phage display library was adopted for the selection of GPC3 specific peptide. There are two kinds of commercially available phage display libraries, linear and cyclic [292]. Linear library phages display either 7-mer (Ph.D.-7) or 12-mer (Ph.D.-12) random peptides fused to coat protein (pIII) of M13 phage, while cyclic library phages (Ph.D.-C7C) display randomized 7-mer sequence flanked by a pair of cysteine residues which form a disulfide cross-link and cyclized peptides [293, 294]. These libraries have proven useful in identification of structural epitopes [295, 296] and leads for peptide-based therapeutics [297]. Here the C7C cyclic library was not adopted for the attempt of biopanning since it does not offer longer sequence and the disulfide-constrained peptide limits the 3D configurations the peptide is able to take.

Our first attempt to perform peptide selection in 7-mer library and the candidates was unsuccessful. Results are shown in Table 3.2, with decreasing copy numbers after 3rd and 4th rounds of panning. The majority of these sequences showed up in the panning outcomes for other targets, c-MET and FGFR2, indicating their amplification didn't result from target specificity but rather intrinsic propensity to amplify more efficiently than other sequences. One possible reason for this outcome could be that 7-mer peptides were simply too short to form the 3D structure to recognize any epitope on the target protein. Thus a longer peptide library could potentially provide better targetability.

	3rd(in 60)	4th(in 60)
G Q S E K H L	7	5
T V N F K L Y	6	0
H G G V R L Y	3	0
A P V Q L V R	2	0
W G R I S H V	2	0
D T A L H S L	0	46
Q Q L A V D T	1	0
Q L A V A P S	0	0
S I Y P A E N	1	0
L P V R L D W	1	0
S P N Y N I I	1	0

Table 3.2 7-mer linear library panning results. Phage display results from screening 7-mer phage library against GPC3 core protein. Candidate sequences are arranged in descending order of 3rd and 4th round enrichment number.

Our second attempt of biopanning performed with 12-mer linear library generated some interesting results. As shown in Table 3.3, the first candidate peptide has a stop codon at the 11th amino acid residue, which would have terminate the sequence at the 10th amino acid. However, the presence of the 12th amino acid, tyrosine (T), reveals that certain mechanism was allowing the translation to "read through" the stop codon and produce a 12-mer rather than a 10-mer peptide. A closer look at the sequencing result at nucleotide level is necessary to identify the 11th amino acid.

		3rd(51)	4th(46)
A L L A N H E E L F Stop T		0	2
G L H T S A T N L Y L H		1	6
S G V Y K V A Y D W Q H		1	1
V G V E S C A S R C N N		0	3

Table 3.3 12-mer library panning results. Four 12-mer peptide sequences were identified after 12-mer phage display against GPC3 core protein.

3.1.3.3 Amber mutation

The mechanism that suppressed the stop codon and allowed translation was amber mutation [298]. Amber mutations (UAG) were the first set of nonsense mutations discovered, isolated by Richard Epstein and Charles Steinberg and named after their friend Harris Bernstein (whose last name means "amber" in German). As can be seen in the codon chart in Figure 3.4(A), codon UAG is normally a stop codon. However, the presence of either *supF* or *supE* mutation, Figure 3.4(B), in the anticodons of tRNA of tyrosine (UAC) or glutamine (CAG) can allow the translation of UAG stop codon into either Try or Gln respectively.
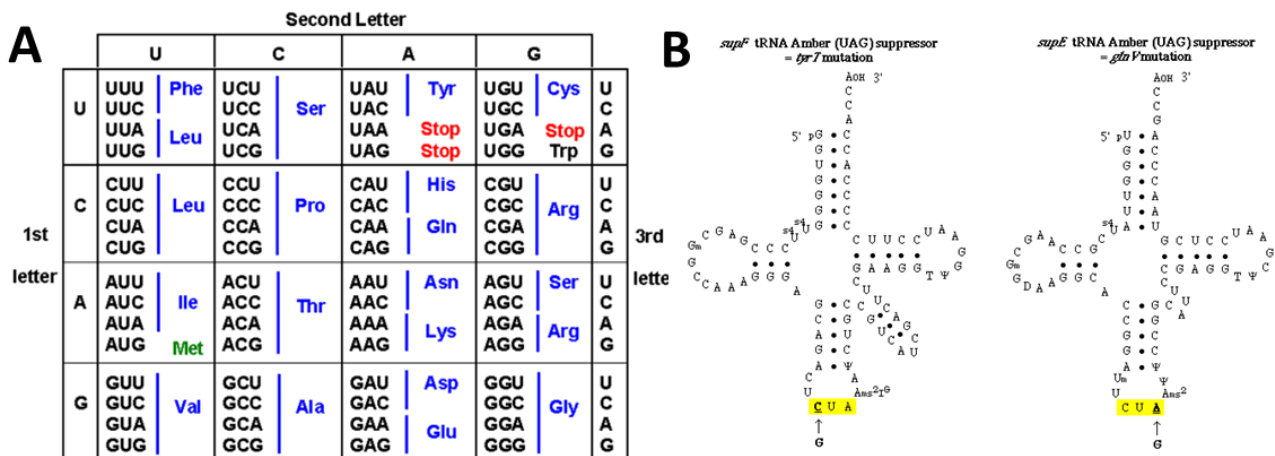
Figure 3.4 Codon chart and amber suppressors. (A) UAG is one of the three Stop codons in the codon chart. (B) Anticodon of tRNA of tyrosine (UAC) or glutamine (CAG) can allow the translation of UAG stop codon into either Try or Gln respectively.

Amber mutation restricted phage library survival inside only genetically specific host. Viruses with amber mutations are characterized by their ability to infect only certain strains of bacteria,

known as amber suppressors. These bacteria carry their own mutation that allows a recovery of function in the mutant viruses. For example, a mutation in the tRNA that recognizes the amber stop codon allows translation to "read through" the codon and produce full-length protein, thereby recovering the normal form of the protein and "suppressing" the amber mutation. Thus, amber mutants are an entire class of virus mutants that can grow in bacteria that contain amber suppressor mutations.

```
Sequencing of primer chain was done in the 5'→3' direction :
5'        A G T C T A A A A A A G C T C C T C A T G A T T A G C A A G A A G A G C      3'  antisense (primer chain)
3'        T C A G A T T T T T T C G A G G A G T A C T A A T C G T T C T T C T C G      5'  sense

5'        G C T C T T C T T G C T A A T C A T G A G G A G C T T T T T T A G A C T      3'  sense
5'        G C U C U U C U U G C U A A U C A U G A G G A G C U U U U U U A G A C U      3'  mRNA (codon)
NH2-      A   L   L   A   N   H   E   E   L   F   Q   T        -COOH  peptide
Peptide#  1   2   3   4   5   6   7   8   9   10  11  12
```

Figure 3.5 Amber suppression in ALL* peptide sequencing result. The 11th amino acid in the DNA sequencing result is translated to glutamine (Q) in presence of supE (*GlnV*) of E. coli host strain ER2738 to suppress UAG stop codon.

The specific E. coli host strain for phage amplification resulted in glutamine as the 11th amino acid in the 12-mer sequence. The recommended E. coli host strain ER2738 [299] (F´ proA+B+ lacIq Δ(lacZ)M15 zzf::Tn10(TetR)/fhuA2 glnV Δ(lac-proAB) thi-1 Δ(hsdS-mcrB)5.[rk– mk– McrBC–]) is a robust F+ strain with a rapid growth rate and is particularly well-suited for M13 propagation. ER2738 is a recA+ strain. Commercially available F+ strains can be substituted for ER2738, but any strain used should be supE (*GlnV*) in order to suppress amber (UAG) stop codons within the library with glutamine. Therefore, the 11th amino acid is translated as a glutamine, rather than tyrosine, as shown in the sequencing result of ALL* peptide, Figure 3.5.

The nature of phage protein translation provided essential confirmation for the success suppression of amber stop codon when direct evidence from fusion protein sequencing is unattainable. The peptides fused coat protein (ALL*-pIII) is translated from the N-terminus

where the 12-mer peptide ALL* precedes pIII. Since pIII is essential for the phages' survival, failure of amber suppressing at 11th amino acid would preclude pIII translation and consequently eliminate the existence of ALL* 12-mer peptide carrying phages. In other word, no ALL* phages would have survived to be DNA sequenced in the first place. Admittedly, direct sequencing of fusion protein would ultimately confirm the actual expression of 12-mer peptide sequence. However, isolating phage proteins from those of E. coli and purifying the few copies of fusion protein from the thousands of native coat proteins on the phage proved extremely challenging, if at all possible, without extensive protein characterization facilities and experience. Thus it is beyond the scope of this thesis to pursue.

3.2 Validation in human tissue with targeting phage

ALL*-Cy5.5 phages were first Cy5.5 labeled to verify peptide specificity for GPC3 expression on human HCC specimens before intensive time (1~2 months) and resources were invested in the synthesis of the Cy5.5 labeled 12-mer peptide for extensive *in vitro* and *ex vivo* validations.

3.2.1 Labeling phage with NIR dye

Cy5.5 labeling on ALL*-Cy5.5 phages can be done quickly and allowed GPC3 specific binding on human HCC tissue to be visualized when Cy5.5 labeled wildtype phages served as control for non-specific binding. After isolation and identification of candidate phage displaying targeting peptide as N-terminal pIII fusions, amplified and purified phages were labeled with near-infrared dye Cy5.5 as imaging agent to validate binding on human HCC tissue. Specifically, Cy5.5 NHS ester solution was prepared at 5 mg/ml in 0.1M bicarbonate buffer, pH8.3 (conjugation buffer). In parallel, an aliquot of 0.5×10^{13} plaque-forming units (pfu) of phages was precipitated with standard polyethylene glycol 8000 (PEG 8000, Sigma) and NaCl solution (20% PEG, 2.5M NaCl) and subsequently re-suspended in 200 uL of conjugation buffer in microfuge tubes. Phage

suspensions were incubated in the dark on a rotator for 2 hours at room temperature with 20 µL

of Cy5.5 NHS ester solution. Following incubation, phages were precipitated (12k rpm for

10min) 3 times with 200uL of PEG and NaCl. The final pellet was dissolved in 200uL 1X TBS,

pH7.5. To confirm the success of the conjugation the UV-absorbance was checked at 673 nm.

The schematic of Cy5.5 labeled ALL* and wildtype (WT)-phages are shown in Figure 3.6(A)

and Figure 3.6(B) respectively.
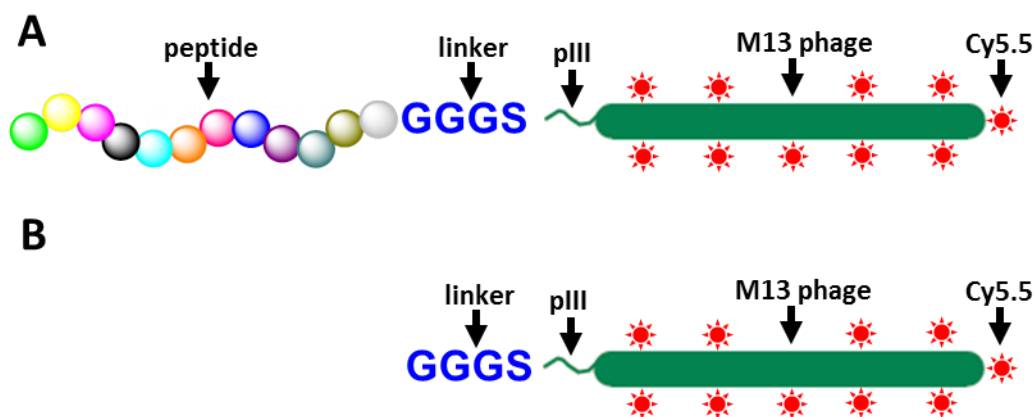
Figure 3.6 NIR dye labeled GPC3 targeting phages. Schematic of (A) ALL* and (B) wildtype phages labeled with Cy5.5 dye.

3.2.2 Binding of GPC3 targeting phages and antibody to human HCC

Cy5.5 labeled ALL*-Cy5.5 phages and wildtype phages were applied to paraffin embedded

human HCC and normal liver specimens respectively to perform microscopic validation of

peptide binding to GPC3 overexpression in HCC. Specimens of human HCC and normal liver

specimens were obtained from biopsy during HCC resection surgery. Deparaffinization, and

antigen retrieval was performed as previously described. Sections were incubated with ALL*

peptide displaying phages labeled with NIR dye Cy5.5 (4 µM) in 1 × TBS for 10 min at RT, or

overnight at 4 °C with 1:200 dilution of primary monoclonal rabbit anti-GPC3 antibody (Abcam

Inc, SP86). The antibody stained sections were washed three times with PBS and incubated with

1:500 dilution of Alexa Fluor 488-labeled secondary goat anti-rabbit antibody (Invitrogen) for 1

h at RT. The sections were then washed once with PBS, and mounted with ProLong Gold reagent containing DAPI (Invitrogen). Confocal microscopy (Leica TCS SP5 Microsystems) was performed with a 20× objective. The mean fluorescence intensities from three boxes (dimensions of 20 × 20 μm^2) located within HCC, cirrhosis and normal portion of each specimen were measured respectively. Regions that showed intensity saturation were avoided. Sections were processed for routine histology (H&E) that was reviewed by a hepatobiliary pathologist.
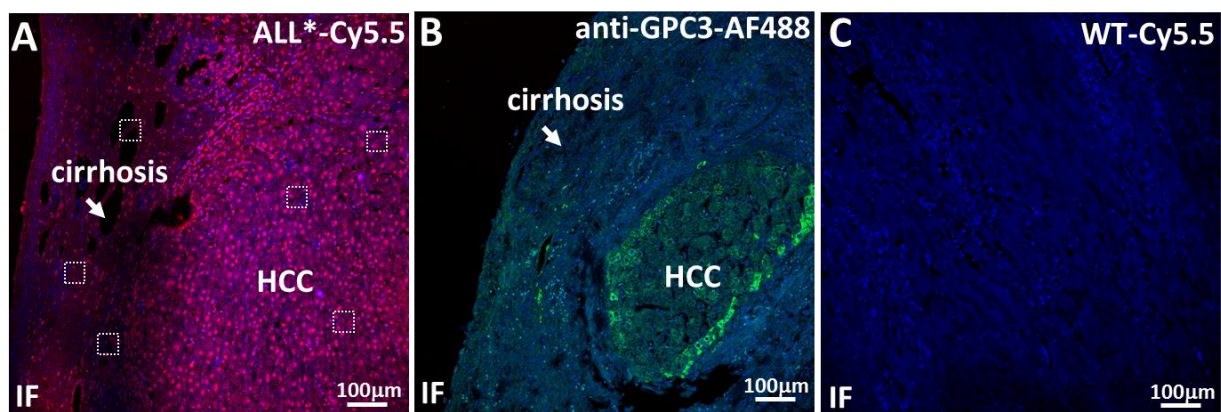
Figure 3.7 Immunofluorescence of Cy5.5 labeled phages and antibody on human HCC tissue. We observed specific binding of (A) ALL*-Cy5.5 phages and (B) anti-GPC3-AF488 antibody to HCC over cirrhosis (arrow) in human tissue on immunofluorescence. (C) No staining was observed from Cy5.5-labeled wild-type phages on human HCC tissue.

We found increased cell surface staining of ALL*-Cy5.5 phages compared with Cy5.5 labeled wildtype phages to HCC versus surrounding cirrhotic tissue (arrow), Figure 3.7(A & C). We performed immunofluorescence with a known antibody to validate over expression of GPC3 in mouse colonic dysplasia, Figure 3.7(B). Minimal staining was observed for either peptide with normal human liver tissue, Figure 3.8(A-B). Fluorescence intensities (mean±SD) measured for HCC, cirrhosis and normal (n=10) were 90.69 ± 11.22, 41.01 ± 12.56 and 8.05 ± 2.19, respectively, *P<0.01 by unpaired t-tests, Figure 3.8(C). These results indicate ALL*-Cy5.5 phages can specifically bind to overexpressed GPC3 in human HCC, creating contrast against normal and cirrhotic tissue.
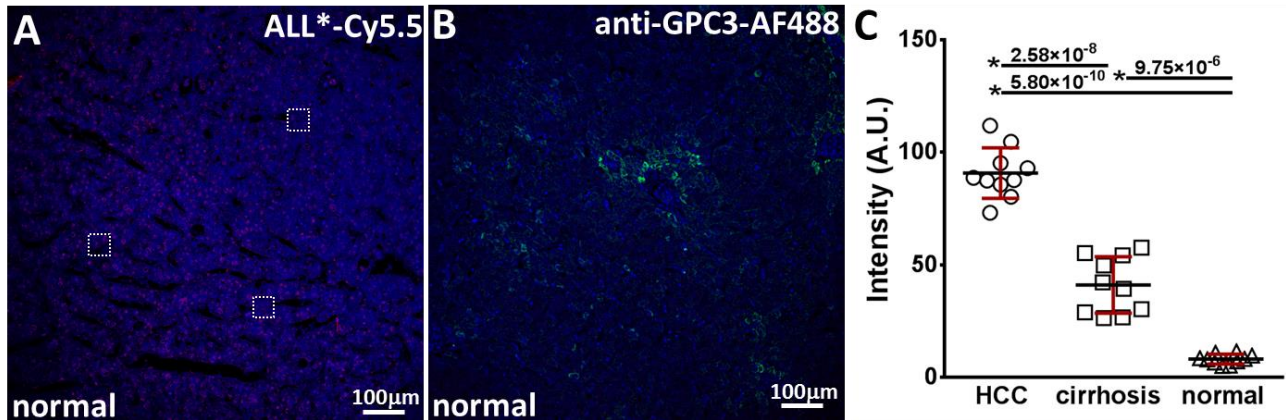
Figure 3.8 Immunofluorescence of Cy5.5 labeled phages and antibody on normal human liver. (A) ALL*-Cy5.5 phages or (B) AF488-labeled anti-GPC3 antibody showed minimal immunofluorescence was seen on normal human liver. (C) Fluorescence intensities (mean±SD) measured for HCC (n=10), cirrhosis and normal were 90.69 ± 11.22, 41.01 ± 12.56 and 8.05 ± 2.19, respectively, *$P<0.01$ by unpaired t-tests.

3.2.3 GPC3 expression in human HCC on immunohistochemistry
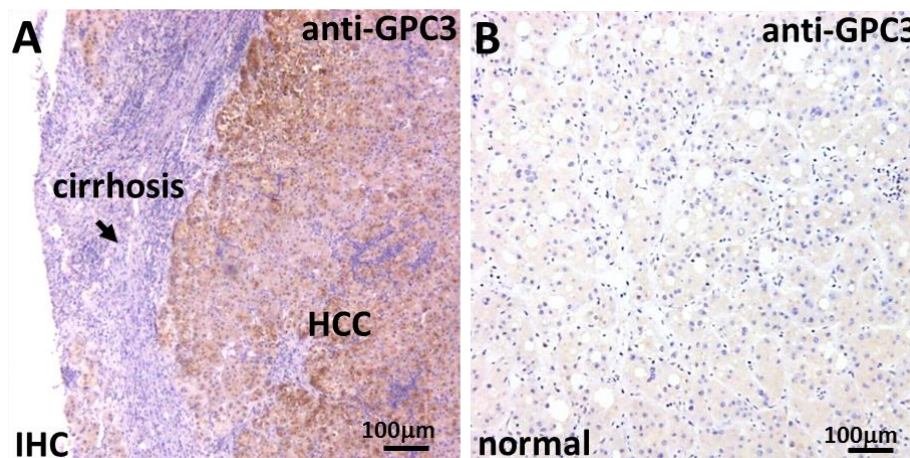
Figure 3.9 IF and IHC on human HCC tissue with antibody. (A) Increased expression of GPC3 in human HCC specimens compared to liver cirrhosis was confirmed on immunohistochemistry using anti-GPC3 antibody (GαR), scale bar 100 μm. (B) minimal reactivity was seen on immunohistochemistry of normal human liver.

Immunohistochemistry was performed as described in Section 2.2.1.4, with a known GPC3 antibody (1:100, Abcam Inc, SP86), to provide additional confirmation on overexpression of GPC3 in human HCC, Figure 3.9(A). Normal liver section with the same primary antibody (control) shows minimal reactivity, Figure 3.9(B). Controls were prepared using secondary antibody, Elite Vectastain ABC reagent, and DAB (without primary anti-GPC3 antibody). Serial sections were processed for histology (H&E). Corresponding histology (H&E) of human HCC and normal liver tissue is shown, Figure 3.10 (A-B).

70
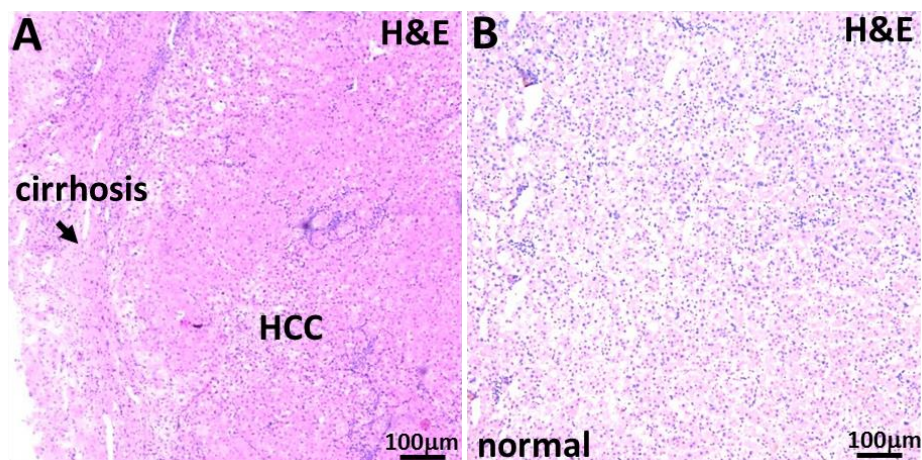
Figure 3.10 H&E histology of human HCC and normal liver tissue. (A) Corresponding histology (H&E) for HCC and cirrhosis is shown. (B) Corresponding histology (H&E) for normal liver is shown.

3.3 Peptide synthesis and labeling

Despite their ability to distinguish HCC on human specimens, phages cannot be clinically translated due to their biohazard and health risks to patients. The GPC3 targeting 12-mer peptide sequence had to be synthesized and labeled with NIR dye for further *in vitro* and *ex vivo* validations. On the phages, the displayed peptide (12-mer) is expressed at the N-terminus of pIII, i.e., the first residue of the mature protein is the first randomized position. The peptide is followed by a short spacer GGGS (Gly-Gly-Gly-Ser) and then the wildtype pIII sequence, Figure 3.6. Therefore, a linker sequence, GGGSK, was designed in synthesized peptide in order to replicate the chemical environment of targeting sequence displayed on the phages. The lysine (K) residue was placed at the C-terminal of the sequence to conjugate with Cy5.5 NHS (N-hydroxysuccinimide) ester through the amine group. The long carbon chain on lysine's R-group offset the dye molecule way from the targeting sequence to minimize steric hindrance during binding. Cy5.5 was chosen for its high quantum yield and photostability [130] as discussed in more detail in Section 2.1.3.

3.3.1 Synthesis and labeling procedures

We synthesized Cy5.5-labeled peptides using standard Fmoc-mediated solid-phase synthesis as previously described in Section 2.1.3. The resulting labeled GPC3 targeting peptide (ALLANHEELFQT) structure is shown in Figure 3.11(A). A scrambled peptide sequence (QLELTFHANLEA) with the same amino acid components is also and synthesized as control, hereafter QLE*-Cy5.5, Figure 3.11(B).
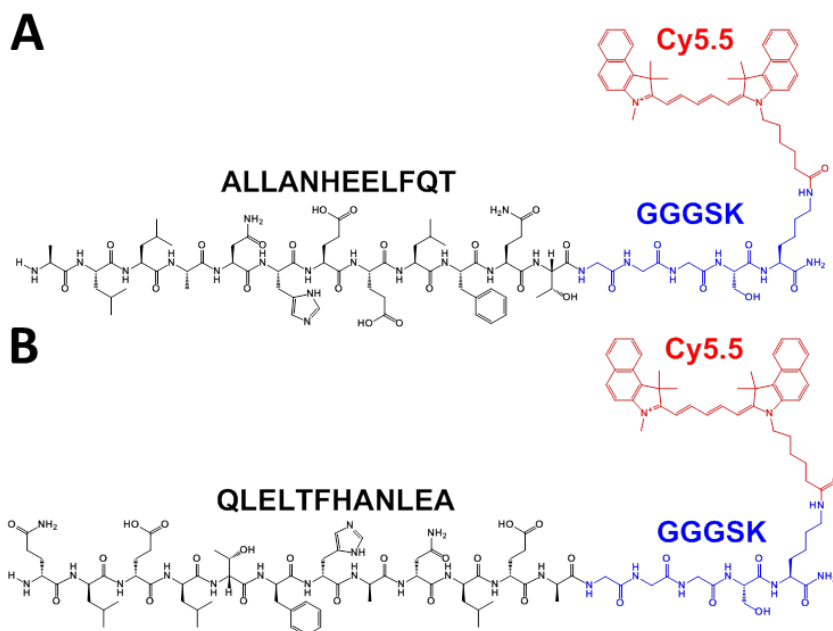
Figure 3.11 Chemical structure of 12mer targeting peptide and scrambled control. (A) Chemical structure of 12 amino acid peptide ALLANHEELFQT (black) with GGGSK linker (blue) and Cy5.5 fluorophore (red), hereafter ALL*-Cy5.5. (B) Scrambled control peptide QLELTFHANLEA (black), hereafter QLE*-Cy5.5.

From 3D space filing structure simulations, both the overall shape and local chemical environment are different after scrambling the targeting peptide, Figure 3.12(A-B). This could account for the loss in targeting ability of the scrambled peptide and serve as experiment control for non-specific binding. The N-terminals of peptides where the 12-mer sequences begin are denoted with arrow heads while arrows mark the positions of Cy5.5 labels.

A

B

ALL-Cy5.5

QLE-Cy5.5
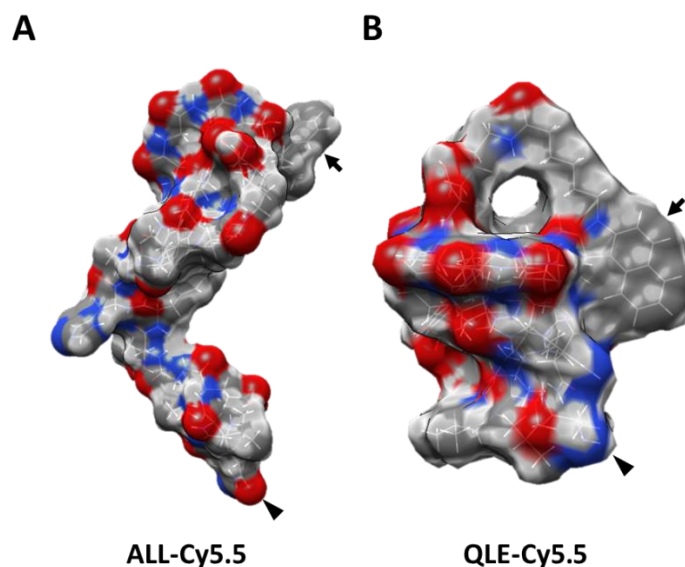
Figure 3.12 3D space filing structures of both (A) targeting and (B) scrambled control peptides with Cy5.5 label. 3D space filing structures of peptides show site for attachment of Cy5.5 label (arrows). 12-mer sequences begins at N-terminus (arrowheads). Both the overall shapes and local chemical environments are different in the two probes. Color code: grey - C; white - H; red - O; blue - N; yellow - S.

3.3.2   Spectral characterization
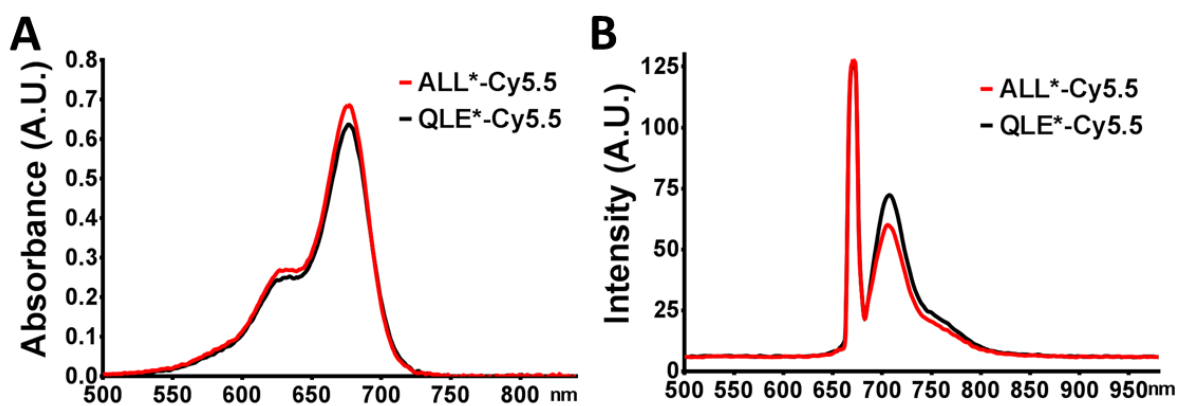
Figure 3.13 Absorbance and fluorescence spectra of labeled 12-mer peptides. (A) Absorbance spectra of Cy5.5-labeled peptides shows peak at $\lambda ex = 677$ nm. (B) Maximum fluorescence emission is seen at $\lambda em = 708$ nm for both peptides.

After NIR dye labeling, spectral characterization confirmed peak absorption/emission wavelengths and molecular weight of peptide probes. Spectra were collected 100 µM concentration with a UV-Vis spectrophotometer in the 500-900 nm range (NanoDrop 2000, Thermo Scientific). Fluorescence emission from a 5 µM peptide solution diluted in PBS was collected with a fiber coupled spectrophotometer (Ocean Optics) using a diode-pumped solid

73

state laser (Technica Laser Inc) with λ_{ex}=671 nm. The spectra were plotted with Origin 6.1 software (OriginLab Corp). The absorbance spectra of ALL*-Cy5.5 and QLE*-Cy5.5 at 10 µM in PBS showed a maximum at 677 nm, Figure 3.13(A). The fluorescence spectra of ALL*-Cy5.5 and QLE*-Cy5.5 at 10 µM concentration in PBS with λ_{ex} = 671 nm excitation revealed a peak emission at 708 nm, Figure 3.13(B). We purified the Cy5.5-labeled peptides to >96% on HPLC, and measured an experimental mass-to-charge (m/z) ratio on mass spectrometry of 2335.22 for both QRH*-Cy5.5 and PEH*-Cy5.5 that agreed with expected molecular weight values, Figure 3.14(A-B).
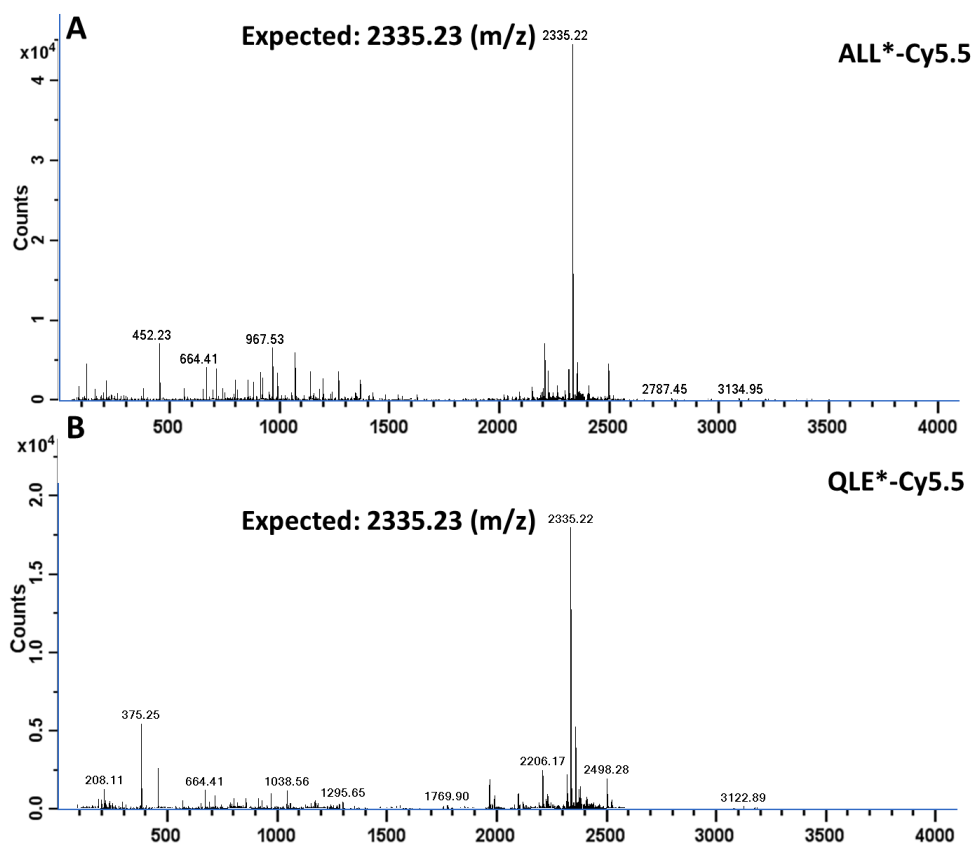
Figure 3.14 Mass spectrometry of Cy5.5-labeled peptides. An experimental mass-to-charge (m/z) ratio was measured for (A) ALL*-Cy5.5 and (B) QLE*-Cy5.5 of 2335.22 (with one C-13), which agrees with the expected value of 2335.23 for both peptides.

3.4   *In vitro* validation of peptide targetability

As Section 3.2 demonstrated, Cy5.5 labeled ALL* peptide carrying phages proved to bind specifically to GPC3 overexpression in HCC specimens. This prompted us to validate the performance of Cy5.5 labeled ALL* peptide, All*-Cy5.5 *in vitro*. To see if ALL*-Cy5.5 probe actually binds to GPC3 on surface of human HCC cell lines were first conducted *in vitro* before *ex vivo* validation in HCC mouse model was undertaken.

3.4.1   GPC3 expression levels in HCC cell lines

Human HCC cells Hep3B, HepG2, and SK-Hep1 were purchased from the ATCC (Manassas, VA) and cultured in Eagle's Minimum Essential Medium (EMEM). All cells were cultured at 37ºC in 5% CO2, and supplemented with 10% fetal bovine serum (FBS) and 1% penicillin/streptomycin. Cell lysates of three cell lines were separated into plasma membrane protein fraction and cytosolic protein fraction respectively using a membrane protein extraction kit (K268-50, Biovision) and protein concentrations were determined by BCA protein assay kit (23225, Thermo Fisher Scientific) before loading for Western blotting. Western blot was performed using a 1:10000 dilution of primary monoclonal rabbit anti-GPC3 antibody (Abcam Inc., EPR5547) per manufacturer instructions. Loading was controlled with a 1:500 dilution of monoclonal mouse anti-β-tubulin (#32-2600, Invitrogen). Western blot showed difference in expression of GPC3 for Hep3B, HepG2 and SK-Hep1, Figure 3.15. The differential GPC3 expression levels in these three HCC cell lines served as the testing field for the specificity of GPC3 binding by peptide probe. Binding intensity in each cell line was expected to correlate with GPC3 abundance and was measured through the fluorescence signal on immunofluorescent imaging.
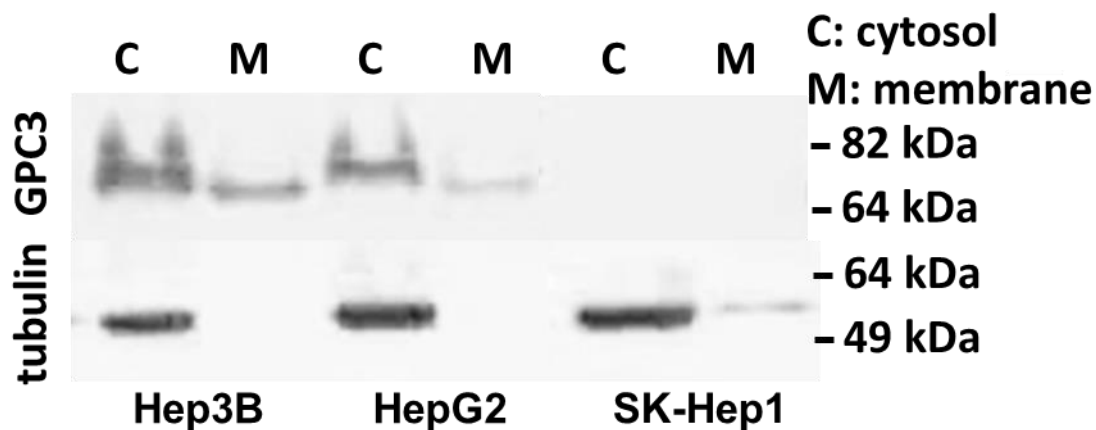
Figure 3.15 GPC3 expression levels in HCC cell lines. Western blot showed GPC3 (molecular weight = 66 kDa) expression levels for HCC cells in cytoplasm (C) and plasma membrane (M). Loading control was performed with tubulin (50 kDa).

3.4.2   GPC3 specific binding on HCC cell lines

Immunofluorescence staining with both peptide probes and GPC3 antibody was performed as described in Section 2.2.2.2. Hep3B, HepG2, and SK-Hep1 and incubated with 5 µM ALL*-Cy5.5 and QLE*-Cy5.5 for 30 min at 4ºC respectively. For antibody staining, Cells were incubated with 1:200 dilution of anti-GPC3 antibody overnight at 4ºC.

Peptide binding to the plasma membrane (arrows) was observed on confocal microscopy and significantly greater fluorescence intensity for ALL*-Cy5.5 than QLE*-Cy5.5 to Hep3B, HepG2 and SK-Hep1 cells was found, Figure 3.16(A-F). An AF488-labeled anti-GPC3 antibody also showed significantly greater signal than the control peptide, Figure 3.16(G-I).
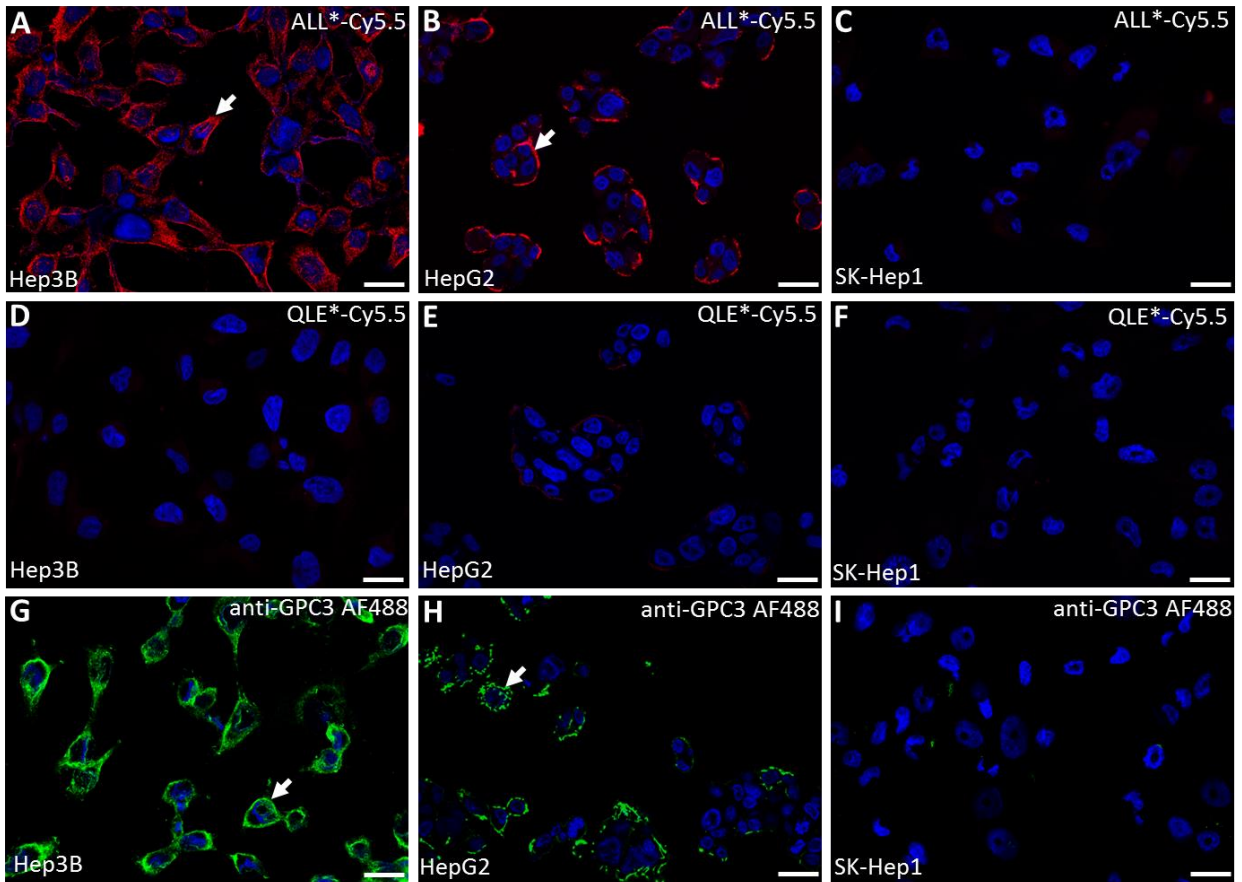
Figure 3.16 Immunofluorescence on HCC cell lines. On confocal microscopy, we observed strong fluorescence intensity from ALL*-Cy5.5 binding to the surface (arrow) of (A) Hep3B and (B) HepG2 human HCC cells, and minimal signal with (C) SK-Hep1 cells. (D-F) Minimal signal is observed with the scrambled control peptide QLE*-Cy5.5 for all cells. Strong binding (arrow) is also observed with AF488-labeled anti-GPC3 antibody used as a positive control for (G) Hep3B and (H) HepG2 and minimal signal with (I) SK-Hep1.

Quantified results were summarized in Figure 3.17. The intensity difference for Hep3B vs SK-Hep1 was significantly larger for ALL* than for the same difference for QLE* (P=3.8×10^{-10}, 8.2-fold larger), and the HepG2 vs SK-Hep1 difference was also significantly larger (P=4.6×10^{-5}, 3.3-fold larger). The Hep3B vs SK-Hep1 difference was also larger for antibody than QLE (P=2.3×10^{-8}, 6.0-fold larger). Fluorescence intensities from 3 independent images were quantified using custom Matlab (Mathworks) software. Intensity was measured with 6 replicates per condition and fitted to an ANOVA model with terms for 9 means to log-transformed data.
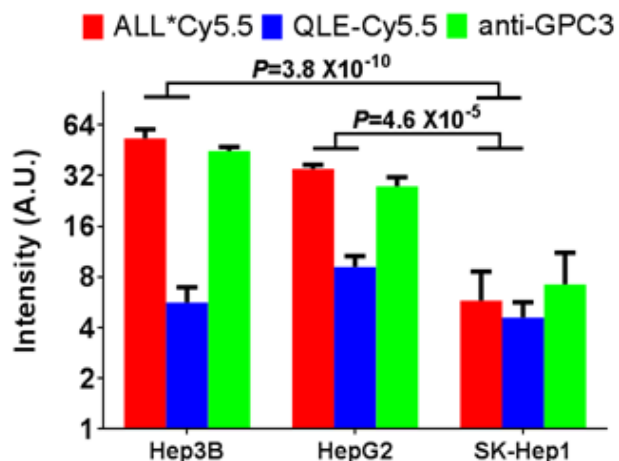
Figure 3.17 Quantification of immunofluorescent staining on HCC cell lines. The intensity difference for Hep3B vs SK-Hep1 was significantly larger for ALL* than for the same difference for QLE* ($P=3.8\times10^{-10}$, 8.2-fold larger), and the HepG2 vs SK-Hep1 difference was also significantly larger ($P=4.6\times10^{-5}$, 3.3-fold larger). The Hep3B vs SK-Hep1 difference was also larger for antibody than QLE ($P=2.3\times10^{-8}$, 6.0-fold larger). Intensity was measured with 6 replicates per condition and fitted to an ANOVA model with terms for 9 means to log-transformed data.

3.4.3 siRNA knockdown of GPC3 and co-localization

Short interfering RNA (siRNA) knockdown is a technology that degrades target messenger RNA to 'knock down' the production of a protein in the cell. The combination of siRNA-treated cells and a specific antibody will result in a significant drop in signal compared to an untreated sample by Western blot. This rigorous validation strategy for peptide target specificity by incorporating negative control is an essential part of experimental design described below.

We examined GPC3 knockdown in Hep3B cells using ON-TARGETplus human GPC3 siRNA (#L-011868-00-0005), ON-TARGETplus Non-targeting pool (#D-001810-10-05), and DharmaFECT transfection reagents (Thermo Scientific). Briefly, cells were seeded in 6-well culture plates at 30% confluence EMEM medium supplemented with 10% fetal bovine serum without antibiotics. The next day, cells were transfected with siRNA at a final concentration of 5 µM/L using oligofectamine (Thermo Scientific). Knockdown of GPC3 was confirmed by western blot. Cells were first washed in PBS and then lysed in RIPA buffer containing 1% Nonidet P40, 0.5% sodium deoxycholate, 0.1% SDS, 10 mg/ml phenylmethylsulfonylfluoride,

78

and 1 mM sodium orthovanadate. Aliquots were placed on ice for 30 min and centrifuged at 14,000 RPM for 10 min. Protein aliquots were denatured in loading buffer at 95ºC for 5 min, separated on SDS-polyacrylamide gels (SDS-PAGE), and transferred onto PVDF membranes. The membrane was blocked with blocking buffer (5% skim milk in 0.1% PBST) for 30 min. The membranes were incubated with anti-GPC3 primary antibody (1:10000 dilution, rabbit monoclonal, Abcam Inc., EPR5547) at 4ºC overnight. After washing 5X with PBST and 5X with PBS, the membrane was incubated for 1 hour in peroxidase-conjugated secondary antibody (1:5000 dilution; GE Healthcare), and were developed using the western blot chemiluminescent substrate (GE Healthcare). The luminescent signal was detected by exposure to X-ray film (Denville Scientific). Western blot shows effective GPC3 knockdown, Figure 3.18.
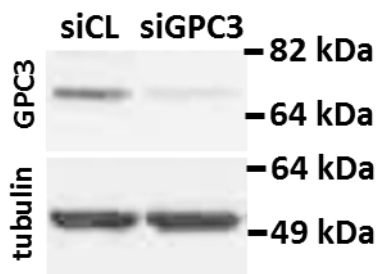
Figure 3.18 Western Blot of GPC3 knockdown in Hep3B cells. Western blot shows GPC3 expression level in Hep3B cells transfected with siGPC3 targeting siRNA and siCL non-targeting siGPC3 (control).

We performed siRNA knockdown experiments with Hep3B cells to validate specific binding of ALL*-Cy5.5 to GPC3. On confocal microscopy, ALL*-Cy5.5 (red) and AF488-labeled anti-GPC3 antibody (green) bound strongly to the surface (arrows) of control Hep3B cells (transfected with siCL, non-targeting siRNA), Figure 3.19(A-B). Minimal binding was observed when staining with scrambled control peptide QLE*-Cy5.5, Figure 3.19(C). Significantly reduced fluorescence intensities were observed for Hep3B knockdown cells (transfected with siGPC3, targeting siRNA), Figure 3.19(D-E). QLE*-Cy5.5 scrambled peptide stains negative on knocked down cells, Figure 3.19(F).
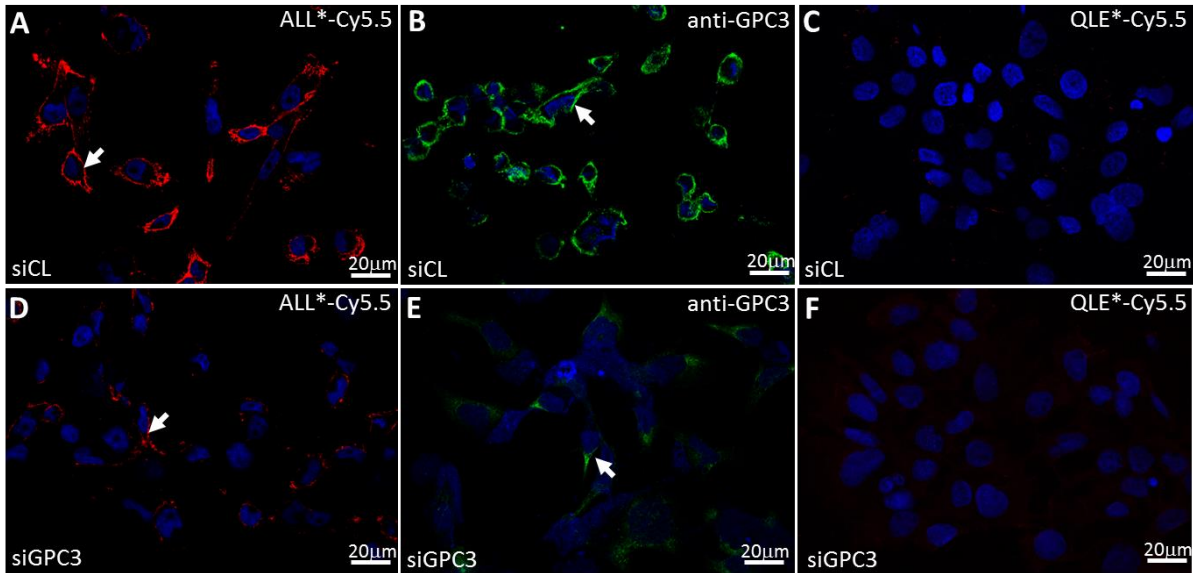
Figure 3.19 IF of GPC3 knockdown. (A) ALL*-Cy5.5 (54.3±6.0) and B) AF488-labeled anti-GPC3 (37.7±7.5) binds significantly greater to the surface (arrows) of siCL treated Hep3B control cells compared to D,E) siGPC3 knockdown cells (14.7±1.5 and 8.8±2.7 respectively). (C, F) scrambled control peptide QLe*-Cy5.5 doesn't bind to either siCL or siGPC3 treated Hep3B cells.

Fluorescence intensity was reduced to 27% in cells knocked down in GPC3 expression with peptide and 23% with antibody, as quantified in Figure 3.20. The siCL vs siGPC3 difference was 7.4 times bigger for ALL than the same difference for QLE (P=7.8×10^{-5}), and the difference for antibody was 8.9 times bigger than for QLE (P=2.5×10^{-5}), by ANOVA on log-transformed data. Results were an average of 6 images collected independently.
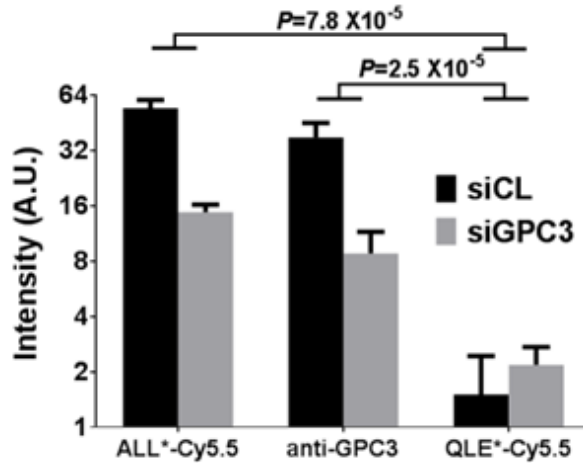
Figure 3.20 Quantification of GPC3 knockdown. Quantified fluorescence intensities. The siCL vs siGPC3 difference was 7.4 times bigger for ALL than the same difference for QLE ($P=7.8\times10^{-5}$), and the difference for antibody was 8.9 times bigger than for QLE ($P=2.5\times10^{-5}$), by ANOVA on log-transformed data. Results were an average of 6 images collected independently.

3.4.4 Competition for peptide binding

To prove the receptor specificity of targeting peptide, competition assay between fluorochrome labeled and unlabeled peptide are generally performed. Particularly for this study, specific binding of ALL*-Cy5.5 to HT29 cells was validated on competitive inhibition with unlabeled ALL* peptide. ~7500 Hep3B cells were grown to ~70% confluence on cover slips in triplicate. Unlabeled ALL* peptide at 0, 50, 100, 150, 250 and 500 µM were added and incubated with the cells for 30 min at 4ºC. The cells were washed 3X with PBS, and further incubated with 2 µM of ALL*-Cy5.5 for another 30 min at 4ºC. The cells were washed 3X with PBS and fixed with 4% PFA for 10 min. The cells were washed with PBS and mounted with ProLong Gold reagent containing DAPI (Invitrogen). Confocal fluorescence images were collected at each concentration, and intensities from 3 independent images were quantified using custom Matlab (Mathworks) software.
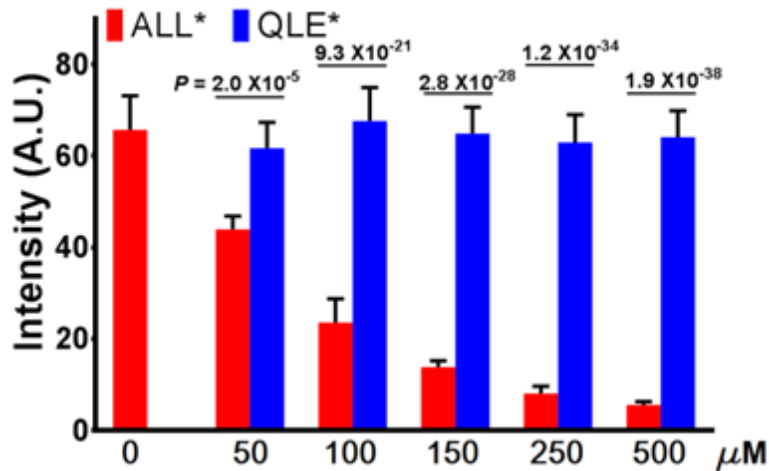
Figure 3.21 *In vitro* competition confirms specificity of targeting peptide. Fluorescence intensities (mean ± SD) showed a significant decrease in ALL*-Cy5.5 binding to Hep3B cells with addition of unlabeled ALL* at concentrations of 50 μM and higher. P values by ANOVA model with terms for 11 means were shown above each result. Addition of unlabeled QLE* (scrambled control) peptide showed no change. Each result was an average of 6 independent measurements.

Binding occurred with the peptide rather than the fluorophore was confirmed by adding unlabeled ALL* to compete with ALL*-Cy5.5 to Hep3B cells. We found the fluorescence intensities decreased significantly in a concentration dependent manner, Figure 3.21. Fluorescence intensities (mean ± SD) showed a significant decrease in ALL*-Cy5.5 binding to Hep3B cells with addition of unlabeled ALL* at concentrations of 50 μM and higher. P values by ANOVA model with terms for 11 means were shown above each result. Addition of unlabeled QLE* (scrambled control) peptide showed no change. Each result was an average of 6 independent measurements.

3.4.5   Characterization of peptide binding kinetics

We measured the apparent dissociation constant of the GPC3 peptide to Hep3B cells as an assessment of binding affinity. ALL*-Cy5.5 was serially diluted in PBS at concentrations of 0, 5, 10, 25, 50, 75, 100, 125, 150 and 200 nM. Approximately 10^6 Hep3B cells were incubated with ALL*-Cy5.5 at 4 °C for 1 h and washed with cold PBS. The mean fluorescence intensities were measured with flow cytometry (BD LSR Fortessa, BD Biosciences). The equilibrium

dissociation constant $k_d = 1/k_a$ was calculated by performing a least-squares fit of the data to the nonlinear equation $I = (I_0 + I_{max} k_a[X]) / (I_0 + k_a[X])$. I_0 and I_{max} denoted the initial and maximum fluorescence intensities, corresponding to no peptide and at saturation, respectively, and [X] represents the concentration of the bound peptide. Graphpad prism (v. 6.02, Graphpad Software Inc.) analysis software was used to plot data and fit curve to calculate k_d and k_a.

The apparent association time constant of the peptide to Hep3B cells was measured to assess binding kinetics. Hep3B cells were grown to ~80% confluence in 10 cm dishes, and detached with PBS-based cell dissociation buffer (Invitrogen). Approximately 10^6 cells were incubated with 5 μM ALL*-Cy5.5 at 4 °C for various time intervals ranging from 0 to 40 min. The cells were centrifuged, washed with cold PBS, and fixed with 4% PFA. Flow cytometry was performed, and the median fluorescence intensity (y) was ratioed with that of Hep3B cells without addition of peptide at different time points (t) using Flowjo (v. 10.1r5, FlowJo, LLC) software. The rate constant k was calculated by fitting the data to a first-order kinetics model, $y(t) = I_{max}[1 - \exp(-kt)]$, where I_{max} = maximum value, using OriginPro (v. 9.2.214 academic, OriginLab Corp.) and Graphpad Prism 5.0 software.
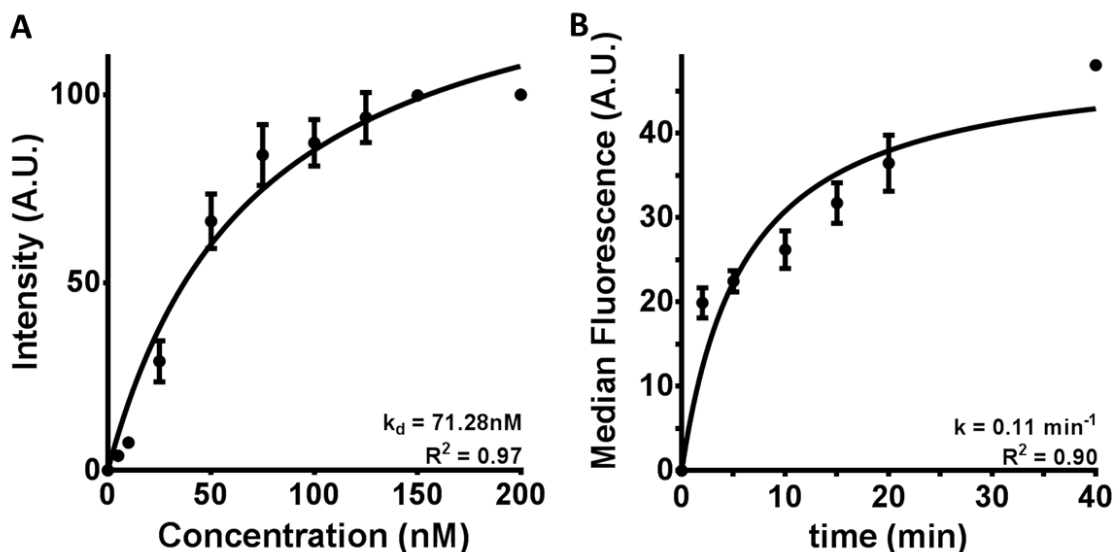
Figure 3.22 Apparent dissociation constant and association time constant. (A) apparent dissociation constant k_d = 71 nM, R^2= 0.97, and (B) apparent association time constant k = 0.11 min^{-1} (i.e. 1/k=9.09 min), R^2= 0.90, for binding of ALL*-Cy5.5 to Hep3B cells using flow cytometry. Results for each measurement were representative of 3 independent experiments.

We measured the binding parameters of ALL*-Cy5.5 to Hep3B cells using flow cytometry, and found an apparent dissociation constant of k_d = 71.28 nM, R^2 = 0.97, Figure 3.22(A), and an apparent association time constant of k = 0.11 min^{-1} (i.e. 1/k=9.09 min), R^2 = 0.90, to support rapid binding with systemic administration, Figure 3.22(B). The first-order kinetics model rather than a linear regression model was adopted for fitting the association kinetics data because of the restraint that the fitted curve must pass data point (0,0) (R^2=0.33 for linear regression fitting).

3.5 *Ex vivo* validation of peptide targetability

After *in vitro* validation and binding kinetics characterization on HCC cells overexpressing GPC3, *ex vivo* binding assays with in an animal HCC model can challenge specificity of peptide probe with non-HCC cells in the harvested xenograft tumor and provide evidence needed to justify *in vivo* imaging applications of peptide probe.

3.5.1 HCC xenograft mouse model

Cells of the human hepatocellular (HCC) cell lines Hep3B and SK-Hep1 (American Type Culture Collection, Manassas, VA) were grown in Eagle's Minimum Essential Medium (EMEM) containing 5% fetal bovine serum and routinely cultured in a humidified incubator with 5% CO_2 at 37ºC. Hep3B cells were diluted in growth factor reduced (GFR) Matrigel Matrix (Corning), and injected into one flank of female (to avoid male dominance within a cage) nude athymic mice (nu/nu, Jackson Laboratory, n=26) at 4 to 6 weeks of age with weight between 20 to 25 grams. Control group mice (n=26) were injected with SK-Hep1 cells instead. 5×10^6 cells were implanted per mouse. Anesthesia was induced and maintained via a nose cone with inhaled isoflurane mixed with oxygen at a concentration of 2 to 4% at a flow rate of 0.5 L/min for all *in vivo* animal experiments, Figure 4.8. Mice were fed alfalfa-free diet (TD.97184, Harlan Teklad, WI) to prevent auto fluorescence from chlorophyll in food.
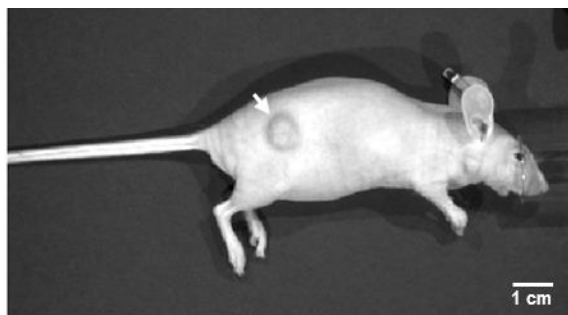
Figure 3.23 Hep3B xenograft mouse model. Subcutanesou xenograft (arrow) was implanted from human HCC cell line, Hep3B, on the flank of nude mouse.

3.5.2 Ultrasound imaging

Tumor size was monitored weekly for 6 weeks with ultrasound imaging as described in Section 2.3.2. Representative images are shown 2 weeks following cancer cell injection with ultrasound (US), Figure 3.24(A), and color Doppler imaging reveals blood vessels around the tumor, Figure 3.24(B).

85
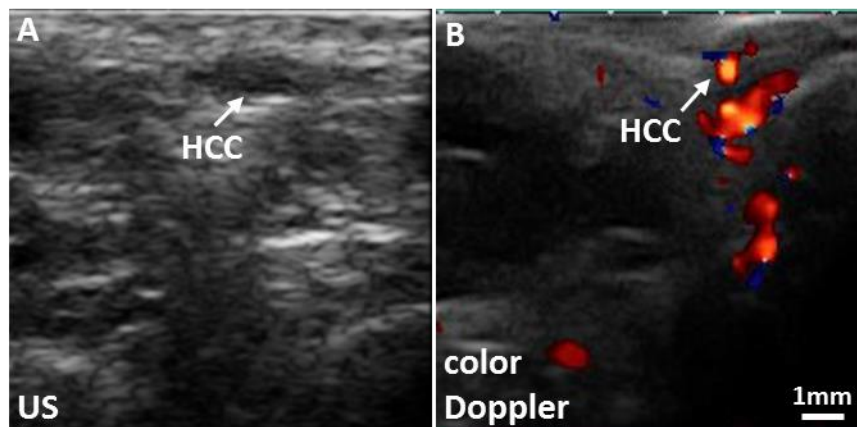
Figure 3.24 Ultrasound imaging of HCC xenograft. Representative images of subcutaneous HCC tumor (arrow) at 2 weeks post-inoculation are shown with A) ultrasound (US) and color Doppler ultrasound showing flow of blood around the tumor (Red: out of the page; Blue: into the page).

3.5.3 MRI imaging

Tumor size was confirmed with Magnetic resonance imaging (MRI) as described in Section 2.3.2. Figure 3.25(A) showed the location and size of xenograft. Segmented MR images were reconstructed into a 3D rendering image in Figure 3.25(B). Tumor growth increased exponentially after 2 weeks of implantation when average diameter of xenograft reached 5mm. A peak tumor volume (±SD) of 3584 ± 869 mm^3 was found at the end point (week 6) of tumor monitoring on US, Figure 3.25(C). A correlation of r = 0.99 was found between tumor size on US and MRI, Figure 3.25(D).
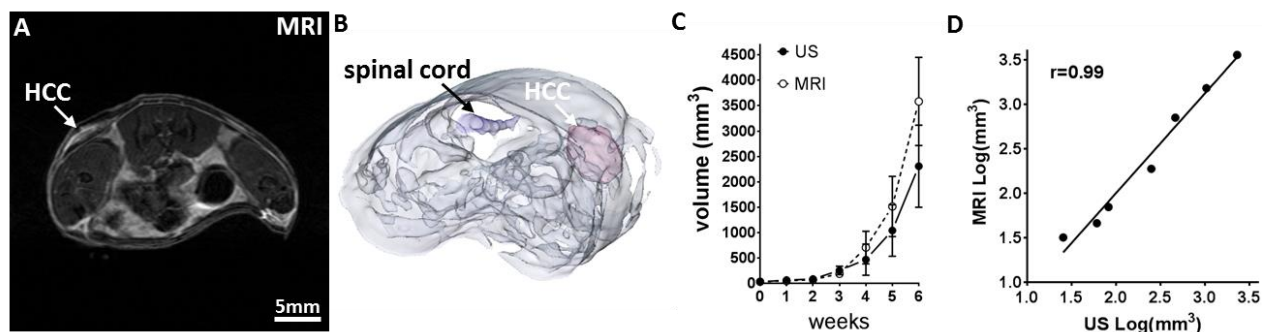
Figure 3.25 MR imaging of HCC xenograft tumor growth monitoring. (A) MRI (T1 weighted contrast-enhanced) image of HCC xenograft tumor (arrow). (B) Segmentation of 3D rendering (reconstructed from a series of 25 MR images) of MR imaging to highlight relative size and position of HCC tumor and spinal cord. (C) Mean (±SD) dimensions for n=10 tumors from US and MRI images from post inoculation weeks 1-6 are shown. (D) Correlation between MRI and ultrasound tumor volume measurements was found to be r=0.99 (linear regression with log log plot).

3.5.4 *Ex vivo* fluorescence imaging of mouse HCC xenograft

We collected confocal images to perform microscopic validation of peptide binding *ex vivo*. Specimens of HCC xenograft in nude mice were resected at 2 week post inoculation, paraffin embedded and cut into 10 μm sections. Sections were processed for immunofluorescent staining as described in Section 2.2.1.3 with either 5 μM of ALL*-Cy5.5 and QLE*-Cy5.5 for 30 min at 4ºC respectively or with 1:200 dilution of primary rabbit anti-human anti-GPC3 antibody (Abcam Inc, SP86) and AF488-labeled secondary antibody. Adjacent sections were processed for histology (H&E). Fluorescence intensities were measured from sets of 3 (dashed white) boxes with dimensions of 20×20 μm^2, Figure 3.26(A), and quantified in Figure 3.27.

We found increased cell surface staining of ALL*-Cy5.5 compared with QLE*-Cy5.5 to Hep3B xenograft (arrows), Figure 3.26(A-B). Overexpression of GPC3 on cell surface of Hep3B xenograft was confirmed with GPC3 antibody, Figure 3.26(C). No staining was observed for either peptide with SK-Hep1 xenograft, Figure 3.26(D-E), which had no GPC3 expression, Figure 3.26(F). Minimal staining was observed with ALL*-Cy5.5 on normal mouse liver tissue, Figure 3.26(G), but no staining was observed with QLE*-Cy5.5, Figure 3.26(H). The same staining level was observed with GPC3 antibody, Figure 3.26(I).
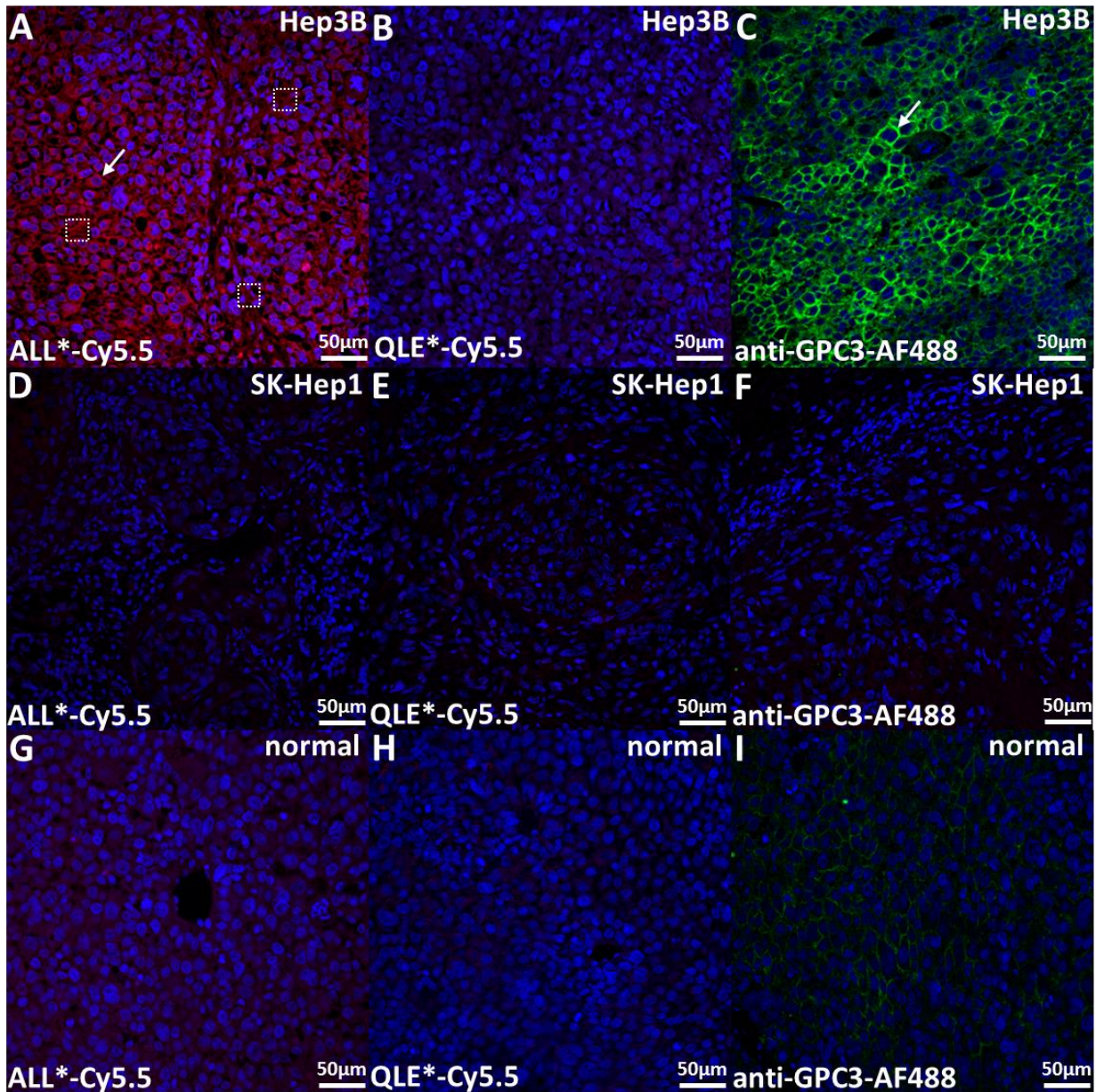
Figure 3.26 Validation of specific peptide binding to GPC3 overexpressed by mouse HCC xenograft tumors. On confocal microscopy, we found intense staining of (A) ALL*-Cy5.5 compared to (B) QLE*-Cy5.5 to sections of Hep3B xenograft tumors. Fluorescence intensities were measured from sets of 3 (dashed white) boxes with dimensions of 20×20 μm^2. (C) With a known GPC3 antibody, we confirmed overexpression of GPC3 on cell surface of Hep3B xenograft (arrows) (D-E) No staining of ALL*-Cy5.5 and QLE*-Cy5.5 was observed to sections of SK-Hep1 xenograft tumors. (F) With a known antibody, we confirmed negative expression of GPC3 in SK-Hep1 xenograft (G-H) Minimal staining was observed with either ALL*-Cy5.5 or QLE*-Cy5.5 to normal liver (I) low GPC3 expression was observed with anti-GPC3 antibody staining.

Greater intensity from peptide binding to HCC than normal was found with 2.22-fold difference,

$P = 8.0 \times 10^{-15}$ by two-sample t-test, n=26, Figure 3.27(A). The corresponding ROC curve showed

96.2% sensitivity and 92.3% specificity for distinguishing HCC from normal liver with an area under curve of AUC = 0.98, Figure 3.27(B).
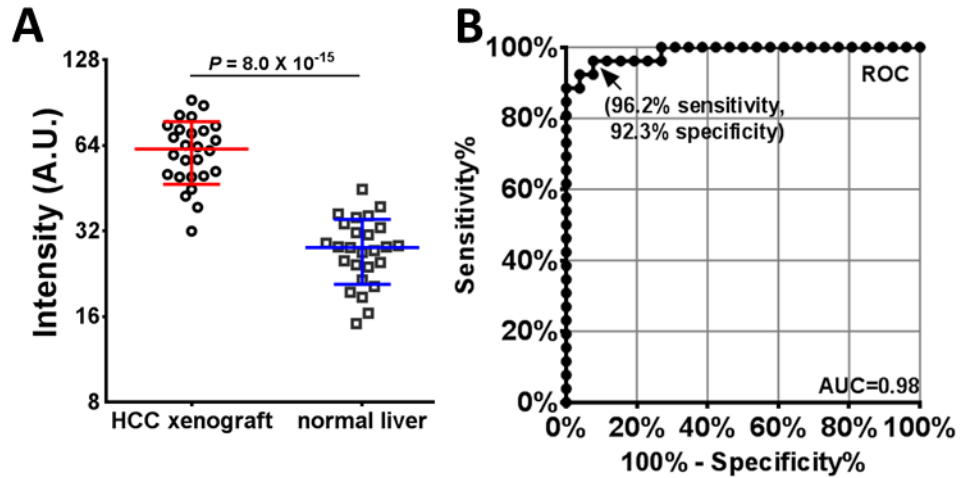
Figure 3.27 Quantification of IF on mouse tissue. (A) Greater intensity from peptide binding to HCC than normal was found with 2.22-fold difference, $P = 8.0\times10^{-15}$ by two-sample t-test, n=26. (B) The corresponding ROC curve showed 96.2% sensitivity and 92.3% specificity for distinguishing HCC from normal liver with an area under curve of AUC = 0.98.

Histology (H&E) showed features of enlarged nuclei (arrow) and highly invasive vasculature (arrowhead) in Hep3B xenograft tumor sections, Figure 3.28(A). A nest of SK-Hep1 tumor cells with large irregular round nuclei (arrow) and infiltrating blood vessels lined with flattened endothelial cells (arrowhead) can be seen, Figure 3.28(B). Corresponding histology (H&E) for normal liver showed lobule with central vein (arrowhead) surrounded by radially aligned plates of hepatocytes, Figure 3.28(C).
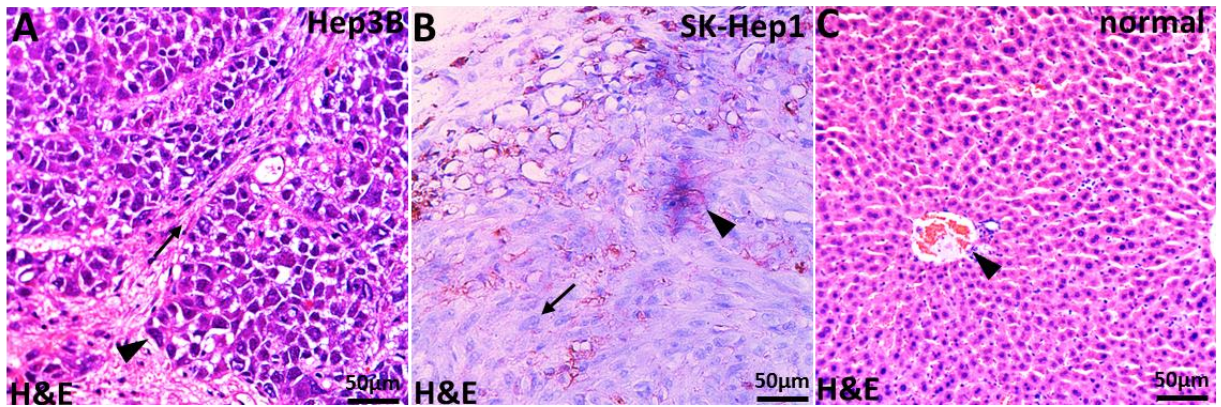
Figure 3.28 H&E histology of HCC xenograft and normal liver. (A) Histology (H&E) of Hep3B xenograft shows features of enlarged nuclei (arrow) and highly invasive vasculature (arrowhead). (B) A nest of SK-Hep1 tumor cells with large irregular round nuclei (arrow) and infiltrating blood vessels lined with flattened endothelial cells (arrowhead) can be seen. (C) Histology of normal mouse liver shows lobule with central vein (arrowhead) surrounded by radially aligned plates of hepatocytes.

Co-localization of binding by peptide (red) and antibody (green) occurred in dysplasia, Pearson's correlation coefficient $\rho = 0.57$, Figure 3.29(A). However, scrambled peptide QLE*-Cy5.5 stained minimally and non-specifically on Hep3B xenograft, which did not co-localize with that of the antibody, Pearson's correlation coefficient $\rho = 0.10$, Figure 3.29(B).
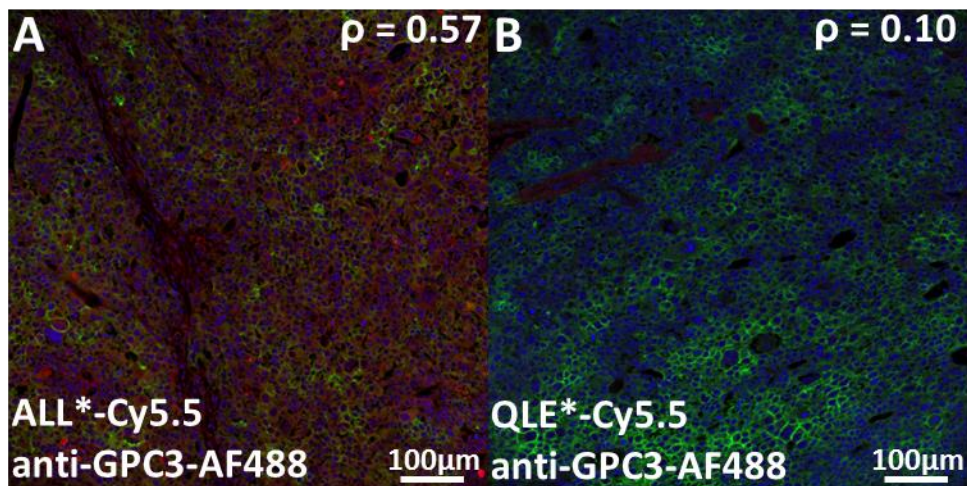
Figure 3.29 Co-localization of targeting and control peptide. (A) Binding of ALL*-Cy5.5 and anti-GPC3-AF488 colocalized to surface of cells in xenograft HCC tissue, Pearson's coefficient $\rho = 0.57 \pm 0.08$. (B) Binding of QLE*-Cy5.5 and anti-GPC3-AF488 did not colocalize to surface of cells in xenograft HCC tissue, Pearson's coefficient $\rho = 0.10 \pm 0.04$.

90

3.6   *In vivo* validation of GPC3 peptide targetability

The *in vitro* and *ex vivo* validations in Section 3.4 and 3.5 of ALL*-Cy5.5 probe binding to GPC3 in both HCC cell lines and resected mouse xenograft respectively have provided valuable evidence of ALL *-Cy5.5 probe's ability to detect cell surface GPC3 overexpression in HCC. Rather than being applied directly onto cultured cells or tumor sections, *in vivo* animal tumor model validation challenges the delivery of peptide to tumor site after injecting the probe into the blood stream of the mouse. Therefore, the probe's performance in *in vivo* imaging of HCC mouse model would inform the potential of clinical translation value of the probe in HCC patients.

3.6.1   *In vivo* whole body fluorescent imaging

Near NIR labeled GPC3-targeting peptide 250μL 300μM ALL*-Cy5.5 were injected via tail vein in mice bearing subcutaneous HCC xenograft tumors and tracked over time before and after injection with the IVIS Spectrum *in vivo* imaging system (PerkinElmer, MA). At 0.5, 1, 2, 4, and 24 hours following tail vein injections, mice were imaged (ventral and dorsal presentations) with a 675nm excitation wavelength, 710nm emission filter and a 0.05 second exposure time. Fluorescence signal was measured as average radiance ($p/sec/cm^2/sr$) in tumor area with Living Image software (v4.5.2, Caliper Life Sciences, MA). Same amount of scrambled control peptide, QLE*-Cy5.5 and free dye Cy5.5 were injected and imaged under the same conditions. Target-to-background ratios were calculated by dividing signal from the tumor with that from non-tumor bearing flank in ROIs of equal area on each mouse. Mice were fed alfalfa-free diet (TD.97184, Harlan Teklad, WI) to prevent auto fluorescence from chlorophyll in food.
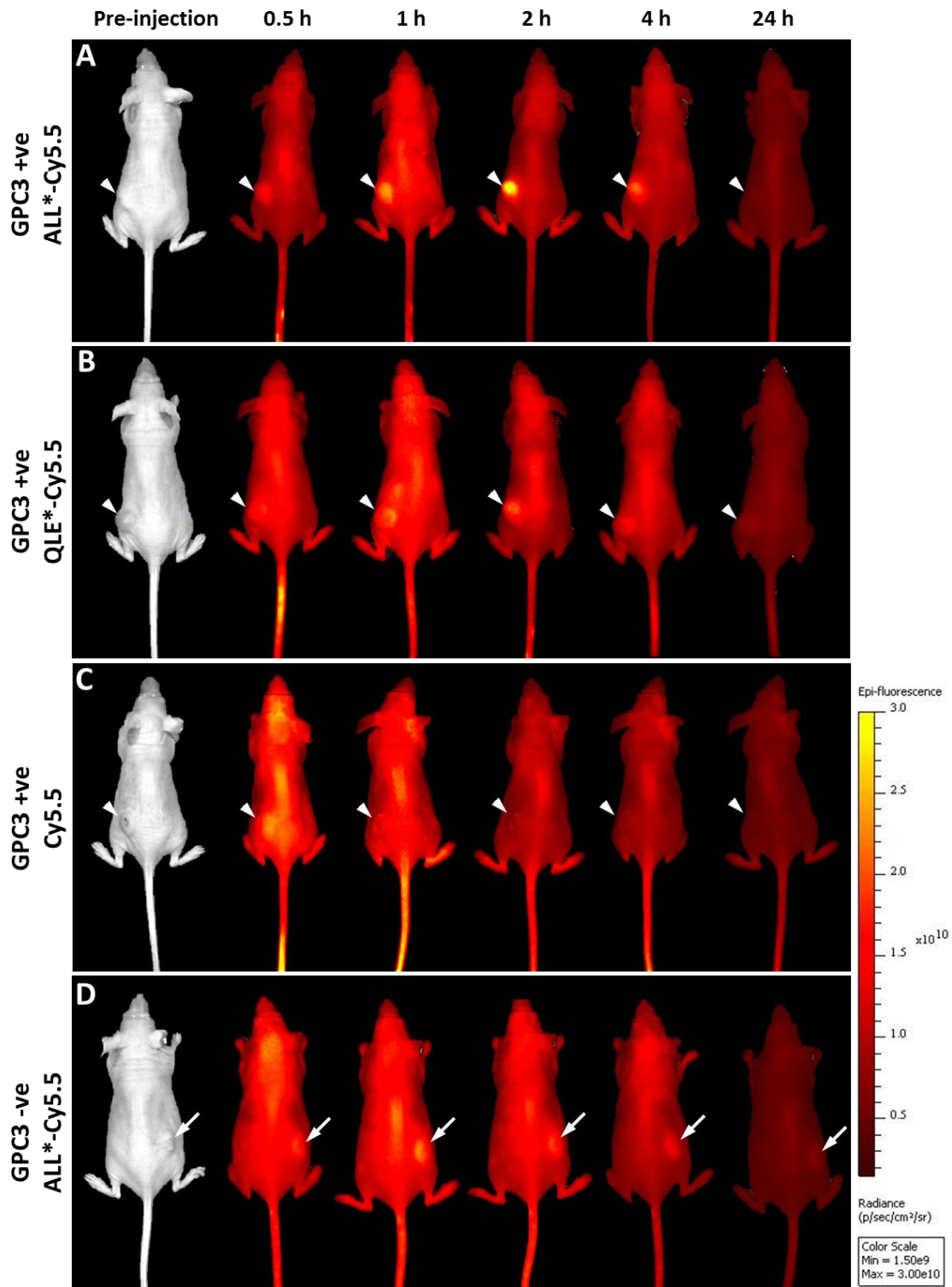
Figure 3.30 Time course of whole body fluorescence imaging in mice injected with peptide. Representative whole-body images show peak uptake in GPC3 positive tumor (from Hep3B cells, arrowheads) at 2 hours after i.v. injection of A) ALL*-Cy5.5. Results are also shown for B) scrambled peptide QLE*-Cy5.5 and C) unlabeled Cy5.5 dye alone over the time course of 0.5 ~ 24 hours. (D) Whole-body time course images was taken 2 hrs after ALL*-Cy5.5 was injected in mice bearing GPC3 negative tumor (from SK Hep-1 cells, arrows).

Mice bearing HCC xenograft tumor (arrowheads) were i.v. injected GPC3 targeting peptide ALL*-Cy5.5, scrambled control peptide QLE*-Cy5.5 and unlabeled Cy5.5 free dye alone. ALL*-Cy5.5 was also injected in mice bearing GPC3 negative tumor (from SK Hep-1 cells, arrows) as control of EPR effect. Pre-injection imaging confirmed no autofluorescence was present. NIR images were taken over the time course of 0.5 ~ 24 hours post injection, Figure 3.30(A-D).
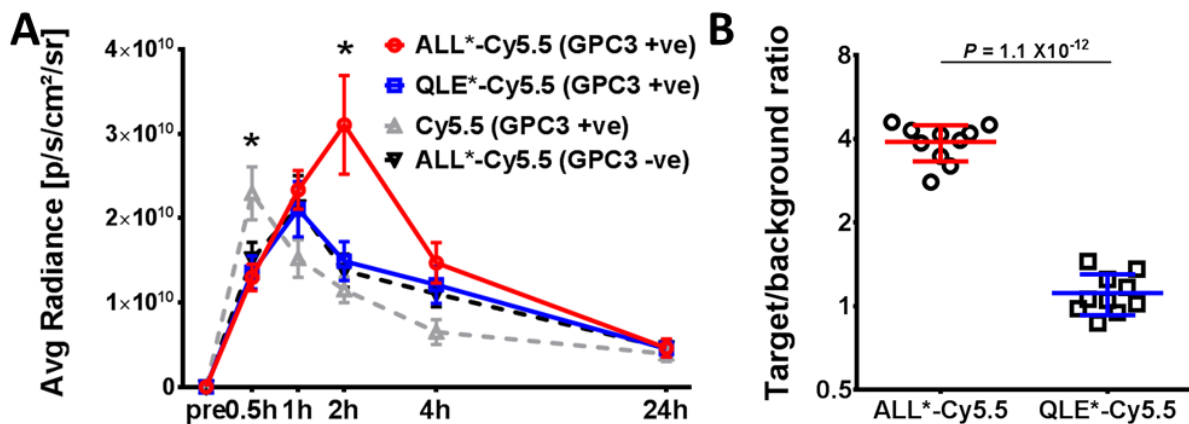
Figure 3.31 Quantification of *in vivo* whole body fluorescence imaging. (A) Quantitative analysis of log-transformed data showed the mean signal from ALL*-Cy5.5 to be significantly higher than that of scrambled control peptide and free dye alone at 2 hours post injection ($P = 1.4 \times 10^{-8}$ and 1.7×10^{-12} respectively). Signal from Cy5.5 dye alone peaked at 0.5 hour post injection and was significantly higher than either peptide ($P = 3.7 \times 10^{-6}$ and 1.5×10^{-5} respectively). Signal from ALL*-Cy5.5 on GPC3 negative tumors served as negative control for EPR effect. (B) Mean±SD target-to-background (T/B) ratio of ALL*-Cy5.5 at 2 hours was 3.91±0.58 versus 1.12±0.19 for QLE*-Cy5.5, $P = 1.1 \times 10^{-12}$.

Quantitative analysis of log-transformed data shows the mean signal from ALL*-Cy5.5 to be significantly higher than that of scrambled control peptide and free dye alone at 2 hours post injection ($P = 1.4 \times 10^{-8}$ and 1.7×10^{-12} respectively). Signal from Cy5.5 dye alone was non-specific to tumor site, which peaked at 0.5 hour post injection and was significantly higher than either peptide ($P = 3.7 \times 10^{-6}$ and 1.5×10^{-5} respectively). Figure 3.31(A). Mean±SD target-to-background (T/B) ratio of ALL*-Cy5.5 at 2 hours was 3.91±0.58 vs 1.12±0.19 for QLE*-Cy5.5, $P = 1.1 \times 10^{-12}$., Figure 3.31(B).

3.6.2   Biodistribution of peptide in organs

To assess the biodistribution of peptide probe, mice (n = 5) were sacrificed 2 hours after injection of 250μL 300μM ALL*-Cy5.5. The organs were harvested and imaged *ex vivo*. Mice injected with scrambled control peptide QLE*-Cy5.5 and free dye Cy5.5 were imaged with the same filters and exposure time as Section 3.6.1. ALL*-Cy5.5 was also injected in GPC3 negative tumor bearing mice as EPR control. Absence of auto fluorescence was confirmed in PBS injected mice. The amount of fluorescent signal in each organ was quantified as a percentage of total fluorescence signal (p/s) in each mouse.
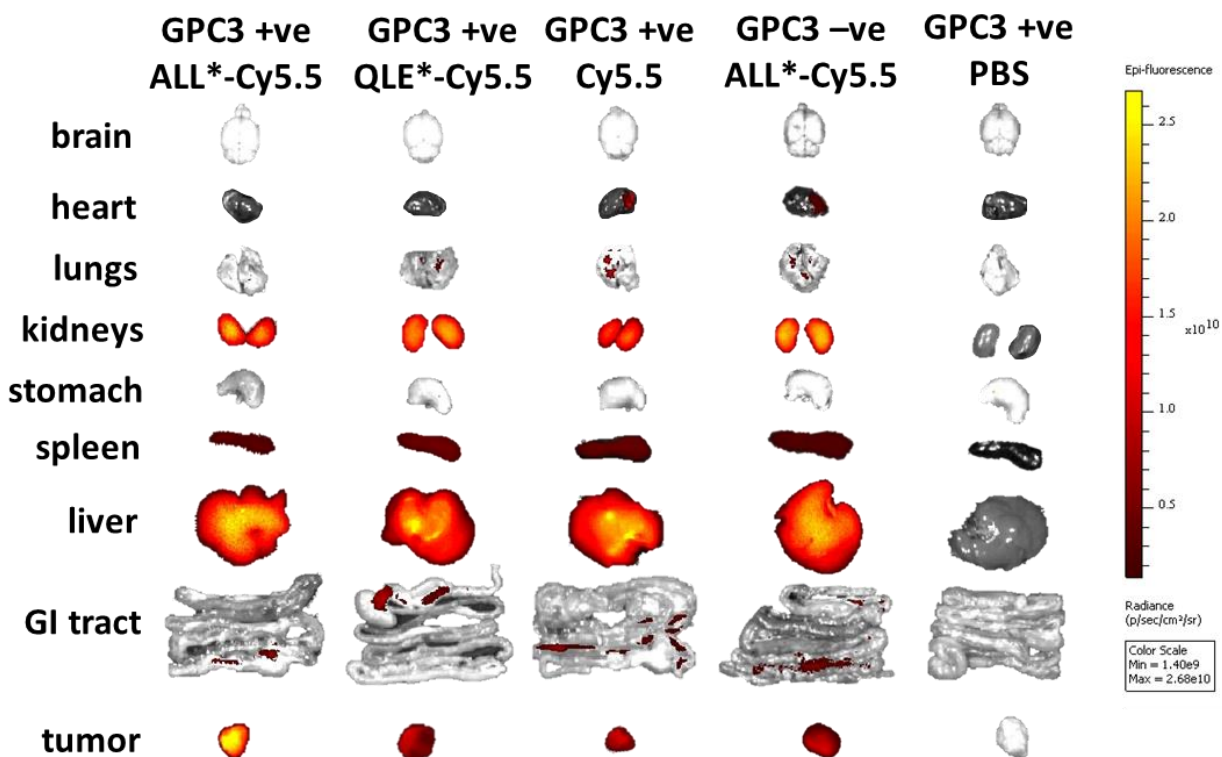
Figure 3.32 Fluorescent imaging of peptide in major organs after systemic injection. Representative fluorescence images of excised organs 2 hours following intravenous injection of ALL*-Cy5.5, scrambled peptide QLE*-Cy5.5, Cy5.5 dye alone, and PBS on GPC3 positive tumor bearing mice. In addition, ALL*-Cy5.5 was also injected in GPC3 negative tumor bearing mice as control.

To investigate tissue uptake of peptide in mice, *ex vivo* fluorescence images were taken of internal organs as well as resected tumor at 2 hours post injection of probes, Figure 3.32. Free

Cy5.5 dye and Cy5.5 labeled targeting and scrambled peptides accumulated most in the liver and kidneys of mice, followed by GI tract and spleen. Much higher targeting peptide accumulation was observed in tumor than all other groups. Probe distribution inside liver could potentially mask signals from tumor in clinical setting of image guided surgery. This concern was best addressed with orthotopic xenograft model described in Section 5.1.3. Minimal accumulation was observed in brain, heart and stomach. No fluorescent signal was observed in negative control group injected with same volume of PBS.
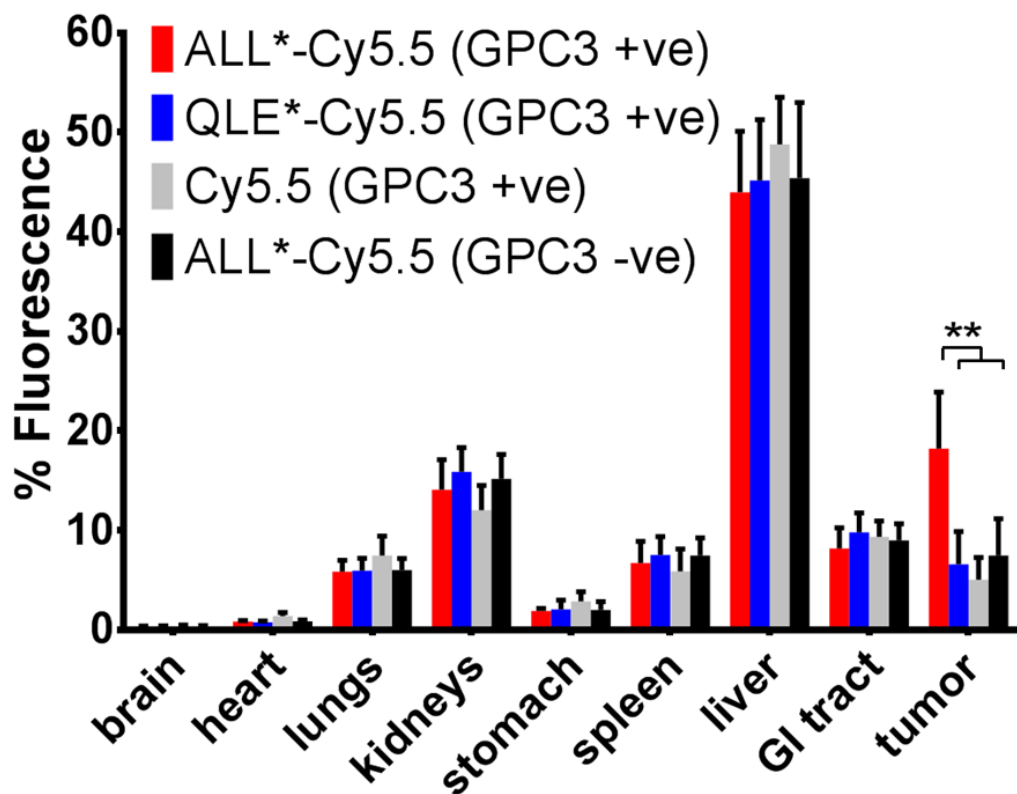
Figure 3.33 Biodistribution of peptide in mouse organs after systemic injection. Quantification of fluorescent signals in each organ. Signal in the tumor was significantly higher in ALL*-Cy5.5 injected mice than the scrambled control probe, Cy5.5 dye alone, or on GPC3 negative tumor (P = 6.5×10^{-4}, 2.3×10^{-4} and 2.2×10^{-3} respectively, n = 5), by ANOVAs for each tissue.

Quantification of fluorescent signals in each organ showed signal in the tumor was significantly higher in ALL*-Cy5.5 injected mice than the scrambled control probe, Cy5.5 dye alone, or on

GPC3 negative tumor (P = 6.5×10^{-4} and 2.3×10^{-4} and 2.2×10^{-3} respectively, n = 5), by ANOVAs for each tissue. Figure 3.33.

3.6.3 *In vivo* laparoscopic fluorescence image

In vivo laparoscopic fluorescence image were collected with the same instrument described in Section 2.3. Nude mice with human HCC xenograft 2 weeks post implantation were tail vein injected with 200μL 300μM GPC3 peptide ALL*-Cy5.5. Laparoscopic images were taken 2 hours post injection in both fluorescence and reflection mode simultaneously. Following imaging, resected xenografts were fixed and formalin embedded for immunohistochemistry and immunofluorescence staining as described previously.
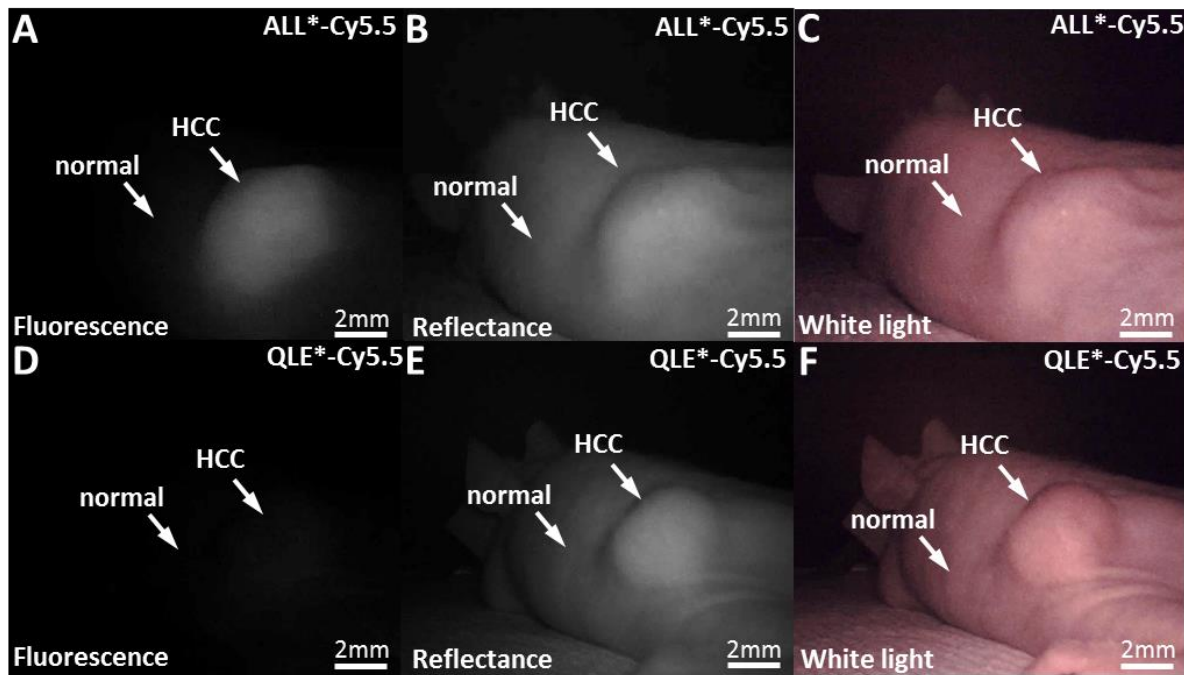
Figure 3.34 *In vivo* fluorescence laparoscopic imaging of HCC xenograft. Representative (A) Fluorescence and (B) reflectance images of mouse injected with ALL*-Cy5.5 were collected with the NIR laparoscope 2 hours after intravenous injection of ALL*-Cy5.5. (C) Representative white light images. Representative (D) Fluorescence, (E) reflectance and (F) white light images of mouse injected with QLE*-Cy5.5 in a different mouse.

Fluorescence and reflectance images, Figure 3.34(A-B), were collected with the NIR laparoscope 2 hours after intravenous injection of the GPC3-targeting peptide, ALL*-Cy5.5, in Hep3B

xenograft bearing mice. The same set of images were collected with scrambled peptide QLE*-Cy5.5 in a different tumor bearing mouse, Figure 3.34(D-E). White light images were collected for mouse injected with targeting peptide ALL*-Cy5.5, Figure 3.34(C), and scrambled peptide QLE*-Cy5.5, Figure 3.34(F).

Automatic ROI identification from heat map digital images was performed as described in Section 2.3.5. Heat map digital image that rectifies imaging distance was generated by taking the ratio between corresponding fluorescence and reflectance images pixel by pixel, Figure 3.35(A). Region of interest (ROI) was segmented by automatic imaging processing from ratio image following Otsu's method, Figure 3.35(B). The same set of images were analyzed for scrambled peptide QLE*-Cy5.5 in a different tumor bearing mouse, Figure 3.35(C-D).
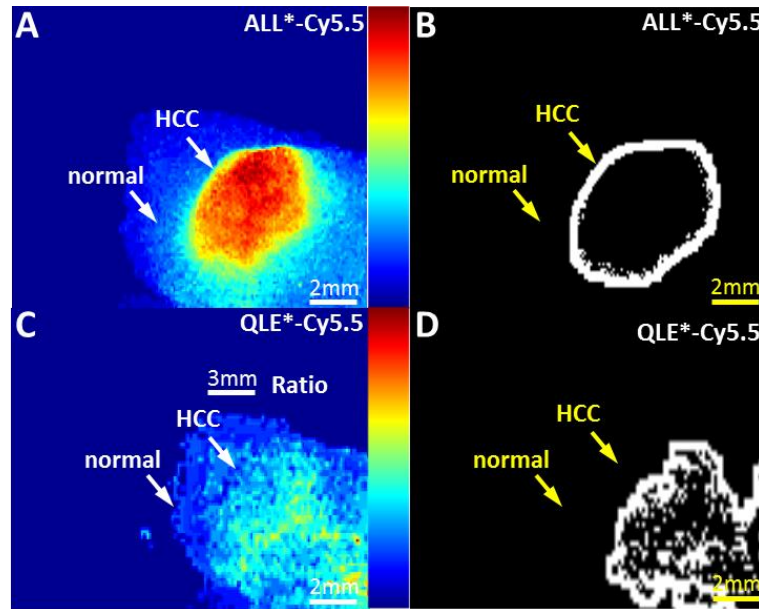
Figure 3.35 Segmentation of ROIs from heat map images. (A) Heat map corrects for imaging distance by taking the ratio between co-registered fluorescence and reflectance images. (B) Region of interest was segmented by imaging processing algorithm using ratio image. (C-D) The same set of images were generated with scrambled peptide QLE*-Cy5.5 in a different tumor.

ROI in images of targeted peptide resulted in an average target-to-background ratio of ALL*-Cy5.5 (6.2±0.9) significantly higher (P=3.5×10^{-7} on log-transformed data, 2.9-fold larger) than that of QLE*-Cy5.5 (2.1±0.5), by two-sample t-test with n = 8 mice in each group, Figure 3.36.
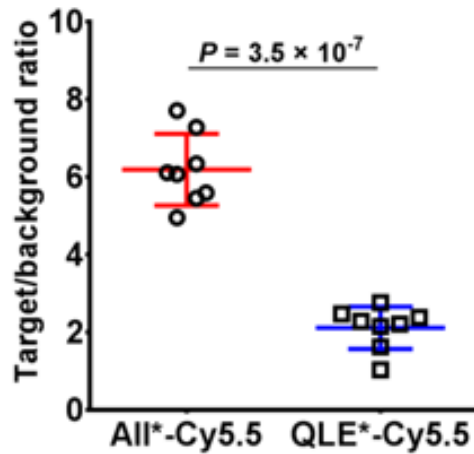
Figure 3.36 Target-to-background ratios of segmented laparoscopic images. Target-to-background ratio of ALL*-Cy5.5 (6.2±0.9) is significantly higher (P=3.5×10^{-7} on log-transformed data, 2.9-fold larger) than that of QLE*-Cy5.5 (2.1±0.5), by two-sample t-test with n = 8 mice in each group.

On immunohistochemistry, anti-GPC3 antibody stained strongly on cellular membrane (arrow) of tumor cells surrounding infiltrating blood vessel (arrow head) in resected HCC tumor xenograft, Figure 3.37(A). On confocal fluorescence microscopy, intense staining of ALL*-Cy5.5 to surface of Hep3B human HCC cells (arrowheads) on excised tumor xenograft were shown at 40X magnification, Figure 3.37(B).
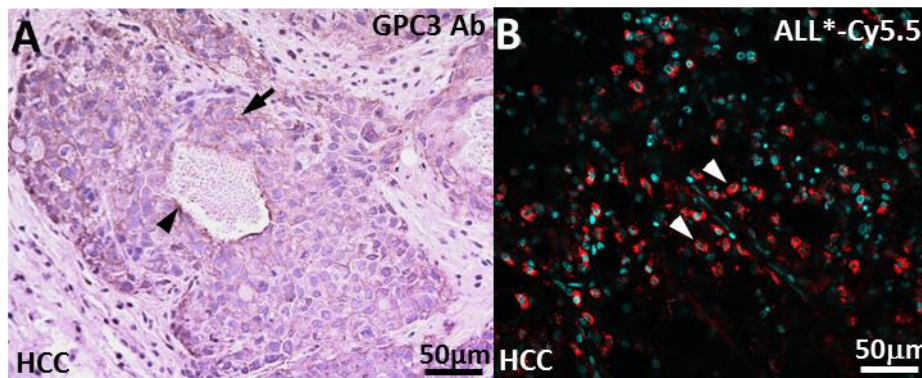
Figure 3.37 IHC and IF for GPC3 expression in HCC xenograft. (A) Immunohistochemistry (IHC) with anti-GPC3 antibody showed increased reactivity to HCC. A nest of tumor cells with large irregular round nuclei (arrows) and infiltrating blood vessels lined with flattened endothelial cells (arrowhead) can be seen. (B) Immunofluorescence image of fresh resected HCC tumor xenograft 2 hours after ALL*-Cy5.5 injection.

3.6.4 *In vivo* hand held dual-axis confocal microscopic imaging

A custom made hand held dual-axis confocal microscopic system was used to visualize peptide binding to HCC xenograft tumor with cellular resolution *in vivo*. Meanwhile, this instrument is capable of collecting both horizontal and vertical cross section of tissue image *in vivo*, and thus can validate the probe penetration into tumor with systemic delivery [138].
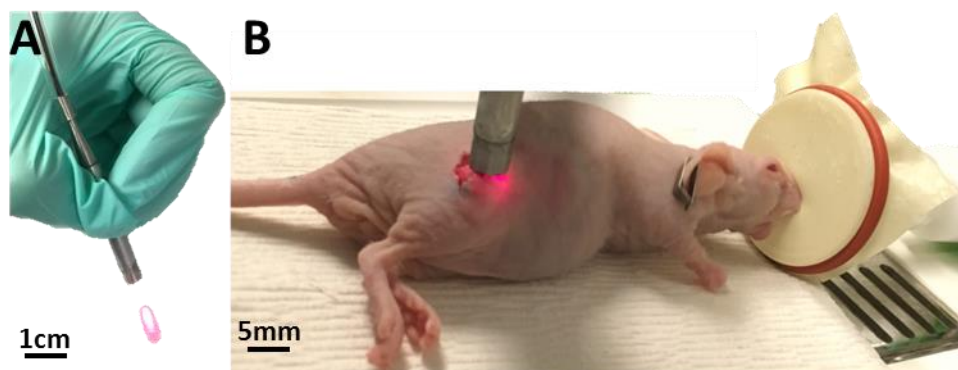
Figure 3.38 Hand-held dual-axis confocal microscope for *in vivo* imaging. (A) Handheld dual axes confocal endomicroscope was used to collect real-time *in vivo* images with sub-cellular resolution. (B) The distal tip of instrument was placed in contact (inset) with the lesion in live tumor-bearing mouse. Strong uptake (arrow) of ALL*-Cy5.5 is seen in tumor on optical sections collected in the

The probe was small enough to be comfortably held in the surgeon's hand during surgery, Figure 3.38(A), for *in vivo* imaging of biomarker expression. Its diameter was 5.5 mm and delivered 671nm near-infrared laser at 2 mW. Mouse carrying HCC xenograft tumor overexpressing GPC3 was first injected with 250μL 300μM ALL*-Cy5.5 peptide intravenously and after 2 hours the probe was held in contact with exposed subcutaneous tumor to acquire *in vivo* peptide binding images, Figure 3.38 (B). Images were collected in either the vertical or horizontal plane with 430 μm depth or 1000×1000 μm^2 area, respectively, at 5 frames per second. With measured lateral resolution of 2.49 μm and axial resolution of 4.98 μm, each peptide stained cell can be clearly

seen (arrows). A reconstructed 3D MIP image reveals all the stained cells in the tumor.
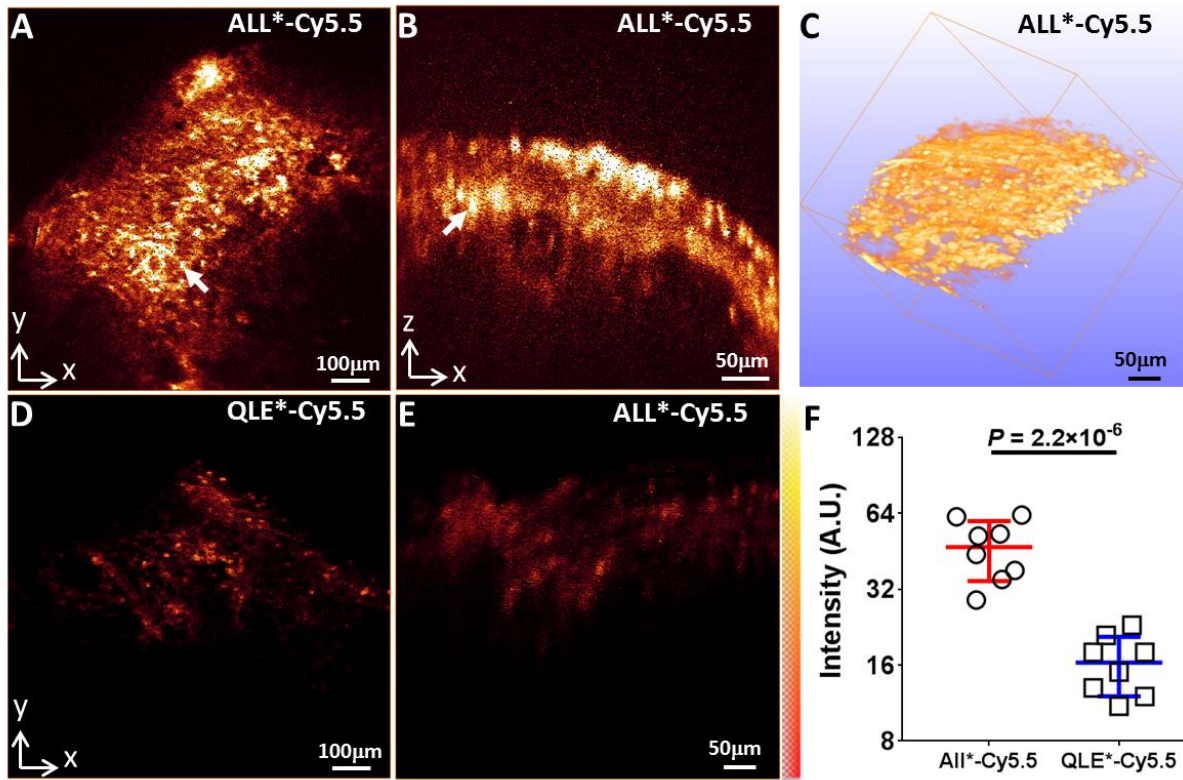
Figure 3.39 *In vivo* dual-axis confocal imaging of HCC xenograft. Strong uptake (arrow) of ALL*-Cy5.5 is seen in tumor on optical sections collected in the (A) horizontal (1000×1000 μm^2) and (B) vertical (1000×430 μm^2) planes, respectively. (C) A series of vertical cross-section images were reconstructed into 3D MIP volume. (D) Minimal staining was observed in xenograft tumor from control peptide QLE*-Cy5.5. (F) 2.9-fold increase (47 ± 13 vs 16 ± 4, P = 2.2×10^{-6}) in fluorescent intensity was observed in ALL*-Cy5.5 injected mice at tumor compared to control peptide QLE*-Cy5.5.

Figure 3.39 captured strong uptake (arrows) of ALL*-Cy5.5 in tumor on optical sections collected in the horizontal (1000×1000 μm^2, Video 3.1) Figure 3.39(A) and vertical (1000×430 μm^2, Video 3.2) Figure 3.39(B) planes, respectively. A series of vertical cross-section images were reconstructed into 3D MIP volume (Video 3.3), Figure 3.39(C). Minimal staining was observed in xenograft tumor from control peptide QLE*-Cy5.5 in the horizontal and vertical planes, Figure 3.39(D-E). Fluorescent signal of ALL*-Cy5.5 is significantly higher (P=2.2×10^{-6} on log-transformed data, 2.9-fold larger) than that of QLE*-Cy5.5, by two-sample t-test with n = 8 mice in each group, Figure 3.39(F).
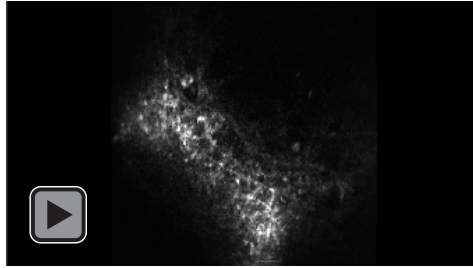
Video 3.1 Horizontal plane *in vivo* confocal recording
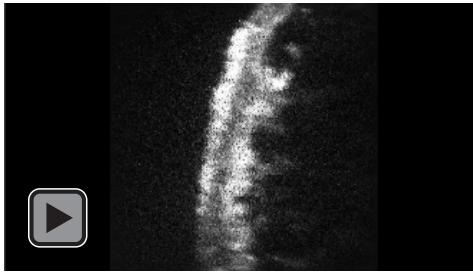
Video 3.2 Vertical plane *in vivo* confocal recording
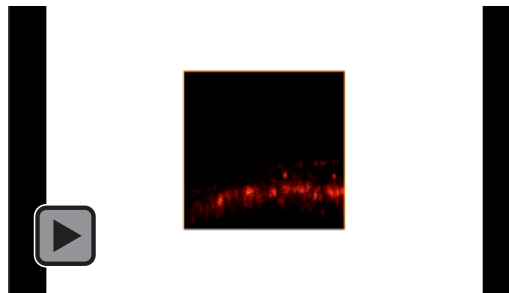
Video 3.3 3D *in vivo* image of ALL*-Cy5.5 in HCC

3.6.5 Toxicity
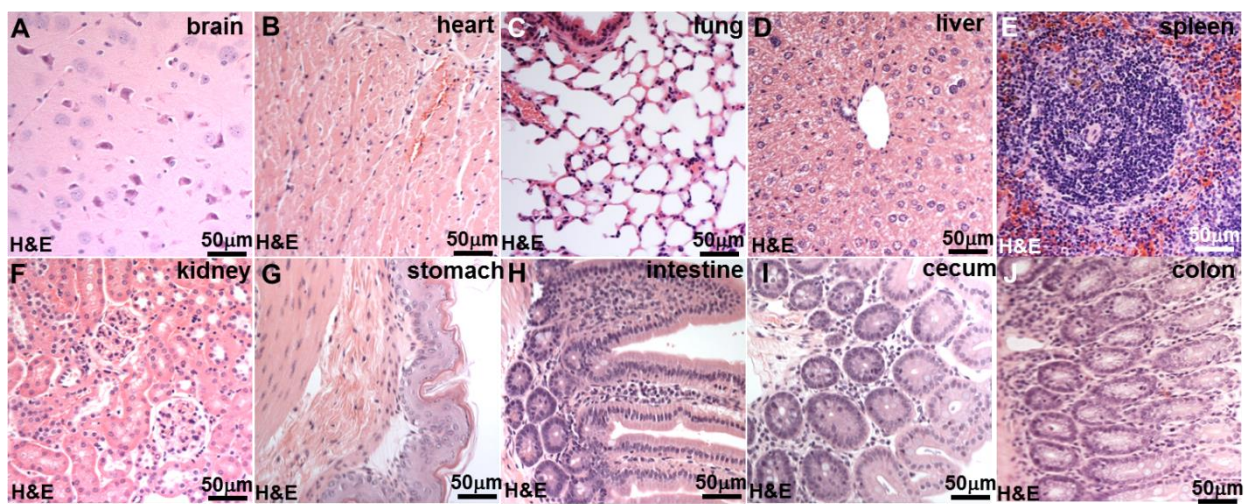
Figure 3.40 Histology of vital organs post peptide administration. Mice bearing human HCC xenograft tumors were sacrificed 2 hours post-injection of ALL*-Cy5.5. No signs of acute peptide toxicity were seen in A) brain, B) heart, C) lung, D) liver, E) spleen, F) kidney, G) stomach, H) intestine, I) cecum, J) colon.

Vital organs were harvested post peptide administration in mice to evaluate acute toxicity of peptide probe with histology observation. Mice bearing human HCC xenograft tumors were sacrificed 2 hours post-injection of ALL*-Cy5.5. No signs of acute peptide toxicity were seen in brain, heart, lung, liver, spleen, kidney, stomach, intestine, cecum, colon, Figure 3.40(A-J).

3.7 Human tissue validation

Up till now, all the experiments were conducted with human cell lines with known GPC3 expression levels. How well GPC3 targeting peptide perform on diverse human tissues with unknown GPC3 expression levels would shed light on the clinical translation potential of this probe. To this end, patient biopsy samples were collected from U.S. and China respectively, and immunofluorescent staining was performed on different tissue types.

3.7.1 Microscopic validation on U.S. patent liver biopsies

Specific peptide binding to human HCC was confirmed on patient biopsies (n=41) *ex vivo* from University of Michigan Hospital. On immunofluorescence, ALL*-Cy5.5 showed negative staining (red) to human normal liver tissue from specimens, Figure 3.41(A). Antibody staining (green) of the same tissue confirmed minimal GPC3 expression, Figure 3.41(B). Binding by ALL*-Cy5.5 peptide (red) and AF488-labeled anti-GPC3 antibody (green) co-localizes on normal liver specimen with Pearson's correlation coefficient of $\rho = 0.62$, Figure 3.41(C). Co-stained regions were also imaged at 40X, Figure 3.41(D) and 100X (red dashed box in Panel D), Figure 3.41(E) magnifications. Minimal staining was observed in adenoma tissue with Pearson's correlation coefficient of $\rho = 0.63$, Figure 3.41(F-J), and moderate diffuse staining was observed in cirrhotic liver tissue with Pearson's correlation coefficient of $\rho = 0.57$, Figure 3.41(K-O). Strong intense staining with Pearson's correlation coefficient of $\rho = 0.66$ was observed in HCC tissue, Figure 3.41(P-S). Cell surface staining (arrow) is shown in Figure 3.41(T).
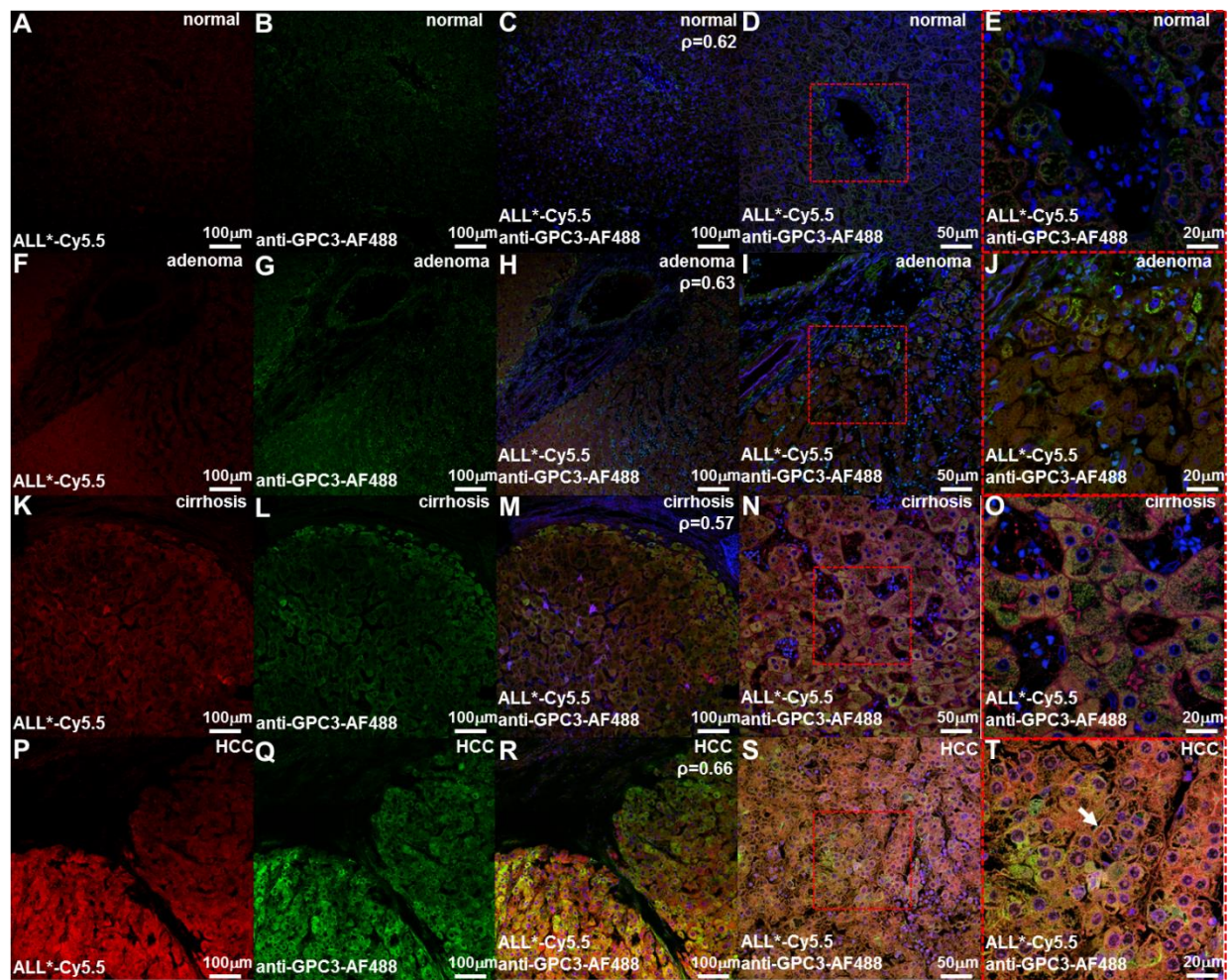
Figure 3.41 Specific peptide binding to human HCC *ex vivo*. (A) On immunofluorescence (IF), ALL*-Cy5.5 showed negative staining (red) to human normal liver tissue from specimens. (B) Antibody staining (green) of the same tissue confirmed minimal GPC3 expression. (C) Binding by ALL*-Cy5.5 peptide (red) and AF488-labeled anti-GPC3 antibody (green) co-localizes on normal liver specimen with Pearson's correlation coefficient of $\rho = 0.62$. Co-stained regions were also imaged at (D) 40X and (E) 100X (red dashed box in Panel D) magnifications. (F-J) Minimal staining was observed in adenoma tissue with Pearson's correlation coefficient of $\rho = 0.63$ and (K-O) moderate diffuse staining was observed in cirrhotic liver tissue with Pearson's correlation coefficient of $\rho = 0.57$. (P-S) Strong intense staining with Pearson's correlation coefficient of $\rho = 0.66$ was observed in HCC tissue (T) showing cell surface staining (arrow).

Figure 3.42(A) summarized quantitative comparison of ALL*-Cy5.5 binding to human HCC with normal liver, adenoma and cirrhosis tissue. We fit an ANOVA model with terms for 4 conditions and 41 patients (n=7 for normal and adenoma, n= 12 for cirrhosis and n=15 for HCC) to log-transformed data and found a 3.43-fold greater (P=8.6×10^{-10}) signal for ALL*-Cy5.5 in HCC than normal, and 2.48-fold increase (P=2.7×10^{-6}) from adenoma and 2.05-fold increase (P=2.7×10^{-6}) from cirrhosis. The corresponding ROC curve showed 93% sensitivity at 88%

103

specificity for distinguishing HCC from all non-HCC tissue with an area under curve of AUC = 0.98, Figure 3.42(B). ROC curve shows 87% sensitivity at 100% specificity for distinguishing HCC from cirrhosis with an area under curve of AUC = 0.97, Figure 3.42(C).
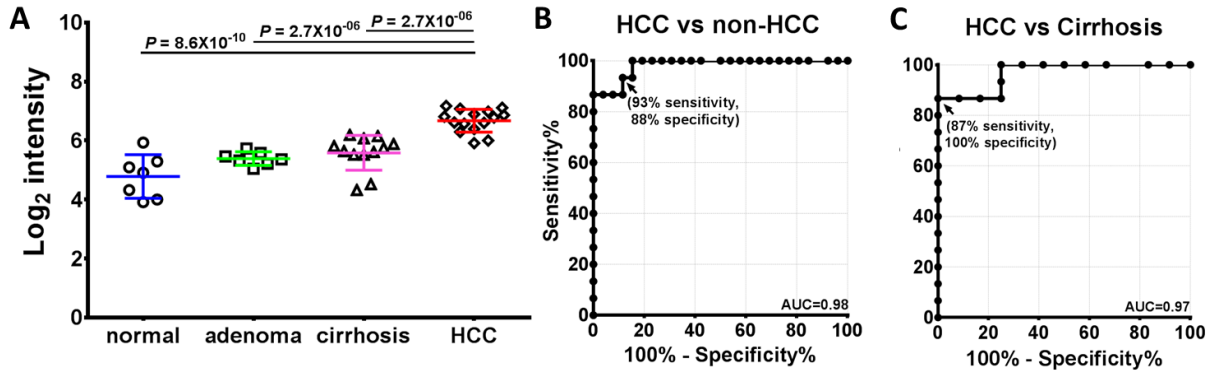
Figure 3.42 Quantification of peptide staining on human biopsies. (A) Quantitative comparison of ALL*-Cy5.5 binding to human HCC with normal liver, adenoma and cirrhosis tissue. We fit an ANOVA model with terms for 4 conditions and 41 patients (n=7 for normal and adenoma, n= 12 for cirrhosis and n=15 for HCC) to log-transformed data and found a 3.43-fold greater (P=8.6×10^{-10}) signal for ALL*-Cy5.5 in HCC than normal, and 2.48-fold increase (P=2.7×10^{-6}) from adenoma and 2.05-fold increase (P=2.7×10^{-6}) from cirrhosis. (B) The corresponding ROC curve showed 93% sensitivity at 88% specificity for distinguishing HCC from all non-HCC tissue with an area under curve of AUC = 0.98. (C) ROC curve shows 87% sensitivity at 100% specificity for distinguishing HCC from cirrhosis with an area under curve of AUC = 0.97.

Immunohistochemistry (IHC) with anti-GPC3 antibody stained negative on normal liver, moderately on adenoma and cirrhosis human tissue, Figure 3.43(A-C). Intense staining was observed in HCC human tissue, Figure 3.43(D). Figure 3.43(E-H) show corresponding representative histology (H&E) for normal, adenoma, cirrhosis and HCC. All 41 biopsies were diagnosed by pathologist and the patients' medical history and histology notes were recorded in Table 3.4.
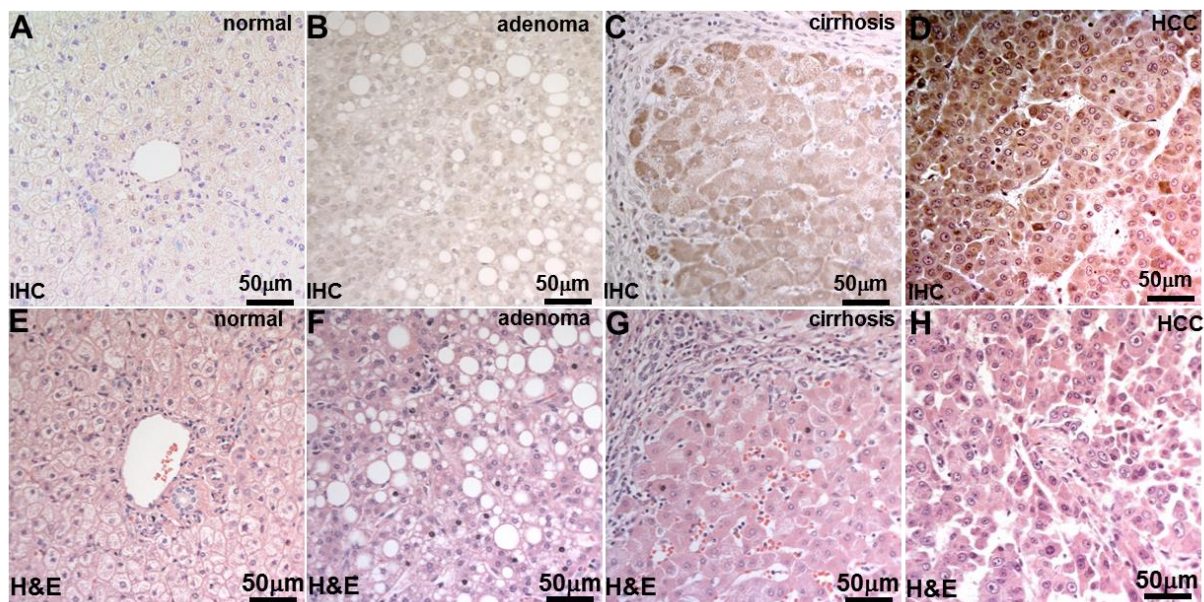
Figure 3.43 IHC and histology of patient biopsies. Immunohistochemistry (IHC) with anti-GPC3 antibody stains negative on (A) normal liver, (B) moderately on adenoma and (C) cirrhosis human tissue. (D) Intense staining was observed in HCC human tissue. Corresponding representative histology (H&E) for (E) normal, (F) adenoma, (G) cirrhosis and (H) HCC.

ID	Diagnosis	Patient history and histology notes
1	HCC	Hep C. Background not cirrhotic.
2	HCC	NASH cirrhosis.
3	HCC	Hep C.
4	HCC	Cryptogenic cirrhosis. Includes fibro lamellar pattern.
5	HCC	Hep C. Not cirrhotic but bridging fibrosis.
6	HCC	NASH, bridging. Not cirrhotic.
7	HCC	Hep C cirrhosis.
8	HCC	Background not cirrhotic.
9	HCC	Cryptogenic cirrhosis.
10	HCC	Hep C. Not cirrhotic but bridging fibrosis.
11	HCC	Hep C cirrhosis.
12	HCC	Not cirrhotic.
13	HCC	Hep C cirrhosis.
14	HCC	HCV and HBV.
15	HCC	Alcoholic cirrhosis.
16	Cirrhosis	Alcoholic cirrhosis, no malignancy.
17	Cirrhosis	Hep C cirrhosis, no malignancy.
18	Cirrhosis	Hep C cirrhosis, no malignancy.
19	Cirrhosis	Hep C cirrhosis, no malignancy.
20	Cirrhosis	Biliary cirrhosis, no malignancy.
21	Cirrhosis	Alcoholic cirrhosis, no malignancy.
22	Cirrhosis	Hep C cirrhosis, no malignancy.
23	Cirrhosis	Hep C cirrhosis, no malignancy.
24	Cirrhosis	Hep C cirrhosis, no malignancy.
25	Cirrhosis	Alcoholic cirrhosis, no malignancy.
26	Cirrhosis	NASH cirrhosis / alpha1-Antitripin deficiency carrier.
27	Cirrhosis	Hep C cirrhosis.
28	HCA	Hepatic adenoma (area with fat). Multiple adenomas. No malignancy.
29	HCA	Hepatic adenoma (area with fat). No malignancy.
30	HCA	Hepatic adenoma (area with fat). No malignancy.
31	HCA	Normal appearing background tissue (has multiple hepatic adenomas).
32	HCA	Hepatic adenoma (small area with fat). History of lung adenocarcinoma (not in this resection).
33	HCA	Hepatic adenoma (area with fat). No malignancy.
34	HCA	Metastatic colorectal adenocarcinoma. Small amount of normal.
35	Normal	FNH, no malignancy.
36	Normal	FNH, no malignancy.
37	Normal	Hemangioma, no malignancy.
38	Normal	Hemangioma, no malignancy.
39	Normal	Hemangioma, no malignancy.
40	Normal	Hemangioma, no malignancy.
41	Normal	Hemangioma, no malignancy.

Table 3.4 Diagnosis and patient medical history of human tissue samples

3.7.2 Microscopic validation on Chinese patent liver biopsies

Many HCC cases in Asian countries such as China are HBV related while it's much less common in North America where HCV background is more prevalent. To further validate the targeting of peptide, preliminary experiment was conducted on patient HCC biopsies from

Peking University People's Hospital, Figure 3.44. On confocal microscopy, we found intense staining of ALL*-Cy5.5 (red) to sections of human hepatocellular carcinoma Figure 3.44(A). Increased fluorescence intensity was observed for staining of anti-GPC3-AF488 antibody (green) to human hepatocellular carcinoma, Figure 3.44 (B). On immunohistochemistry with a known GPC3 antibody, we confirmed overexpression of GPC3 in human HCC, Figure 3.44 C).
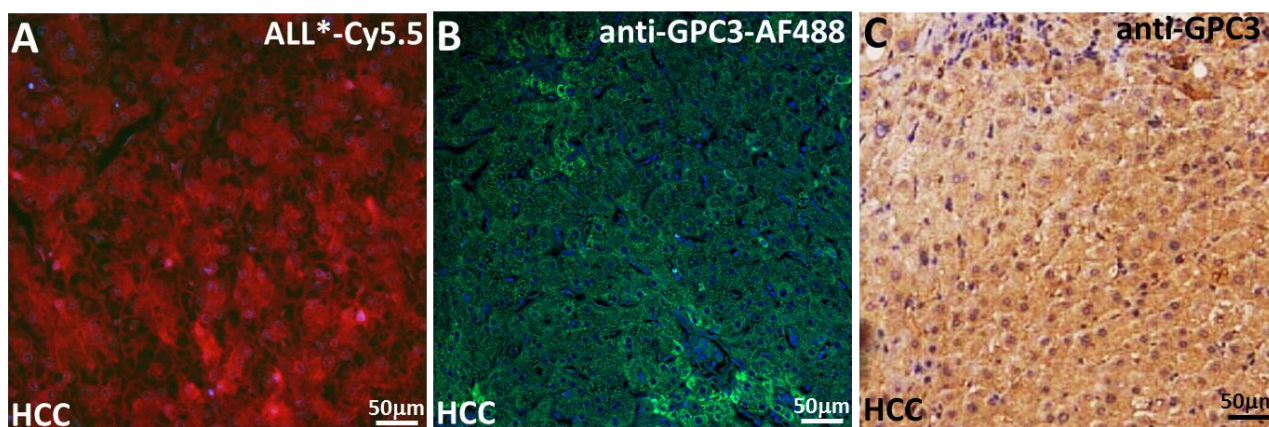
Figure 3.44 ALL* peptide validation on Human HCC. (A) On confocal microscopy, we found Intense staining of ALL*-Cy5.5 (red) to sections of human hepatocellular carcinoma. (B) Increased fluorescence intensity was observed for staining of anti-GPC3-AF488 antibody (green) to human hepatocellular carcinoma. (C) On immunohistochemistry with a known GPC3 antibody, we confirmed overexpression of GPC3 in human HCC.

3.8 Discussions

Compared to previous attempts to identify HCC targeting peptide, ALL*-Cy5.5 probe showed superiority in terms of clear target molecule identity, higher affinity and clinically favorable pharmacokinetic profile. Lo et al have previously identified 12-mer peptide, SP94, that specifically binds to HCC cells such as HepG2 and Huh-7, but not to hepacocytes [182]. Subsequent studies have conjugated the peptide to nanocarriers, bacteriophage MS2 virus-like particles, and radiopharmaceutical labels as cell specific drug delivery and imaging probes [183-186]. However, the bio-panning was performed with human HCC cell line and thus the target was unknown. Recently, one study used human recombinant GPC3 protein in phage display

screening to identify a 12-mer GPC3 targeting peptide sequence, TJ12P1 (sequence: DHLASLWWGTEL), and measured its dissociation constant to be $k_d=280.4 \pm 33.51$ nM [187]. In their *in vivo* study using Cy5.5 labeled peptide, homing of peptide to HepG2 xenograft tumor took 4 hours. In the current study, the dissociation constant of ALL*-Cy5.5 peptide was $k_d=71.28$ nM (inversely correlated to affinity) with shorter *in vivo* imaging peak time of 2 hours post injection. The reduced probe delivery time can be more manageable in clinical translational applications. The nearly four-fold improvement in affinity from the previous work could be attributed to the addition of amino acid linker sequence, GGGSK, between targeting peptide sequence and the near-infrared dye Cy5.5, reducing steric hindrance from the dye moiety upon target binding. As mentioned by the authors of TJ12P1 peptide, liver uptake of the peptide could be caused by the hydrophobicity of the probe, which in turn, could affect its distribution time to the tumor. TJ12P1-Cy5.5 probe has 0 overall charge, 7 (out of 12, 58%) hydrophobic amino acids and 2 polar uncharged amino acids while ALL*-Cy5.5 probe has 1 positive overall charge (including linker sequence), 9 (out of 17, 53%) hydrophobic amino acids and 4 polar uncharged amino acids. The increased charge and polarity of the probe could have helped hydrogen bond forming to improve solubility and distribution time of the probe.

There are various ways to control for EPR effect when a targeted delivery to tumor with leaky vasculature is studied [300, 301]. For instance, targeted nanoparticles can be used as sensors to detect molecular interactions [301-303]. In one study, EGFR-targeted gold nanospheres aggregated in endosomes after undergoing receptor-mediated endocytosis [304]. This resulted in plasmon coupling and a red shift in the absorption spectrum, which is detectable with photoacoustic imaging. Therefore, nanoparticles in the endosomes of cells overexpressing EGFR can be detected and distinguished from free nanoparticles in the tumor, which may have

accumulated via the EPR effect [79]. In this study, probe accumulations from EPR effect were accounted for with scrambled control peptide, free NIR dye alone and target absent tumor and probe accumulation due to EPR was found to be insignificant and nonspecific.

Since one marker may not be sufficient to detect all HCC cases, adoption of a panel of HCC markers may be a good choice. The most common combination of HCC markers is GPC3, HSP70 and glutamine synthetase (GS) [305-307]. Using a 3-marker panel with a minimum of two positives, (regardless of which), the sensitivity and specificity for the detection of eHCC-G1 were respectively 72% and 100% [308, 309]. The most sensitive combination was HSP70+/GPC3+ (59%) when a 2-marker panel was used [308, 310, 311]. However, combination of more biomarkers may increase false negatives as well. In contrast, the combination of three positive markers revealed a negative detection of 100% large regenerative (LRN) and low grade dysplastic (LGDN), 73% high grade dysplastic (HGDN) and 3% early HCC grade 1 (eHCC-G1) [308].

3.9 Summary

A peptide with strong binding affinity against GPC3 was identified and validated both *in vitro* and *ex vivo*. Our study has furnished a reliable peptide-based imaging probe, ALL*-Cy5.5, which can be used to monitor GPC3, with high specificity and resolution via *in vivo* optical imaging technologies. We found peak uptake at 2 hours post injection and clearance by ~24 hours. Specific peptide bind to individual HCC cells was visualized *in vivo* on xenograft bearing mice. The peptide probe demonstrated superior diagnostic performance on diverse liver tissue samples from North America and China, with 93% sensitivity at 88% specificity for distinguishing HCC from all non-HCC tissue. This time frame is significantly faster than most antibodies and applicable in clinical settings. We successfully visualized a large fraction of the

volume of HCC tumors, and may be able to improve imaging contrast and depth with use of optimal contrast agents, such as nanoparticles [239]. This topic will be explored in Chapter 4.

Chapter 4   Targeted *in vivo* photoacoustic imaging with gold nanoshell

4.1   Motivation

To further improve the contrast and depth of tumor imaging, contrast agents tailored for optimized photoacoustic imaging are critically needed. With surface plasmon resonance (SPR) absorption of light at longer wavelength and higher extinction efficiency than organic fluorophores such as Cy5.5, metallic nanoparticles have been widely incorporated in targeted photoacoustic imaging (PAI) [114, 312-314]. Previously, gold nanospheres [79], gold nanrods [315], silica-coated gold nanorods [316], and silver nanoplates [317] have been labeled with monoclonal EGFR antibodies to image cells overexpressing EGFR [318] with photoacoustic imaging. By strategically conjugating ALL* to the surface of GNS, we can create a novel diagnostic platform for PAI to detect satellite tumor beneath HCC resection margin with high contrast in future clinical applications.

4.1.1   Gold nanoshell for PAI

As a new type of gold nanostructures, gold nanoshells (GNSs) have significant advantages in optical and photoacoustic imaging because they are high in absorption-to-scattering ratio, plasmon-tunable in the near-infrared (NIR) spectral range and easily surface functionalized [319-321]. Gold nanoshells are concentric sphere nanoparticles consisting of a dielectric silica core and a gold shell [322, 323] which serves as the absorber of near-infrared (NIR) laser energy, Figure 4.1. By changing the size, geometry and internal structure of the GNSs, the relative magnitude of light being absorbed and scattered can be tuned to maximize energy absorption

111

[323]. By varying core-to-shell dimension ratio [324, 325], the plasmon-derived optical resonance of gold can be dramatically shifted in wavelength from the visible to the near and mid-infrared over a wavelength range that spans the region of highest physiological transmissivity [323, 326]. These shells are also easily conjugated to antibodies and other biomolecules [327-329]. Several potential biomedical applications are under development, including immunoassays, controlled drug delivery, photothermal cancer therapy, and imaging contrast agents [326, 328-334].
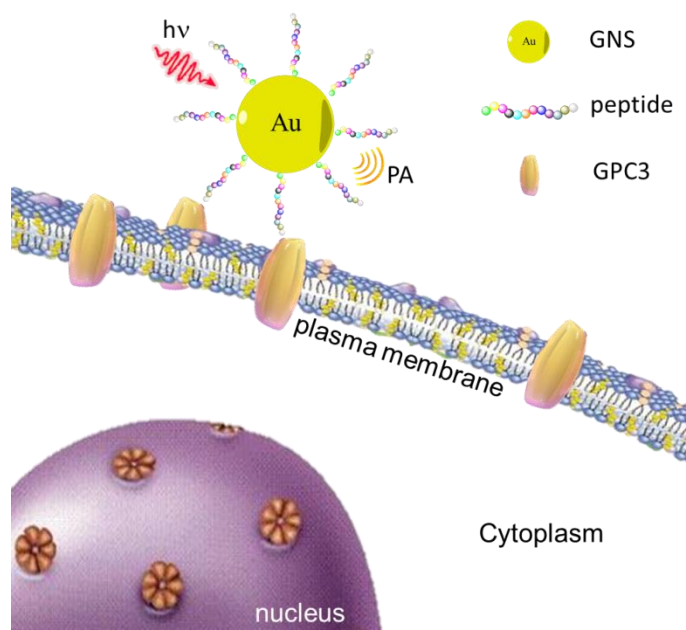
Figure 4.1 Schematic of nanoshell probe design. Targeted gold nanoshell recognizes GPC3 on plasma membrane and serves as photoacoustic imaging contrast agent upon NIR laser excitation in HCC.

Optical absorbing-dominant GNSs in the near-infrared region are valuable for PA imaging [312, 335]. Light extinction, derived from scattering and absorption, is not only dependent on the total particle radius, but also on the inner dielectric core dimensions [323, 336, 337]. Extinction coefficient depends linearly on the total size but it is independent of the core/shell ratio [215, 338, 339]. The absorption contribution to extinction decreases as the overall diameter increases [323]. The absorption cross-section of GNS is more than five orders of magnitude larger than those of

conventional organic dyes, such as IRDye-800 and indocyanine green (ICG) [114, 340]. GNS-based PA imaging can enable the enhanced photoacoustic imaging (PAI) of the tumor, as well as delivery of photothermal therapy (PTT). In previous study, GNS was demonstrated to be biocompatible and can generate heat efficiently upon NIR laser irradiation [319]. However their potential as specific nanosensors for targeted *in vivo* PAI of HCC has not been studied yet. In this study, the use of GNS with surface coated 12-mer peptide ALL* as targeted *in vivo* photoacoustic imaging contrast agent for HCC detection was investigated.

4.1.2 Stability and bioavailability

The use of gold nanoparticles (GNPs) requires an appropriate colloidal stability [341, 342]. During the past decade colloidal GNPs have become attractive materials due to an increasing interest in their potential applications in biotechnology, molecular diagnostics and biomedicine [343-348]. Because of their unique properties such as size and shape-dependent optical and electronic features, good biocompatibility and the ability to bind ligands containing thiols, phosphines and amines, they have emerged as useful tools for the design of biosensors [344], the development of methods for cancer detection [349, 350] and potential vehicles for drug delivery [351]. The immobilization of organic molecules or biomolecules onto GNPs surface significantly promotes their dispersion in aqueous solutions and improves the stability of the colloidal suspensions [352]. Lipoic acid (LA) has been extensively used for the functionalization of gold surfaces [353]. In most cases, LA has been conjugated with polyethyleneglycol (PEG) units giving decorated LA-appended-polyethyleneglycol functionalized gold nanoparticles, thereby showing better stabilities than their acyclic disulfide and single thiol counterparts [353-356].

Systemic delivery of nanoparticles also faces the challenge of overcoming immune response [357-359]. Most nanomaterials, when administered into the blood, are taken up within minutes or

hours by the phagocytic cells of the mononuclear phagocyte system (MPS) inside the liver and spleen [360-362]. The body's reticuloendothelial system sweeps foreign nanoparticles (NPs) out of the circulation before reaching the intended target [363, 364]. By preventing opsonization, the addition of polyethylene glycol (PEG) drastically increases the blood half-life of all nanomaterials [365, 366]. The synthesis of these long-circulating "stealth" nanoparticles improves accumulation in the target tissue [367]. PEGylated particles were shown to have decreased protein binding, increased blood circulation time, and decreased cytotoxicity [368]. GNSs used in this study were coated with PEG to improve the solubility and bioavailability of the nanoprobe.

4.1.3   Regulatory and clinical implications

Targeted nanoshell points in the future direction of clinical application and approval [369-371]. With the rapidly growing interest in nanoparticle research, the toxicity of nanoparticles is becoming an increasingly important issue in nanotechnology [372-374]. Based on an Web of Science search produced by Institute for Scientific Information (ISI), the number of publications concerning nanoparticle toxicity has grown exponentially over the years, with 2735 papers being published on the subject since 2000 [375]. Nevertheless, many nanoparticle systems have been approved by either the FDA (U.S.) or EMA (Europe) and are used in the clinic to either treat or diagnose disease [376]. For imaging applications, nanoparticles have been clinically approved as contrast agent for both MR [377, 378] and ultrasound [379, 380] imaging. Interestingly, while nanoparticles and targeting antibodies are both approved for clinical use, systems combining these two technologies are lacking in both approved products and in clinical trials [370, 381]. PEG-coated gold nanoshell (non-targeting) is one of the four inorganic nanoparticle therapies and diagnostics currently undergoing clinical trial [376]. Thus using surface functionalized

peptide as active targeting mechanisms to improve biodistribution of PEG-coated gold nanoshell has a promising outlook of pushing nanoparticle drug delivery system further and impacting clinical care even more in the future.

4.2 GPC3 targeting GNS synthesis and characterization

4.2.1 Surface functionalization

Monomeric linear peptides ALLANHEELFQT, hereafter ALL*, and its scrambled control QLELTFHANLEA, hereafter QLE*, (molecular weight = 1385.54 for both peptides) were synthesized as described in Section 3.3.1. Deprotection of lysine side chain exposed the amine group for coupling with Tetrafluorophenyl (TFP). ALL* and QLE* peptides were then conjugated to lipoamido-dPEG$_{12}$-TFP in anhydrous DMF under basic condition for 1 hour, Figure 4.2.
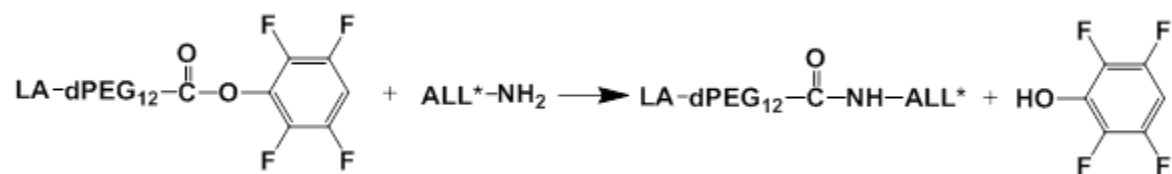
Figure 4.2 ALL* peptide is conjugated to PEG in anhydrous DMF under basic condition for 1 hour.

Nanoshell (Nanospectra Biosciences, Inc, TX) were surface coated with GPC3 targeting peptide ALL* and scrambled control peptide QLE* through a lipoamido-dPEG$_{12}$-TFP ester linker (Quanta BioDesign, Ltd., OH) using lipoic acid (LA) as an anchoring ligand [356] to improve biocompatibility and systemic circulation [382, 383], Figure 4.3.
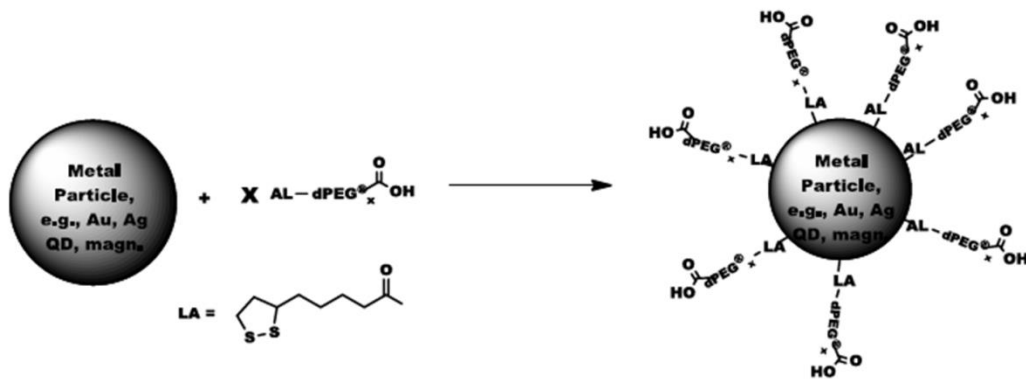
Figure 4.3 Schematic of how PEG binds to metal surface using lipoic acid (LA) as an anchoring ligand.

Five milliliters of the aqueous solution of ALL*-PEG-LA and QLE*-PEG-LA (100 mg/ml) were added to 5 ml of GNSs suspended in water (9.0×10^{10} GNSs/ml) respectively, and the mixture was stirred overnight at room temperature. To remove the unreacted PEG precursor from the solution, GNSs were centrifuged at 13,000 rpm for 10 min, the supernatant was decanted, and the particles were resuspended in PBS; this was done three times. Peptide-PEG-coated GNSs were suspended in 5 ml of PBS and stored at 4 °C. Physical size and morphology of the GNS were characterized with transmission electron microscopy (TEM) (JOEL JEM-1400) and Cs-Corrected HAADF (high angle annular dark field) scanning transmission electron microscopy (STEM) (JEOL 2100F). Hydrodynamic size and surface charge of the GNS conjugates were evaluated using dynamic light scattering (DLS) spectroscopy. The size and charge analysis of GNS (carbonate ion coated), GNS-PEG, GNS-ALL and GNS-QLE was carried out using Zetasizer Nano series (ZSP) from Malvern with Zetasizer software 6.0 as the interface.

GNS was prepared in a K_2CO_3 solution. Lipoamido-dPEG$_{12}$-TFP ester was attached to GNSs by mixing PEG-LA with aqueous solution of GNSs overnight at room temperature using lipoic acid (LA) as an anchoring ligand. Polyethylene glycol (PEG)-coated gold nanoshells were then

conjugated with targeting, Figure 4.4(A), and scrambled, Figure 4.4(B), peptides via a common peptide spacer sequence GGGSK.
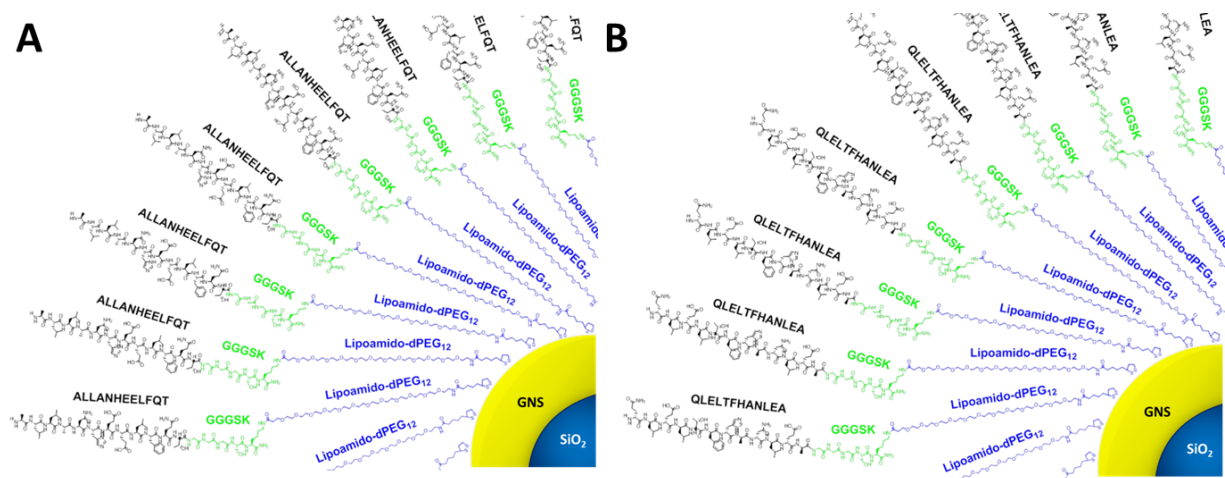
Figure 4.4 Schematic representation of surface functionalization of GNS. (A) 12-mer targeting peptide and (B) scrambled control peptide (black) were coated to the GNS surface respectively through GGGSK linker (green) and lipoamide-dPEG$_{12}$ spacer (blue).

4.2.2 Size and stability

Figure 4.5 shows the TEM image of GNS for size measurement and confirmation of the spherical gold shell morphology. 15-17nm thick Au shell (black) coated the silica core (grey).
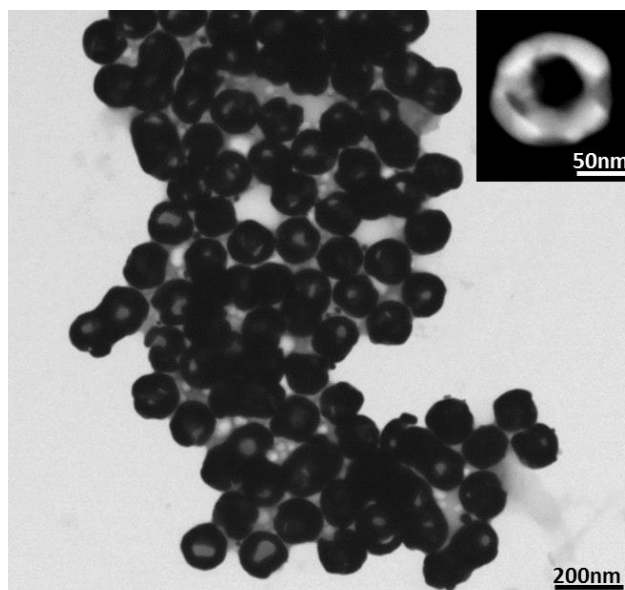
Figure 4.5 TEM image of GNSs. TEM image of GNSs displayed spherical particles with average size of 136.3 ±7.7nm (n > 150). 15-17nm thick gold shell (black) coated the silica core (grey). Inset image showed one GNS particle in high angle annular dark field (HAADF) scanning transmission electron microscopy (STEM)

The average diameter of GNS was 136.3 ±7.7nm (n > 150, polydispersity index = 0.19), which was consistent with the measurement by dynamic light scattering (DLS) in Table 4.1. The bare GNS had net negative potential (−27.1±3.8 mV) due to the presence of carbonate ions on the surface. Introducing a layer of lipoamido-dPEG12-TFP ester to the GNSs masked the negative charge and resulted in almost neutral GNS-PEGs (3.1±2.4 mV) due to the replacement of carbonate ions by PEG. After conjugation with ALL and QLE peptides, the charge value was reversed to negative (−25.1±4.3 mV and −20.6±3.1 mV), due to the large amount of negatively charged peptide units conjugated to PEG chains.

	GNS	GNS-PEG	GNS-ALL	GNS-QLE
Size (nm)	132.0±5.4	141.3±5.9	148.9±5.2	149.7±4.8
Zeta potential (mV)	-27.1±3.8	3.1±2.4	-25.1±4.3	-20.6±3.1

Table 4.1 Size and zeta potential of gold nanoshells. Nanoshell sizes were measured after different surface modifications. Negative surface charge was observed after conjugating peptide on particle surface.

No precipitation was observed for ALL*-GNS s after storage at 4 °C for three months and their

sizes remained nearly the same, Figure 4.6.
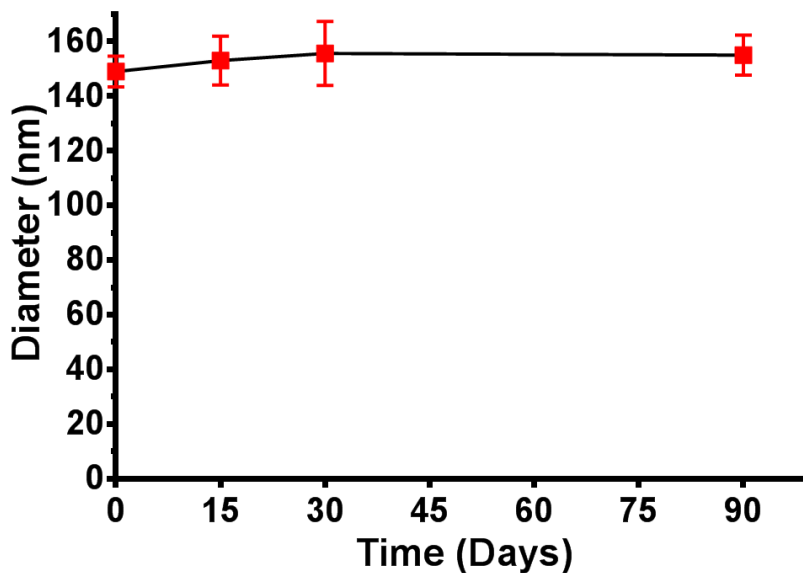
Figure 4.6 Stability of GNSs over time. GNSs were kept in liquid suspension and the size stayed stable for three months.

In addition, the physiological stability of peptide conjugated GNSs was tested in cell culture

medium (10^{11}/mL, Eagle's Minimum Essential Medium (EMEM) with 10% FBS). No obvious

changes in their size and absorption were observed after incubation for 24 h. These data indicate

good chemical and physiological stability of GNS for *in vivo* imaging applications.

4.2.3 Light extinction

The extinction coefficient of ALL*-GNS peaked at 770nm which coincided with that of the

photoacoustic instrument laser output energy in the NIR range (680—950 nm), Figure 4.7.
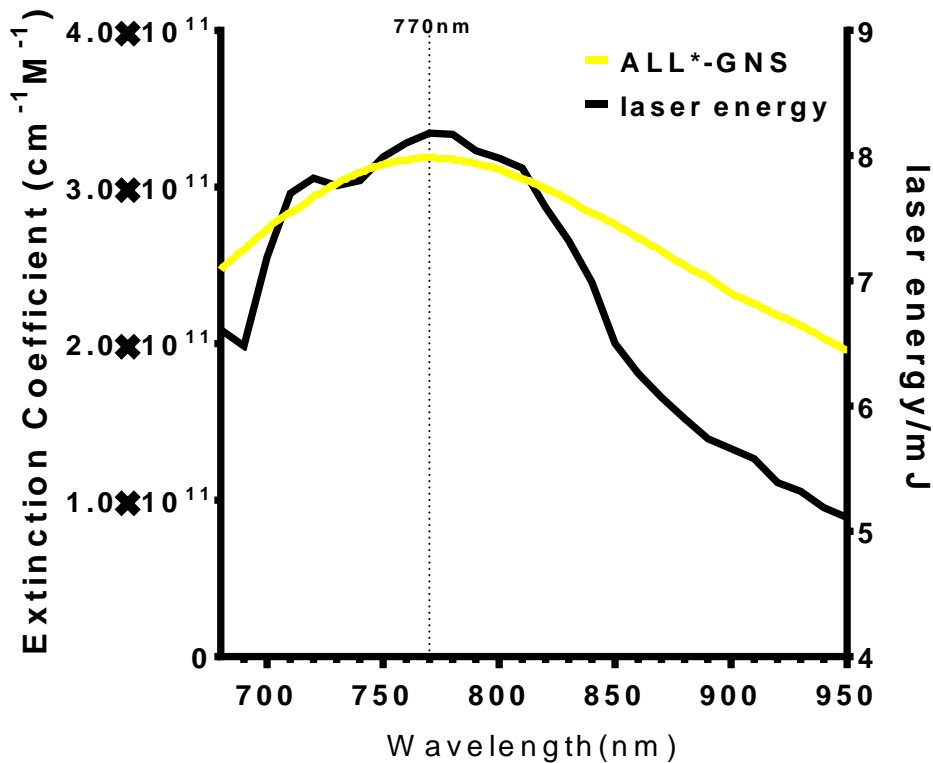
Figure 4.7 Extinction coefficient of GNS. Extinction coefficient of ALL*-GNS over the near-infrared range (680-950nm) peaked at 770nm, the same wavelength as the maximal laser energy output of photoacoustic imaging instrument.

4.3 Photoacoustic imaging of HCC xenograft tumor

We used the photoacoustic tomography system described in Section 2.4.4 with the same set of imaging parameters except excitation wavelength. A transparent imaging tray located above the transducers was used to contain anesthetized animals, Figure 4.8(A). A dimple in the imaging tray was designed to place the xenograft tumor in the center of imaging field, Figure 4.8 (B-C). At 2 weeks post inoculation, animals (n = 8) were administered 200 μL 1×10^{11}/mL ALL*-GNS, and placed inside the tray with the subcutaneous tumor positioned inside a water-filled dimple to couple the ultrasound signal. We acquired images with λ_{ex} = 770 nm at 0, 1, 2, 4, 8, and 12 hours. Preliminary study was performed to determine wash out time after injecting either targeting or control peptide.
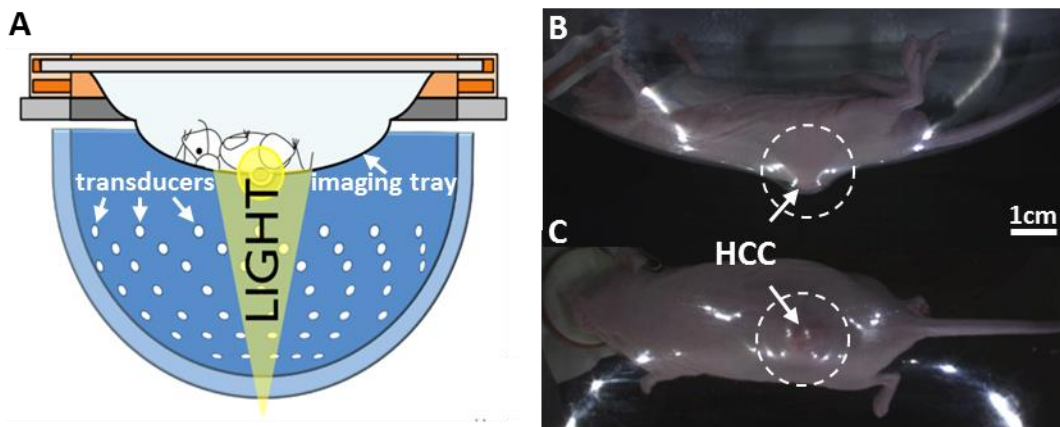
Figure 4.8 Hep3B xenograft mouse model. (C) A schematic showing the relative positions of mouse, imaging tray, light path and transducers during photoacoustic imaging, adapted with permission from http://www.endrainc.com. (B) Nude mouse with flank xenograft Hep3B tumor was placed inside a transparent imaging tray in supine position. The mouse was under anesthesia by inhaling 2% isoflurane delivered through nose cone (left). Flank HCC tumor (arrow) was positioned inside a dimple (dashed circle) at the bottom of imaging tray so that it will be at the center of field of view on photoacoustic images. White light camera took the image from the left side of mouse outside the imaging tray. (C) Another white light camera took the image of the mouse from the bottom of the imaging tray (looking along the laser light path) to make sure the HCC tumor (arrow) is placed in the center of the dimple (dashed circle).

The 3D maximum intensity projection (MIP) images were reconstructed after completion of imaging using data acquired from all 128 transducers at each view with a back-projection algorithm as described in Section 2.4.5. Representative photoacoustic images were shown at a mean ($\pm$SD) depth of 9.7$\pm$1.4 mm 0 to 2.1 cm below the skin surface. This imaging depth was achieved using 2.5 mJ/cm^2 laser fluence on the tissue surface, which is only 1/8 of the American National Standards Institute (ANSI) safety limit (20 mJ/cm^2) [56, 57]. At this time, the tumors had reached a mean ($\pm$SD) size of 45.96$\pm$8.91 mm^3 by ultrasound measurement. For ALL*-GNS injected group, the tumors showed increased signal in a heterogeneous pattern with visible blood vessels, Figure 4.9(A-F). The contrast in tumors remarkably increased in the first two hours after injection, indicating the gradual accumulation of ALL*-GNS in tumors. Imaging was repeated with QLE*- GNS, Figure 4.9(G-L). For additional control, images from HCC with and GNS-PEG alone (PEGylated nanoshell without peptide), Figure 4.9(M-R), were shown. For QLE*-GNS and GNS-PEG injected groups, no significant enhancement in PA images was observed compared with non-tumor bearing flank. Ultrasound image of tumor was taken to determine size

of tumor ROI in photoacoustic imaging quantification, Figure 4.9(S). White light photograph of tumor bearing mouse in the photoacoustic imaging tray was taken to provide anatomic information on the position of tumor on the mouse, Figure 4.9(T). The circle marks the FOV of PAI and the arrow points to the Hep3B subcutaneous xenograft. A volume rendered image of the tumor at 2 hours post injection was reconstructed in Figure 4.10. The 3D MIP rendering of tumor and surrounding vasculature from 2D PA signal was animated in Video 4.1.
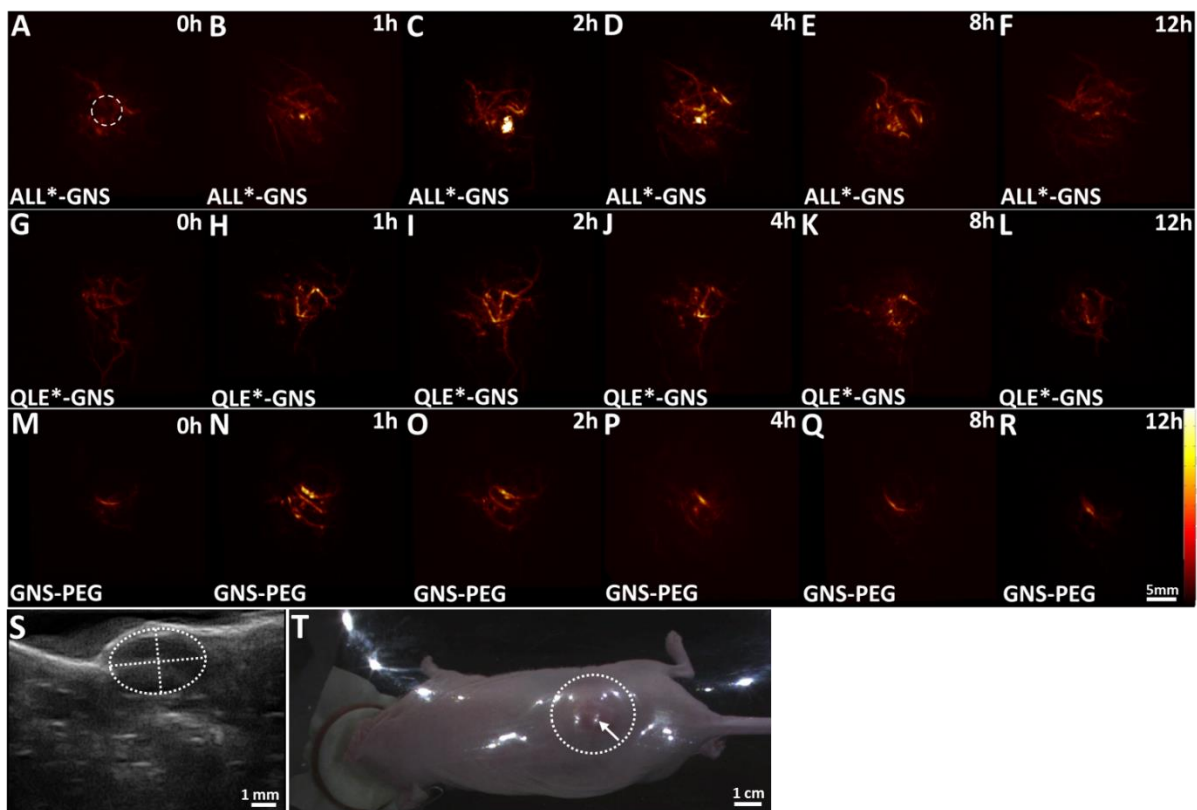
Figure 4.9 Photoacoustic imaging of HCC with targeted gold nanoshell. Representative MIP images at depth of 2.1 cm were collected at 0, 1, 2, 4, 8 and 12 hours after injection with (A-F) targeted ALL*-GNS and (G-L) scrambled control probe QLE*-GNS are shown. In panel (A), the dashed circle defined region of interest (ROI) used to measure signal from tumor, and the same area in the image of normal flank (not shown) opposite to tumor implanted flank was used to measure background. (M-R) Images of tumor with injection of GNS alone (no peptide) were taken. The targeting probe demonstrated tumor uptake after 1 hour, peaked at 2 hours and cleared in 12 hours. (S) Xenograft size was measured with dashed elliptical ROI in ultrasound image of HCC and the longer axis was used as circular ROI diameter in PAI quantification. (T) White light image was taken of HCC tumor (arrow) bearing mice inside PA imaging tray in supine position. Dashed circle marked the PAI field of view.
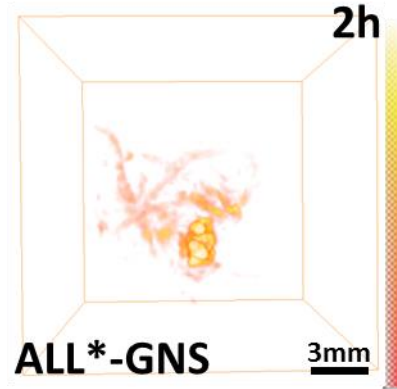
Figure 4.10 3D reconstruction of targeted gold nanoshell in HCC. 3D rendering of photoacoustic signal from ALL*-GNS in HCC tumor at 2 hrs post injection.

Video 4.1 3D PAI of nanoparticle in HCC

4.3.1 Pharmacokinetics of GPC3 targeting GNS

To quantify the pharmacokinetics of GPC3 targeting GNS, the average photoacoustic intensity from the tumor in each MIP image was measured using a circular region of interest (ROI) (white circles in Figure 4.9(A)) with diameter determined from US, Figure 4.9(S), and an identical ROI area was used in the image from the normal flank of mouse at corresponding time points to normalize PA signal at tumors. The normalized time curve of average PA signal was plotted in Figure 4.11. For QLE*-GNS and GNS-PEG injected groups, the PA enhancements peaked at 1 h after injection by 1.3 and 1.37- fold. Then the signal gradually returned to the original level after 12 h. This temporal signal increase showed a small effect of tumor permeability and retention (EPR) [58, 59] in the leaky tumor vasculature [60]. For ALL*-GNS injected group, the PA enhancement was 1.72, 4.45 3.03 and 1.41-fold at 1, 2, 4, and 8 h after injection, with peak

123

enhancement at 2 h after injection. Then the signal reduced to original level after 12 h. Statistical significance between the groups was assessed at each time point using two-tailed Student's t-test. The remarkable difference between the two groups in time-signal curves clearly demonstrated the tumor targeting ability of ALL*-GNS.
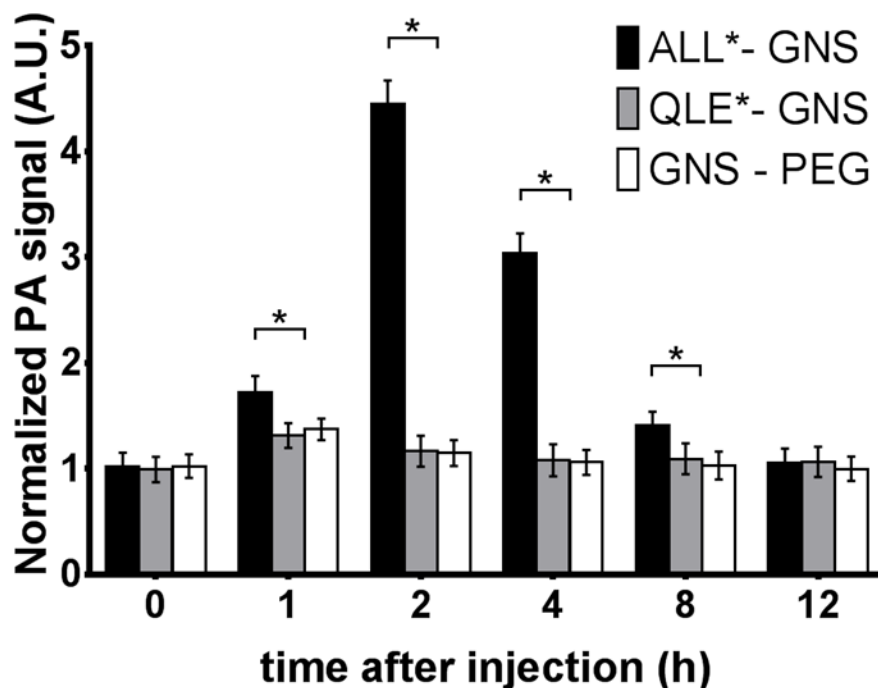
Figure 4.11 Time course of ROI quantification of PA signal (n = 8). The targeting probe ALL*-GNS demonstrated tumor uptake after 1 hour, peaked at 2 hours and cleared in 12 hours. Peak contrast occurred at 2 hours post injection. Error bars represent standard deviation. *p < 0.05.

4.3.2 Biodistribution of GPC3 targeting GNS

To understand the biodistribution of ALL*-GNS *in vivo*, gold concentrations in various organs and tumors was analyzed after one-dose injection. The extraction of gold from tissues/organs was done as described previously [55] with certain modifications. Nude mice with Hep3B xenografts were i.v. injected with 200 µ L, 40 mg/mL (i.e. 2mg/g body weight, concentration = 10^{11}/ml) of ALL*-GNS and sacrificed at 2 h and 24 h post-injection (n = 5/group) respectively. The brain, liver, spleen, lungs, kidneys, heart, stomach, GI tract, and tumor were collected, weighed and lyophilized. The dried tissues were then completely lysed in 10 ml of aqua regia in

screwcap glass bottles (20ml) separately. Excess aqua regia was evaporated at room temperature. The residues were then redissolved in 10ml of 0.05M HCl, ultrasonicated for 20min and the resultant samples were analyzed by inductively coupled plasma - optical emission spectroscopy (ICP-OES) (Optima 2000 DV) with Winlab software (Perkin-Elmer). Biodistribution in each organ was quantified as percentage of injection dose (% ID).
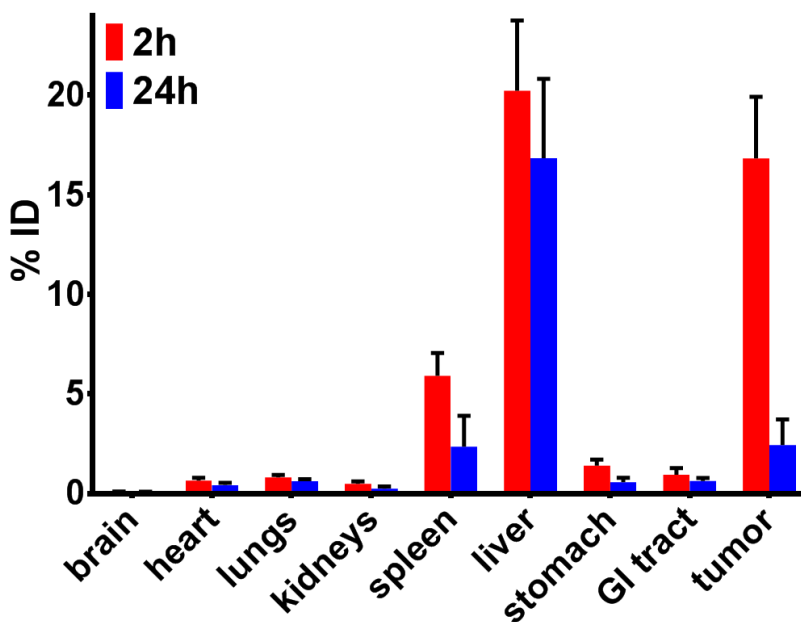
Figure 4.12 Biodistribution of targeted gold nanoshell in organs after systemic administration was measured by inductively coupled plasma - optical emission spectroscopy (ICP-OES) at 2 h and 24 h (2mg/g body weight) after i.v. injection of ALL*-GNS (n = 5/group).

The result exhibited a high accumulation in the reticuloendothelial system (RES) including the liver and spleen, Figure 4.12. Over 16.83% ID ALL*-GNS, the second highest accumulation, was retained in the tumor at 2 hour post-injection, which was similar with previous report [384]. The concentration of gold 24 hours after injection remained high in RES, while the uptake in the other organs decreased significantly.

4.3.3 Cytotoxicity of GPC3 targeting GNS *in vitro*

In vitro viability of GNSs treated Hep3B cells was calculated as a percentage relative to that of cells treated with the same volume of PBS (whose viability was arbitrarily defined as 100%). GNS solutions at concentrations of 1×10^{10}, 5×10^{10}, 1×10^{11}, and 5×10^{11}, 1×10^{12} GNSs/mL were applied to cells for 24 h. All treated cells resulted in viabilities above 91% regardless of surface chemistry. Error bars represented standard deviations of five separate measurements, Figure 4.13.
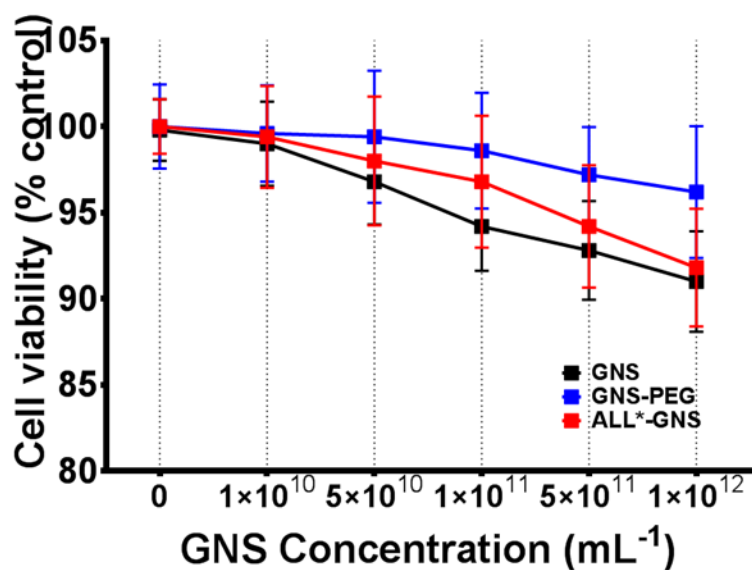
Figure 4.13 Cytotoxicity of gold GNSs. More than 91% of cultured Hep3B cells survived after incubating with bare or surface modified GNS for 24 hours.

4.3.4 Biosafety of GPC3 targeting GNS *in vivo*

The body weight of mice was measured every other day for 16 days following systemic administration of PBS, GNS-PEG and ALL*-GNS, respectively. It's noteworthy that despite the high accumulation in RES, the body weight of mice did not show significant change over 2 weeks as shown in Figure 4.14, indicating the excellent biocompatibility of GNS *in vivo*.

126
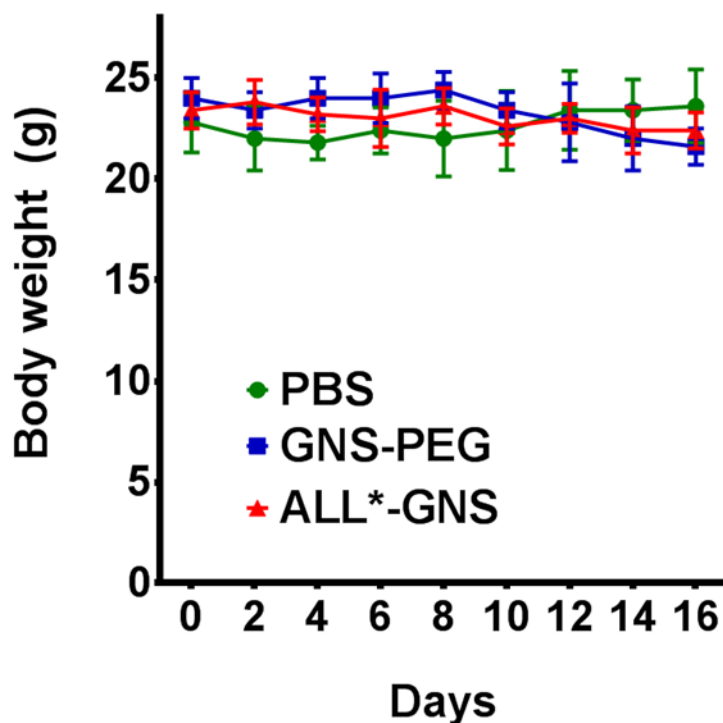
Figure 4.14 Change of body weight in mice after gold nanoshell injection. Mouse body weight was monitored over 16 days for the PBS, GNS-PEG, and ALL*-GNS treated groups (n = 5/group).

4.4 Discussions

While a wide variety of nanoparticles such as carbon nanotubes and gold nanostructures provided a platform for signal enhancement [329, 385], each possesses certain unique characteristics suitable for different applications. Examples of nanoparticles that can be used to label peptides for increased signal include iron oxide [83], CuS [386], gold nanorods [75], gold nanospheres [79, 387], carbon nanotubes [84, 238] and polymer nanoparticles [388-391]. Carbon nanotubes are considered more biocompatible [392], absorb over a broad spectrum [318], and possess superior photoacoustic signal strengths compared to metallic NPs[393]. Polymer NPs can be more photostable than gold nanorods and photoacoustically brighter than carbon nanotubes with pulsed laser irradiation [394, 395]. Despite not giving the utmost photoacoustic contrast among all nanoparticles, metallic nanoparticles have easily tunable and very strong

127

absorption that can also be used for photothermal therapy after tumor delivery [85, 396-398], which is aligned with the proposed future work in multispectral labeling in Section 5.1.2 and photothermal therapy in Section 5.1.6. Furthermore, spherical solid gold nanoparticles with 100-150 nm diameters have plasmon resonance peaks in the visible region (572-614nm), and thus will not be resonant in the NIR range for photoacoustic imaging [399]. Therefore, gold nanoshell with NIR resonance peak was used in this study.

Different nanoparticle sizes can have implications in terms of probe delivery and biodistribution. Nanoparticles with diameters smaller than 6 nm are quickly eliminated from the body because they can be excreted by the kidneys [220] and thus not suitable for our targeted probe delivery application. On the other hand, nanoparticles with diameters larger than 200 nm tend to accumulate in the spleen and liver [400], where they are endocytosed by the MPS cells [401]. Previous study on the effect of size (15—200nm) on gold nanoparticle biodistribution after intravenous administration revealed gold NPs of all sizes were mainly accumulated in organs like liver, lung and spleen [402]. They also found that 15 and 50 nm GNPs were able to pass blood-brain barrier (BBB) [402, 403]. Such uncontrolled passage into the brain may not be desirable in translation of small nanoparticle into clinical applications. The size dependent biodistribution of nanoparticles narrowed down our probe size choice in the 50—200 nm range.

In order to reduce the non-specific accumulation of GPC3-targeting nanoshells in healthy tissues, especially liver and spleen, greater than 100 nm size of nanoparticle were used. When injected into the blood stream, the delivery of nanoparticles to tumor site via passive accumulation through the leaky tumor vasculature is known as enhanced permeability and retention (EPR) effect [79, 213]. The EPR effect varies between tumor types [404], but in general favors accumulation of sub-100nm structures [405]. It was demonstrated that tumor accumulation can

be mediated by high nanoparticle avidity and are weakly dependent on their plasma clearance rate [405]. The photoacoustic signal in tumors after targeting probe injection represents the combined effect of targetability and EPR effect, while that after scrambled control probe injection resulted solely from EPR effect which was mostly confined within the blood vessels.

Finally, two more competing forces dictated the nanoprobe choice for targeted *in vivo* photoacoustic imaging study presented above. On one hand, the absorption contribution to light extinction property of gold nanoshells decreases as the overall diameter increases [215, 338, 339]. On the other hand, passage into the brain extracellular space can be restricted if the size of a nanocarrier exceeds 100 nm [406]. While the upper limit of pore size in the BBB that enables passive flow of molecules across it is usually <1 nm, particles with tens of nanometers in size [407] can also cross the BBB by carrier-mediated transport [408]. Thus in this study we chose GNSs of medium size (136.3±7.7nm) to prevent brain accumulation and maximize light absorption for strong PA signal.

Under regulated biomarkers is one major hallmark of malignant tumor [409]. Overexpression of GPC3 expedites tumor invasion and metastasis [410]. Therefore, in the new era of precision medicine, imaging tumor associated biomarkers is critical for assessing the tumor behavior, predicting the therapeutic response and maximizing the treatment benefit. Benefited from the sensitivity of PAI and PA-enhancing effect of ALL*-GNS, we extended the imaging depth to centimeters under skin *in vivo* with fast imaging speed and high spatial resolution. It is interesting to note that we used a laser fluence of ~2.5 mJ/cm^2, which is much lower than the ANSI safety limit for skin exposure (~20 mJ/cm^2) [411]. Future research would extend this work to targeted treatment of HCC such as photothermal therapy to achieve localized ablation of

tumor through heat absorption of GNS. With further development, this theranostic platform can be promising in clinical translation.

4.5 Summary

Compared to *in vivo* photoacoustic imaging with Cy5.5-labled peptide, PAI with GPC3 targeting gold nanoshells visualized HCC tumors at greater depth (2.1cm vs 1.8cm), with improved contrast (T/B = 4.45 vs 2.25) at peak tumor uptake and faster pharmacokinetics (peak time = 2hrs vs 3hrs, clearance time = 12 hrs vs 24 hrs). Injection of control peptide coated GNSs validated specificity of targeted nanoprobe accumulation independent of EPR effect. Cell viability and *in vivo* toxicity studies ensured biosafety and biocompatibility of ALL*-GNS for systemic delivery. *In vivo* imaging via photoacoustic tomography with molecular probe conjugated GNS offers a safe, effective and rapid imaging technique for noninvasive *in vivo* monitoring and semi-quantitative analysis of HCC tumor growth and GPC3 expression with great clinical translation potential.

Chapter 5   Future work and conclusions

5.1   Future studies

We propose further studies encompassing four themes: biomarker (differential expression in subpopulations and biomarker panel for diagnosis), imaging (orthotopic/PDX tumor model), surgical planning (3D-printed tumor microenvironment) and therapy (GNS mediated PTT and targeted drug delivery). Preliminary results toward these future directions are discussed below.

5.1.1   Differential GPC3 expression in patient subpopulations

A closer examination of the patient gene expression profile data presented in Figure 3.1 revealed differential GPC3 expression levels among patient subpopulations categorized by etiologies, a phenomenon found by other researchers as well [412]. While HCC tumors (T) showed higher expression with both hepatitis B virus (HBV) and hepatitis C virus (HCV) infection had a significantly higher (2.6 and 7.7 fold-changes, $P=1.6\times10^{-5}$ and $P=2.1\times10^{-16}$ respectively) GPC3 expression compared to normal (N) liver tissue within the same infection, overexpression in HCV cases was much more elevated (3.2 fold-change, $P=4.7\times10^{-5}$) than those in HBV cases, Figure 5.1. The question remains whether the same pattern can be found in protein expression levels of GPC3 in different HCC subpopulations. The sample size in our human tissue experiment was not big enough to draw conclusions. Immunochemical studies involving more human HCC patient biopsy samples from each disease background would be one way to test this hypothesis.
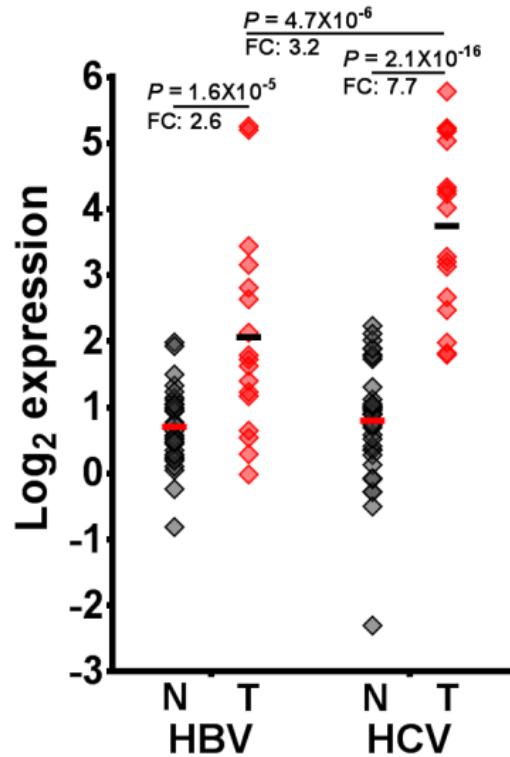
Figure 5.1 Differential GPC3 overexpression in HCC patient subpopulations. While HCC tumors (T) showed higher expression with both hepatitis B virus (HBV) and hepatitis C virus (HCV) infection had a significantly higher (2.6 and 7.7 fold-changes, $P=1.6\times10^{-5}$ and $P=2.1\times10^{-16}$ respectively) GPC3 expression compared to normal (N) liver tissue within the same infection, overexpression in HCV cases was much more elevated (3.2 fold-changes, $P=4.7\times10^{-5}$) than those in HBV cases.

5.1.2 Multispectral tumor imaging with nanoparticles

Common to most of cancers, heterogeneity in genetic expression across different patients is an essential characteristic of HCC [412]. HCC can present a combination of various biomarkers (Section 3.1.1), and not a single biomarker is expected to express in all HCC patient population. To detect HCC lesion with greater sensitivity, a panel of peptides against different targets can be utilized. GPC3 and EGFR are overexpressed in 40-70% and 80% in HCC respectively. We have so far developed peptides that target GPC3 and EGFR. Administer the two peptides simultaneously could expand our knowledge on HCC development by answering some key questions such as the co-expressing rate of GPC3 and EGFR in various stages of HCC. Meanwhile, some practical concerns over the interaction, or even competition, between peptide

probes in the combination formula and how it should be administered (simultaneously vs sequentially) must be taken into consideration in the experiment design.
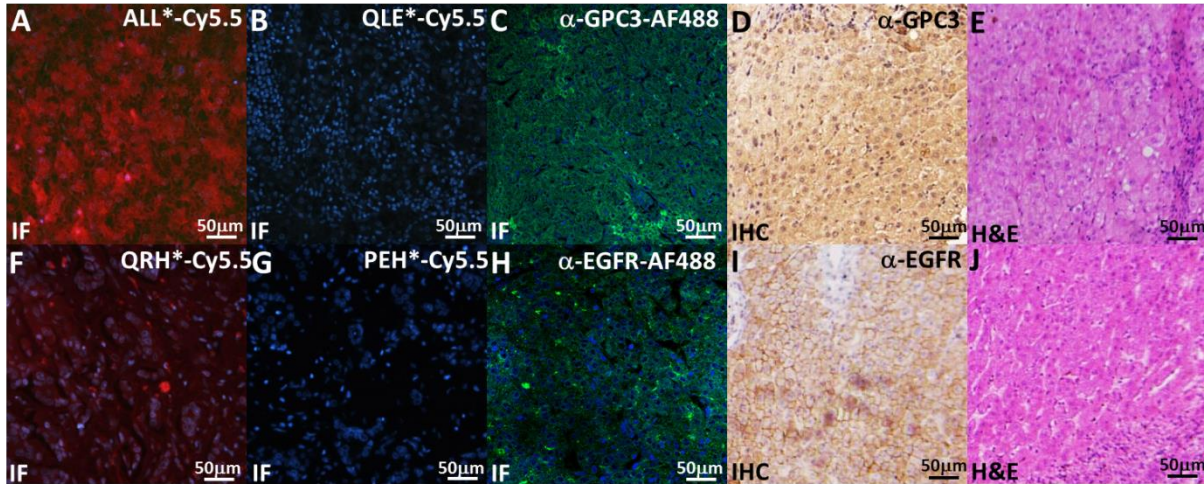
Figure 5.2 GPC3 and EGFR peptides binds to human HCC tissue sections. Immunofluorescent staining was performed on human HCC liver tissue with (A) GPC3-targeting peptide ALL*-Cy5.5 (red, intense staining), (B) scrambled control peptide QLE*-Cy5.5 (red, negative staining), (C) AF488 labeled anti-GPC3 antibody (green). (D) Immunohistochemical staining of HCC tissue with anti-GPC3 antibody and (E) corresponding histological section with H&E staining. Similarly, immunofluorescent staining was performed on human HCC liver tissue with (F) EGFR-targeting peptide QRH*-Cy5.5 (red, intense staining), (G) scrambled control peptide PEH*-Cy5.5 (red, negative staining), (H) AF488 labeled anti-EGFR antibody (green). (I) Immunohistochemical staining of HCC tissue with anti-EGFR antibody and (J) corresponding histological section with H&E staining.

Preliminary results of positive staining by individual peptide probes on human biopsies showed potential for a more sensitive diagnostic tool with two peptides combined. On confocal microscopy, we found intense staining of GPC3 targeting peptide ALL*-Cy5.5 (red) to sections of human hepatocellular carcinoma, Figure 5.2(A), compared to control peptide, Figure 5.2(B). Increased fluorescence intensity was observed for staining of anti-GPC3-AF488 antibody (green) to human hepatocellular carcinoma, Figure 5.2(C). On immunohistochemistry with a known antibody, we confirmed overexpression of GPC3 in human HCC, Figure 5.2(D). Corresponding H&E histology of HCC is shown in Figure 5.2(E). Similarly, EGFR targetability by QRH-Cy5.5 peptide and EGFR overexpression in human HCC tissue sections are shown in Figure 5.2(F-J).

Labeling of probes is one of the key issues to be addressed for multispectral detection [413]. Spectrally distinct label for each targeting probe in the mix is preferred since share label wouldn't be able to keep track of the identity of biomarker being detected. Coating of metallic shells on silica allows one to tune the absorption band from visible to infrared region [325]. The position of the SPR band is sensitive towards relative thickness of core-to-shell ratio [414]. Thus by changing the shell thickness, one can tune the SPR band position in the desired wavelength range, Figure 5.3. Metallic nanoshells having plasmon resonance in the infrared region are well suited for biological applications, as this range of the electromagnetic spectrum is transparent for biological tissues [415]. Therefore it is possible to label EGFR and GPC3 targeting peptides with gold nanoshells of different SPR and perform multispectral imaging to illuminate the roles each biomarker plays in HCC development and how they interact with each other.
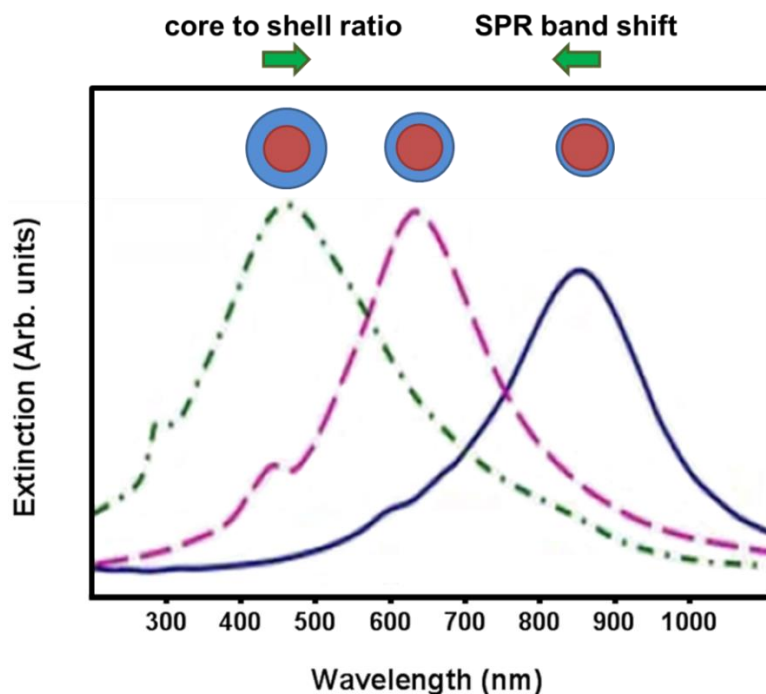
Figure 5.3 Tuning SPR band by core to shell ratio of GNS. As core-to-shell ratio of gold nanoshells increases, its peak absorption wavelength (i.e. SPR band) shifts to the right of spectrum (i.e. longer wavelength).

5.1.3   Orthotopic and patient derived xenograft

The biodistribution results in Section 3.6.2 raised the concern that fluorescent signal from liver could mask tumor signal should the xenograft were implanted on the liver, which could hinder the clinical translation of image guided surgery. Orthotopic tumor model of HCC can address this issue while patient derived xenograft (PDX) can recapitulate the genetic heterogeneity [416-418] discussed in Section 5.1.2. In a preliminary study, we examined the pharmacokinetics of Cy5.5 labeled ALL* displaying and wildtype (WT-phage) phages in mice (n=5 in each group) bearing orthotopic HCC tumor (from Hep3B cells). We observed accumulation of ALL*- phages to the site of liver xenograft with a distinctive peak at 1.5hrs after tail vein injection of $2*10^{11}$ pfu ALL*- phages, Figure 5.4(A). Minimal signal remained in liver after 24 hours and some showed up in the bladder, indicating the path of probe clearance through urinary tract. In contrast, mice (n=5) injected with WT- phages also saw accumulation in the liver presumably due to the high vascularity and the probe being metabolized in the liver, Figure 5.4(B). Signal from the NIR dye peaked at 30min and gradually tapered off until 24 hours. All images were quantified in term of normalized photon flux (mean±SD) and plotted in Figure 5.4(C). This preliminary result added confidence in the ability of peptide to generate visible contrast at tumor from surrounding liver tissue even after signal was attenuated through the muscles and skin. However, additional studies are needed before solid conclusions can be drawn, such as imaging using synthesized peptides rather than phages, inoculating orthotopic tumors with patient derived xenografts rather than standard HCC cell lines, and examination of tumor margin at peak uptake time by dissecting the liver.
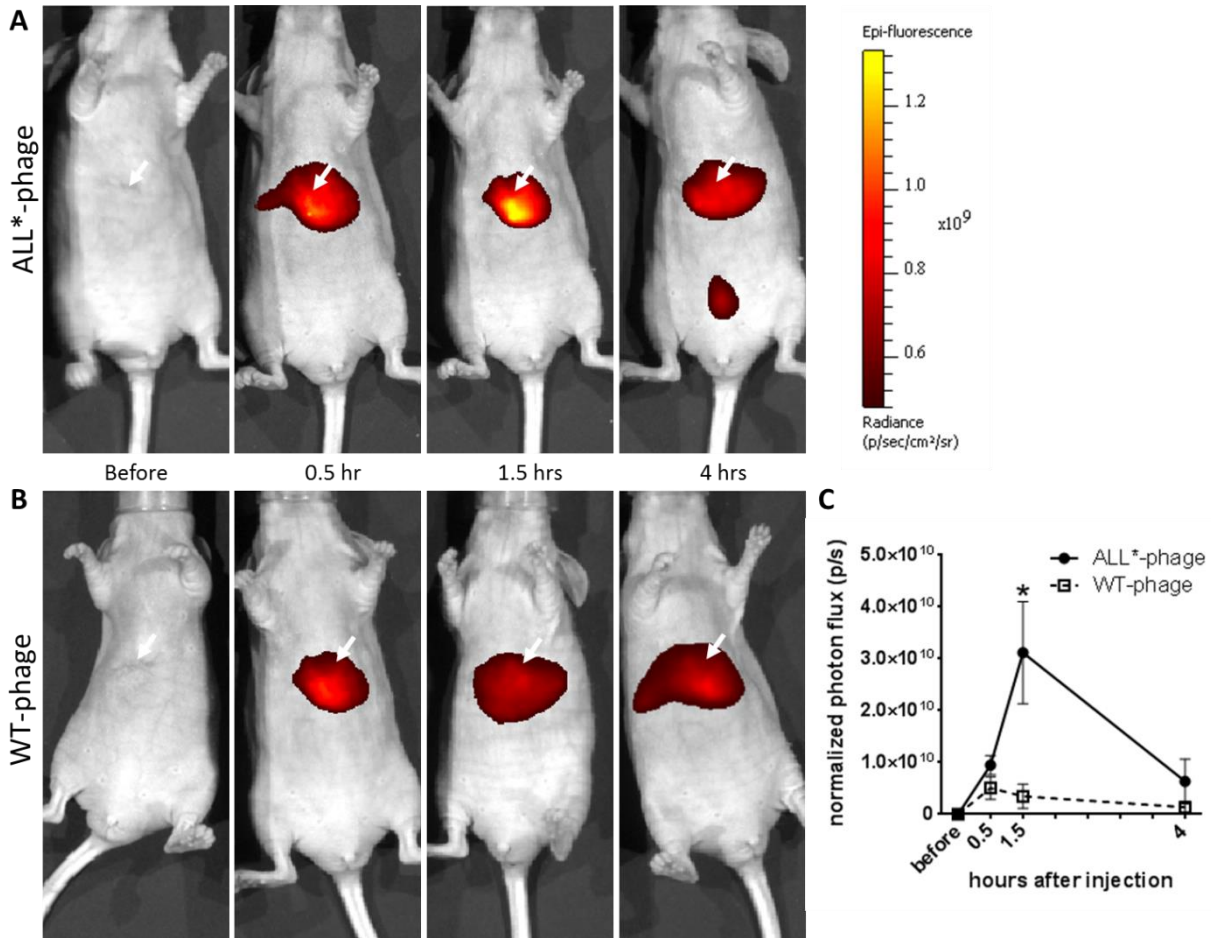
Figure 5.4 *In vivo* GPC3 targeting in orthotopic HCC mouse model. (A) nude mice with orthotopically embedded HCC tumor (arrow) in the liver was underwent whole-body fluorescent imaging after tail vein injection of Cy5.5 labeled ALL*-phages over the time course of four hours. Peak fluorescent signal was observed at 1.5 hours post injection. (B) Cy5.5 labeled wild type phages showed some fluorsent intensity increase at the tumor at 0.5 hr post injection. (C) fluorescent signal from GPC3-targeting peptide dysplaying phage peaked at 1.5 hours and was significantly higher than that of wild type phages ($3.1 \times 10^{10} \pm 9.8 \times 10^{9}$ vs. $3.5 \times 10^{9} \pm 2.3 \times 10^{9}$, P=$3.6 \times 10^{-3}$).

5.1.4   3D printing for surgical planning

While originally conceived of as a way to help surgeons with complicated or extremely delicate surgical procedures, doctors are discovering some unexpected benefits from using 3D printed replicas of patients' organs for surgical preplanning for more common surgeries [419-421]. So much of the surgical techniques that are used today involve surgical preplanning using MRI or CT data [422], which provides an image of exactly what the surgeon will be cutting into, especially when the doctor is using laparoscopic or robotic surgical tools [423, 424]. 3D data from photoacoustic tomography imaging in this thesis were presented as a 2D images, which

may not always give surgeons the clearest picture of tumor location. Turning that 3D data into a 3D printable model allows doctors to get a much better idea of the tumor's blood supply and microenvironment, and make better treatment recommendations and surgical plans.

The photoacoustic image of HCC tumor in Figure 4.10 can be segmented and rendered into a 3D spatial structure for both the tumor (pink) and the blood vessels (gold) around it, as shown in Figure 5.5. A real life size, or even scaled up, 3D polymer model could be printed with a 3D printer. This would not only help doctors offer patients more accurate treatment options, but also allow the actual surgical procedure to go smoother for the surgeons. Knowing exactly there the vessels lied around the tumor could also minimize bleeding and reduce surgery time.
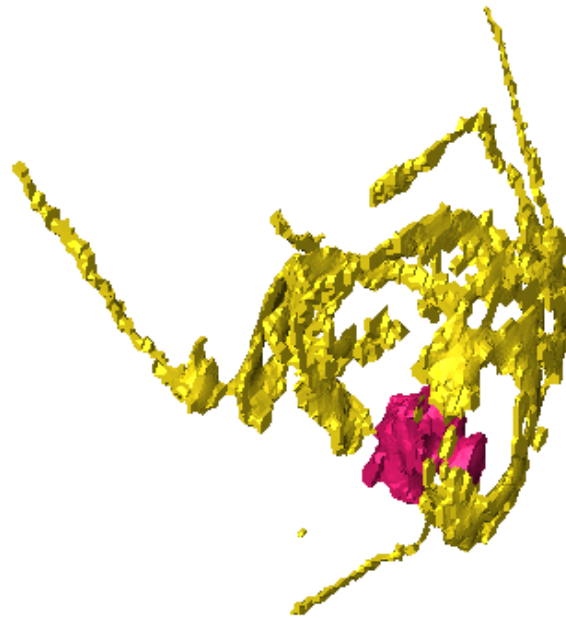
Figure 5.5 3D PAI model of HCC lesion with surrounding blood vessels. 3D reconstructed photoacoustic image can be 3D printed as physical model for surgery planning. Tumor (pink) was segmented from surrounding vasculature (gold).

5.1.5 Targeted chemotherapy

Targeted drug delivery can improve the efficacy of chemotherapy by increasing drug concentration at tumor site while reducing cytotoxicity at healthy tissue [425, 426]. GPC3 has proven to be an attractive chemotherapy target for HCC [53, 245]. Cell surface GPC3 is believed to promote tumor growth and development [244, 427]. Recent studies have elucidated the role of GPC3 as co-receptor or storage pocket for several growth factors including Wnts, FGFs and bone morphogenetic proteins [247, 262, 263, 265, 267]. In addition, silencing GPC3 expression by siRNA or shRNA in HCC cell lines HepG2, Hep3B, Huh-7 and Huh-4 can inhibit cell proliferation [272, 428]. Interruption of the interactions between GPC3 and various signaling pathways may induce tumor cell death and ablation of tumor growth [128]. Four GPC3 antibodies are being developed for liver cancer therapy [261, 272, 429-431]. Humanized mouse antibody GC33 has undergone phase I clinical trials for advanced or metastatic HCC either alone or in combination with FDA-approved chemo drug sorafenib [429]. The specific binding affinity of ALL* to GPC3 can be exploited by incorporating chemotherapeutic drugs in nanoplatforms using ALL* for HCC-targeted drug delivery and therapy.

5.1.6 Photothermal therapy
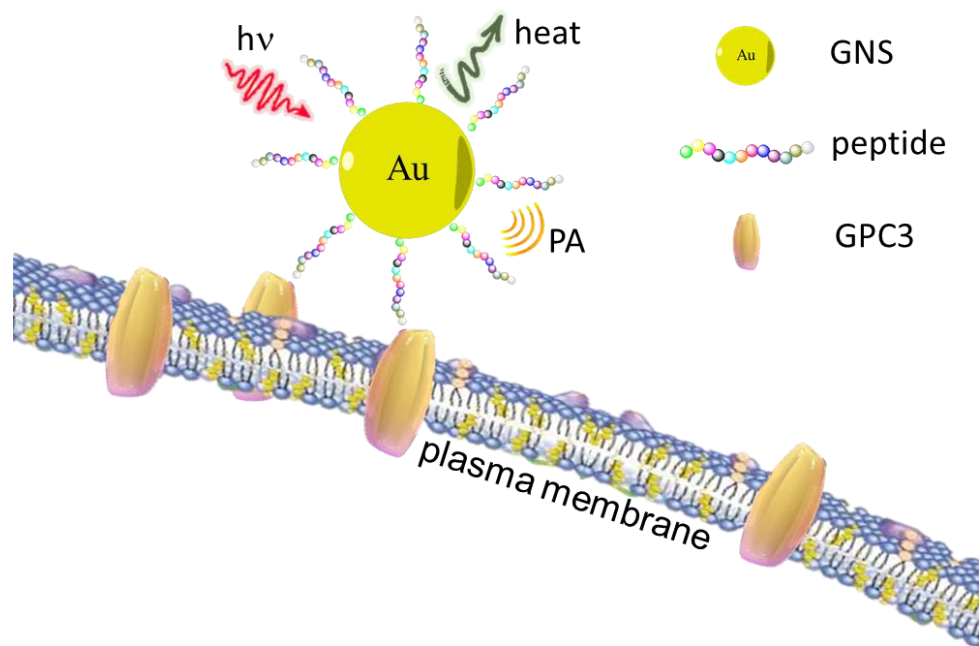
Figure 5.6 GPC3 targeting GNS as theranostic agent. Targeted gold nanoshell delivers photothermal therapy under photoacoustic imaging guidance in HCC.

The GPC3 targeting photoacoustic probe is a promising nano theranostic platform for target specific tumor imaging and localized photothermal therapy [432-434], Figure 5.6. The extent of thermal damage to tissue depends on tissue sensitivity, temperature and exposure time [435-437]. *In vitro* studies showed that the rate of cell death is exponential with respect to temperature over a limited temperature range (40–55 °C) [438, 439]. PTT of 3W/cm^2 coherent diode laser (808nm) for 3 minutes at a single tumor site can slow the growth of distant pre-established melanoma tumors in three weeks [440]. Nanoshell-treated tumors resulted in an average temperature increase of 37.4 ± 6.6°C on NIR (820nm) exposure for 4–6 min [441]. This therapy raised temperatures well above the damage threshold necessary to induce irreversible tissue damage [442] and did so by using laser dosages that were 10- to 25-fold less than those used in earlier studies with ICG [443].

The targeted delivery of photothermal nanotherapeutics can achieve noninvasive, localized imaging guided photothermal ablation of HCC *in vivo* [444, 445]. Metallic NPs can be used in tandem with infrared heating for therapy; nanoshells and nanorods are the most common examples [330, 383, 399, 446, 447]. By using two benign moieties (NIR light and nanoshells), The GPC3 specific gold nanoshell enabled photothermal therapy (PTT) as a promising ablation strategy that utilizes optically tuned gold nanoshells to generate heat upon exposure to near-infrared radiation [383]. Moreover, the combination of PTT with immunotherapy can improve the therapeutic efficacy on both primary tumor and metastatic cancer cells in the distant sites in a complementary manner [447-449]. Bear et al found gold nanoshell based PTT could promote the expression of proinflammatory cytokines and chemokines, and induce the maturation of dendritic cells (DC) within tumor-draining lymph nodes, leading to the priming of antitumor CD8+ effector T cell responses [447]. However, nanoparticles are foreign bodies that can cause inflammation in liver [450, 451] and increase circulation time [452]. Among nanomaterial-based agents already approved by the FDA [453], all but one of these agents are therapeutics [454]. Thus PTT with targeted GNS can be a great way to push forward regulatory approval of theranostics nanoparticle agents in the clinic.

5.2 Conclusions

Molecular cancer imaging strategy was proposed to address an important clinical problem, the accurate detection of hepatocellular carcinoma (HCC). Targeted peptide probes against cell surface molecules of biological significance, EGFR and Glypican-3, have been successfully developed and characterized. Longitudinal studies in the mouse model of HCC have been demonstrated using various *in vivo* imaging systems. In parallel, the application of these probes after fluorescent labeling for photoacoustic imaging was also investigated. While photoacoustic

imaging produces anatomical and physiological information of cancer, this work improved the technique by using molecularly targeted image contrast for cancer by using affinity peptides targeted to cancer cells. Findings in regards to the specificity of each of the probes, binding efficiency and bioavailability was investigated in cultured cells, in *ex vivo* tissues (human and mouse) as well as in mouse models. These targeting probes showed great promise for clinical translation with high specificity, sensitivity and fast pharmacokinetics. The findings provide compelling evidence that the developed imaging agents have the desired specificity and sensitivity as well as biocompatibility for future clinical translation. Further development and research would extend this work to better diagnosis, imaging and targeted treatment of HCC.

REFERENCES

1. Zhu, R.X., W.-K. Seto, C.-L. Lai, et al., *Epidemiology of hepatocellular carcinoma in the Asia-Pacific region.* Gut and liver, 2016. **10**(3): p. 332.
2. Ferlay, J., I. Soerjomataram, R. Dikshit, et al., *Cancer incidence and mortality worldwide: sources, methods and major patterns in GLOBOCAN 2012.* Int J Cancer, 2015. **136**: p. E359-86.
3. Yang, J.D. and L.R. Roberts, *Hepatocellular carcinoma: A global view.* Nat Rev Gastroenterol Hepatol, 2010. **7**(8): p. 448-58.
4. Mittal, S. and H.B. El-Serag, *Epidemiology of hepatocellular carcinoma: consider the population.* J Clin Gastroenterol, 2013. **47 Suppl**: p. S2-6.
5. Chatenoud, L., P. Bertuccio, C. Bosetti, et al., *Childhood cancer mortality in America, Asia, and Oceania, 1970 through 2007.* Cancer, 2010. **116**(21): p. 5063-74.
6. Howlader, N., A. Noone, M. Krapcho, et al., *SEER Cancer Statistics Review, 1975-2013.*, 2015, National Cancer Institute: Bethesda, MD.
7. Center, M., R. Siegel, and A. Jemal, *Global cancer facts & figures 3rd Edition.* Atlanta: American Cancer Society, 2015: p. 1-62.
8. Shah, S.A., P.D. Greig, S. Gallinger, et al., *Factors associated with early recurrence after resection for hepatocellular carcinoma and outcomes.* J Am Coll Surg, 2006. **202**(2): p. 275-83.
9. Capurro, M., I.R. Wanless, M. Sherman, et al., *Glypican-3: a novel serum and histochemical marker for hepatocellular carcinoma.* Gastroenterology, 2003. **125**(1): p. 89-97.
10. Bruix, J. and M. Sherman, *Management of hepatocellular carcinoma.* Hepatology, 2005. **42**(5): p. 1208-36.
11. Massarweh, N.N., J.O. Park, F. Farjah, et al., *Trends in the utilization and impact of radiofrequency ablation for hepatocellular carcinoma.* J Am Coll Surg, 2010. **210**(4): p. 441-8.
12. Hemming, A.W., M.S. Cattral, A.I. Reed, et al., *Liver transplantation for hepatocellular carcinoma.* Annals of surgery, 2001. **233**(5): p. 652.
13. Raza, A. and G.K. Sood, *Hepatocellular carcinoma review: current treatment, and evidence-based medicine.* World journal of gastroenterology: WJG, 2014. **20**(15): p. 4115.
14. Kudo, M., *Hepatocellular carcinoma 2009 and beyond: from the surveillance to molecular targeted therapy.* Oncology, 2008. **75 Suppl 1**: p. 1-12.
15. Maluccio, M. and A. Covey, *Recent progress in understanding, diagnosing, and treating hepatocellular carcinoma.* CA Cancer J Clin, 2012. **62**(6): p. 394-9.
16. Belghiti, J. and R. Kianmanesh, *Surgical treatment of hepatocellular carcinoma.* Hpb, 2005. **7**(1): p. 42-49.
17. Yeh, M.M., R.S. Yeung, S. Apisarnthanarax, et al., *Multidisciplinary perspective of hepatocellular carcinoma: A Pacific Northwest experience.* World journal of hepatology, 2015. **7**(11): p. 1460.

18. Shah, S.A., S.P. Cleary, A.C. Wei, et al., *Recurrence after liver resection for hepatocellular carcinoma: risk factors, treatment, and outcomes.* Surgery, 2007. **141**(3): p. 330-9.

19. Joo, I., *The role of intraoperative ultrasonography in the diagnosis and management of focal hepatic lesions.* Ultrasonography, 2015. **34**(4): p. 246.

20. Zhu, Z.W., H. Friess, L. Wang, et al., *Enhanced glypican-3 expression differentiates the majority of hepatocellular carcinomas from benign hepatic disorders.* Gut, 2001. **48**(4): p. 558-64.

21. Shafizadeh, N., L.D. Ferrell, and S. Kakar, *Utility and limitations of glypican-3 expression for the diagnosis of hepatocellular carcinoma at both ends of the differentiation spectrum.* Mod Pathol, 2008. **21**(8): p. 1011-8.

22. Nakatsura, T., Y. Yoshitake, S. Senju, et al., *Glypican-3, overexpressed specifically in human hepatocellular carcinoma, is a novel tumor marker.* Biochem Biophys Res Commun, 2003. **306**(1): p. 16-25.

23. Bolondi, L., S. Sofia, S. Siringo, et al., *Surveillance programme of cirrhotic patients for early diagnosis and treatment of hepatocellular carcinoma: a cost effectiveness analysis.* Gut, 2001. **48**(2): p. 251-259.

24. Fattovich, G., T. Stroffolini, I. Zagni, et al., *Hepatocellular carcinoma in cirrhosis: incidence and risk factors.* Gastroenterology, 2004. **127**(5): p. S35-S50.

25. Sangiovanni, A., E. Del Ninno, P. Fasani, et al., *Increased survival of cirrhotic patients with a hepatocellular carcinoma detected during surveillance.* Gastroenterology, 2004. **126**(4): p. 1005-1014.

26. Di Bisceglie, A.M., *Hepatitis B and hepatocellular carcinoma.* Hepatology, 2009. **49**(S5).

27. Albiin, N., *MRI of focal liver lesions.* Current medical imaging reviews, 2012. **8**(2): p. 107-116.

28. Panel, T.E., *Guidelines on the diagnosis and treatment of primary liver cancer (2011 edition).* Chinese clinical oncology, 2012. **1**(1).

29. Morise, Z., N. Kawabe, H. Tomishige, et al., *Recent advances in liver resection for hepatocellular carcinoma.* Frontiers in surgery, 2014. **1**.

30. Finn, O.J., *Premalignant lesions as targets for cancer vaccines.* Journal of Experimental Medicine, 2003. **198**(11): p. 1623-1626.

31. Sawyers, C., *Targeted cancer therapy.* Nature, 2004. **432**(7015): p. 294.

32. Bradbury, M.S., E. Phillips, P.H. Montero, et al., *Clinically-translated silica nanoparticles as dual-modality cancer-targeted probes for image-guided surgery and interventions.* Integrative Biology, 2013. **5**(1): p. 74-86.

33. Xing, H., X. Zheng, Q. Ren, et al., *Computed tomography imaging-guided radiotherapy by targeting upconversion nanocubes with significant imaging and radiosensitization enhancements.* Scientific reports, 2013. **3**.

34. Nguyen, Q.T. and R.Y. Tsien, *Fluorescence-guided surgery with live molecular navigation — a new cutting edge.* Nature reviews cancer, 2013. **13**(9): p. 653-662.

35. Li, C., *A targeted approach to cancer imaging and therapy.* Nature materials, 2014. **13**(2): p. 110-115.

36. Olson, E.S., T. Jiang, T.A. Aguilera, et al., *Activatable cell penetrating peptides linked to nanoparticles as dual probes for in vivo fluorescence and MR imaging of proteases.* Proceedings of the National Academy of Sciences, 2010. **107**(9): p. 4311-4316.

37.   Wang, H., H. Yan, A. Fu, et al., *TIP-1 translocation onto the cell plasma membrane is a molecular biomarker of tumor response to ionizing radiation.* PloS one, 2010. **5**(8): p. e12051.

38.   Yang, Y., W. Toy, L.Y. Choong, et al., *Discovery of SLC3A2 cell membrane protein as a potential gastric cancer biomarker: implications in molecular imaging.* Journal of proteome research, 2012. **11**(12): p. 5736-5747.

39.   Turtoi, A., E. De Pauw, and V. Castronovo, *Innovative proteomics for the discovery of systemically accessible cancer biomarkers suitable for imaging and targeted therapies.* The American journal of pathology, 2011. **178**(1): p. 12-18.

40.   Gao, Y. and A.E. Teschendorff, *Epigenetic and genetic deregulation in cancer target distinct signaling pathway domains.* Nucleic acids research, 2016. **45**(2): p. 583-596.

41.   Vogelstein, B., N. Papadopoulos, V.E. Velculescu, et al., *Cancer genome landscapes.* science, 2013. **339**(6127): p. 1546-1558.

42.   Alberts, B., A. Johnson, J. Lewis, et al., *The molecular basis of cancer-cell behavior.* 2002.

43.   Martin, G.S., *Cell signaling and cancer.* Cancer cell, 2003. **4**(3): p. 167-174.

44.   Berasain, C., M. Ujue Latasa, R. Urtasun, et al., *Epidermal Growth Factor Receptor (EGFR) Crosstalks in Liver Cancer.* Cancers (Basel), 2011. **3**(2): p. 2444-61.

45.   Berasain, C., M. Ujue Latasa, R. Urtasun, et al., *Epidermal growth factor receptor (EGFR) crosstalks in liver cancer.* Cancers, 2011. **3**(2): p. 2444-2461.

46.   Berasain, C., M.J. Perugorria, M.U. Latasa, et al., *The epidermal growth factor receptor: a link between inflammation and liver cancer.* Experimental biology and medicine, 2009. **234**(7): p. 713-725.

47.   Munz, M., P.A. Baeuerle, and O. Gires, *The emerging role of EpCAM in cancer and stem cell signaling.* Cancer research, 2009. **69**(14): p. 5627-5629.

48.   Sierra, J.R. and M.-S. Tsao, *c-MET as a potential therapeutic target and biomarker in cancer.* Therapeutic advances in medical oncology, 2011. **3**(1_suppl): p. S21-S35.

49.   Organ, S.L. and M.-S. Tsao, *An overview of the c-MET signaling pathway.* Therapeutic advances in medical oncology, 2011. **3**(1_suppl): p. S7-S19.

50.   Witsch, E., M. Sela, and Y. Yarden, *Roles for growth factors in cancer progression.* Physiology, 2010. **25**(2): p. 85-101.

51.   Wheeler, D.L., M. Iida, and E.F. Dunn, *The role of Src in solid tumors.* The oncologist, 2009. **14**(7): p. 667-678.

52.   Liu, Z. and J. Klominek, *Inhibition of proliferation, migration, and matrix metalloprotease production in malignant mesothelioma cells by tyrosine kinase inhibitors.* Neoplasia, 2004. **6**(6): p. 705-712.

53.   Fleming, B.D. and M. Ho, *Glypican-3 Targeting Immunotoxins for the Treatment of Liver Cancer.* Toxins, 2016. **8**(10): p. 274.

54.   Gao, W., H. Kim, and M. Ho, *Human monoclonal antibody targeting the heparan sulfate chains of glypican-3 inhibits HGF-mediated migration and motility of hepatocellular carcinoma cells.* PloS one, 2015. **10**(9): p. e0137664.

55.   Totoki, Y., K. Tatsuno, S. Yamamoto, et al., *High-resolution characterization of a hepatocellular carcinoma genome.* Nat Genet, 2011. **43**(5): p. 464-9.

56.   Sung, W.K., H. Zheng, S. Li, et al., *Genome-wide survey of recurrent HBV integration in hepatocellular carcinoma.* Nat Genet, 2012. **44**(7): p. 765-9.

57. Li, M., H. Zhao, X. Zhang, et al., *Inactivating mutations of the chromatin remodeling gene ARID2 in hepatocellular carcinoma.* Nat Genet, 2011. **43**(9): p. 828-9.

58. Guichard, C., G. Amaddeo, S. Imbeaud, et al., *Integrated analysis of somatic mutations and focal copy-number changes identifies key genes and pathways in hepatocellular carcinoma.* Nat Genet, 2012. **44**(6): p. 694-8.

59. Fujimoto, A., Y. Totoki, T. Abe, et al., *Whole-genome sequencing of liver cancers identifies etiological influences on mutation patterns and recurrent mutations in chromatin regulators.* Nat Genet, 2012. **44**(7): p. 760-4.

60. Zhou, J., B.P. Joshi, X. Duan, et al., *EGFR Overexpressed in Colonic Neoplasia Can be Detected on Wide-Field Endoscopic Imaging.* Clin Transl Gastroenterol, 2015. **6**: p. e101.

61. Lanaya, H., A. Natarajan, K. Komposch, et al., *EGFR has a tumor-promoting role in liver macrophages during hepatocellular carcinoma formation.* Nature cell biology, 2014. **16**(10): p. 972.

62. Komposch, K. and M. Sibilia, *EGFR signaling in liver diseases.* International journal of molecular sciences, 2015. **17**(1): p. 30.

63. Weldon, D., Y. Williams, and A. Patel, *Single-cell biomarker detection identifies heterogeneity within cancer populations.* The FASEB Journal, 2016. **30**(1 Supplement): p. 515.4-515.4.

64. Cyll, K., E. Ersvær, L. Vlatkovic, et al., *Tumour heterogeneity poses a significant challenge to cancer biomarker research.* British Journal of Cancer, 2017.

65. Steininger, R.J., S. Rajaram, L. Girard, et al., *On comparing heterogeneity across biomarkers.* Cytometry Part A, 2015. **87**(6): p. 558-567.

66. Yamauchi, N., A. Watanabe, M. Hishinuma, et al., *The glypican 3 oncofetal protein is a promising diagnostic marker for hepatocellular carcinoma.* Modern Pathology, 2005. **18**(12): p. 1591.

67. Liu, B., S. Paranjpe, W.C. Bowen, et al., *Investigation of the role of glypican 3 in liver regeneration and hepatocyte proliferation.* The American journal of pathology, 2009. **175**(2): p. 717-724.

68. Filmus, J. and M. Capurro, *Glypican‐3: a marker and a therapeutic target in hepatocellular carcinoma.* FEBS Journal, 2013. **280**(10): p. 2471-2476.

69. Gao, W. and M. Ho, *The role of glypican-3 in regulating Wnt in hepatocellular carcinomas.* Cancer reports, 2011. **1**(1): p. 14.

70. Lee, S., J. Xie, and X. Chen, *Activatable molecular probes for cancer imaging.* Current topics in medicinal chemistry, 2010. **10**(11): p. 1135-1144.

71. Chen, K. and X. Chen, *Design and development of molecular imaging probes.* Current topics in medicinal chemistry, 2010. **10**(12): p. 1227-1236.

72. Alford, R., M. Ogawa, P.L. Choyke, et al., *Molecular probes for the in vivo imaging of cancer.* Molecular BioSystems, 2009. **5**(11): p. 1279-1291.

73. Mallidi, S., G.P. Luke, and S. Emelianov, *Photoacoustic imaging in cancer detection, diagnosis, and treatment guidance.* Trends in biotechnology, 2011. **29**(5): p. 213-221.

74. Dragulescu-Andrasi, A., S.-R. Kothapalli, G.A. Tikhomirov, et al., *Activatable oligomerizable imaging agents for photoacoustic imaging of furin-like activity in living subjects.* Journal of the American Chemical Society, 2013. **135**(30): p. 11015-11022.

75. Agarwal, A., S. Huang, M. O'Donnell, et al., *Targeted gold nanorod contrast agent for prostate cancer detection by photoacoustic imaging.* Journal of applied physics, 2007. **102**(6): p. 064701.

76. Li, P.-C., C.-W. Wei, C.-K. Liao, et al., *Photoacoustic imaging of multiple targets using gold nanorods.* Ultrasonics, Ferroelectrics, and Frequency Control, IEEE Transactions on, 2007. **54**(8): p. 1642-1647.

77. Li, P.-C., C.-R.C. Wang, D.-B. Shieh, et al., *In vivo photoacoustic molecular imaging with simultaneous multiple selective targeting using antibody-conjugated gold nanorods.* Opt Express, 2008. **16**(23): p. 18605-18615.

78. Kim, J.-W., E.I. Galanzha, E.V. Shashkov, et al., *Golden carbon nanotubes as multimodal photoacoustic and photothermal high-contrast molecular agents.* Nat Nanotechnol, 2009. **4**(10): p. 688-694.

79. Mallidi, S., T. Larson, J. Tam, et al., *Multiwavelength photoacoustic imaging and plasmon resonance coupling of gold nanoparticles for selective detection of cancer.* Nano Lett, 2009. **9**(8): p. 2825-31.

80. Glassman, P.M. and J.P. Balthasar, *Mechanistic considerations for the use of monoclonal antibodies for cancer therapy.* Cancer biology & medicine, 2014. **11**(1): p. 20.

81. Wang, W., E. Wang, and J. Balthasar, *Monoclonal antibody pharmacokinetics and pharmacodynamics.* Clinical Pharmacology & Therapeutics, 2008. **84**(5): p. 548-558.

82. Harding, F.A., M.M. Stickler, J. Razo, et al., *The immunogenicity of humanized and fully human antibodies: residual immunogenicity resides in the CDR regions.* mAbs, 2010. **2**(3): p. 256-265.

83. Chen, K., J. Xie, H. Xu, et al., *Triblock copolymer coated iron oxide nanoparticle conjugate for tumor integrin targeting.* Biomaterials, 2009. **30**(36): p. 6912-6919.

84. Zerda, A.d.l., Z. Liu, S. Bodapati, et al., *Ultrahigh sensitivity carbon nanotube agents for photoacoustic molecular imaging in living mice.* Nano Lett, 2010. **10**(6): p. 2168-2172.

85. Lu, W., M.P. Melancon, C. Xiong, et al., *Effects of photoacoustic imaging and photothermal ablation therapy mediated by targeted hollow gold nanospheres in an orthotopic mouse xenograft model of glioma.* Cancer Res, 2011. **71**(19): p. 6116-6121.

86. Li, M.-L., J.-T. Oh, X. Xie, et al., *Simultaneous molecular and hypoxia imaging of brain tumors in vivo using spectroscopic photoacoustic tomography.* Proceedings of the IEEE, 2008. **96**(3): p. 481-489.

87. Thurber, G.M., M.M. Schmidt, and K.D. Wittrup, *Antibody tumor penetration: transport opposed by systemic and antigen-mediated clearance.* Advanced drug delivery reviews, 2008. **60**(12): p. 1421-1434.

88. Janeway Jr, C.A., P. Travers, M. Walport, et al., *The structure of a typical antibody molecule.* 2001.

89. Joshi, B.P., J. Zhou, A. Pant, et al., *Design and Synthesis of Near-Infrared Peptide for in Vivo Molecular Imaging of HER2.* Bioconjugate chemistry, 2015. **27**(2): p. 481-494.

90. Warram, J.M., E. de Boer, A.G. Sorace, et al., *Antibody-based imaging strategies for cancer.* Cancer and Metastasis Reviews, 2014. **33**(2-3): p. 809-822.

91. Juhl, K., A. Christensen, M. Persson, et al., *Peptide-based optical uPAR imaging for surgery: in vivo testing of ICG-Glu-Glu-AE105.* PloS one, 2016. **11**(2): p. e0147428.

92. Cai, W., K. Chen, Z.-B. Li, et al., *Dual-function probe for PET and near-infrared fluorescence imaging of tumor vasculature.* Journal of Nuclear Medicine, 2007. **48**(11): p. 1862-1870.

93. Wester, H.-J. and H. Kessler, *Molecular targeting with peptides or peptide-polymer conjugates: just a question of size?* Journal of Nuclear Medicine, 2005. **46**(12): p. 1940-1945.

94. Caboche, S., V. Leclere, M. Pupin, et al., *Diversity of monomers in nonribosomal peptides: towards the prediction of origin and biological activity.* Journal of bacteriology, 2010. **192**(19): p. 5143-5150.

95. Epand, R.M. and H.J. Vogel, *Diversity of antimicrobial peptides and their mechanisms of action.* Biochimica et Biophysica Acta (BBA)-Biomembranes, 1999. **1462**(1): p. 11-28.

96. Hundsberger, H., K. Önder, P. Schuller-Götzburg, et al., *Assembly and use of high-density recombinant peptide chips for large-scale ligand screening is a practical alternative to synthetic peptide libraries.* BMC genomics, 2017. **18**(1): p. 450.

97. Zorzi, A., S.J. Middendorp, J. Wilbs, et al., *Acylated heptapeptide binds albumin with high affinity and application as tag furnishes long-acting peptides.* Nat Commun, 2017. **8**: p. 16092.

98. Thayer, A.M., *Making peptides at large scale.* Chem Eng News, 2011. **89**(22): p. 81-85.

99. Bommarius, B., H. Jenssen, M. Elliott, et al., *Cost-effective expression and purification of antimicrobial and host defense peptides in Escherichia coli.* Peptides, 2010. **31**(11): p. 1957-1965.

100. Marqus, S., E. Pirogova, and T.J. Piva, *Evaluation of the use of therapeutic peptides for cancer treatment.* Journal of biomedical science, 2017. **24**(1): p. 21.

101. AlDeghaither, D., B.G. Smaglo, and L.M. Weiner, *Beyond peptides and mAbs—Current status and future perspectives for biotherapeutics with novel constructs.* The Journal of Clinical Pharmacology, 2015. **55**(S3).

102. Landry, J., Y. Ke, G.-L. Yu, et al., *Measuring affinity constants of 1450 monoclonal antibodies to peptide targets with a microarray-based label-free assay platform.* Journal of immunological methods, 2015. **417**: p. 86-96.

103. Ishizawa, T., N. Fukushima, J. Shibahara, et al., *Real-time identification of liver cancers by using indocyanine green fluorescent imaging.* Cancer, 2009. **115**(11): p. 2491-504.

104. Gotoh, K., T. Yamada, O. Ishikawa, et al., *A novel image-guided surgery of hepatocellular carcinoma by indocyanine green fluorescence imaging navigation.* J Surg Oncol, 2009. **100**(1): p. 75-9.

105. Aoki, T., D. Yasuda, Y. Shimizu, et al., *Image-guided liver mapping using fluorescence navigation system with indocyanine green for anatomical hepatic resection.* World J Surg, 2008. **32**(8): p. 1763-7.

106. Choi, J.-Y., J.-M. Lee, and C.B. Sirlin, *CT and MR imaging diagnosis and staging of hepatocellular carcinoma: part II. Extracellular agents, hepatobiliary agents, and ancillary imaging features.* Radiology, 2014. **273**(1): p. 30-50.

107. Hennedige, T. and S.K. Venkatesh, *Imaging of hepatocellular carcinoma: diagnosis, staging and treatment monitoring.* Cancer Imaging, 2012. **12**(3): p. 530.

108. Farid, S.G., K.R. Prasad, and G. Morris-Stiff, *Operative terminology and post-operative management approaches applied to hepatic surgery: Trainee perspectives.* World journal of gastrointestinal surgery, 2013. **5**(5): p. 146.

109. Belghiti, J. and S. Ogata, *Preoperative optimization of the liver for resection in patients with hilar cholangiocarcinoma.* HPB, 2005. **7**(4): p. 252-253.

110. Ahmed, S.U., M. Zair, K. Chen, et al., *Generation of subcutaneous and intrahepatic human hepatocellular carcinoma xenografts in immunodeficient mice.* Journal of visualized experiments: JoVE, 2013(79).

111.   Lakshman, M. and A. Needles, *Screening and quantification of the tumor microenvironment with micro-ultrasound and photoacoustic imaging.* Nature Methods, 2015. **12**(4).

112.   Bialecki, E.S. and A.M. Di Bisceglie, *Diagnosis of hepatocellular carcinoma.* Hpb, 2005. **7**(1): p. 26-34.

113.   Oliva, M.R. and S. Saini, *Liver cancer imaging: role of CT, MRI, US and PET.* Cancer imaging, 2004. **4**(Spec No A): p. S42.

114.   Wu, D., L. Huang, M.S. Jiang, et al., *Contrast Agents for Photoacoustic and Thermoacoustic Imaging: A Review.* International Journal of Molecular Sciences, 2014. **15**(12): p. 23616-23639.

115.   Haedicke, K., C. Brand, M. Omar, et al., *Sonophore labeled RGD: a targeted contrast agent for optoacoustic imaging.* Photoacoustics, 2017. **6**: p. 1-8.

116.   Yao, J. and L.V. Wang, *Sensitivity of photoacoustic microscopy.* Photoacoustics, 2014. **2**(2): p. 87-101.

117.   Liu, Z., Luke D. Lavis, and E. Betzig, *Imaging Live-Cell Dynamics and Structure at the Single-Molecule Level.* Molecular Cell, 2015. **58**(4): p. 644-659.

118.   Chen, Z.Y., Y.X. Wang, Y. Lin, et al., *Advance of molecular imaging technology and targeted imaging agent in imaging and therapy.* Biomed Res Int, 2014. **2014**: p. 819324.

119.   Isherwood, B., P. Timpson, E.J. McGhee, et al., *Live cell in vitro and in vivo imaging applications: accelerating drug discovery.* Pharmaceutics, 2011. **3**(2): p. 141-70.

120.   Haddadin, I.S., A. McIntosh, S. Meisamy, et al., *Metabolite quantification and high‐field MRS in breast cancer.* NMR in Biomedicine, 2009. **22**(1): p. 65-76.

121.   Heijblom, M., D. Piras, M. Brinkhuis, et al., *Photoacoustic image patterns of breast carcinoma and comparisons with Magnetic Resonance Imaging and vascular stained histopathology.* Scientific reports, 2015. **5**: p. 11778.

122.   Smith, A.M., M.C. Mancini, and S. Nie, *Bioimaging: second window for in vivo imaging.* Nature nanotechnology, 2009. **4**(11): p. 710-711.

123.   Weissleder, R., *A clearer vision for in vivo imaging.* Nat Biotechnol, 2001. **19**(4): p. 316-7.

124.   Mehrmohammadi, M., S. Joon Yoon, D. Yeager, et al., *Photoacoustic imaging for cancer detection and staging.* Current molecular imaging, 2013. **2**(1): p. 89-105.

125.   Park, J.O., Z. Stephen, C. Sun, et al., *Glypican-3 targeting of liver cancer cells using multifunctional nanoparticles.* Mol Imaging, 2011. **10**(1): p. 69-77.

126.   Gu, Y., Y. Zeng, D.J. Guo, et al., *Preparation of a glypican-3-targeting hepatocellular carcinoma MR probe and its molecular imaging in HepG2 cells.* Zhonghua Gan Zang Bing Za Zhi, 2014. **22**(2): p. 142-7.

127.   Zhao, P., X. Yang, S. Qi, et al., *Molecular imaging of hepatocellular carcinoma xenografts with epidermal growth factor receptor targeted affibody probes.* Biomed Res Int, 2013. **2013**: p. 759057.

128.   Zhu, D., Y. Qin, J. Wang, et al., *Novel Glypican-3-Binding Peptide for in Vivo Hepatocellular Carcinoma Fluorescent Imaging.* Bioconjug Chem, 2016. **27**(3): p. 831-9.

129.   Li, Y.L., Y. Hu, J. Xiao, et al., *Investigation of SP94 Peptide as a Specific Probe for Hepatocellular Carcinoma Imaging and Therapy.* Scientific Reports, 2016. **6**.

130.   Luo, S., E. Zhang, Y. Su, et al., *A review of NIR dyes in cancer targeting and imaging.* Biomaterials, 2011. **32**(29): p. 7127-38.

131.   Chauhan, V.P., T. Stylianopoulos, Y. Boucher, et al., *Delivery of Molecular and Nanoscale Medicine to Tumors: Transport Barriers and Strategies.* Annual Review of Chemical and Biomolecular Engineering, Vol 2, 2011. **2**: p. 281-298.

132.   Lee, S., J. Xie, and X.Y. Chen, *Peptides and Peptide Hormones for Molecular Imaging and Disease Diagnosis.* Chemical Reviews, 2010. **110**(5): p. 3087-3111.

133.   Hong, G., A.L. Antaris, and H. Dai, *Near-infrared fluorophores for biomedical imaging.* 2017. **1**: p. 0010.

134.   Pauli, J., M. Grabolle, R. Brehm, et al., *Suitable labels for molecular imaging--influence of dye structure and hydrophilicity on the spectroscopic properties of IgG conjugates.* Bioconjug Chem, 2011. **22**(7): p. 1298-308.

135.   Zhou, Q., Z. Li, J. Zhou, et al., *In vivo photoacoustic tomography of EGFR overexpressed in hepatocellular carcinoma mouse xenograft.* Photoacoustics, 2016. **4**(2): p. 43-54.

136.   Gad, S.C., K.L. Sharp, C. Montgomery, et al., *Evaluation of the toxicity of intravenous delivery of auroshell particles (gold-silica nanoshells).* Int J Toxicol, 2012. **31**(6): p. 584-94.

137.   Li, M.-L., J.C. Wang, J.A. Schwartz, et al., *In-vivo photoacoustic microscopy of nanoshell extravasation from solid tumor vasculature.* Journal of Biomedical Optics, 2009. **14**(1): p. 010507-010507-3.

138.   Li, G., H. Li, X. Duan, et al., *Visualizing epithelial expression in vertical and horizontal planes with dual axes confocal endomicroscope using compact distal scanner.* IEEE Transactions on Medical Imaging, 2017.

139.   Li, Z., Q. Zhou, J. Zhou, et al., *In vivo fluorescence imaging of hepatocellular carcinoma xenograft using near-infrared labeled epidermal growth factor receptor (EGFR) peptide.* Biomedical Optics Express, 2016. **7**(9): p. 3163-3169.

140.   Hirsch, F.R., M. Varella-Garcia, P.A. Bunn, et al., *Epidermal growth factor receptor in non–small-cell lung carcinomas: correlation between gene copy number and protein expression and impact on prognosis.* Journal of Clinical Oncology, 2003. **21**(20): p. 3798-3807.

141.   Bhargava, R., W.L. Gerald, A.R. Li, et al., *EGFR gene amplification in breast cancer: correlation with epidermal growth factor receptor mRNA and protein expression and HER-2 status and absence of EGFR-activating mutations.* Mod Pathol, 2005. **18**(8): p. 1027-33.

142.   Hanawa, M., S. Suzuki, Y. Dobashi, et al., *EGFR protein overexpression and gene amplification in squamous cell carcinomas of the esophagus.* Int J Cancer, 2006. **118**(5): p. 1173-80.

143.   Jimeno, A., A.C. Tan, J. Coffa, et al., *Coordinated epidermal growth factor receptor pathway gene overexpression predicts epidermal growth factor receptor inhibitor sensitivity in pancreatic cancer.* Cancer Res, 2008. **68**(8): p. 2841-9.

144.   Reuter, C.W., M.A. Morgan, and A. Eckardt, *Targeting EGF-receptor-signalling in squamous cell carcinomas of the head and neck.* Br J Cancer, 2007. **96**(3): p. 408-16.

145.   Nicholson, R.I., J.M.W. Gee, and M.E. Harper, *EGFR and cancer prognosis.* European journal of cancer, 2001. **37**: p. 9-15.

146.   Masuda, H., D. Zhang, C. Bartholomeusz, et al., *Role of epidermal growth factor receptor in breast cancer.* Breast cancer research and treatment, 2012. **136**(2): p. 331-345.

147. Troiani, T., E. Martinelli, A. Capasso, et al., *Targeting EGFR in pancreatic cancer treatment.* Curr Drug Targets, 2012. **13**(6): p. 802-10.

148. Siegelin, M.D. and A.C. Borczuk, *Epidermal growth factor receptor mutations in lung adenocarcinoma.* Laboratory Investigation, 2014. **94**(2): p. 129-137.

149. Ito, Y., T. Takeda, M. Sakon, et al., *Expression and clinical significance of erb-B receptor family in hepatocellular carcinoma.* Br J Cancer, 2001. **84**(10): p. 1377-83.

150. Schiffer, E., C. Housset, W. Cacheux, et al., *Gefitinib, an EGFR inhibitor, prevents hepatocellular carcinoma development in the rat liver with cirrhosis.* Hepatology, 2005. **41**(2): p. 307-14.

151. El-Bassiouni, A., M. Nosseir, M. Zoheiry, et al., *Immunohistochemical expression of CD95 (Fas), c-myc and epidermal growth factor receptor in hepatitis C virus infection, cirrhotic liver disease and hepatocellular carcinoma.* APMIS, 2006. **114**(6): p. 420-7.

152. Buckley, A.F., L.J. Burgart, V. Sahai, et al., *Epidermal growth factor receptor expression and gene copy number in conventional hepatocellular carcinoma.* Am J Clin Pathol, 2008. **129**(2): p. 245-51.

153. Yoneda, N., Y. Sato, A. Kitao, et al., *Epidermal growth factor induces cytokeratin 19 expression accompanied by increased growth abilities in human hepatocellular carcinoma.* Lab Invest, 2011. **91**(2): p. 262-72.

154. Höpfner, M., A.P. Sutter, A. Huether, et al., *Targeting the epidermal growth factor receptor by gefitinib for treatment of hepatocellular carcinoma.* J Hepatol, 2004. **41**(6): p. 1008-1016.

155. Uslu, S., H. Kirimlioglu, and U. Ince, *Analysis of Epidermal Growth Factor Receptor Expression in Hepatocellular Carcinoma: A Comparision of Fluorescence in Situ Hybridization and Immunochemistry.* Journal of Gastroenterology and Hepatology Research, 2014. **3**(8): p. 1193-1197.

156. Matsuo, M., H. Sakurai, and I. Saiki, *ZD1839, a Selective Epidermal Growth Factor Receptor Tyrosine Kinase Inhibitor, Shows Antimetastatic Activity Using a Hepatocellular Carcinoma Model1.* Molecular cancer therapeutics, 2003. **2**(6): p. 557-561.

157. Lo, H.-W., S.-C. Hsu, W. Xia, et al., *Epidermal growth factor receptor cooperates with signal transducer and activator of transcription 3 to induce epithelial-mesenchymal transition in cancer cells via up-regulation of TWIST gene expression.* Cancer Res, 2007. **67**(19): p. 9066-9076.

158. Lupberger, J., M.B. Zeisel, F. Xiao, et al., *EGFR and EphA2 are host factors for hepatitis C virus entry and possible targets for antiviral therapy.* Nat Med, 2011. **17**(5): p. 589-95.

159. Klutz, K., D. Schaffert, M.J. Willhauck, et al., *Epidermal Growth Factor Receptor-targeted (131)I-therapy of Liver Cancer Following Systemic Delivery of the Sodium Iodide Symporter Gene.* Molecular Therapy, 2011. **19**(4): p. 676-685.

160. Yang, L., H. Mao, Y.A. Wang, et al., *Single Chain Epidermal Growth Factor Receptor Antibody Conjugated Nanoparticles for in vivo Tumor Targeting and Imaging.* Small (Weinheim an der Bergstrasse, Germany), 2009. **5**(2): p. 235-243.

161. Luo, H., R. Hernandez, H. Hong, et al., *Noninvasive brain cancer imaging with a bispecific antibody fragment, generated via click chemistry.* Proceedings of the National Academy of Sciences of the United States of America, 2015. **112**(41): p. 12806-12811.

162. Ke, S., X. Wen, M. Gurfinkel, et al., *Near-infrared optical imaging of epidermal growth factor receptor in breast cancer xenografts.* Cancer Research, 2003. **63**(22): p. 7870-7875.

163. Nitin, N., K.J. Rosbach, A. El-Naggar, et al., *Optical molecular imaging of epidermal growth factor receptor expression to improve detection of oral neoplasia.* Neoplasia, 2009. **11**(6): p. 542-551.

164. Hudson, S.V., J.S. Huang, W. Yin, et al., *Targeted noninvasive imaging of EGFR-expressing orthotopic pancreatic cancer using multispectral optoacoustic tomography.* Cancer research, 2014. **74**(21): p. 6271-6279.

165. Mallidi, S., P.P. Joshi, K. Sokolov, et al. *On sensitivity of molecular specific photoacoustic imaging using plasmonic gold nanoparticles.* in *Engineering in Medicine and Biology Society, 2009. EMBC 2009. Annual International Conference of the IEEE.* 2009. IEEE.

166. Hughes, J.P., S. Rees, S.B. Kalindjian, et al., *Principles of early drug discovery.* British Journal of Pharmacology, 2011. **162**(6): p. 1239-1249.

167. van der Meel, R., L.J. Vehmeijer, R.J. Kok, et al., *Ligand-targeted particulate nanomedicines undergoing clinical evaluation: current status.* Adv Drug Deliv Rev, 2013. **65**(10): p. 1284-98.

168. Zhu, A.X., K. Stuart, L.S. Blaszkowsky, et al., *Phase 2 study of cetuximab in patients with advanced hepatocellular carcinoma.* Cancer, 2007. **110**(3): p. 581-9.

169. Siegel, A.B., E.I. Cohen, A. Ocean, et al., *Phase II trial evaluating the clinical and biologic effects of bevacizumab in unresectable hepatocellular carcinoma.* J Clin Oncol, 2008. **26**(18): p. 2992-8.

170. Lu, R.M., Y.L. Chang, M.S. Chen, et al., *Single chain anti-c-Met antibody conjugated nanoparticles for in vivo tumor-targeted imaging and drug delivery.* Biomaterials, 2011. **32**(12): p. 3265-74.

171. Farokhzad, O.C., S. Jon, A. Khademhosseini, et al., *Nanoparticle-aptamer bioconjugates: a new approach for targeting prostate cancer cells.* Cancer Res, 2004. **64**(21): p. 7668-72.

172. Gabizon, A., H. Shmeeda, A.T. Horowitz, et al., *Tumor cell targeting of liposome-entrapped drugs with phospholipid-anchored folic acid-PEG conjugates.* Adv Drug Deliv Rev, 2004. **56**(8): p. 1177-92.

173. Lee, R.J. and P.S. Low, *Folate-mediated tumor cell targeting of liposome-entrapped doxorubicin in vitro.* Biochim Biophys Acta, 1995. **1233**(2): p. 134-44.

174. Chen, W.C., G.C. Completo, D.S. Sigal, et al., *In vivo targeting of B-cell lymphoma with glycan ligands of CD22.* Blood, 2010. **115**(23): p. 4778-86.

175. Chames, P., M. Van Regenmortel, E. Weiss, et al., *Therapeutic antibodies: successes, limitations and hopes for the future.* British Journal of Pharmacology, 2009. **157**(2): p. 220-233.

176. Peters, C. and S. Brown, *Antibody–drug conjugates as novel anti-cancer chemotherapeutics.* Bioscience Reports, 2015. **35**(4): p. e00225.

177. Sullivan, L.A. and R.A. Brekken, *The VEGF family in cancer and antibody-based strategies for their inhibition.* mAbs, 2010. **2**(2): p. 165-175.

178. Hutt, M., A. Färber-Schwarz, F. Unverdorben, et al., *Plasma Half-life Extension of Small Recombinant Antibodies by Fusion to Immunoglobulin-binding Domains.* The Journal of Biological Chemistry, 2012. **287**(7): p. 4462-4469.

179. Preithner, S., S. Elm, S. Lippold, et al., *High concentrations of therapeutic IgG1 antibodies are needed to compensate for inhibition of antibody-dependent cellular cytotoxicity by excess endogenous immunoglobulin G.* Mol Immunol, 2006. **43**(8): p. 1183-93.

180. Scott, A.M., J.D. Wolchok, and L.J. Old, *Antibody therapy of cancer.* Nat Rev Cancer, 2012. **12**(4): p. 278-287.

181. Laverman, P., J.K. Sosabowski, O.C. Boerman, et al., *Radiolabelled peptides for oncological diagnosis.* European Journal of Nuclear Medicine and Molecular Imaging, 2012. **39**(Suppl 1): p. 78-92.

182. Lee, S., J. Xie, and X. Chen, *Peptides and peptide hormones for molecular imaging and disease diagnosis.* Chem Rev, 2010. **110**(5): p. 3087-111.

183. Boohaker, R.J., M.W. Lee, P. Vishnubhotla, et al., *The Use of Therapeutic Peptides to Target and to Kill Cancer Cells.* Current medicinal chemistry, 2012. **19**(22): p. 3794-3804.

184. Fields, G.B. and R.L. Noble, *Solid phase peptide synthesis utilizing 9-fluorenylmethoxycarbonyl amino acids.* Int J Pept Protein Res, 1990. **35**(3): p. 161-214.

185. Zhang, W.-J., Y.-X. Sui, A. Budha, et al., *Affinity peptide developed by phage display selection for targeting gastric cancer.* World Journal of Gastroenterology : WJG, 2012. **18**(17): p. 2053-2060.

186. Zou, X., C. Chen, X. Huang, et al., *Phage-free peptide ELISA for ochratoxin A detection based on biotinylated mimotope as a competing antigen.* Talanta, 2016. **146**: p. 394-400.

187. Lin, Y., R. Weissleder, and C.H. Tung, *Novel near-infrared cyanine fluorochromes: synthesis, properties, and bioconjugation.* Bioconjug Chem, 2002. **13**(3): p. 605-10.

188. Ballou, B., G.W. Fisher, T.R. Hakala, et al., *Tumor detection and visualization using cyanine fluorochrome-labeled antibodies.* Biotechnol Prog, 1997. **13**(5): p. 649-58.

189. Zhang, H., *Cy5.5-CGRRRQRRKKRG-Labeled T lymphocytes*, in *Molecular Imaging and Contrast Agent Database (MICAD)*2004: Bethesda (MD).

190. Liu, Z., S.J. Miller, B.P. Joshi, et al., *In vivo targeting of colonic dysplasia on fluorescence endoscopy with near-infrared octapeptide.* Gut, 2013. **62**(3): p. 395-403.

191. Ayers, G.D., E.T. McKinley, P. Zhao, et al., *Volume of preclinical xenograft tumors is more accurately assessed by ultrasound imaging than manual caliper measurements.* J Ultrasound Med, 2010. **29**(6): p. 891-901.

192. Graham, K.C., L.A. Wirtzfeld, L.T. MacKenzie, et al., *Three-dimensional high-frequency ultrasound imaging for longitudinal evaluation of liver metastases in preclinical models.* Cancer Research, 2005. **65**(12): p. 5231-5237.

193. Graham, K.C., L.A. Wirtzfeld, L.T. MacKenzie, et al., *Three-dimensional high-frequency ultrasound imaging for longitudinal evaluation of liver metastases in preclinical models.* Cancer Res, 2005. **65**(12): p. 5231-7.

194. Wong, B.W., J.M. Luk, I.O. Ng, et al., *Identification of liver–intestine cadherin in hepatocellular carcinoma—a potential disease marker.* Biochemical and biophysical research communications, 2003. **311**(3): p. 618-624.

195. Mims III, F.M., *Alexander Graham Bell and the Photophone: The Centennial of the Invention of Light-Wave Communications, 1880–1980.* Optics News, 1980. **6**(1): p. 8-16.

196. Wickramasinghe, H., R. Bray, V. Jipson, et al., *Photoacoustics on a microscopic scale.* Applied Physics Letters, 1978. **33**(11): p. 923-925.

197. Tam, A.C., *Applications of photoacoustic sensing techniques.* Reviews of Modern Physics, 1986. **58**(2): p. 381.

198. Wang, L., *Photo acoustic tomography.* Scholarpedia, 2014. **9**(2): p. 10278.

199. Kruger, R., D. Reinecke, G. Kruger, et al. *HYPR-spectral photoacoustic CT for preclinical imaging.* in *SPIE BiOS: Biomedical Optics.* 2009. Bellingham, WA International Society for Optics and Photonics.

200. Albensi, B.C., E.V. Ilkanich, G. Dini, et al., *Elements of scientific visualization in basic neuroscience research.* BioScience, 2004. **54**(12): p. 1127-1137.

201. Khalil, M.M., J.L. Tremoleda, T.B. Bayomy, et al., *Molecular SPECT Imaging: An Overview.* Int J Mol Imaging, 2011. **2011**: p. 796025.

202. Xu, M. and L.V. Wang, *Photoacoustic imaging in biomedicine.* Review of scientific instruments, 2006. **77**(4): p. 041101.

203. Xia, J., J. Yao, and L.V. Wang, *Photoacoustic tomography: principles and advances.* Electromagnetic waves (Cambridge, Mass.), 2014. **147**: p. 1.

204. Wang, L.V. and S. Hu, *Photoacoustic tomography: in vivo imaging from organelles to organs.* Science, 2012. **335**(6075): p. 1458-1462.

205. Xu, X., H. Liu, and L.V. Wang, *Time-reversed ultrasonically encoded optical focusing into scattering media.* Nature photonics, 2011. **5**(3): p. 154-157.

206. Judkewitz, B., Y.M. Wang, R. Horstmeyer, et al., *Speckle-scale focusing in the diffusive regime with time reversal of variance-encoded light (TROVE).* Nature photonics, 2013. **7**(4): p. 300-305.

207. Kratzer, W., V. Fritz, R.A. Mason, et al., *Factors affecting liver size: a sonographic survey of 2080 subjects.* J Ultrasound Med, 2003. **22**(11): p. 1155-61.

208. Hall, A., C. Elcombe, J. Foster, et al., *Liver hypertrophy: a review of adaptive (adverse and non-adverse) changes—conclusions from the 3rd International ESTP Expert Workshop.* Toxicologic pathology, 2012. **40**(7): p. 971-994.

209. Beard, P., *Biomedical photoacoustic imaging.* Interface focus, 2011. **1**(4): p. 602-631.

210. Zhang, H.F., K. Maslov, G. Stoica, et al., *Functional photoacoustic microscopy for high-resolution and noninvasive in vivo imaging.* Nat Biotechnol, 2006. **24**(7): p. 848-51.

211. Wang, Y., X. Xie, X. Wang, et al., *Photoacoustic tomography of a nanoshell contrast agent in the in vivo rat brain.* Nano Lett, 2004. **4**(9): p. 1689-1692.

212. Zhang, Q., N. Iwakuma, P. Sharma, et al., *Gold nanoparticles as a contrast agent for in vivo tumor imaging with photoacoustic tomography.* Nanotechnology, 2009. **20**(39): p. 395102.

213. Maeda, H., J. Wu, T. Sawa, et al., *Tumor vascular permeability and the EPR effect in macromolecular therapeutics: a review.* J Control Release, 2000. **65**(1-2): p. 271-84.

214. Kobayashi, H., R. Watanabe, and P.L. Choyke, *Improving conventional enhanced permeability and retention (EPR) effects; what is the appropriate target?* Theranostics, 2014. **4**(1): p. 81.

215. Jain, P.K., K.S. Lee, I.H. El-Sayed, et al., *Calculated absorption and scattering properties of gold nanoparticles of different size, shape, and composition: applications in biological imaging and biomedicine.* The Journal of Physical Chemistry B, 2006. **110**(14): p. 7238-7248.

216. Murahari, M.S. and M.C. Yergeri, *Identification and usage of fluorescent probes as nanoparticle contrast agents in detecting cancer.* Current pharmaceutical design, 2013. **19**(25): p. 4622-4640.

217.   Alford, R., H.M. Simpson, J. Duberman, et al., *Toxicity of organic fluorophores used in molecular imaging: literature review.* Molecular Imaging, 2009. **8**(6): p. 341.

218.   Yoo, J.-W., E. Chambers, and S. Mitragotri, *Factors that control the circulation time of nanoparticles in blood: challenges, solutions and future prospects.* Current pharmaceutical design, 2010. **16**(21): p. 2298-2307.

219.   Kirtane, A.R., *STRATEGIES TO IMPROVE PLASMA CIRCULATION OF NANOPARTICLES.* 2014.

220.   Choi, H.S., W. Liu, P. Misra, et al., *Renal clearance of quantum dots.* Nature Biotechnology, 2007. **25**(10): p. 1165-1170.

221.   Yu, M. and J. Zheng, *Clearance pathways and tumor targeting of imaging nanoparticles.* ACS nano, 2015. **9**(7): p. 6655-6674.

222.   Yang, L., H. Mao, Y.A. Wang, et al., *Single chain epidermal growth factor receptor antibody conjugated nanoparticles for in vivo tumor targeting and imaging.* Small, 2009. **5**(2): p. 235-243.

223.   Cao, H.S.T., S. Kaushal, C.A. Metildi, et al., *Tumor-Specific Fluorescent Antibody Imaging Enables Accurate Staging Laparoscopy in an Orthotopic Model of Pancreatic Cancer.* Hepatogastroenterology, 2012. **59**(118): p. 1994.

224.   Iyer, A.K., G. Khaled, J. Fang, et al., *Exploiting the enhanced permeability and retention effect for tumor targeting.* Drug Discov Today, 2006. **11**(17-18): p. 812-8.

225.   Zanganeh, S., H. Li, P.D. Kumavor, et al., *Photoacoustic imaging enhanced by indocyanine green-conjugated single-wall carbon nanotubes.* Journal of biomedical optics, 2013. **18**(9): p. 096006-096006.

226.   Fransvea, E., A. Paradiso, S. Antonaci, et al., *HCC heterogeneity: molecular pathogenesis and clinical implications.* Analytical Cellular Pathology, 2009. **31**(3): p. 227-233.

227.   Yamashita, T., J. Ji, A. Budhu, et al., *EpCAM-positive hepatocellular carcinoma cells are tumor-initiating cells with stem/progenitor cell features.* Gastroenterology, 2009. **136**(3): p. 1012-1024. e4.

228.   Huynh, H., K. Pierce Chow, K.C. Soo, et al., *RAD001 (everolimus) inhibits tumour growth in xenograft models of human hepatocellular carcinoma.* Journal of cellular and molecular medicine, 2009. **13**(7): p. 1371-1380.

229.   Marangoni, E., A. Vincent-Salomon, N. Auger, et al., *A new model of patient tumor-derived breast cancer xenografts for preclinical assays.* Clinical Cancer Research, 2007. **13**(13): p. 3989-3998.

230.   Dong, X., J. Guan, J.C. English, et al., *Patient-Derived First Generation Xenografts of Non–Small Cell Lung Cancers: Promising Tools for Predicting Drug Responses for Personalized Chemotherapy.* Clinical Cancer Research, 2010. **16**(5): p. 1442-1451.

231.   Tentler, J.J., A.C. Tan, C.D. Weekes, et al., *Patient-derived tumour xenografts as models for oncology drug development.* Nature reviews Clinical oncology, 2012. **9**(6): p. 338-350.

232.   Huynh, H., K.C. Soo, P.K. Chow, et al., *Xenografts of human hepatocellular carcinoma: a useful model for testing drugs.* Clinical Cancer Research, 2006. **12**(14): p. 4306-4314.

233.   Huynh, H., V.C. Ngo, J. Fargnoli, et al., *Brivanib alaninate, a dual inhibitor of vascular endothelial growth factor receptor and fibroblast growth factor receptor tyrosine kinases, induces growth inhibition in mouse models of human hepatocellular carcinoma.* Clinical Cancer Research, 2008. **14**(19): p. 6146-6153.

234. Huynh, H., V.C. Ngo, H.N. Koong, et al., *AZD6244 enhances the anti-tumor activity of sorafenib in ectopic and orthotopic models of human hepatocellular carcinoma (HCC).* J Hepatol, 2010. **52**(1): p. 79-87.

235. Marquardt, J.U., P.R. Galle, and A. Teufel, *Molecular diagnosis and therapy of hepatocellular carcinoma (HCC): An emerging field for advanced technologies.* Journal of Hepatology, 2012. **56**(1): p. 267-275.

236. Kadimisetty, K., S. Malla, N.P. Sardesai, et al., *Automated Multiplexed ECL Immunoarrays for Cancer Biomarker Proteins.* Analytical Chemistry, 2015. **87**(8): p. 4472-4478.

237. Zhu, K., Z. Dai, and J. Zhou, *Biomarkers for hepatocellular carcinoma: progression in early diagnosis, prognosis, and personalized therapy.* Biomarker Research, 2013. **1**(1): p. 10.

238. De la Zerda, A., C. Zavaleta, S. Keren, et al., *Carbon nanotubes as photoacoustic molecular imaging agents in living mice.* Nat Nanotechnol, 2008. **3**(9): p. 557-62.

239. Bouchard, L.-S., M.S. Anwar, G.L. Liu, et al., *Picomolar sensitivity MRI and photoacoustic imaging of cobalt nanoparticles.* Proceedings of the National Academy of Sciences, 2009. **106**(11): p. 4085-4089.

240. de la Zerda, A., S. Bodapati, R. Teed, et al., *Family of enhanced photoacoustic imaging agents for high-sensitivity and multiplexing studies in living mice.* ACS Nano, 2012. **6**(6): p. 4694-4701.

241. Ueda, T., M. Honda, K. Horimoto, et al., *Gene expression profiling of hepatitis B- and hepatitis C-related hepatocellular carcinoma using graphical Gaussian modeling (vol 101, pg 238, 2013).* Genomics, 2013. **101**(6): p. 376-376.

242. Roessler, S., E.L. Long, A. Budhu, et al., *Integrative genomic identification of genes on 8p associated with hepatocellular carcinoma progression and patient survival.* Gastroenterology, 2012. **142**(4): p. 957-966 e12.

243. Roessler, S., H.L. Jia, A. Budhu, et al., *A unique metastasis gene signature enables prediction of tumor relapse in early-stage hepatocellular carcinoma patients.* Cancer Res, 2010. **70**(24): p. 10202-12.

244. Ho, M. and H. Kim, *Glypican-3: a new target for cancer immunotherapy.* European journal of cancer (Oxford, England : 1990), 2011. **47**(3): p. 333-338.

245. Ofuji, K., K. Saito, T. Yoshikawa, et al., *Critical analysis of the potential of targeting GPC3 in hepatocellular carcinoma.* Journal of Hepatocellular Carcinoma, 2014. **1**: p. 35-42.

246. Wang, L., M. Yao, L.H. Pan, et al., *Glypican-3 is a biomarker and a therapeutic target of hepatocellular carcinoma.* Hepatobiliary Pancreat Dis Int, 2015. **14**(4): p. 361-6.

247. Filmus, J., M. Capurro, and J. Rast, *Glypicans.* Genome Biol, 2008. **9**(5): p. 224.

248. Haruyama, Y. and H. Kataoka, *Glypican-3 is a prognostic factor and an immunotherapeutic target in hepatocellular carcinoma.* World J Gastroenterol, 2016. **22**(1): p. 275-83.

249. Xu, C., Z. Yan, L. Zhou, et al., *A comparison of glypican-3 with alpha-fetoprotein as a serum marker for hepatocellular carcinoma: a meta-analysis.* J Cancer Res Clin Oncol, 2013. **139**(8): p. 1417-24.

250. Taketa, K., *Alpha-fetoprotein: reevaluation in hepatology.* Hepatology, 1990. **12**(6): p. 1420-32.

251. Johnson, P.J., *The role of serum alpha-fetoprotein estimation in the diagnosis and management of hepatocellular carcinoma.* Clin Liver Dis, 2001. **5**(1): p. 145-59.

252. Collier, J. and M. Sherman, *Significance of elevated alpha-fetoprotein in the absence of hepatocellular carcinoma in chronic viral hepatitis.* Viral Hepatitis Reviews, 1998. **4**(1): p. 31-41.

253. Ho, M., *Advances in Liver Cancer Antibody Therapies.* BioDrugs, 2011. **25**(5): p. 275-284.

254. Yasuda, E., T. Kumada, H. Toyoda, et al., *Evaluation for clinical utility of GPC3, measured by a commercially available ELISA kit with Glypican‑3 (GPC3) antibody, as a serological and histological marker for hepatocellular carcinoma.* Hepatology Research, 2010. **40**(5): p. 477-485.

255. Yamauchi, N., A. Watanabe, M. Hishinuma, et al., *The glypican 3 oncofetal protein is a promising diagnostic marker for hepatocellular carcinoma.* Mod Pathol, 2005. **18**(12): p. 1591-8.

256. Wang, X.Y., F. Degos, S. Dubois, et al., *Glypican-3 expression in hepatocellular tumors: diagnostic value for preneoplastic lesions and hepatocellular carcinomas.* Hum Pathol, 2006. **37**(11): p. 1435-41.

257. Shirakawa, H., T. Kuronuma, Y. Nishimura, et al., *Glypican-3 is a useful diagnostic marker for a component of hepatocellular carcinoma in human liver cancer.* Int J Oncol, 2009. **34**(3): p. 649-56.

258. Midorikawa, Y., S. Ishikawa, H. Iwanari, et al., *Glypican-3, overexpressed in hepatocellular carcinoma, modulates FGF2 and BMP-7 signaling.* Int J Cancer, 2003. **103**(4): p. 455-65.

259. Liu, X., S.K. Wang, K. Zhang, et al., *Expression of glypican 3 enriches hepatocellular carcinoma development-related genes and associates with carcinogenesis in cirrhotic livers.* Carcinogenesis, 2015. **36**(2): p. 232-42.

260. Ho, M. and H. Kim, *Glypican-3: a new target for cancer immunotherapy.* Eur J Cancer, 2011. **47**(3): p. 333-8.

261. Feng, M. and M. Ho, *Glypican-3 antibodies: a new therapeutic target for liver cancer.* FEBS Lett, 2014. **588**(2): p. 377-82.

262. Song, H.H., W. Shi, Y.Y. Xiang, et al., *The loss of glypican-3 induces alterations in wnt signaling.* Journal of Biological Chemistry, 2005. **280**(3): p. 2116-2125.

263. Capurro, M.I., Y.Y. Xiang, C. Lobe, et al., *Glypican-3 promotes the growth of hepatocellular carcinoma by stimulating canonical Wnt signaling.* Cancer Res, 2005. **65**(14): p. 6245-54.

264. Song, H.H., W. Shi, and J. Filmus, *OCI-5/rat glypican-3 binds to fibroblast growth factor-2 but not to insulin-like growth factor-2.* Journal of Biological Chemistry, 1997. **272**(12): p. 7574-7577.

265. Gao, W., H. Kim, M. Feng, et al., *Inactivation of Wnt signaling by a human antibody that recognizes the heparan sulfate chains of glypican-3 for liver cancer therapy.* Hepatology, 2014. **60**(2): p. 576-87.

266. Miao, H.L., Z.J. Pan, C.J. Lei, et al., *Knockdown of GPC3 inhibits the proliferation of Huh7 hepatocellular carcinoma cells through down‑regulation of YAP.* Journal of cellular biochemistry, 2013. **114**(3): p. 625-631.

267. Capurro, M., T. Martin, W. Shi, et al., *Glypican-3 binds to Frizzled and plays a direct role in the stimulation of canonical Wnt signaling.* J Cell Sci, 2014. **127**(Pt 7): p. 1565-75.

268. Allegretta, M. and J. Filmus, *Therapeutic potential of targeting glypican-3 in hepatocellular carcinoma.* Anti-Cancer Agents in Medicinal Chemistry (Formerly Current Medicinal Chemistry-Anti-Cancer Agents), 2011. **11**(6): p. 543-548.

269. Xue, R., J. Feng, Q. Meng, et al., *The Significance of Glypican‐3 Expression Profiling in the Tumor Cellular Origin Theoretical System for Hepatocellular Carcinoma Progression.* Journal of gastroenterology and hepatology, 2017.

270. Feng, J., R. Zhu, C. Chang, et al., *CK19 and glypican 3 expression profiling in the prognostic indication for patients with HCC after surgical resection.* PloS one, 2016. **11**(3): p. e0151501.

271. Zittermann, S.I., M.I. Capurro, W. Shi, et al., *Soluble glypican 3 inhibits the growth of hepatocellular carcinoma in vitro and in vivo.* Int J Cancer, 2010. **126**(6): p. 1291-301.

272. Feng, M., W. Gao, R. Wang, et al., *Therapeutically targeting glypican-3 via a conformation-specific single-domain antibody in hepatocellular carcinoma.* Proc Natl Acad Sci U S A, 2013. **110**(12): p. E1083-91.

273. Sharma, S., *Tumor markers in clinical practice: General principles and guidelines.* Indian Journal of Medical and Paediatric Oncology : Official Journal of Indian Society of Medical & Paediatric Oncology, 2009. **30**(1): p. 1-8.

274. Kaur, S., M.J. Baine, M. Jain, et al., *Early diagnosis of pancreatic cancer: challenges and new developments.* Biomarkers in medicine, 2012. **6**(5): p. 597-612.

275. Das, P.M. and R.C. Bast, *Early detection of ovarian cancer.* Biomarkers in medicine, 2008. **2**(3): p. 291-303.

276. Lin, C.L. and J.H. Kao, *Risk stratification for hepatitis B virus related hepatocellular carcinoma.* J Gastroenterol Hepatol, 2013. **28**(1): p. 10-7.

277. Di Bisceglie, A.M., *Hepatitis B And Hepatocellular Carcinoma.* Hepatology (Baltimore, Md.), 2009. **49**(5 Suppl): p. S56-S60.

278. El-Serag, H.B., *Epidemiology of Viral Hepatitis and Hepatocellular Carcinoma.* Gastroenterology, 2012. **142**(6): p. 1264-1273.e1.

279. Wang, F.H., Y.C. Yip, M. Zhang, et al., *Diagnostic utility of glypican-3 for hepatocellular carcinoma on liver needle biopsy.* Journal of Clinical Pathology, 2010. **63**(7): p. 599-603.

280. Wang, F.M., X. Jing, T. Wang, et al., *Differential Diagnostic Value of GPC3-CD34 Combined Staining in Small Liver Nodules With Diameter Less Than 3 cm.* American Journal of Clinical Pathology, 2012. **137**(6): p. 937-945.

281. Zhang, L.J., H. Liu, L. Sun, et al., *Glypican-3 as a potential differential diagnosis marker for hepatocellular carcinoma: A tissue microarray-based study.* Acta Histochemica, 2012. **114**(6): p. 547-552.

282. Witjes, C.D.M., F.J.W. ten Kate, C. Verhoef, et al., *Immunohistochemical characteristics of hepatocellular carcinoma in non-cirrhotic livers.* Journal of Clinical Pathology, 2013. **66**(8): p. 687-691.

283. Libbrecht, L., T. Severi, D. Cassiman, et al., *Glypican-3 expression distinguishes small hepatocellular carcinomas from cirrhosis, dysplastic nodules, and focal nodular hyperplasia-like nodules.* American Journal of Surgical Pathology, 2006. **30**(11): p. 1405-1411.

284. Yang, X., H. Liu, C.K. Sun, et al., *Imaging of hepatocellular carcinoma patient-derived xenografts using (8)(9)Zr-labeled anti-glypican-3 monoclonal antibody.* Biomaterials, 2014. **35**(25): p. 6964-71.

285. Sham, J.G., F.M. Kievit, J.R. Grierson, et al., *Glypican-3-targeting F(ab')2 for 89Zr PET of hepatocellular carcinoma.* J Nucl Med, 2014. **55**(12): p. 2032-7.

286. Gao, H., K. Li, H. Tu, et al., *Development of T cells redirected to glypican-3 for the treatment of hepatocellular carcinoma.* Clinical Cancer Research, 2014. **20**(24): p. 6418-6428.

287. Sham, J.G., F.M. Kievit, J.R. Grierson, et al., *Glypican-3–Targeted (89)Zr PET Imaging of Hepatocellular Carcinoma.* Journal of nuclear medicine : official publication, Society of Nuclear Medicine, 2014. **55**(5): p. 799-804.

288. Hernandez, R., H. Sun, C.G. England, et al., *CD146-targeted immunoPET and NIRF Imaging of Hepatocellular Carcinoma with a Dual-Labeled Monoclonal Antibody.* Theranostics, 2016. **6**(11): p. 1918-1933.

289. Sham, J.G., F.M. Kievit, J.R. Grierson, et al., *Glypican-3-targeted 89Zr PET imaging of hepatocellular carcinoma.* J Nucl Med, 2014. **55**(5): p. 799-804.

290. Li, M., C.P. Anastassiades, B. Joshi, et al., *Affinity peptide for targeted detection of dysplasia in Barrett's esophagus.* Gastroenterology, 2010. **139**(5): p. 1472-80.

291. Singh, A., S. Poshtiban, and S. Evoy, *Recent advances in bacteriophage based biosensors for food-borne pathogen detection.* Sensors, 2013. **13**(2): p. 1763-1786.

292. Colombo, G., F. Curnis, G.M.S. De Mori, et al., *Structure-Activity Relationships of Linear and Cyclic Peptides Containing the NGR Tumor-homing Motif.* Journal of Biological Chemistry, 2002. **277**(49): p. 47891-47897.

293. Fuh, G. and S.S. Sidhu, *Efficient phage display of polypeptides fused to the carboxy-terminus of the M13 gene-3 minor coat protein.* FEBS Letters, 2000. **480**(2): p. 231-234.

294. Kügler, J., J. Zantow, T. Meyer, et al., *Oligopeptide M13 Phage Display in Pathogen Research.* Viruses, 2013. **5**(10): p. 2531-2545.

295. Luzzago, A., F. Felici, A. Tramontano, et al., *Mimicking of discontinuous epitopes by phage-displayed peptides, I. Epitope mapping of human H ferritin using a phage library of constrained peptides.* Gene, 1993. **128**(1): p. 51-57.

296. Hoess, R.H., A.J. Mack, H. Walton, et al., *Identification of a structural epitope by using a peptide library displayed on filamentous bacteriophage.* The Journal of Immunology, 1994. **153**(2): p. 724-729.

297. Wrighton, N.C., F.X. Farrell, R. Chang, et al., *Small peptides as potent mimetics of the protein hormone erythropoietin.* Science, 1996. **273**(5274): p. 458-64.

298. Brenner, S. and A. Stretton, *The amber mutation.* Journal of cellular physiology, 1964. **64**(S1): p. 43-49.

299. Lin, A., J. Jimenez, J. Derr, et al., *Inhibition of bacterial conjugation by phage M13 and its protein g3p: quantitative analysis and model.* PloS one, 2011. **6**(5): p. e19991.

300. Bae, Y.H. and K. Park, *Targeted drug delivery to tumors: Myths, reality and possibility.* Journal of Controlled Release, 2011. **153**(3): p. 198-205.

301. Alexander-Bryant, A.A., W.S. Vanden Berg-Foels, and X. Wen, *Bioengineering Strategies for Designing Targeted Cancer Therapies.* Advances in cancer research, 2013. **118**: p. 1-59.

302. Bogart, L.K., G. Pourroy, C.J. Murphy, et al., *Nanoparticles for imaging, sensing, and therapeutic intervention*, 2014, ACS Publications.

303. Mallidi, S., S. Kim, A. Karpiouk, et al., *Visualization of molecular composition and functionality of cancer cells using nanoparticle-augmented ultrasound-guided photoacoustics.* Photoacoustics, 2015. **3**(1): p. 26-34.

304. Sokolov, K., M. Follen, J. Aaron, et al., *Real-time vital optical imaging of precancer using anti-epidermal growth factor receptor antibodies conjugated to gold nanoparticles.* Cancer research, 2003. **63**(9): p. 1999-2004.

305. Di Tommaso, L., G. Franchi, Y.N. Park, et al., *Diagnostic value of HSP70, glypican 3, and glutamine synthetase in hepatocellular nodules in cirrhosis.* Hepatology, 2007. **45**(3): p. 725-734.

306. Di Tommaso, L., A. Destro, J.Y. Seok, et al., *The application of markers (HSP70 GPC3 and GS) in liver biopsies is useful for detection of hepatocellular carcinoma.* Journal of hepatology, 2009. **50**(4): p. 746-754.

307. Tremosini, S., A. Forner, L. Boix, et al., *Prospective validation of an immunohistochemical panel (glypican 3, heat shock protein 70 and glutamine synthetase) in liver biopsies for diagnosis of very early hepatocellular carcinoma.* Gut, 2012. **61**(10): p. 1481-1487.

308. Di Tommaso, L., G. Franchi, Y.N. Park, et al., *Diagnostic value of HSP70, glypican 3, and glutamine synthetase in hepatocellular nodules in cirrhosis.* Hepatology, 2007. **45**(3): p. 725-734.

309. Marrero, J.A., *Modern diagnosis of hepatocellular carcinoma: Utilization of liver biopsy and genomic markers.* Journal of Hepatology, 2009. **50**(4): p. 659-661.

310. Di Tommaso, L., A. Destro, J.Y. Seok, et al., *The application of markers (HSP70 GPC3 and GS) in liver biopsies is useful for detection of hepatocellular carcinoma.* Journal of Hepatology, 2009. **50**(4): p. 746-754.

311. Tremosini, S., A. Forner, L. Boix, et al., *Prospective validation of an immunohistochemical panel (glypican 3, heat shock protein 70 and glutamine synthetase) in liver biopsies for diagnosis of very early hepatocellular carcinoma.* Gut, 2012. **61**(10): p. 1481-1487.

312. Li, W. and X. Chen, *Gold nanoparticles for photoacoustic imaging.* Nanomedicine (London, England), 2015. **10**(2): p. 299-320.

313. Cheng, Z., X. Yan, X. Sun, et al., *Tumor Molecular Imaging with Nanoparticles.* Engineering, 2016. **2**(1): p. 132-140.

314. Ho, C.J.H., N.C. Burton, S. Morscher, et al., *Advances in Optoacoustic Imaging: From Benchside to Clinic*, in *Frontiers in Biophotonics for Translational Medicine* 2016, Springer. p. 75-109.

315. Shah, A.J., E.J. Alles, C. Box, et al. *Non-invasive molecular profiling of cancer using photoacoustic imaging of functionalized gold nanorods*. in *SPIE BiOS*. 2014. International Society for Optics and Photonics.

316. Bayer, C.L., Y.-S. Chen, S. Kim, et al., *Multiplex photoacoustic molecular imaging using targeted silica-coated gold nanorods.* Biomedical optics express, 2011. **2**(7): p. 1828-1835.

317. Homan, K.A., M. Souza, R. Truby, et al., *Silver nanoplate contrast agents for in vivo molecular photoacoustic imaging.* ACS nano, 2012. **6**(1): p. 641-650.

318. Luke, G.P., D. Yeager, and S.Y. Emelianov, *Biomedical applications of photoacoustic imaging with exogenous contrast agents.* Annals of biomedical engineering, 2012. **40**(2): p. 422-437.

319. Wang, S., P. Huang, L. Nie, et al., *Single Continuous Wave Laser Induced Photodynamic/Plasmonic Photothermal Therapy Using Photosensitizer‐Functionalized Gold Nanostars.* Advanced materials, 2013. **25**(22): p. 3055-3061.

320. Rodríguez-Lorenzo, L., R. de La Rica, R.A. Álvarez-Puebla, et al., *Plasmonic nanosensors with inverse sensitivity by means of enzyme-guided crystal growth.* Nature materials, 2012. **11**(7): p. 604-607.

321. Kim, C., H.-M. Song, X. Cai, et al., *In vivo photoacoustic mapping of lymphatic systems with plasmon-resonant nanostars.* Journal of materials chemistry, 2011. **21**(9): p. 2841-2844.

322. Oldenburg, S.J., J.B. Jackson, S.L. Westcott, et al., *Infrared extinction properties of gold nanoshells.* Applied Physics Letters, 1999. **75**(19): p. 2897-2899.

323. Weber, V., A. Feis, C. Gellini, et al., *Far-and near-field properties of gold nanoshells studied by photoacoustic and surface-enhanced Raman spectroscopies.* Physical Chemistry Chemical Physics, 2015. **17**(33): p. 21190-21197.

324. Oldenburg, S., R. Averitt, S. Westcott, et al., *Nanoengineering of optical resonances.* Chemical Physics Letters, 1998. **288**(2): p. 243-247.

325. Kalele, S., S.W. Gosavi, J. Urban, et al., *Nanoshell particles: synthesis, properties and applications.* Current Science, 2006. **91**(8): p. 1038-1052.

326. Xiang, L., D. Xing, H. Gu, et al. *Gold nanoshell-based photoacoustic imaging application in biomedicine.* in *2006 International Symposium on Biophotonics, Nanophotonics and Metamaterials.* 2006. IEEE.

327. Loo, C., A. Lowery, N. Halas, et al., *Immunotargeted nanoshells for integrated cancer imaging and therapy.* Nano letters, 2005. **5**(4): p. 709-711.

328. Chen, J., F. Saeki, B.J. Wiley, et al., *Gold nanocages: bioconjugation and their potential use as optical imaging contrast agents.* Nano letters, 2005. **5**(3): p. 473-477.

329. Kim, C., E.C. Cho, J. Chen, et al., *In vivo molecular photoacoustic tomography of melanomas targeted by bioconjugated gold nanocages.* ACS Nano, 2010. **4**(8): p. 4559-64.

330. Hirsch, L.R., R. Stafford, J. Bankson, et al., *Nanoshell-mediated near-infrared thermal therapy of tumors under magnetic resonance guidance.* Proceedings of the National Academy of Sciences, 2003. **100**(23): p. 13549-13554.

331. Wang, Y., X. Xie, X. Wang, et al., *Photoacoustic tomography of a nanoshell contrast agent in the in vivo rat brain.* Nano Letters, 2004. **4**(9): p. 1689-1692.

332. Yavuz, M.S., Y. Cheng, J. Chen, et al., *Gold nanocages covered by smart polymers for controlled release with near-infrared light.* Nat Mater, 2009. **8**(12): p. 935-9.

333. Hirsch, L., J. Jackson, A. Lee, et al., *A whole blood immunoassay using gold nanoshells.* Analytical Chemistry, 2003. **75**(10): p. 2377-2381.

334. Khlebtsov, B. and N. Khlebtsov, *Enhanced solid-phase immunoassay using gold nanoshells: effect of nanoparticle optical properties.* Nanotechnology, 2008. **19**(43): p. 435703.

335. Gobin, A.M., M.H. Lee, N.J. Halas, et al., *Near-infrared resonant nanoshells for combined optical imaging and photothermal cancer therapy.* Nano letters, 2007. **7**(7): p. 1929-1934.

336. Fan, X., W. Zheng, and D.J. Singh, *Light scattering and surface plasmons on small spherical particles.* arXiv preprint arXiv:1407.2345, 2014.

337. Huang, X. and M.A. El-Sayed, *Gold nanoparticles: Optical properties and implementations in cancer diagnosis and photothermal therapy.* Journal of Advanced Research, 2010. **1**(1): p. 13-28.

338. Hu, M., J. Chen, Z.-Y. Li, et al., *Gold nanostructures: engineering their plasmonic properties for biomedical applications.* Chemical Society Reviews, 2006. **35**(11): p. 1084-1094.

339. Lal, S., N.K. Grady, G.P. Goodrich, et al., *Profiling the near field of a plasmonic nanoparticle with Raman-based molecular rulers.* Nano letters, 2006. **6**(10): p. 2338-2343.

340. Chen, J., B. Wiley, Z.Y. Li, et al., *Gold nanocages: engineering their structure for biomedical applications.* Advanced Materials, 2005. **17**(18): p. 2255-2261.

341. Gao, J., X. Huang, H. Liu, et al., *Colloidal stability of gold nanoparticles modified with thiol compounds: bioconjugation and application in cancer cell imaging.* Langmuir, 2012. **28**(9): p. 4464-4471.

342. Jazayeri, M.H., H. Amani, A.A. Pourfatollah, et al., *Various methods of gold nanoparticles (GNPs) conjugation to antibodies.* Sensing and Bio-Sensing Research, 2016. **9**: p. 17-22.

343. Yeh, Y.C., B. Creran, and V.M. Rotello, *Gold nanoparticles: preparation, properties, and applications in bionanotechnology.* Nanoscale, 2012. **4**(6): p. 1871-80.

344. Saha, K., S.S. Agasti, C. Kim, et al., *Gold nanoparticles in chemical and biological sensing.* Chem Rev, 2012. **112**(5): p. 2739-79.

345. Radwan, S.H. and H.M. Azzazy, *Gold nanoparticles for molecular diagnostics.* Expert Rev Mol Diagn, 2009. **9**(5): p. 511-24.

346. Dykman, L. and N. Khlebtsov, *Gold nanoparticles in biomedical applications: recent advances and perspectives.* Chem Soc Rev, 2012. **41**(6): p. 2256-82.

347. Doane, T.L. and C. Burda, *The unique role of nanoparticles in nanomedicine: imaging, drug delivery and therapy.* Chem Soc Rev, 2012. **41**(7): p. 2885-911.

348. Giljohann, D.A., D.S. Seferos, W.L. Daniel, et al., *Gold nanoparticles for biology and medicine.* Angew Chem Int Ed Engl, 2010. **49**(19): p. 3280-94.

349. Llevot, A. and D. Astruc, *Applications of vectorized gold nanoparticles to the diagnosis and therapy of cancer.* Chem Soc Rev, 2012. **41**(1): p. 242-57.

350. Choi, Y.E., J.W. Kwak, and J.W. Park, *Nanotechnology for early cancer detection.* Sensors (Basel), 2010. **10**(1): p. 428-55.

351. Rana, S., A. Bajaj, R. Mout, et al., *Monolayer coated gold nanoparticles for delivery applications.* Adv Drug Deliv Rev, 2012. **64**(2): p. 200-16.

352. Niemeyer, C.M., *Nanoparticles, proteins, and nucleic acids: biotechnology meets materials science.* Angewandte Chemie International Edition, 2001. **40**(22): p. 4128-4158.

353. Li, X., J. Guo, J. Asong, et al., *Multifunctional surface modification of gold-stabilized nanoparticles by bioorthogonal reactions.* J Am Chem Soc, 2011. **133**(29): p. 11147-53.

354. Oh, E., K. Susumu, J.B. Blanco-Canosa, et al., *Preparation of stable maleimide-functionalized au nanoparticles and their use in counting surface ligands.* Small, 2010. **6**(12): p. 1273-8.

355. Ghann, W.E., O. Aras, T. Fleiter, et al., *Syntheses and characterization of lisinopril-coated gold nanoparticles as highly stable targeted CT contrast agents in cardiovascular diseases.* Langmuir, 2012. **28**(28): p. 10398-408.

356. Zhang, G., Z. Yang, W. Lu, et al., *Influence of anchoring ligands and particle size on the colloidal stability and in vivo biodistribution of polyethylene glycol-coated gold nanoparticles in tumor-xenografted mice.* Biomaterials, 2009. **30**(10): p. 1928-1936.

357.   Mitragotri, S., P.A. Burke, and R. Langer, *Overcoming the challenges in administering biopharmaceuticals: formulation and delivery strategies.* Nature reviews. Drug discovery, 2014. **13**(9): p. 655.

358.   Desai, N., *Challenges in development of nanoparticle-based therapeutics.* The AAPS journal, 2012. **14**(2): p. 282-295.

359.   Chen, J., Z. Guo, H. Tian, et al., *Production and clinical development of nanoparticles for gene delivery.* Molecular Therapy-Methods & Clinical Development, 2016. **3**: p. 16023.

360.   Gustafson, H.H., D. Holt-Casper, D.W. Grainger, et al., *Nanoparticle Uptake: The Phagocyte Problem.* Nano today, 2015. **10**(4): p. 487-510.

361.   Oh, N. and J.-H. Park, *Endocytosis and exocytosis of nanoparticles in mammalian cells.* International Journal of Nanomedicine, 2014. **9**(Suppl 1): p. 51-63.

362.   Kettiger, H., A. Schipanski, P. Wick, et al., *Engineered nanomaterial uptake and tissue distribution: from cell to organism.* International Journal of Nanomedicine, 2013. **8**: p. 3255-3269.

363.   Jokerst, J.V., T. Lobovkina, R.N. Zare, et al., *Nanoparticle PEGylation for imaging and therapy.* Nanomedicine (London, England), 2011. **6**(4): p. 715-728.

364.   Nissinen, T., S. Nakki, H. Laakso, et al., *Tailored dual PEGylation of inorganic porous nanocarriers for extremely long blood circulation in vivo.* ACS applied materials & interfaces, 2016. **8**(48): p. 32723-32731.

365.   Gref, R., A. Domb, P. Quellec, et al., *The controlled intravenous delivery of drugs using PEG-coated sterically stabilized nanospheres().* Advanced drug delivery reviews, 1995. **16**(2-3): p. 215-233.

366.   Liu, Y., Y. Hu, and L. Huang, *Influence of Polyethylene Glycol Density and Surface Lipid on Pharmacokinetics and Biodistribution of Lipid-Calcium-Phosphate Nanoparticles.* Biomaterials, 2014. **35**(9): p. 3027-3034.

367.   Albanese, A., P.S. Tang, and W.C. Chan, *The effect of nanoparticle size, shape, and surface chemistry on biological systems.* Annual review of biomedical engineering, 2012. **14**: p. 1-16.

368.   Peracchia, M.T., E. Fattal, D. Desmaele, et al., *Stealth (R) PEGylated polycyanoacrylate nanoparticles for intravenous administration and splenic targeting.* Journal of Controlled Release, 1999. **60**(1): p. 121-128.

369.   Etheridge, M.L., S.A. Campbell, A.G. Erdman, et al., *THE BIG PICTURE ON SMALL MEDICINE: THE STATE OF NANOMEDICINE PRODUCTS APPROVED FOR USE OR IN CLINICAL TRIALS.* Nanomedicine : nanotechnology, biology, and medicine, 2013. **9**(1): p. 1-14.

370.   Anselmo, A.C. and S. Mitragotri, *Nanoparticles in the clinic.* Bioengineering & Translational Medicine, 2016. **1**(1): p. 10-29.

371.   Fakruddin, M., Z. Hossain, and H. Afroz, *Prospects and applications of nanobiotechnology: a medical perspective.* Journal of Nanobiotechnology, 2012. **10**(1): p. 31.

372.   Ray, P.C., H. Yu, and P.P. Fu, *Toxicity and Environmental Risks of Nanomaterials: Challenges and Future Needs.* Journal of environmental science and health. Part C, Environmental carcinogenesis & ecotoxicology reviews, 2009. **27**(1): p. 1-35.

373.   Kong, B., J.H. Seog, L.M. Graham, et al., *Experimental considerations on the cytotoxicity of nanoparticles.* Nanomedicine (London, England), 2011. **6**(5): p. 929-941.

374. Stern, S.T. and S.E. McNeil, *Nanotechnology safety concerns revisited.* Toxicol Sci, 2008. **101**(1): p. 4-21.

375. Kong, B., J.H. Seog, L.M. Graham, et al., *Experimental considerations on the cytotoxicity of nanoparticles.* Nanomedicine (Lond), 2011. **6**(5): p. 929-41.

376. Anselmo, A.C. and S. Mitragotri, *Nanoparticles in the clinic.* Bioengineering & Translational Medicine, 2016.

377. Na, H.B., I.C. Song, and T. Hyeon, *Inorganic nanoparticles for MRI contrast agents.* Advanced materials, 2009. **21**(21): p. 2133-2148.

378. Laurent, S., D. Forge, M. Port, et al., *Magnetic iron oxide nanoparticles: synthesis, stabilization, vectorization, physicochemical characterizations, and biological applications.* Chemical reviews, 2008. **108**(6): p. 2064-2110.

379. Schutt, E.G., D.H. Klein, R.M. Mattrey, et al., *Injectable microbubbles as contrast agents for diagnostic ultrasound imaging: the key role of perfluorochemicals.* Angewandte Chemie International Edition, 2003. **42**(28): p. 3218-3235.

380. Klibanov, A.L., *Microbubble contrast agents: targeted ultrasound imaging and ultrasound-assisted drug-delivery applications.* Investigative radiology, 2006. **41**(3): p. 354-362.

381. Cardoso, M.M., I.N. Peca, and A.C. Roque, *Antibody-conjugated nanoparticles for therapeutic applications.* Curr Med Chem, 2012. **19**(19): p. 3103-27.

382. Stern, J.M., J. Stanfield, W. Kabbani, et al., *Selective prostate cancer thermal ablation with laser activated gold nanoshells.* The Journal of urology, 2008. **179**(2): p. 748-753.

383. O'Neal, D.P., L.R. Hirsch, N.J. Halas, et al., *Photo-thermal tumor ablation in mice using near infrared-absorbing nanoparticles.* Cancer letters, 2004. **209**(2): p. 171-176.

384. Xiao, Y., H. Hong, V.Z. Matson, et al., *Gold Nanorods Conjugated with Doxorubicin and cRGD for Combined Anticancer Drug Delivery and PET Imaging.* Theranostics, 2012. **2**(8): p. 757-68.

385. Kang, B., D. Yu, Y. Dai, et al., *Cancer-cell targeting and photoacoustic therapy using carbon nanotubes as "bomb" agents.* Small, 2009. **5**(11): p. 1292-301.

386. Ku, G., M. Zhou, S. Song, et al., *Copper sulfide nanoparticles as a new class of photoacoustic contrast agent for deep tissue imaging at 1064 nm.* ACS Nano, 2012. **6**(8): p. 7489-7496.

387. Yang, X., E.W. Stein, S. Ashkenazi, et al., *Nanoparticles for photoacoustic imaging.* Wiley Interdiscip Rev Nanomed Nanobiotechnol, 2009. **1**(4): p. 360-8.

388. Pu, K., A.J. Shuhendler, and J. Rao, *Semiconducting polymer nanoprobe for in vivo imaging of reactive oxygen and nitrogen species.* Angewandte Chemie International Edition, 2013. **52**(39): p. 10325-10329.

389. Pu, K., A.J. Shuhendler, J.V. Jokerst, et al., *Semiconducting polymer nanoparticles as photoacoustic molecular imaging probes in living mice.* Nature nanotechnology, 2014. **9**(3): p. 233-239.

390. Liu, J., J. Geng, L.-D. Liao, et al., *Conjugated polymer nanoparticles for photoacoustic vascular imaging.* Polymer Chemistry, 2014. **5**(8): p. 2854-2862.

391. Pu, K., J. Mei, J.V. Jokerst, et al., *Diketopyrrolopyrrole‐Based Semiconducting Polymer Nanoparticles for In Vivo Photoacoustic Imaging.* Advanced Materials, 2015. **27**(35): p. 5184-5190.

392. Liu, Z., W. Cai, L. He, et al., *In vivo biodistribution and highly efficient tumour targeting of carbon nanotubes in mice.* Nature nanotechnology, 2007. **2**(1): p. 47-52.

393. De la Zerda, A., C. Zavaleta, S. Keren, et al., *Carbon nanotubes as photoacoustic molecular imaging agents in living mice.* Nat Nanotechnol, 2008. **3**: p. 557-562.

394. Pu, K., A.J. Shuhendler, J.V. Jokerst, et al., *Semiconducting polymer nanoparticles as photoacoustic molecular imaging probes in living mice.* Nat Nano, 2014. **9**(3): p. 233-239.

395. Guo, L., W. Liu, G. Niu, et al., *Polymer nanoparticles with high photothermal conversion efficiency as robust photoacoustic and thermal theranostics.* Journal of Materials Chemistry B, 2017. **5**(15): p. 2832-2839.

396. Letfullin, R.R., C. Joenathan, T.F. George, et al., *Laser-induced explosion of gold nanoparticles: potential role for nanophotothermolysis of cancer.* 2006. **1**: p. 473-480.

397. Bao, Z., X. Liu, Y. Liu, et al., *Near-infrared light-responsive inorganic nanomaterials for photothermal therapy.* Asian Journal of Pharmaceutical Sciences, 2016. **11**(3): p. 349-364.

398. Mody, V.V., R. Siwale, A. Singh, et al., *Introduction to metallic nanoparticles.* Journal of Pharmacy and Bioallied Sciences, 2010. **2**(4): p. 282-289.

399. Jørgensen, J.T., K. Norregaard, P. Tian, et al., *Single Particle and PET-based Platform for Identifying Optimal Plasmonic Nano-Heaters for Photothermal Cancer Therapy.* Scientific Reports, 2016. **6**.

400. Williams, R.M., J. Shah, B.D. Ng, et al., *Mesoscale Nanoparticles Selectively Target the Renal Proximal Tubule Epithelium.* Nano Letters, 2015. **15**(4): p. 2358-2364.

401. Huang, J., L. Bu, J. Xie, et al., *Effects of Nanoparticle Size on Cellular Uptake and Liver MRI with PVP-Coated Iron Oxide Nanoparticles.* ACS nano, 2010. **4**(12): p. 7151-7160.

402. Sonavane, G., K. Tomoda, and K. Makino, *Biodistribution of colloidal gold nanoparticles after intravenous administration: effect of particle size.* Colloids Surf B Biointerfaces, 2008. **66**(2): p. 274-80.

403. Shilo, M., A. Sharon, K. Baranes, et al., *The effect of nanoparticle size on the probability to cross the blood-brain barrier: an in-vitro endothelial cell model.* Journal of Nanobiotechnology, 2015. **13**: p. 19.

404. Hansen, A.E., A.L. Petersen, J.R. Henriksen, et al., *Positron emission tomography based elucidation of the enhanced permeability and retention effect in dogs with cancer using copper-64 liposomes.* ACS nano, 2015. **9**(7): p. 6985-6995.

405. Sykes, E.A., J. Chen, G. Zheng, et al., *Investigating the impact of nanoparticle size on active and passive tumor targeting efficiency.* ACS nano, 2014. **8**(6): p. 5696-5706.

406. Thorne, R.G. and C. Nicholson, *In vivo diffusion analysis with quantum dots and dextrans predicts the width of brain extracellular space.* Proc Natl Acad Sci U S A, 2006. **103**(14): p. 5567-72.

407. Shilo, M., A. Sharon, K. Baranes, et al., *The effect of nanoparticle size on the probability to cross the blood-brain barrier: an in-vitro endothelial cell model.* Journal of nanobiotechnology, 2015. **13**(1): p. 1.

408. Jain, K.K., *Nanobiotechnology-based strategies for crossing the blood-brain barrier.* Nanomedicine (Lond), 2012. **7**(8): p. 1225-33.

409. Xue, H., B. Lu, and M. Lai, *The cancer secretome: a reservoir of biomarkers.* Journal of Translational Medicine, 2008. **6**: p. 52-52.

410. Nio, K., T. Yamashita, and S. Kaneko, *The evolving concept of liver cancer stem cells.* Molecular Cancer, 2017. **16**(1): p. 4.

411. America, L.I.o., *American National Standard for Safe Use of Lasers* 2000: New York, NY. p. Z136.1-2000.

412. Hoshida, Y., S.M. Nijman, M. Kobayashi, et al., *Integrative transcriptome analysis reveals common molecular subclasses of human hepatocellular carcinoma.* Cancer Res, 2009. **69**(18): p. 7385-92.

413. Stack, E.C., C. Wang, K.A. Roman, et al., *Multiplexed immunohistochemistry, imaging, and quantitation: A review, with an assessment of Tyramide signal amplification, multispectral imaging and multiplex analysis.* Methods, 2014. **70**(1): p. 46-58.

414. Oldenburg, S.J., R.D. Averitt, S.L. Westcott, et al., *Nanoengineering of optical resonances.* Chemical Physics Letters, 1998. **288**(2-4): p. 243-247.

415. Halas, N., *Playing with plasmons: tuning the optical resonant properties of metallic nanoshells.* Mrs Bulletin, 2005. **30**(05): p. 362-367.

416. Wu, T., E. Heuillard, V. Lindner, et al., *Multimodal imaging of a humanized orthotopic model of hepatocellular carcinoma in immunodeficient mice.* 2016. **6**: p. 35230.

417. Lai, Y., X. Wei, S. Lin, et al., *Current status and perspectives of patient-derived xenograft models in cancer research.* Journal of Hematology & Oncology, 2017. **10**(1): p. 106.

418. Mazur, P.K., A. Herner, F. Neff, et al., *Current methods in mouse models of pancreatic cancer.* Methods Mol Biol, 2015. **1267**: p. 185-215.

419. Rengier, F., A. Mehndiratta, H. von Tengg-Kobligk, et al., *3D printing based on imaging data: review of medical applications.* International Journal of Computer Assisted Radiology and Surgery, 2010. **5**(4): p. 335-341.

420. Ventola, C.L., *Medical Applications for 3D Printing: Current and Projected Uses.* Pharmacy and Therapeutics, 2014. **39**(10): p. 704-711.

421. Mironov, V., T. Boland, T. Trusk, et al., *Organ printing: computer-aided jet-based 3D tissue engineering.* Trends in Biotechnology, 2003. **21**(4): p. 157-161.

422. Wang, D., D. Ma, M.L. Wong, et al., *Recent advances in surgical planning & navigation for tumor biopsy and resection.* Quantitative Imaging in Medicine and Surgery, 2015. **5**(5): p. 640-648.

423. Khor, W.S., B. Baker, K. Amin, et al., *Augmented and virtual reality in surgery—the digital surgical environment: applications, limitations and legal pitfalls.* Annals of Translational Medicine, 2016. **4**(23): p. 454.

424. Ukimura, O. and I.S. Gill, *Imaging-assisted endoscopic surgery: Cleveland Clinic experience.* J Endourol, 2008. **22**(4): p. 803-10.

425. Liang, X.-J., C. Chen, Y. Zhao, et al., *Circumventing Tumor Resistance to Chemotherapy by Nanotechnology.* Methods in molecular biology (Clifton, N.J.), 2010. **596**: p. 467-488.

426. Wolinsky, J.B., Y.L. Colson, and M.W. Grinstaff, *Local Drug Delivery Strategies for Cancer Treatment: Gels, Nanoparticles, Polymeric Films, Rods, and Wafers.* Journal of controlled release : official journal of the Controlled Release Society, 2012. **159**(1): p. 10.1016/j.jconrel.2011.11.031.

427. Sun, B., Z. Huang, B. Wang, et al., *Significance of Glypican-3 (GPC3) Expression in Hepatocellular Cancer Diagnosis.* Medical Science Monitor : International Medical Journal of Experimental and Clinical Research, 2017. **23**: p. 850-855.

428. Sun, C.K., M.S. Chua, J. He, et al., *Suppression of glypican 3 inhibits growth of hepatocellular carcinoma cells through up-regulation of TGF-beta2.* Neoplasia, 2011. **13**(8): p. 735-47.

429. Ishiguro, T., M. Sugimoto, Y. Kinoshita, et al., *Anti–glypican 3 antibody as a potential antitumor agent for human liver cancer.* Cancer research, 2008. **68**(23): p. 9832-9838.

430. Phung, Y., W. Gao, Y.G. Man, et al., *High-affinity monoclonal antibodies to cell surface tumor antigen glypican-3 generated through a combination of peptide immunization and flow cytometry screening.* MAbs, 2012. **4**(5): p. 592-9.

431. *Science-Business eXchange.* Distillery Therapeutics Glypican 3 (GPC3). SciBX, 2013. **6**(11).

432. Sneider, A., D. VanDyke, S. Paliwal, et al., *Remotely Triggered Nano-Theranostics For Cancer Applications.* Nanotheranostics, 2017. **1**(1): p. 1-22.

433. Sikkandhar, M.G., A.M. Nedumaran, R. Ravichandar, et al., *Theranostic Probes for Targeting Tumor Microenvironment: An Overview.* Int J Mol Sci, 2017. **18**(5).

434. Choi, K.Y., G. Liu, S. Lee, et al., *Theranostic nanoplatforms for simultaneous cancer imaging and therapy: current approaches and future perspectives.* Nanoscale, 2012. **4**(2): p. 330-342.

435. Yarmolenko, P.S., E.J. Moon, C. Landon, et al., *Thresholds for thermal damage to normal tissues: An update.* International journal of hyperthermia : the official journal of European Society for Hyperthermic Oncology, North American Hyperthermia Group, 2011. **27**(4): p. 320-343.

436. Dewhirst, M.W., B.L. Viglianti, M. Lora-Michiels, et al., *THERMAL DOSE REQUIREMENT FOR TISSUE EFFECT: EXPERIMENTAL AND CLINICAL FINDINGS.* Proceedings of SPIE--the International Society for Optical Engineering, 2003. **4954**: p. 37.

437. van Rhoon, G.C., T. Samaras, P.S. Yarmolenko, et al., *CEM43°C thermal dose thresholds: a potential guide for magnetic resonance radiofrequency exposure levels?* European radiology, 2013. **23**(8): p. 2215-2227.

438. Hall, E.J. and L. Roizin-Towle, *Biological effects of heat.* Cancer Res, 1984. **44**(10 Suppl): p. 4708s-4713s.

439. Dewey, W.C., *Arrhenius relationships from the molecule and cell to the clinic.* Int J Hyperthermia, 1994. **10**(4): p. 457-83.

440. Bear, A.S., L.C. Kennedy, J.K. Young, et al., *Elimination of Metastatic Melanoma Using Gold Nanoshell-Enabled Photothermal Therapy and Adoptive T Cell Transfer.* PLoS ONE, 2013. **8**(7): p. e69073.

441. Hirsch, L.R., R.J. Stafford, J. Bankson, et al., *Nanoshell-mediated near-infrared thermal therapy of tumors under magnetic resonance guidance.* Proceedings of the National Academy of Sciences, 2003. **100**(23): p. 13549-13554.

442. Vogel, A. and V. Venugopalan, *Optical-thermal Response of Laser-irradiated Tissue*, in *Physics in Medicine and Biology*, A. Welch and M. van Gemert, Editors. 2011, Springer Science+Business Media: New York. p. 561-604.

443. Chen, W.R., R.L. Adams, A.K. Higgins, et al., *Photothermal effects on murine mammary tumors using indocyanine green and an 808-nm diode laser: an in vivo efficacy study.* Cancer letters, 1996. **98**(2): p. 169-173.

444. Huang, Y.-F., K. Sefah, S. Bamrungsap, et al., *Selective photothermal therapy for mixed cancer cells using aptamer-conjugated nanorods.* Langmuir, 2008. **24**(20): p. 11860-11865.

445. Melancon, M.P., R.J. Stafford, and C. Li, *Challenges to effective cancer nanotheranostics.* Journal of Controlled Release, 2012. **164**(2): p. 177-182.

446. Ma, Y., X.L. Liang, S. Tong, et al., *Gold Nanoshell Nanomicelles for Potential Magnetic Resonance Imaging, Light-Triggered Drug Release, and Photothermal Therapy.* Advanced Functional Materials, 2013. **23**(7): p. 815-822.

447. Bear, A.S., L.C. Kennedy, J.K. Young, et al., *Elimination of metastatic melanoma using gold nanoshell-enabled photothermal therapy and adoptive T cell transfer.* PLoS One, 2013. **8**(7): p. e69073.

448. Zou, L., H. Wang, B. He, et al., *Current Approaches of Photothermal Therapy in Treating Cancer Metastasis with Nanotherapeutics.* Theranostics, 2016. **6**(6): p. 762-772.

449. Thakor, A.S. and S.S. Gambhir, *Nanooncology: the future of cancer diagnosis and therapy.* CA: a cancer journal for clinicians, 2013. **63**(6): p. 395-418.

450. Cho, W.S., M. Cho, J. Jeong, et al., *Acute toxicity and pharmacokinetics of 13 nm-sized PEG-coated gold nanoparticles.* Toxicol Appl Pharmacol, 2009. **236**(1): p. 16-24.

451. Cho, E.C., J. Xie, P.A. Wurm, et al., *Understanding the role of surface charges in cellular adsorption versus internalization by selectively removing gold nanoparticles on the cell surface with a I2/KI etchant.* Nano Lett, 2009. **9**(3): p. 1080-4.

452. Niidome, T., M. Yamagata, Y. Okamoto, et al., *PEG-modified gold nanorods with a stealth character for in vivo applications.* J Control Release, 2006. **114**(3): p. 343-7.

453. Pillai, G., *Nanomedicines for cancer therapy: an update of FDA approved and those under various stages of development.* SOJ Pharm Pharm Sci, 2014. **1**(2): p. 13.

454. Choi, H.S. and J.V. Frangioni, *Nanoparticles for biomedical imaging: fundamentals of clinical translation.* Molecular imaging, 2010. **9**(6): p. 291.